THE SYNTHESIS OF SEISMIC REFLECTION PROFILES

A dissertation submitted for the degree of

Doctor of Philosophy

at the University of Cambridge

Sandra Gillian Smith

Darwin College

Cambridge

October

1975

PREFACE

Seismic reflection profiling has become an extremely important geophysical method in the fifty years since its inception, and is now the most widely used technique for petroleum exploration. This thesis was inspired by the reflection profiles obtained by Cambridge in the eastern Mediterranean in 1972, which were very different from profiles we had previously obtained in normal oceanic areas, with fascinating and bewilderingly complicated structures. These profiles provoked numerous shipboard discussions on the possible geological interpretations, and it became obvious that we could not separate a simple structure from the complicated record produced by the earth and the instrumental response.

A survey of the literature on seismic reflection profiling revealed that the interpretation of profiles was very imprecise and subject to the whim of the interpreter, and that there was no general method of verifying interpretations. Many geophysicists interpreted profiles as a vertical section through the earth, and although many had realised that this was not correct, no better general methods of interpretation had been developed. The literature survey showed that seismic modelling, which had been used successfully in the interpretation of earthquake records, seismic refraction and variable angle seismic reflections had not been developed for reflection profiling. In this thesis I have examined the effects of the source, the receiver and the earth on a profile and developed a method for the synthesis of reflection profiles, which can be used to test geological interpretations and provide limits on interpretation.

Chapter 1 is a brief introduction to reflection profiling and interpretation problems. Chapter 2 examines the seismic sources and receivers used in reflection profiling and their effect on a profile. Chapter 3 examines the effect of the earth on reflection profiles, and shows how ray theory can be used to describe the propagation of seismic waves. Chapters 2 and 3 are not written as a contribution to theoretical seismology, but to examine the effect of the earth, the source and the receiver on a profile using known theory, and formulae are generally stated without derivation.

Chapter 4 presents a synthetic reflection profiling system which I have developed based on ray theory. Chapter 5 describes the use of this system in modelling standard structures and real profiles, and its use in interpretation.

Chapter 6 describes two reflection profiling grid surveys in the eastern Mediterranean, made in May and June 1974 in order to investigate the effect of side reflections on a profile.

This thesis does not exceed 80,000 words and is my own work except where specific references are made in the text.

Sandra Smith

ACKNOWLEDGEMENTS

Drummond Matthews provided the initial enthusiasm for this thesis, continued encouragement and help, and dynamism during my experiments at sea which was invaluable.

Tim Owen made it possible to get good records by creating such a good reflection profiling system, and I am also very grateful for his willingness to listen to my wilder ideas and for being able to bring them back within the bounds of reality. Anton Ziolkowski made me aware of the painful problems of causality and I thank him for his continued help and patience. Brian Kennett was always willing to discuss problems, and his enthusiasm for all types of seismology was very encouraging. Colin Brewitt-Taylor and David Wright have solved inumerable computing problems, and Derk Jongsma and John Woodside were very helpful in my understanding of the eastern Mediterranean.

The British Petroleum company tolerantly allowed me to learn data processing and industrial seismology with them, and I thank Peter O'Brien, Jack Hosken and Andrew Lucas at Sunbury, Bob Wilkinson and John Fisher at B.P. House.

The N.E.R.C. provided me with a re search grant for two years, and the Department of Geodesy and Geophysics supported me for my final year.

Finally I should like to thank the officers and crew of R.R.S. Shackleton and the members of the marine group at Cambridge who not only helped with my experiments and made them possible, but also made being a mariner very enjoyable.

CONTENTS

CHAPTER 1

SEISMIC REFLECTION PROFILING AND INTERPRETATION PROBLEMS

1.1 Seismic Reflection Profiling

Artificially generated seismic waves can be used to study the earth in three basic ways (Fig 1.1). Reflection profiling uses a source and receiver close together and looks at a narrow section of the earth approximately below the shot point. Moving the source and receiver between shots builds up a continuous seismic profile of the earth along the line of the shot points. The reflections are approximately normal to the interfaces because of the near coincident source and receiver. A detailed description of the reflection profiling method is given in a department internal report (Smith 1972).

Variable angle reflections have a larger source and receiver separation, and seismic waves travel a greater horizontal distance in the earth. These can be used with a constant separation of source and receiver array, moving both of them between shots, as is done with a ship towing an explosive source and a receiver array, or a changing source and receiver separation by movement of the source, receiver or both, as in a two ship experiment with a shot-firing ship steaming away from a ship towing a receiver array. Variable angle reflection has the advantage over profiling that the moveout reflection curves generated by different source and receiver separations can be used to determine velocities.

Seismic refraction uses a larger source and receiver separation such that the angle of incidence at an interface reaches the critical angle, and head waves are generated in the lower layer, which travel large horizontal distances or can be transmitted back to the surface (Fig.1.1). Velocities can be determined because of horizontal head wave paths.

Reflection methods use frequencies above about 10 Hz, as below this frequency the wavelength can become comparable to the bed thickness, and there is interference between reflections from the top and bottom of a bed, which gives a reflection coefficient that varies with frequency. Refraction techniques can use lower frequencies, and can be used to obtain information from greater depths, because penetration is mainly limited by attenuation and this is least for low frequencies.

Reflection profiling is most suitable for use in laterally inhomogeneous areas as each shot looks at only a narrow section of the earth.

1.2 Interpretation Problems

The ideal reflection profile would be a true representation of the geological structure, from which the physical properties of the layers and interfaces could be deduced. In practice a reflection profile is more complicated because of the following effects:

Source and receiver distortion

An ideal source would be a single high amplitude spike, which would have a high resolving power, but long enough in time to have significant energy. Although such a source does not exist a chemical explosive in the absence of interfaces may approximate to this ideal. Other sources generally have worse source waveforms than this and may be very oscillatory and of long duration, giving low resolving power (Chapter 2.2). This complicates records as instead of an ideal short spike for each reflection there is a longer waveform which may overlap other arrivals.

Receivers also affect the record as they are usually frequency band limited due to the electrical response of the receiver, and angular and frequency limited due to the geometry of the receiver array (Chapter 2.4) all of which distort the received waveform.

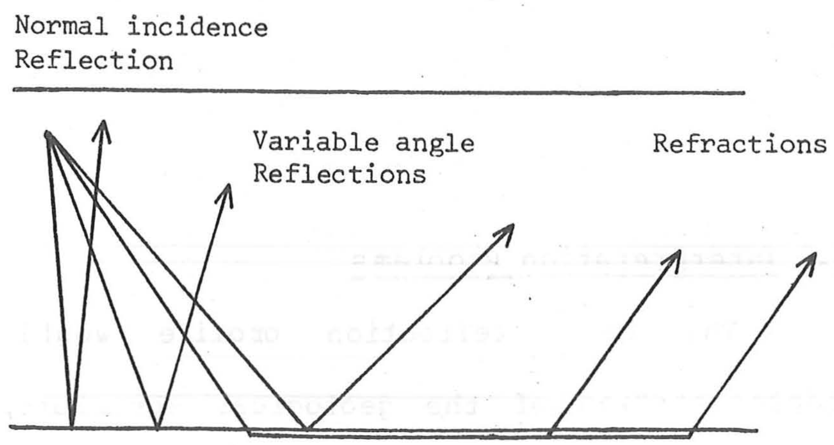

Fig. 1.1
Seismic reflection profiling, variable angle reflections and refractions

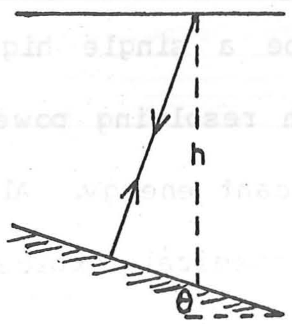

Fig.1.2
The ray path for dipping interfaces

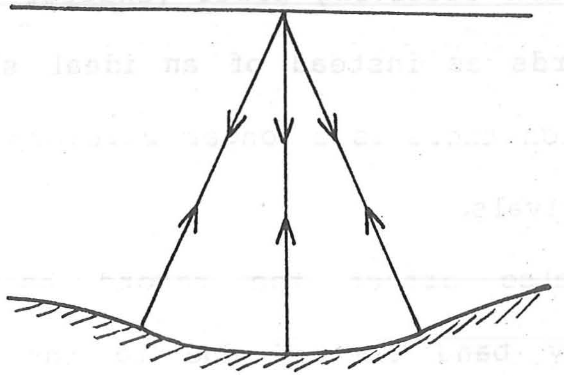

Fig 1.3
The ray paths for reflections from a curved reflector

Geometrical distortion

Seismic sources do not just radiate energy in a desired downward direction, but are omnidirectional. The depths of interfaces can be calculated from the profile by using velocities to convert travel times to depths only if interfaces are planar and horizontal. Dipping interfaces appear shallower on the profile than their true position as the normal incidence reflection occurs at an angle to the vertical (Fig.1.2). The apparent depth decreases with higher angles of dip: the ray travels a distance $h\cos\theta$ where h is the true depth of the interface vertically below the shot point. Structures recorded on reflection profiles are different from the true structure because of this. A curved reflector may give reflections from more than one point on a reflector for every shot point, producing a very complicated profile (Fig.1.3). Generally if the curvature of the reflector exceeds that of the wavefront, more than one reflection will originate from it.

Reflection profiling attempts to build up subsurface information along a line, in two dimensions. The profile appears two-dimensional, but contains reflections from three dimensions unless the structures are infinitely extended in the plane perpendicular to the profile. Side reflections are non-vertical reflections which come from out of the plane of the profile. Interpretation of the profile as a two-dimensional structure needs to distinguish side reflections, but this is difficult to do. Stacking of traces during data processing attenuates side reflections to some extent, and in some cases it is possible to recognise side reflections by their character — position, shape and frequency content.

Physical distortion

The earth itself produces undesired effects, such as a free surface reflection, multiple reflections, attenuation and dispersion, diffractions and wave conversions (Chapter 3) which make interpretation more difficult.

1.3 Interpretation techniques

Digital processing of records can produce a clearer record for interpretation; the signal to noise ratio can be increased to help identification of reflectors, multiples can be attenuated, the source waveform can be condensed in time to a shorter waveform, and reflectors can be migrated to their true depth and position. This gives a profile which appears to be almost a geological section, and is much easier to interpret, but demands a large amount of computer time and contains distortions in the amplitude and shape of the arrivals due to the processing. This distortion may not be important if the profiles are used only for measuring travel times, but a lot of information about the reflector and the earth above it is contained in the arrival amplitude and shape, and may be lost.

An alternative method of interpretation is synthesis of a seismic profile from a geological model, for comparison with the measured profile. This gives a validity check on interpretations, provides a test of alternative interpretations and limits on the interpretation, and is the only means of understanding very complex areas where processing is not usually very effective.

This thesis uses the second approach, synthesis of profiles. Synthetic seismograms are commonly used in earthquake interpretation and refraction and variable angle reflection interpretation, but a method of synthesis of reflection profiles has not been published.

The synthetic system developed in this thesis is for marine profiles as the real profiles used as a basis for modelling are marine. Similarly, the source and receiver used in the calculation of the source waveform and the receiver effect are those used in the Cambridge reflection profiling system. The synthetic system may be altered simply to model land profiles, or to allow for a different source and receiver.

CHAPTER 2

THE SOURCE AND RECEIVER EFFECT

2.1 Introduction

This chapter examines the waveforms that make up a received reflection profile and the way in which these can be synthesized. In order to model a received waveform it is necessary to know the source waveform, the effect of the sea surface reflection on the source waveform, the response of the array as a multiple detector, the effect of the sea surface reflection at the receiver and its electrical response. Whilst the source waveform and the electrical response of the receiver are constant and need only be calculated once for each model, the sea surface reflection and array effects are dependent on the ray path and must be calculated searately for each arrival.

Processing of records tends to eliminate the different effects of source and receiver for each arrival, by stacking of records and by deconvolution, which uses an operator calculated from a whole trace, not for each arrival. Processed records can only be modelled if a modelling system with variable source-receiver offsets is developed and the model for each offset processed by the same techniques applied to the real records.

2.2 Sources

Types

A comprehensive discussion of seismic sources is given in Kramer et al (1968), and sources and their characteristics will only be mentioned briefly here.

Chemical explosive may be used as a reflection profiling source, but in its basic form this is rare, due to a low repetition rate, dangerous nature and inefficiency. It is more commonly used in a form where a semi-automatic form of firing is possible in a more efficient way, such as the Flexotir system, where a small charge is fired in a perforated steel sphere, which damps out oscillations, or a line charge which has very little oscillation.

Airguns are a useful sound source as they are effecient, safe, and can have a relatively high repetition rate. Their main disadvantage is a very oscillatory signal, although this can be reduced (see next section).

Sparkers and gas exploders are lower power sources. They are safe and have a high repetition rate, but also have an oscillatory signal.

Characteristics

Sources are omnidirectional unless one of their dimensions is comparable to the seismic wavelength. A line explosive is the only source in general use which is not omnidirectional, and it has a directionality in the vertical plane through the line source and the maximum energy is transmitted in a downward direction at a small angle to the vertical, (Kramer et al 1968, Limond 1972).

The arrival of the detonation front from a chemical explosive at the water boundary or the release of a volume of air at high pressure into the water radiates an intense pressure wave outwards. The pressure rise is almost instantaneous, and is followed by a slower decay, producing a radiated shock wave with a steep front and a roughly exponential decay. If the peak pressure is very high the water behaves inelastically and the velocity of the wave depends on the pressure. The peak pressure decreases very rapidly due to heat dissipation, faster than the inverse first power law of distance for acoustic waves, until the pressure has dropped sufficiently and the wave becomes an acoustic wave.

The gas bubble continues expanding after radiating the shock wave, the internal pressure decreasing until it reaches the ambient pressure, but outward motion persists because of the inertia of the water. The bubble begins to contract because the internal pressure becomes lower than the ambient pressure, until resistance to compression of the gas stops the contraction rapidly as the internal pressure increases above the ambient and the bubble begins to expand, producing an oscillating system, which radiates a pressure wave with each oscillation. Although the bubble pulses are much lower in peak pressure amplitude than the initial shock wave, they radiate an appreciable amount of seismic energy because of their considerably longer time duration.

The bubble pulses are a nuisance as they lengthen the signal and decrease its resolving power. There are two general ways of reducing the bubble pulses; to suppress them at the source or remove them from the record by processing. Suppression of the bubble pulses at the source can be done by using the source near the surface so that the bubble blows out at the surface instead of oscillating, although this is very wasteful of energy; by damping the oscillating bubble by cage-like devices which reduce the bubble pulses significantly but also reduce the intial pulse slightly (for example the Flexotir seismic system and airgun wave-shaping devices); by throttling further air into the bubble to keep the pressure above the ambient and prevent it from bubble begins to contract because the internal pressure becomes lower than the ambient pressure, until resistance to compression of the gas stops the contraction rapidly as the internal pressure increases above the ambient and the bubble begins to expand, producing an oscillating system, which radiates a pressure wave with each oscillation. Although the bubble pulses are much lower in peak pressure amplitude than the initial shock wave, they radiate an appreciable amount of seismic energy because of their considerably longer time duration.

The bubble pulses are a nuisance as they lengthen the signal and decrease its resolving power. There are two general ways of reducing the bubble pulses; to suppress them at the source or remove them from the record by processing. Suppression of the bubble pulses at the source can be done by using the source near the surface so that the bubble blows out at the surface instead of oscillating, although this is very wasteful of energy; by damping the oscillating bubble by cage-like devices which reduce the bubble pulses significantly but also reduce the intial pulse slightly (for example the Flexotir seismic system and airgun wave-shaping devices); by throttling further air into the bubble to keep the pressure above the ambient and prevent it from oscillating, although this also reduces the initial amplitude (airgun wave-shaping devices); by the use of tuned airgun arrays of different size guns so that the initial pulse from each gun adds together but the bubble pulses cancel; by using a line source, which has a reduced bubble pulse, or by using an implosion device from which no oscillating bubble is produced. These methods cause either a reduction of the energy in the source waveform, or need a more complicated source, so many systems use sources with bubble pulses and attempt to remove them from the record by data processing. An account of this is given by Treitel and Robinson (1969).

The amplitude of a chemical explosion is related to charge weight by:

$$\text{Amplitude} = b\ W^k$$

where W = weight of explosive. The best value of k for marine explosions in the 0-100 Hz band seems to be $^2/_3$ (O'Brien 1960, Barnhard 1967, Blundell & Parks 1971). The amplitude also increases with depth but not in a simple manner. The first bubble pulse period is related to explosive weight and depth by:

$$T_1 = \frac{2.6\ W^{1/3}}{(h+10)^{5/6}}$$

(Lavergne 1970)

where W is in Kg and h is the depth in m. The period decreases slightly for successive pulses.

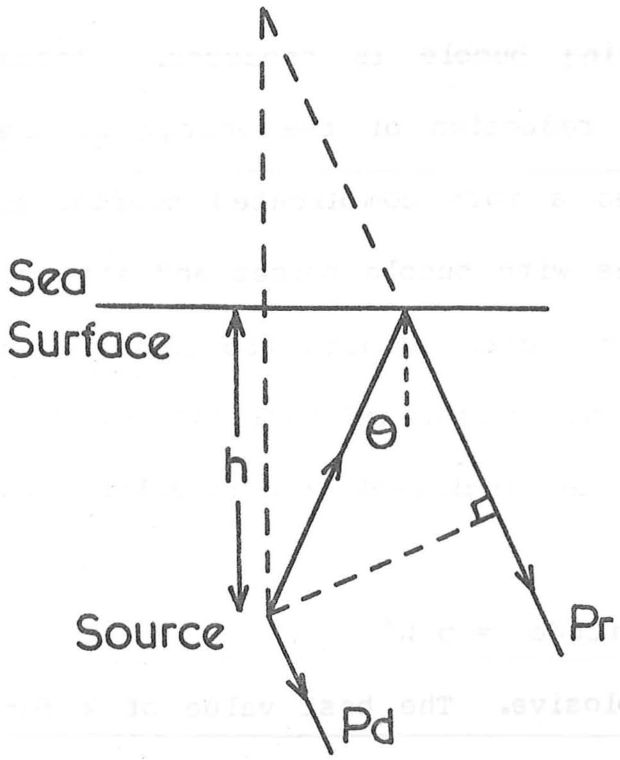

Fig. 2.1

The sea surface reflection effect

For airguns, bubble pulse periods increase and frequencies decrease with higher air pressures, larger chamber volumes and shallower depths (Giles 1969, Ziolkowski 1970, Schulze-Gatterman 1972). Therefore to get the lowest frequencies and greatest penetration larger weights of explosive or high pressure, large volume airguns should be used at shallow depths. However a lot of energy is lost at shallow depths when the bubble breaks the surface, and the sea surface reflection interferes with the direct wave cancelling some downwards-directed energy.

The sea suface reflection effect

Energy that is radiated towards the sea surface is reflected back downwards and interferes with the direct downward ray from the source (Fig. 2.1). The downward travelling source waveform is a combination of the direct wave, Pd, and the reflected wave, Pr (Fig. 2.3, after Ziolkowski 1971). If the water depth is large compared with the source depth, Pd and Pr are parallel, and Pr has a time delay of $2h\cos\theta/v$ where v is the water velocity. For a sufficiently large water depth the amplitudes of Pd and Pr in the combined wave will be equal, but Pr will have an opposite sign as the sea surface reflection coefficient is -1. (Compare with section 2.3 where the waveform is measured at a non-infinite distance). The sea surface reflection effect alters the frequency spectrum of the waveform, as frequencies with a wavelength which is an integral multiple of 2hcosθ are cancelled, and frequencies with a wavelength given by:

$$2h\cos\theta = (2n-1)\,\lambda/2$$

are enhanced, where n is a positive integer. The downward travelling energy is a maximum if the bubble pulse frequency is enhanced. For an oscillation frequency of 20 Hz and a vertically downward travelling wave the energy is maximised at a depth of 12.5 m.

There is an equivalent sea surface reflection effect at a receiver.

The sea surface reflection effect is effective in any vertical plane through the source or receiver.

<u>Source waveforms for a reflection profile modelling system</u>

A modelling system needs a source waveform for each of many ray paths, with varying values of θ. Pd must be known independently of Pr to calculate the combined waveform, and Pd may be calculated or measured. It cannot be obtained from the profile by processing as this contains also the effects of Pr, the earth and the receiver for many ray paths.

1. Prediction

This has been attempted for chemical explosions by various authors (eg Arons 1948, O'Brien 1960) and for marine airguns by Ziolkowski (1970) and Schulze-Gattermann (1972) using bubble oscillation theory.

2. Measurement

It is difficult to measure Pd independently of Pr, as although very near the source the amplitude of Pd is much greater than Pr, the near-field of the source has non-linear wave propagation and the waveform measured is not the far-field waveform. The waveform will also change with variations in depth of the source and it is necessary to measure the waveform continuously during profiling, which is difficult in practice.

Because of these problems, if the waveform can be predicted accurately it is better and easier to use than measured waveforms. The Cambridge profiling system uses airguns as a sound source, and in May 1973 I measured airgun waveforms under carefully controlled experimental conditions for comparison with predicted waveforms. The next section describes this experiment. No attempt has been made to separate Pd and Pr; the waveforms are compared with waveforms predicted with Pd and Pr. Previous attempts have been made to measure airgun waveforms (Giles 1968, Ziolkowski 1970, Mayne and Quay 1971, Schulze-Gattermann 1972, Giles and Johnston 1973)

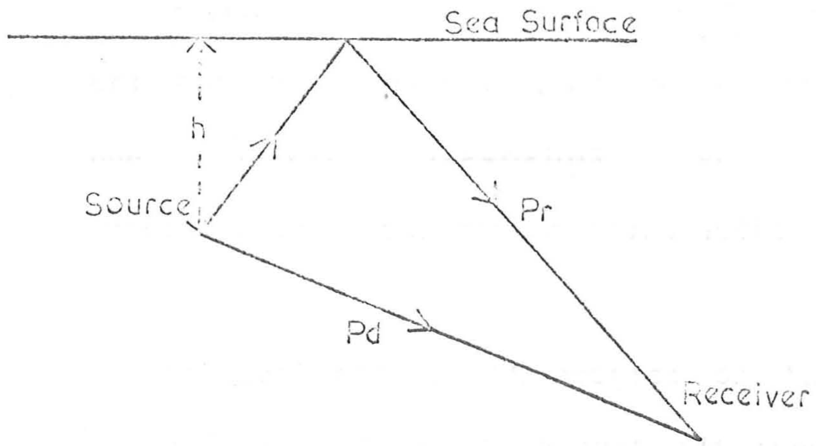

Fig. 2.2
The direct wave, Pd, and the reflected wave,Pr.

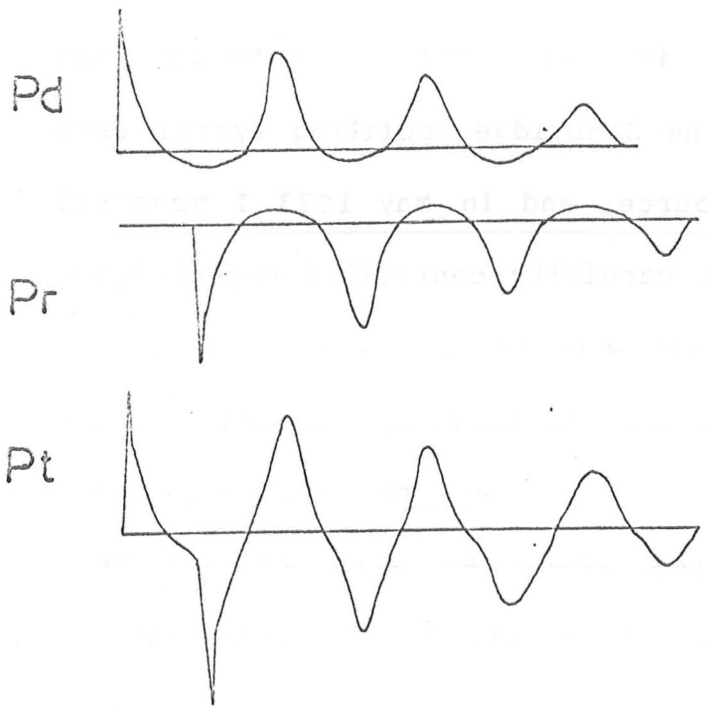

Fig. 2.3
The measured wave, Pt, formed from Pd and Pr.

but these do not satisfy all the requirements for a carefully controlled measurement.

2.3 The measurement of airgun waveforms

The requirements for measurement are:

1. Known impulse response of the recording system.
2. Adequate depth of water so that energy reflected from the sea bed does not interfere with direct sound to the receiver.
3. Known geometry of gun and receiver. A receiver records a direct wave from the gun and also a wave reflected from the sea surface. (Fig. 2.2) The shape of the waveform recorded depends on the distance travelled by the direct wave, Dd, and the distance travelled by the reflected wave, Dr. Fig. 2.3 is after Ziolkowski (1971) and shows the direct waveform, Pd, the reflected waveform, Pr, and Pt, the received waveform, which is the sum of Pd and Pr. The relative amplitudes of Pd and Pr in Pt is given approximately by the ratio:

$$Pd:Pr = Dr:Dd$$

assuming symmetrical spreading and amplitude inversely proportional to distance travelled, for small amplitude oscillations. As Dd becomes larger the amplitudes of Pd and Pr in Pt tend to be equal.
4. Measurement at sufficient depth. I wished to measure

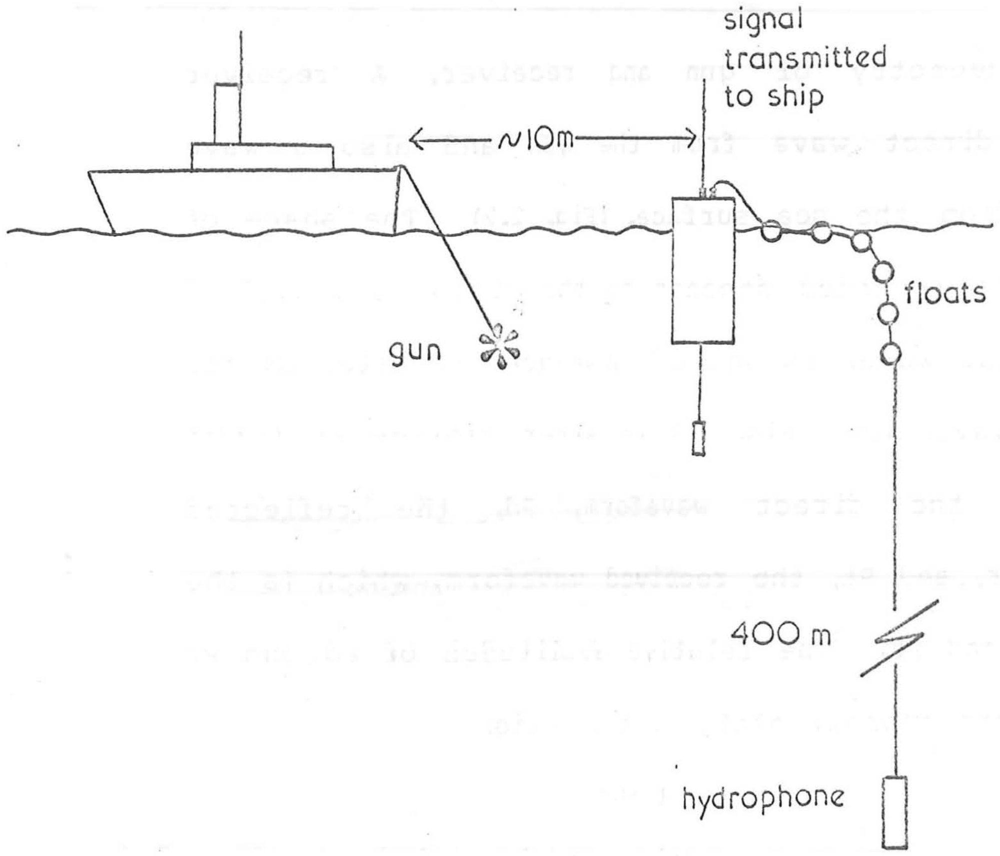

Fig. 2.4
The experimental arrangement used for measuring airgun waveforms.

airgun waveforms produced by a gun when it is being used for deep sea profiling, in water depths of usually greater than 2 km. As the recorded waveform varies with the geometry of source and receiver it is necessary to have a receiver at this depth to measure the waveform going into the sea bed. Unfortunately the waveform reflected from the sea bed would interfere with the downgoing wave for a reflector near the sea bed, so this is impossible. In practice it is necessary to record an approximation to the deep sea waveform. When the receiver is vertically below the gun:

$$Dr = Dd + 2h$$

where h is the gun depth, and when the receiver is sufficiently deep so that Dd >> 2h:

$$Dr/Dd \simeq 1$$

so that Pd/Pr $\simeq$ 1 in Pt and the waveform is a sufficient approximation to that measured at depth. For less than 5% error in Dr/Dd = 1 this demands a Dr > 400 m with h = 10 m.

Experimental Measurement

The experimental arrangement is shown in Fig. 2.4. A hydrophone (a cylindrical lead titanate-zirconte pressure transducer potted in epoxy resin) and a pre-amplifier were suspended 400 m below a sonoradio buoy. The hydrophone was weighted to keep it vertically below the

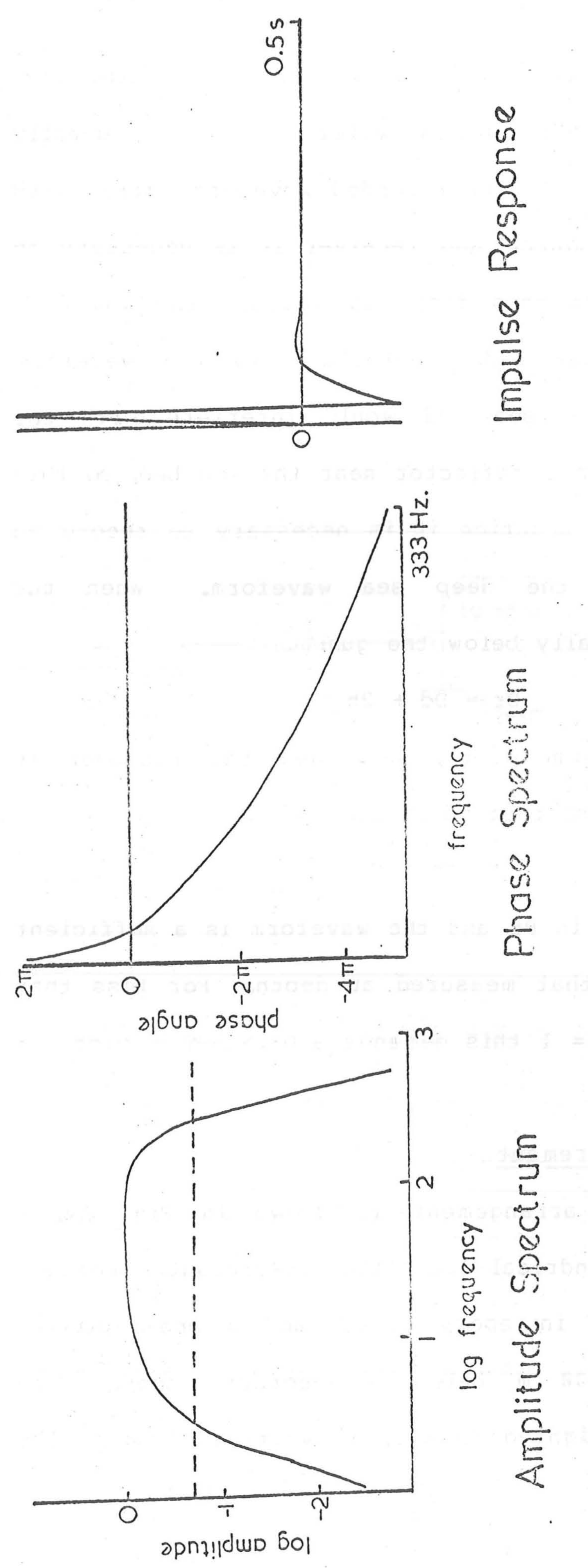

Fig. 2.5
The amplitude and phase spectra of the recording system and impulse response of the system.
The amplitude spectrum above the dashed line is measured and the spectrum below the dashed line is calculated.

buoy , and vertical motions of the cable due to up and down movement of the buoy were damped out by spherical floats attached to the top of the cable. This kept the 400 m of cable approximately stationary in the water while the buoy moved up and down with the waves. The ship steamed slowly past the buoy firing a Bolt airgun, passing within 10 m of the buoy. Gun chamber sizes of 160 in^3 and 300 in^3 were used. A calibrated pressure transducer was used continuously to monitor the gun depth. Airgun signals were transmitted from the buoy to the ship, displayed on a jet-pen recorder and recorded on magnetic tape. This was repeated with the gun at different depths.

The impulse response of the whole recording system from hydrophone to tape recorder was measured: a fixed frequency voltage was input in series with the hydrophone, passed through the recording system, compared with the input signal, and amplitude and phase shift measured. The details of the measurement and the results are in a department internal report (Smith & Owen 1973). It was not possible to define the low amplitude parts of the frequency response accurately by measurement, so these were calculated from electrical circuit theory (Girling & Good 1969). At higher amplitudes the calculated response was in agreement with

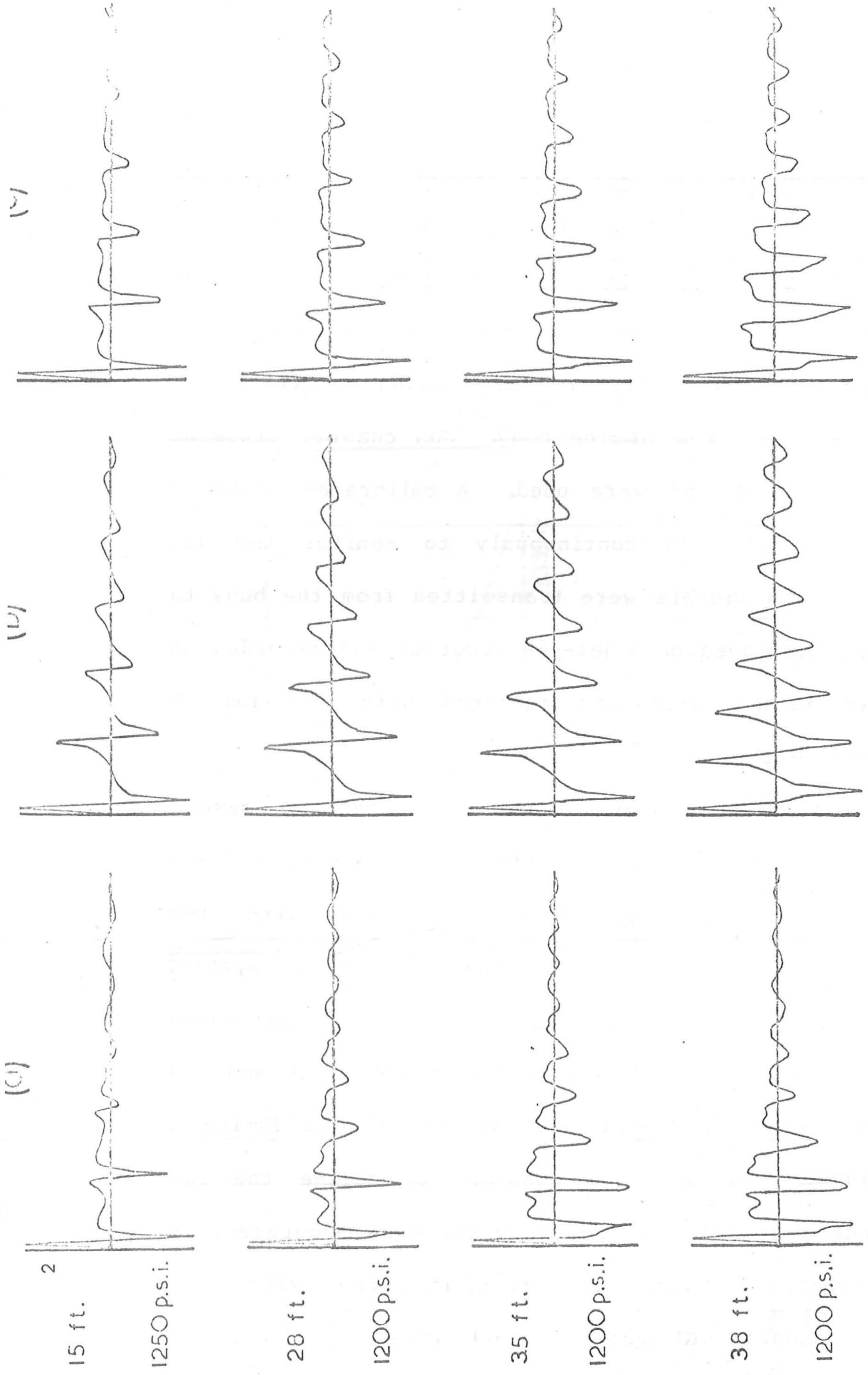

Fig. 2.6 160 in^3 gun. (a) measured waveform; (b) theoretical waveform; (c) theoretical waveform convolved with the impulse response of the recording system. Amplitudes are normalised and the waveform duration is 0.5 s.

the measured response. The amplitude and phase spectra for the recording system and the impulse response of the system (the Fourier transform of the frequency spectrum) are shown in Fig. 2.5. The pass band of the system is 4-160 Hz at -3 dB level.

Results

The waveforms recorded for the 160 in^3 and 300 in^3 guns are shown in Figs. 2.6a and 2.7a.

Attempts have been made to predict airgun waveforms from bubble oscilation theory by Ziolkowski (1970) and Schulze-Gattermann (1972). Schulze-Gattermann's theory applies to small amplitude oscillations, whereas Ziolkowski's allows for finite amplitude oscillation, so is more useful. Ziolkowski's theory was used to compute airgun waveforms for the same conditins of chamber volume, firing pressure, depth and geometry of gun and receiver as the measured waveforms. Damping constants of 2.5 and 1.8 s^{-1} were chosen for the 160 and 300 in^3 guns, as this provided the best match to the measured waveforms. This is in agreement with the damping constant of $31.6/\sqrt{V}$ where V= gun chamber volume in in^3 suggested by Ziolkowski (pers.comm.). These predicted waveforms are shown in Figs. 2.6b and 2.7b. After convolution with the impulse response of the recording system they are shown in Figs.

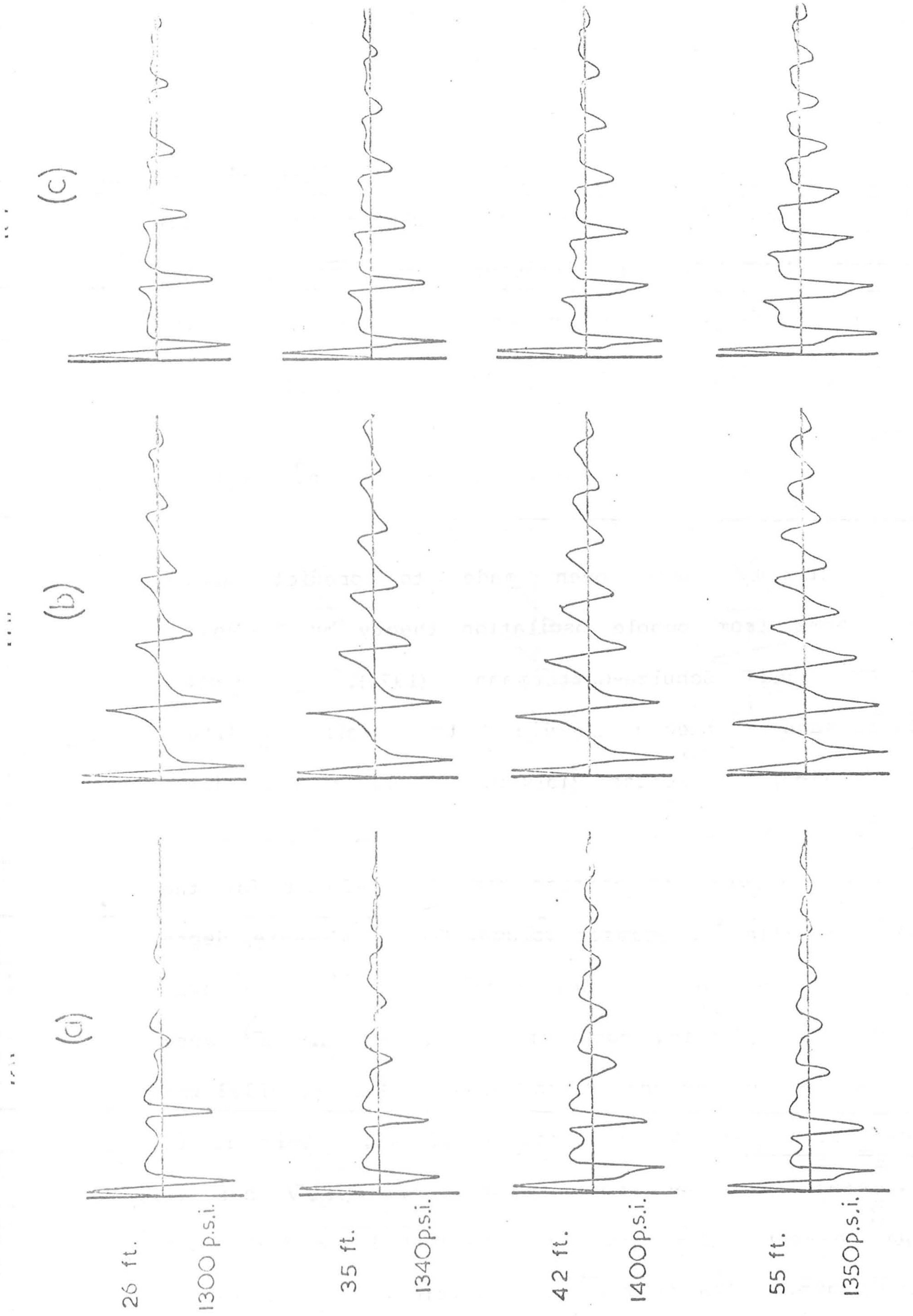

Fig. 2.7 300 in^3 gun. (a) measured waveform; (b) theoretical waveform; (c) theoretical waveform convolved with the impulse response of the recording system. Amplitudes are normalised and the waveform duration is 0.5 s.

2.6c and 2.7c, for comparison with the measured waveforms.

The general form of the convolved waveforms approximates to the measured waveforms, indicating that bubble oscillation theory provides a reasonable description of airgun waveforms. The main difference is that the bubble oscillation period decreases slightly faster than predicted. Ziolkowski (1970) noted this, and suggested that this was due to the proximity of the air-water free surface.

2.4 Receivers

Introduction

Receivers are designed to produce the maximum signal to noise ratio for the required signals. By using N detectors, over which the signal correlates but the noise does not a $\sqrt{N}$ increase in signal to noise ratio can be achieved. A comprehensive discussion of sources of noise for marine arrays is given by Bedenbender (1970).

Ambient sea noise is dependent on the sea state and Bedenbender reports that this effect is greatest at low frequencies, and that the noise level increases by 18 dB as the sea state increases from 0-6. The ship generated noise, from the propeller, engines and other machinery is minimised by the use of a longitudinal array of detectors which discriminates against signals from its ends which are not in phase over the array, and is also reduced by using a long lead cable from the ship to the array. Long cables have the disadvantage of picking up electrical noise from the ship's power supply and radio transmissions, and the latter can completely swamp the seismic signal. Flow noise is caused by passage of the array through the water; this is least at low speeds, and is reduced by towing the array at depths out of the area of wave noise by weighting the end of the towing cable, and by using neutrally buoyant streamer sections filled with oil of known density to keep the streamer horizontal in the water. There is mechanical noise due to longitudinal surges and transverse motion of the array; the effect of longitudinal surges is reduced by using a spring section at the head of the array to damp out ship vibrations and accelerations, and by using pairs of hydrophones connected together back to back so that accelerations are cancelled; transverse motion is reduced by using a long tail rope attached to a floating buoy which provides a continuity of tension at the end of the array and reduces the tendency of the array to snake.

The frequency response of a hydrophone is usually a few Hz to KHz so it is sufficiently broad band that the signal is not distorted, although the recording electronics reduces the high frequency cutoff to hundreds of Hz.

The effect of receivers on a waveform

There are three effects, the electrical response of the receiver, the associated electronics and display system, the sea surface reflection effect, and the line array effect, the last two of which are dependent on the ray path of the reflection.

1. The electrical response of the receiver

The impulse response or frequency response of the receiver must be measured, or if the system is simple , calculated. This may be done by measuring the response of the system to an impulse, which is difficult to do in practice as an impulsive delta function theoretically has no energy, and system noise makes the measurement unreliable, or by measuring the system response to a step function and differentiating the output, or by measuring the amplitude and phase shift at individual frequencies over the frequency range. The hydrophones must also have a uniform frequency response with variations in pressure amplitude over this range.

The Cambridge system uses a Géomechanique streamer whose electrical response is given by Géomechanique, with a Cambridge designed input amplifier and analogue tape the signal is not distorted, although the recording electronics reduces the high frequency cutoff to hundreds of Hz.

The effect of receivers on a waveform

There are three effects, the electrical response of the receiver, the associated electronics and display system, the sea surface reflection effect, and the line array effect, the last two of which are dependent on the ray path of the reflection.

1. The electrical response of the receiver

The impulse response or frequency response of the receiver must be measured, or if the system is simple , calculated. This may be done by measuring the response of the system to an impulse, which is difficult to do in practice as an impulsive delta function theoretically has no energy, and system noise makes the measurement unreliable, or by measuring the system response to a step function and differentiating the output, or by measuring the amplitude and phase shift at individual frequencies over the frequency range. The hydrophones must also have a uniform frequency response with variations in pressure amplitude over this range.

The Cambridge system uses a Géomechanique streamer whose electrical response is given by Géomechanique, with a Cambridge designed input amplifier and analogue tape

B.

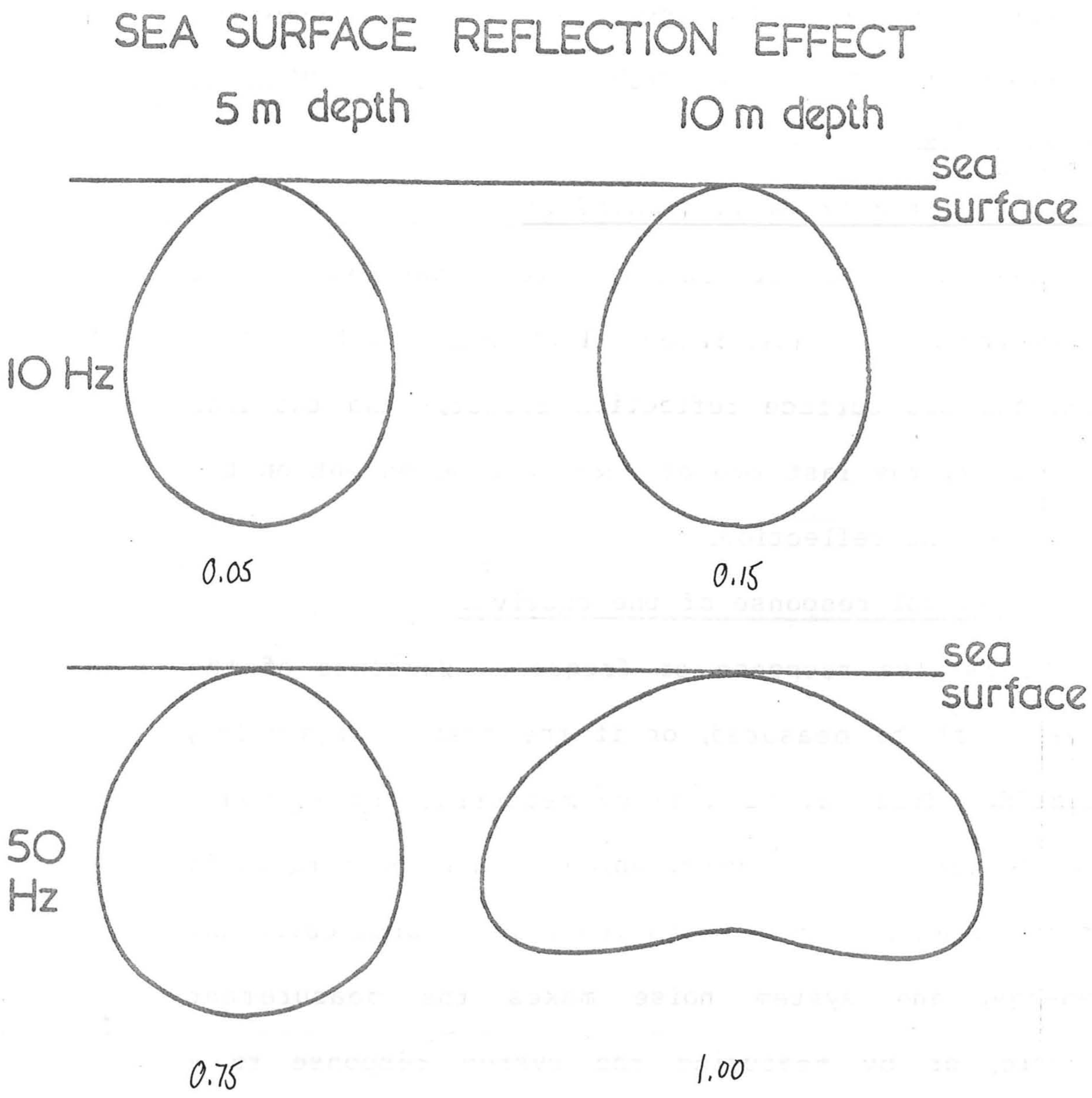

Fig. 2.8
Polar plots of the angular response of the sea surface reflection effect at a point detector for frequencies of 10 and 50 Hz and depths of 5 and 10 m.

Amplitudes have been normalised; the relative maximum amplitudes pre-normalisation are given.

recording system and output in variable intensity, variable area or wiggly line formats. The response of the system was calculated and is described in detail in a department internal report (Smith and Owen 1975) and this is used in modelling reflection profiles (Chapter 5).

2. The sea surface reflection effect

This is similar to the effect on a source waveform; the waveform arriving at a point detector is a combination of the direct wave from the sea bed and the wave reflected at the sea surface which is delayed in time and has a sign reversal. It provides some frequency and angular discrimination, varying with depth, and the effect for different depths and frequencies was computed and is shown on a polar diagram in Fig. 2.8. The effect discriminates against arrivals at high angles of incidence, and in any vertical plane through the detector, not just in the plane of the array; it is this effect which provides the only angular discrimination for side reflections. For higher frequencies and larger depths the maximum response is not in the vertically downwards direction (Fig. 2.8).

It is difficult to visualize the effect of the sea surface reflection on a received waveform from the polar plots of Fig. 2.8, so I computed the effect on two waveforms for various receiver depths. This used an

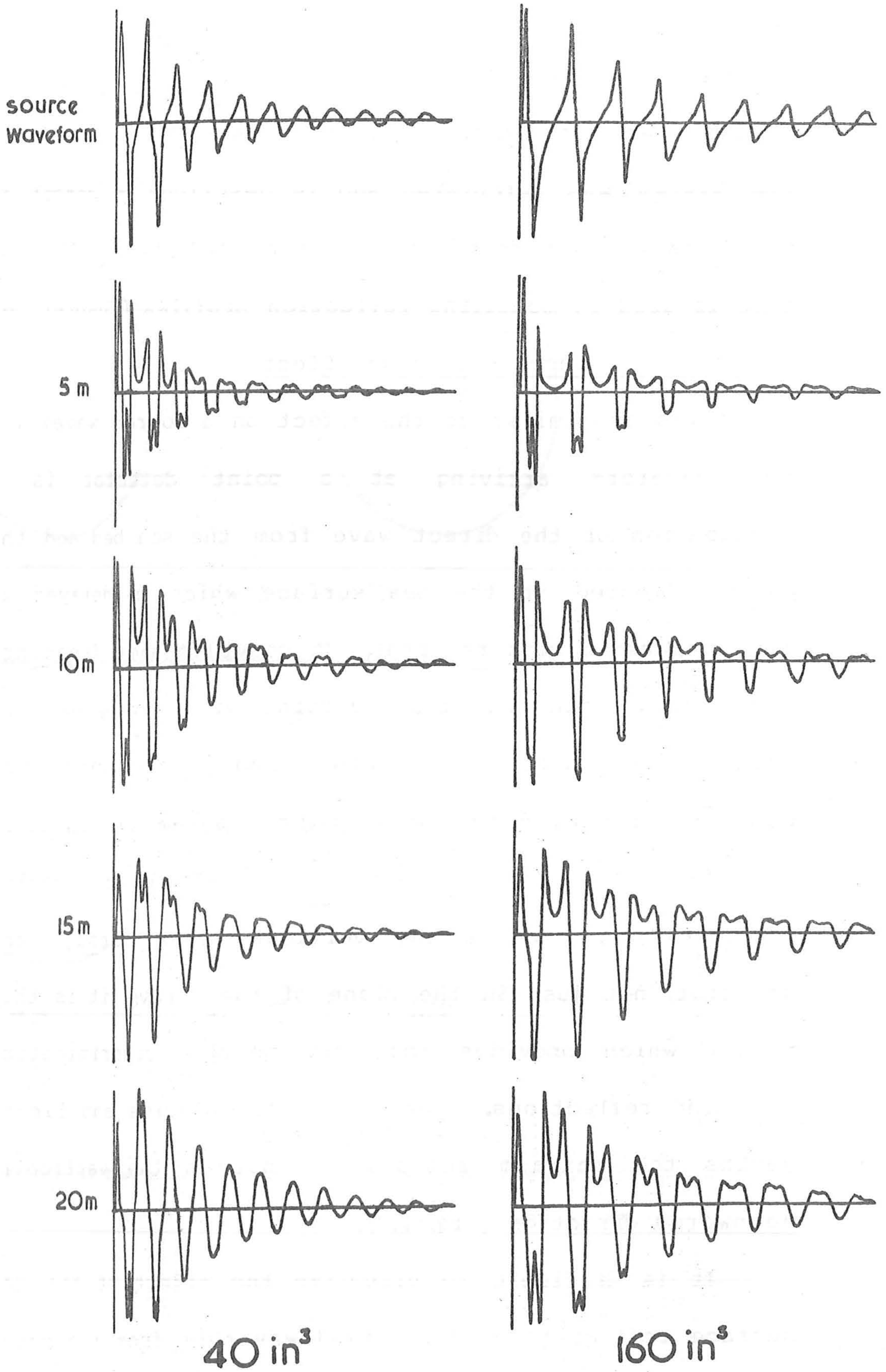

Fig. 2.9
The effect of the sea surface reflection at a receiver on theoretical 40 and 160 in^3 airgun waveforms for different receiver depths and vertical incidence. The source waveform is predicted from the theory of Ziolkowski (1970) and includes a sea surface reflection at the source at a depth of 12 m. Amplitudes are normalised and the waveform duration is 0.5 s.

airgun waveform predicted by the theory of Ziolkowski (1970), and combined this with its sea surface reflection to give a source waveform. The received wave was formed by a combination of this with the wave reflected from the sea surface above the receiver for various depths. The effect changes the waveform character considerably (Fig. 2.9) and it may become very asymmetric, but the effect is very dependent on the source waveform used and the receiver depth and angle of incidence.

3. The line array effect

This effect provides an angular discrimination in the plane of the array, and occurs when the wave incident at the receiver is not vertical, and the wavefront reaches one detector in the array before the next (Fig. 2.10). The array response is the sum of the simultaneous arrivals at all the detectors, so there is the possibility of enhancement of some frequencies in the waveform and discrimination against others, depending on the time delay between the wave reaching adjacent receivers; if this is a complete wave period this frequency will be enhanced.

Most arrays consist of equally spaced hydrophones that contribute equally to the combined waveform, but arrays with variable gains and spacing can be used to

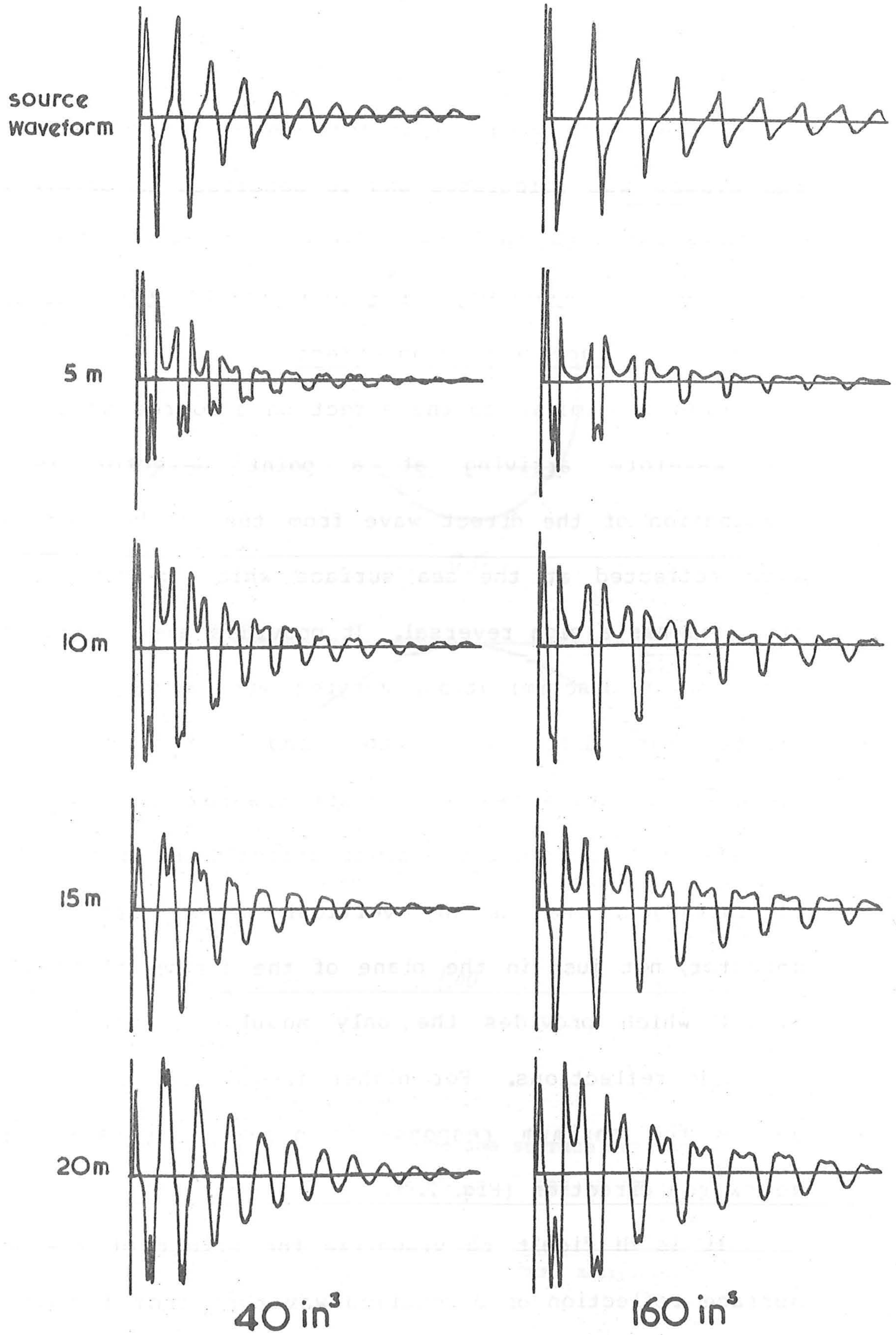

Fig. 2.9

The effect of the sea surface reflection at a receiver on theoretical 40 and 160 in^3 airgun waveforms for different receiver depths and vertical incidence. The source waveform is predicted from the theory of Ziolkowski (1970) and includes a sea surface reflection at the source at a depth of 12 m. Amplitudes are normalised and the waveform duration is 0.5 s.

airgun waveform predicted by the theory of Ziolkowski (1970), and combined this with its sea surface reflection to give a source waveform. The received wave was formed by a combination of this with the wave reflected from the sea surface above the receiver for various depths. The effect changes the waveform character considerably (Fig. 2.9) and it may become very asymmetric, but the effect is very dependent on the source waveform used and the receiver depth and angle of incidence.

3. The line array effect

This effect provides an angular discrimination in the plane of the array, and occurs when the wave incident at the receiver is not vertical, and the wavefront reaches one detector in the array before the next (Fig. 2.10). The array response is the sum of the simultaneous arrivals at all the detectors, so there is the possibility of enhancement of some frequencies in the waveform and discrimination against others, depending on the time delay between the wave reaching adjacent receivers; if this is a complete wave period this frequency will be enhanced.

Most arrays consist of equally spaced hydrophones that contribute equally to the combined waveform, but arrays with variable gains and spacing can be used to

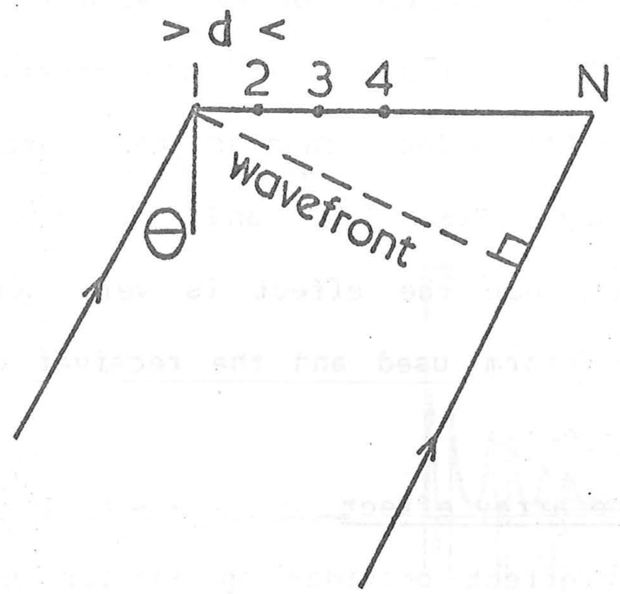

Fig. 2.10
A plane wavefront arriving at a linear array of N detectors.

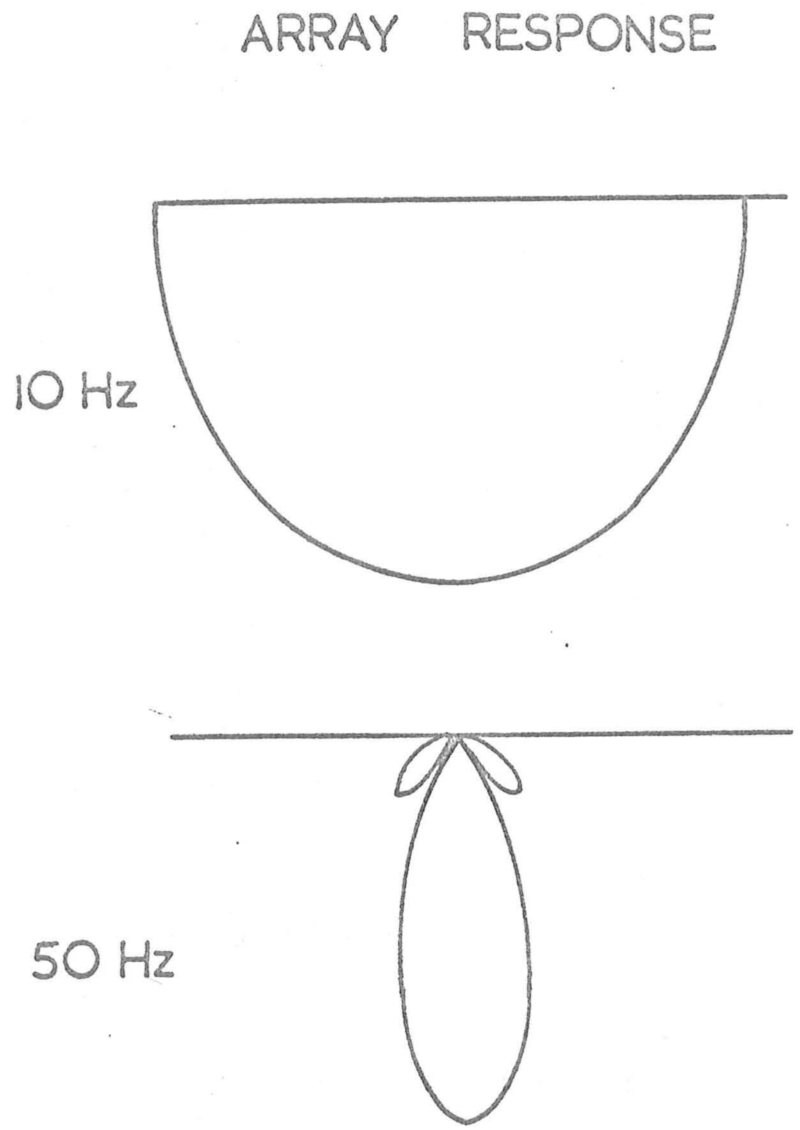

Fig. 2.11
Polar plots of the angular response of a receiver array at frequencies of 10 and 50 Hz. The array has 50 equally spaced and weighted hydrophones in a 60 m section.

provide specific angular and frequency responses. (Savit et al 1968, Schoenberger 1970).

The time domain response for an equally spaced and weighted array can be derived simply; consider a receiver as in Fig. 2.10 with N equally spaced and weighted detectors a distance d apart, and a plane wavefront arriving at the receiver at an angle Θ to the vertical. The wavefront arrives at each detector at a time $t = d\sin\theta/v$ greater than the element adjacent to it, where v is the water velocity, and the array response is the sum of the responses at each detector. For a 50 hydrophone array 60 m long and $\theta = 30^{o}$ the time shift of the waveform across the array is 17 ms.

The frequency domain resonse can be derived by analogy to the Fraunhofer diffraction grating response. (Jenkins & White 1957). For a simple harmonic plane wave the phase will change by equal amounts α from one receiver to the next, where:

$$\alpha = 2\pi d\sin\theta/\lambda$$

The composite signal is the sum of the individual signals from each detector. Taking the amplitude at a single receiver as unity, the composite complex amplitude, A, is the sum of the individual responses:

$$A = (1+e^{i\alpha}+ e^{2i\alpha}\ldots\ldots\ldots + e^{(N-1)i\alpha})$$

which reduces to:

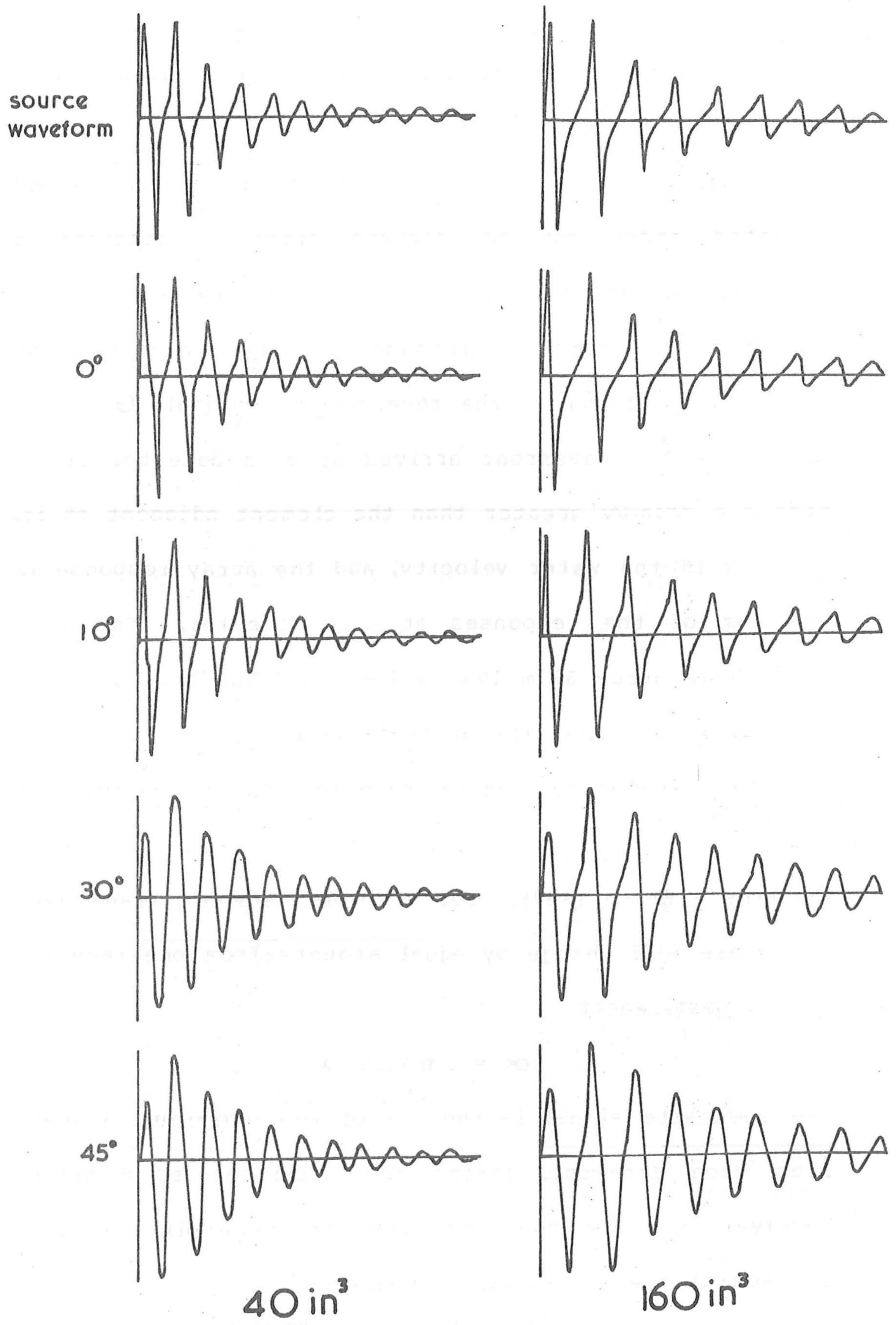

Fig. 2.12
The effect of a line receiver array on theoretical 40 and 160 in^3 airgun waveforms for different angles of incidence. The array is 60 m long with 50 equally spaced and weighted hydrophones.

$$A = \frac{\sin(N\alpha/2)}{\sin(\alpha/2)} e^{i(N-1)\alpha/2}$$

(eg Jenkins & White 1957, Officer 1958). For any ray path (fixed θ) the frequency response can be determined. The factor $\sin(N\alpha/2)/\sin(\alpha/2)$ is the ratio of the amplitude of the composite signal to the amplitude at a single detector, and the $e^{i(N-1)\alpha/2}$ term is the phase change of the composite signal to that the first detector.

The effect of the array on amplitude as a function of incident angle was computed an is shown on a polar plot in Fig. 2.11 for frequencies of 10 and 50 Hz. There is a strong discrimination against rays at large angles of incidence at high frequencies, and this angular discrimination due to the array effect is much stronger than that due to the sea surface reflection effect, but is only effective in the plane of the array.

The array effect on a waveform for various angles of incidence is shown in Fig. 2.12. I computed this using the same source waveform as in Fig. 2.9, Fourier transformed it into the frequency domain, combined it with the line array response for the angle of incidence (equivalent to time domain convolution) and retransformed the resulting waveform back into the time domain. There is a strong low pass filtering effect of the array at higher angles of incidence, and the

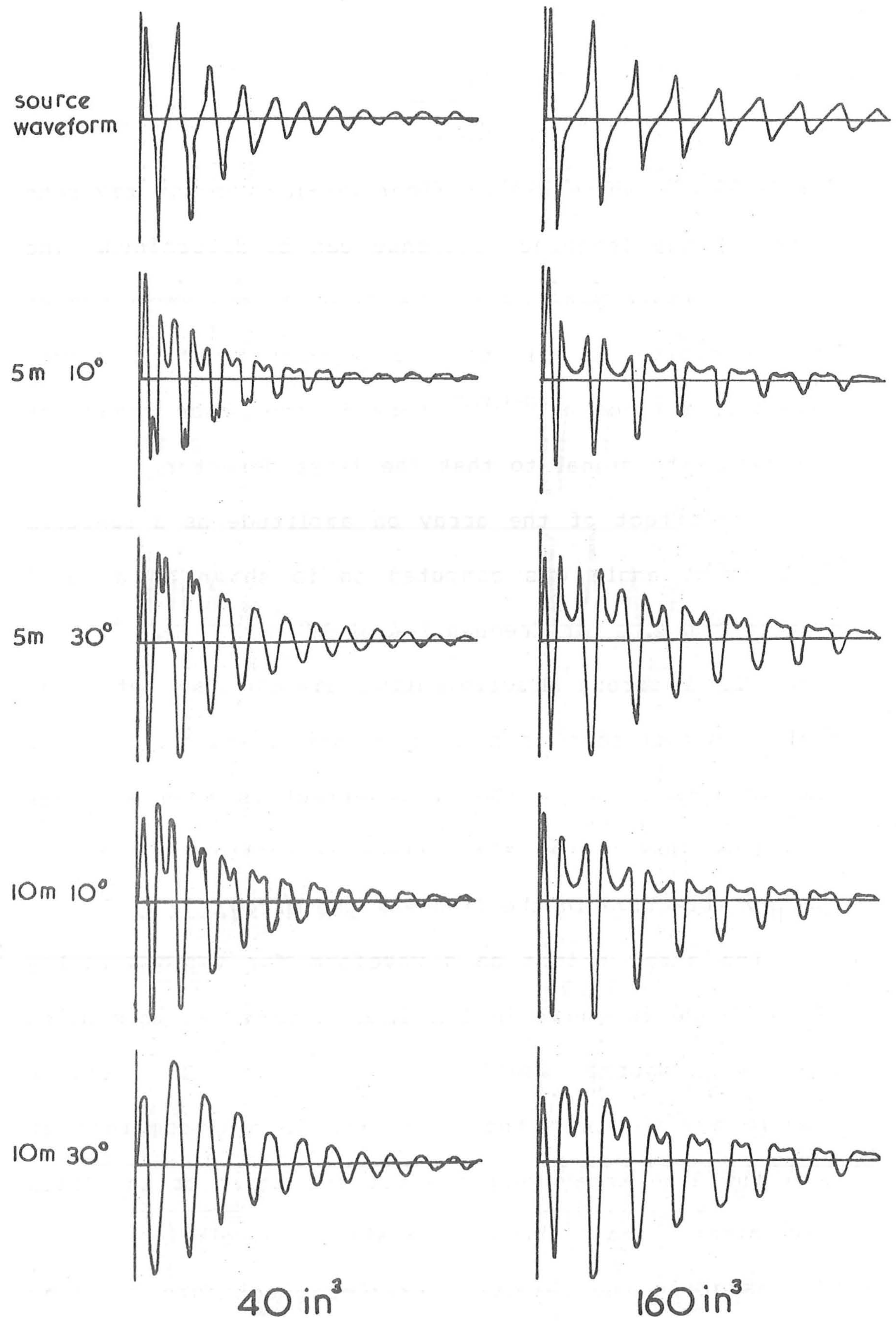

Fig 2.13
The combined effect of the line receiver array and the sea surface reflection for different depth and angles of incidence.

amplitude of the initial spike is also severely reduced as it contains many high frequencies, becoming much lower in amplitude than the second positive spike.

Fig. 2.13 shows the combined effect of the sea surface reflection and line array effect on a waveform for various depths and angles of incidence. I computed this by the methods used to compute Figs. 2.9 and 2.12. The combined effects cause a drastic alteration of the original source waveform, producing a waveform which may be very asymmetric (160 in^3, 5 m, 10^0) or with an initial spike reduced in amplitude.

The effects of electrical response (the same for all arrivals) and array and sea surface reflection effects are simple to compute and are included in the modelling program (chapter 5).

CHAPTER 3

THE EARTH RESPONSE

This chapter examines the effect of the earth on reflection profiles. It looks at how ray theory can be used to describe the propagation of seismic waves in the earth, and at wave conversions, reflection coefficients, attenuation and dispersion, diffraction, and multiple reflections. The theory used in this chapter is relatively well known, and no attempt has been made to derive the equations used.

The results of this chapter are used in Chapter 4 to derive a reflection profile modelling system.

3.1 The ray theory approach to wave propagation

Wave equations

The equations of motion for a homogeneous, isotropic, elastic medium assuming small displacements and no body forces (eg. gravity) are:

$$\rho \frac{\partial^2 u}{\partial t^2} = (\lambda+\mu)\frac{\partial \Delta}{\partial x} + \mu \nabla^2 u \qquad 3.1$$

$$\rho \frac{\partial^2 v}{\partial t^2} = (\lambda+\mu)\frac{\partial \Delta}{\partial y} + \mu \nabla^2 v \qquad 3.2$$

$$\rho \frac{\partial^2 w}{\partial t^2} = (\lambda+\mu)\frac{\partial \Delta}{\partial z} + \mu \nabla^2 w \qquad 3.3$$

(eg. Ewing, Jardetsky and Press 1957) where ρ is the density, (u,v,w) is the displacement, λ and μ the elastic constants (the Lamé parameters), Δ the dilatation, the increase in volume per unit volume, and ∇^2 is the operator $\frac{\partial^2}{\partial x^2} + \frac{\partial^2}{\partial y^2} + \frac{\partial^2}{\partial z^2}$. The equations of motion give the two wave equations:

$$\rho \frac{\partial^2 \Delta}{\partial t^2} = (\lambda + 2\mu)\nabla^2\Delta \qquad 3.4$$

$$\rho \frac{\partial^2 \Theta_i}{\partial t^2} = \mu \nabla^2 \Theta_i \qquad i = x,y,z \qquad 3.5$$

where Θ_i, $i = x,y,z$ is a rotation. The solutions of the wave equations show that two elastic waves can exist, a compressional-dilatational wave, (P), with a velocity $\sqrt{\frac{\lambda+2\mu}{\rho}}$, and a rotational wave, (S), with a velocity of $\sqrt{\frac{\mu}{\rho}}$.

<u>The asymptotic ray series</u>

The use of the wave equations to model the behaviour of seismic waves is extremely laborious and is in practice limited to modelling horizontally layered structures. Laterally varying media must use ray theoretical methods. The following description of the asymptotic ray method is based essentially on Červeny & Ravindra (1971).

The equation of motion for inhomogeneous, isotropic, elastic media is:

$$\rho \frac{\partial^2 \underline{w}}{\partial t^2} = (\lambda+\mu)\nabla(\nabla.\underline{w}) + \mu\nabla^2\underline{w} + \nabla\lambda(\nabla.\underline{w}) + \nabla\mu \times (\nabla \times \underline{w}) + 2(\nabla\mu.\nabla)\underline{w} \qquad 3.6$$

where $\underline{w}$ is the displacement vector. The equation of motion for inhomogeneous media cannot generally be separated into two wave equations. Assume that a solution of the equation of motion can be expressed as an infinite power series of inverse frequency and a space dependent vector which is independent of frequency:

$$\underline{W} = \exp\left[i\omega(t-\Upsilon)\right]\sum_{k=0}^{\infty}(i\omega)^{-k}\underline{W}_k \qquad 3.7$$

where Υ and $\underline{W}_k$ are independent of ω and t. Υ is called a phase function and $\underline{W}_k$ (k = 0,1,2....), the coefficients of the ray series. The moving surfaces of constant phase, t = Υ(x,y,z) are wave fronts and the orthogonal trajectories of these surfaces are rays.

The function Υ(x,y,z) must be analytic for the asymptotic ray series, equation 3.7, to be valid. The ray expansion is not valid in the vicinity of foci, caustic surfaces or critical points. The size of the region in which the ray expansion is not valid is frequency dependent; for high frequencies this is small, and for low frequencies, larger. Wave methods must be used in these regions. The ray expansion is only strictly valid if velocity gradients are small compared with wavelength, and the radii of curvature of interfaces is larger than the wavelength. The ray expansion will not predict diffrations, as these occur at discontinuities or where the radius of curvature of an interface is smaller than the wavelength.

The zero-order solution of the asymptotic ray series

The zero-order solution of the asymptotic ray series considers only the first term in the ray expansion:

$$\underline{W} = \exp[i\omega(t-\Upsilon)]\,\underline{W}_o \qquad 3.8$$

Except in the vicinity of foci, caustics or critical points the error in using only the first term of the series tend to zero as the frequency becomes higher. The zero-order solution, equation 3.8, is independent of frequency, and corresponds to a solution using the principles of geometrical optics. Higher order terms in the series are corrections to this solution. Hron et al (1974) compared a partial ray expansion of the zero-order solution with the exact wave solution for a horizontally layered structure, and showed that the zero-order solution was a good approximation to the exact wave solution if a sufficient number of rays are used. The accuracy is limited by the number of rays traced in a partial expansion. Cisternas et al (1973) have produced a method for a complete ray expansion, but it is limited to horizontally layered media. Ray amplitudes decrease rapidly with increasing numbers of reflections and conversions, and partial ray expansions usually limit the number of rays used to those with an amplitude above a chosen level.

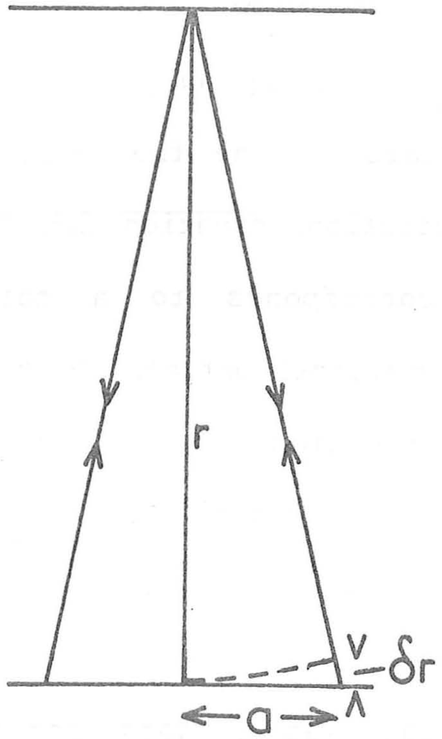

Fig. 3.1
The reflection of a ray from a finite area of a reflector

The basic equations of geometrical optics are the eikonal equations:

$$\left(\frac{\partial \tau}{\partial x}\right)^2 + \left(\frac{\partial \tau}{\partial y}\right)^2 + \left(\frac{\partial \tau}{\partial z}\right)^2 = (\nabla \tau)^2 = \frac{1}{\alpha^2} \qquad 3.9$$

where

$$\alpha = \sqrt{\frac{\lambda + 2\mu}{\rho}}$$

and

$$\left(\frac{\partial \tau}{\partial x}\right)^2 + \left(\frac{\partial \tau}{\partial y}\right)^2 + \left(\frac{\partial \tau}{\partial z}\right)^2 = (\nabla \tau)^2 = \frac{1}{\beta^2} \qquad 3.10$$

where

$$\beta = \sqrt{\frac{\mu}{\rho}}$$

These equations relate wavefronts, rays and arrival time with seismic velocity. Snell's law, which relates the angles of incidence and refraction at interfaces with velocities can be derived using the eikonal equations (Červený and Ravindra 1971) and this is used in tracing rays across interfaces.

The size of a ray

Rays are normally defined as of infinitesimal size, but in considering reflections it is convenient to consider ray tubes subtending a finite solid angle at the source. If such a tube is reflected at a plane reflector at a distance r from the source (Fig. 3.1) then rays are reflected approximately in phase from a finite area of the reflector. The radius over which the rays do not differ in phase by

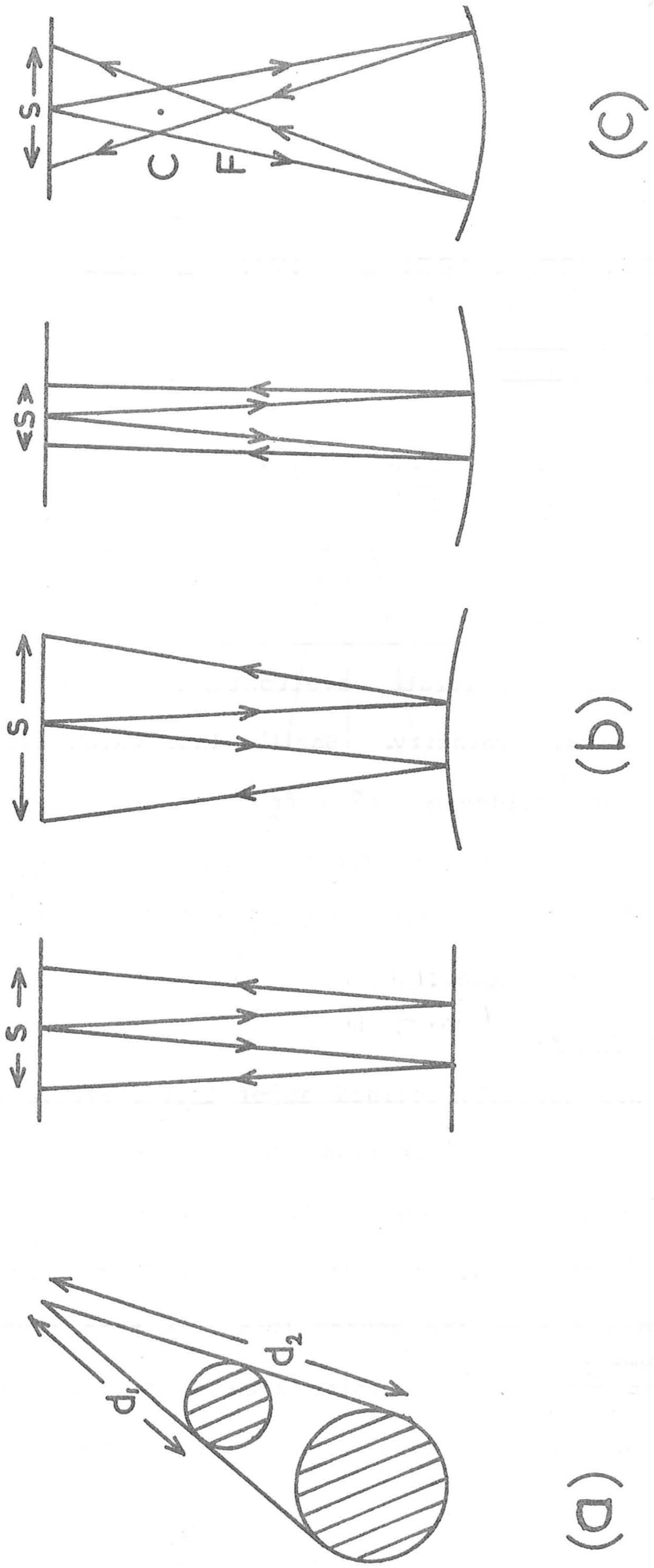

Fig. 3.2

a. The increase in wavefront area of a ray tube with distance in a homogeneous medium.

b. Ray tubes reflected from a plane interface, an anticline, and a syncline, showing divergence and convergence.

c. The focussing of a ray tube due to a buried centre of curvature. C = centre of curvature, F = focus for these rays

more than half a wavelength, by analogy with Fresnel zones is:

$$a^2 + r^2 = (r + \frac{\lambda}{4})^2$$

$$a^2 = \frac{\lambda}{4}(2r + \frac{\lambda}{4})$$

This is for a two way travel path, so that δr must be less than $\frac{\lambda}{4}$. For r = 1 km and a frequency of 30 Hz in water, a is about 150 m. This area increases generally with depth if there are no focussing effects. It is this finite area of reflection which limits ray theory to interfaces with radii of curvature considerably larger than the wavelength. Diffractions are produced from interfaces with smaller radii of curvature, as the ray is not in phase over the interface.

Spreading of ray paths

Ray theory considers that the amplitude at any point is given by the size of an elementary ray tube at that point. Consider a ray tube in a homogeneous perfectly elastic medium and a point source (Fig. 3.2a). The ray paths will be straight and the energy in the ray tube remains constant, so the energy flow across unit area of the wavefront decreases as the wavefront area increases in size. The ratio of the energy flow/unit area at two points distances d_1 and d_2 from the source is given by the ratio of the area of the wavefronts at these points. For the homogeneous and perfectly elastic medium the ray tube increases in area as d^2, so the energy flow/unit area decreases as $1/d^2$, and amplitude decreases as 1/d. This is geometric, or spherical spreading.

A ray tube in an inhomogeneous medium does not have amplitude inversely proportional to distance travelled as refraction at velocity interfaces deviates the ray path and changes the wavefront area in an elementary ray tube. Velocity usually increases with depth, so that the wavefront area increases faster than the square of the distance, so energy decay is more rapid than in a homogeneous medium. Reflection at impedance contrasts also reduces the energy in the ray tube (section 3.2) and if the medium is not perfectly elastic attenuation also reduces the amplitude (section 3.3). This section looks at the changes in amplitude due to ray path alteration only.

The variation of amplitude with distance in a horizontally plane-layered medium has been derived by O'Brien and Lucas (1971) and Newman (1973). The effect of dipping and curved interfaces on amplitudes is complicated to compute analytically but can be simply calculated by tracing ray tubes to determine the wavefront area. A ray tube changes shape when reflected or refracted from a curved interface giving convergence and increased energy flow/unit area over concave upward interfaces (synclines) and divergence and decreased energy flow/unit area over convex upward interfaces (anticlines). The effect of this on ray tubes is shown in Fig. 3.2b. The area of the ray tube on return to the surface is proportional to S^2. This is smallest for the syncline and greatest for the anticline, giving the strongest reflection over the syncline and weakest over the anticline. (See also Chapter 5 models).

Curved interfaces cause ray theory to break down in certain cases. Ray theory cannot predict behaviour where intensity changes rapidly, for example at a focus, where there is a concentration of rays (Born & Wolf 1964). Fig. 3.2c shows a ray tube focussed due to a buried centre of curvature of the surface. Rays from the source are reflected from the curved surface and are focussed at F, and return to the surface. There will always be a buried focus if there is a centre of curvature below the line of shot points. It is not so obvious that there is a change in phase on passing through F. If F is merely the focal plane of the surface the phase change is $\pi/2$, but if the curvature is three-dimensional with the same curvature perpendicular to this section, F is a focal point and the phase change is π, a reversal of sign. This has been described for light by Born & Wolf (1964), and for seismics by Dix (1952) and has been demonstrated experimentally for seismics by Hilterman (1970). The $\pi/2$ phase change has a drastic effect on the shape of the received waveform.

3.2 Wave conversion and reflection coefficients

A reflection occurs when there is a change in impedance (the product of P or S velocity and density). The reflection amplitude is independent of frequency if the radius of curvature of the interface is large compared with the wavelength, and if the layer thickness is also large compared with the wavelength. When the layer thickness is of comparable or smaller size than the wavelength the reflection amplitude varies with frequency due to interference between reflections from the top and bottom of a layer. This may be constructive or destructive depending on the layer thickness and the nature of the reflection from the top and bottom of the layer.

A ray incident at an interface generally produces reflected and transmitted P and S waves except that no S waves will be propagated within a fluid medium. The amplitudes of the reflected and transmitted waves depends on the P and S velocities, densities and angle of incidence. The reflection coefficient is the ratio of the amplitude of a reflected wave to the amplitude of the incident wave, and may be derived using the boundary conditions at the interface, which require continuity of displacement and stress across the interface. The expressions for generalised reflection and transmission coefficients are long, and have been derived by many authors, and tables of reflection and transmission coefficients for various values of velocity, density and incident angles have been published. Červeny and Ravindra (1971) provide a comprehensive bibliography to these.

The conversion of P waves to S waves is generally small at the low angles of incidence occurring in reflection profiling. At solid-solid interfaces this is between 0-5% for incident angles up to 30°, but S wave conversion is much greater if the medium is fliud and may reach 20%. The expression for the calculation of reflection coefficients can be considerably simplified if S wave conversion is ignored, and a ray tracing system becomes much simpler as a system for tracing P waves only is required. The ray tracing system for reflection profiles described in the next chapter ignores S wave conversion. The greatest error in ignoring S wave conversion is at fluid-solid interfaces, the sea bed in marine profiling.

The expression for reflection coefficient ignoring

S wave conversion is:

$$R_{12} = \frac{\dfrac{\rho_2}{\rho_1} - \sqrt{\dfrac{v_1^2/v_2^2 - \sin^2\theta}{1 - \sin^2\theta}}}{\dfrac{\rho_2}{\rho_1} + \sqrt{\dfrac{v_1^2/v_2^2 - \sin^2\theta}{1 - \sin^2\theta}}} \qquad 3.11$$

(eg Officer 1958) where R_{12} is the reflection coefficient between media 1 and 2 for a wave incident in medium 1, ρ and V are the density and seismic velocity in the medium, and θ is the angle of incidence. $R_{21} = -R_{12}$, and for a stack of n interfaces at any angle the combined reflection coefficient for a wave transmitted through the upper layers, reflected at the n^{th} interface and retransmitted through the upper layers is:

$$R_{1n} = R_{n,n+1}\,(1-R_{12}{}^2)(1-R_{23}{}^2)\ldots(1-R_{n-1,n}{}^2) \qquad 3.12$$

The expression for reflection coefficient, 3.11, applies to a sharp interface. A transitional interface generally reduces the amplitude of the reflection. Clowes et al (1968) show that for a Moho-type interface, a linear transition layer 1/4 wavelength thick would have a reflection coefficient ten times less than the reflection coefficient from a sharp interface, and a linear transition layer one wavelength thick would reduce the reflection coefficient by about thirty times.

3.3 Attenuation and Dispersion

The form of a plane-wave pulse travelling in a homogeneous, isotropic and ideally elastic medium does not change with distance travelled, as there is no energy dissipated. If the medium is anelastic, as are all natural materials to some extent, the form of the pulse will change. Attenuation is the change of the amplitude spectrum of the pulse due to dissipation of energy, and dispersion is the change in the phase spectrum, so that each frequency component contributing to the pulse travels with a different phase velocity, and is attenuated to a different extent.

A plane wave propagating in an anelastic medium has an attenuation-dispersion factor of:

$$e^{i(k+i\alpha)x} \qquad 3.13$$

where α is the attenuation coefficient and κ the dispersion coefficient. A quantitative measure of absorption is given by the dimensionless factor Q, which is proportional to the ratio of the peak energy in a periodic motion to the energy lost in a cycle. A high value of Q imples a low value of absorption. Q is related to α by:

$$\alpha = \frac{\pi f}{Qv} \qquad 3.14$$

where f = frequency and V = velocity.

Absorption involves the transfer of vibrational energy of motion to heat. In liquids α is generally propotional to f^2, due to a viscous absorption mechanism, and in solids α is generally proportional to f, not change with distance travelled, as there is no energy dissipated. If the medium is anelastic, as are all natural materials to some extent, the form of the pulse will change. Attenuation is the change of the amplitude spectrum of the pulse due to dissipation of energy, and dispersion is the change in the phase spectrum, so that each frequency component contributing to the pulse travels with a different phase velocity, and is attenuated to a different extent.

A plane wave propagating in an anelastic medium has an attenuation-dispersion factor of:

$$e^{i(k+i\alpha)x} \tag{3.13}$$

where α is the attenuation coefficient and κ the dispersion coefficient. A quantitative measure of absorption is given by the dimensionless factor Q, which is proportional to the ratio of the peak energy in a periodic motion to the energy lost in a cycle. A high value of Q imples a low value of absorption. Q is related to α by:

$$\alpha = \frac{\pi f}{QV} \tag{3.14}$$

where f = frequency and V = velocity.

Absorption involves the transfer of vibrational energy of motion to heat. In liquids α is generally propotional to f^2, due to a viscous absorption mechanism, and in solids α is generally proportional to f, due to a solid friction attenuation mechanism. The attenuation in sea water is very low, about 10^{-3} dB km^{-1} at 100 Hz (Thorp 1965), which is 10^2 - 10^3 times less than earth attenuation, and can generally be ignored. Saturated sea bottom sediments have α proportional to f^n where n is generally greater than 1; Shumway (1960) reports n = 1.79.

The value of Q generally increases with depth in the crust (attenuation decreases). Marine sediments down to about 300 m may have a Q of 10-25 (Tullos & Reid 1969), and McDonal et al (1958) report a Q value of 30 for an upper Cretaceous shale at depths less than 300 m. O'Brien & Lucas (1971) find Q values of 20-200 for 300-3,000 m deep sections. Values of Q for the whole crust have been estimated as 300 by Clowes & Kanasewich (1972) and as 260 by Press (1964).

Attenuation measurements in the field and in the laboratory have shown that for P waves in dry rocks α varies linearly with frequency (eg McDonal et al 1958; O'Brien & Lucas 1971). The existence of measurable dispersion is disputed; Wuenschel (1965) showed that a small amount of dispersion existed in McDonal et al's measurements, but O'Brien and Lucas found no significant dispersion in an analysis of well logs.

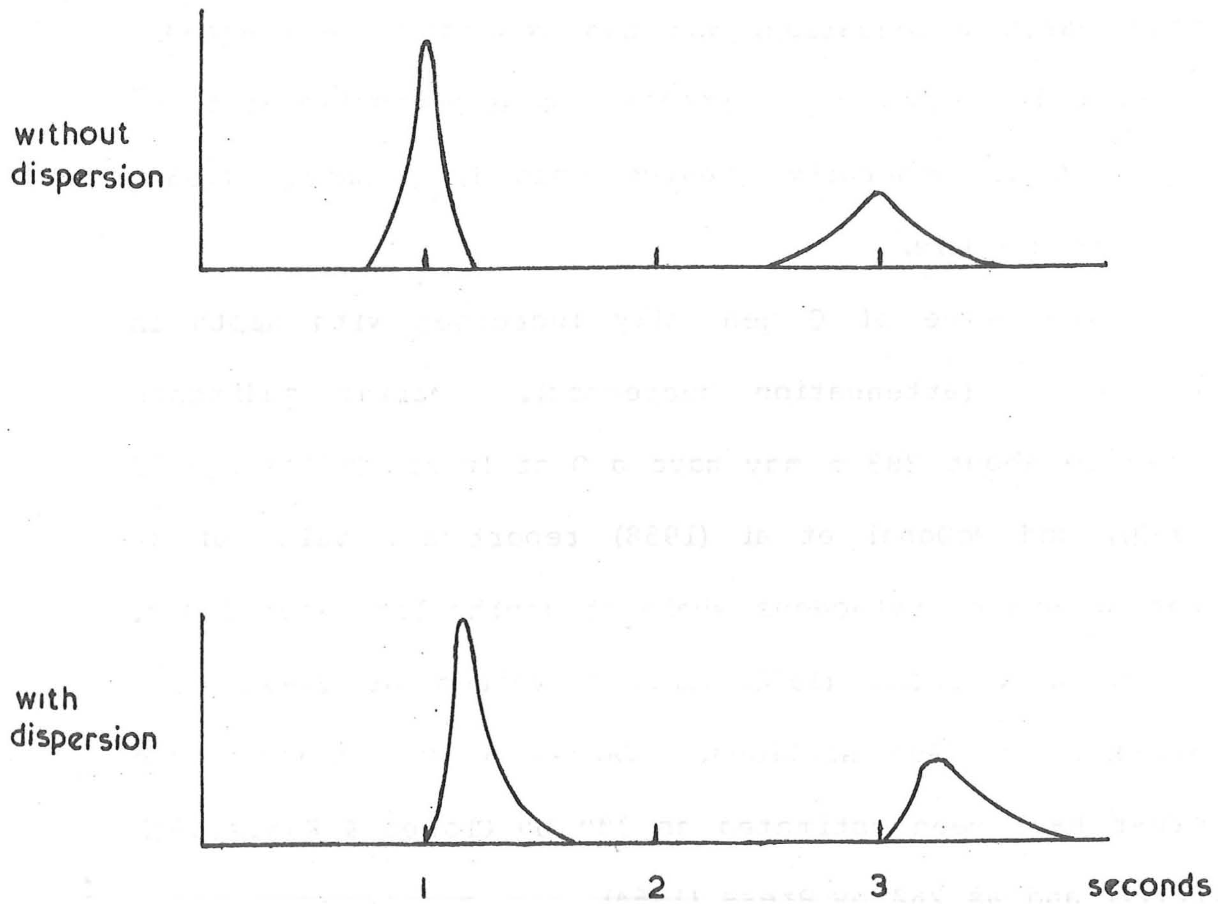

Fig.3.3
Propagation of a spike pulse showing waveforms at 1 and 3 seconds in the presence of attenuation with and without dispersion

Seismic wave motion is generally assumed to be linear, for example Bullen (1963) and Ewing, Jardetsky & Press (1957) and if this is so the presence of attenuation demands the presence of dispersion in order to get a causal arrival of the pulse, which is necessary for real physical processes. Attenuation without dispersion would give a pulse spread about the arrival time (Fig. 3.3). Using the assumption of a linear attenuation mechanism and the Principle of Causality the dispersion coefficient K(f) may be calculated from the attenuation coefficient $\alpha(f)$, as by Futterman (1962) who uses the Kramers-Krönig dispersion relationship, or by Strick (1970) who uses a Hilbert transform method. Futterman shows that the phase velocity and attenuation are related by:

$$v_o/v - 1 = -\ln(f/f_o)/\pi Q \qquad 3.15$$

where v is the phase velocity at frequency f, and v_o the phase velocity at frequency f_o, so if the phase velocity is known at one frequency it can be calculated for other frequencies. K(f) is then the dispersed wavenumber:

$$K(f) = 2\pi f/v(f) \qquad 3.16$$

In the frequency band 1-150 Hz the dispersion calculated

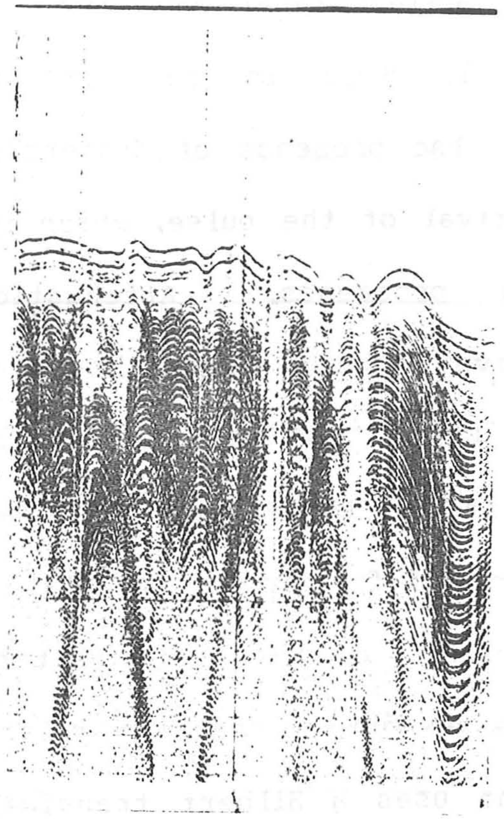

Fig. 3.4
Diffractions

by this method should be 3% for a Q = 50. This has little effect on arrival times for the relatively short times of interest in reflection profiling, but has a significant effect on the shape and causality of the reflected pulse.

3.4 Diffraction

Diffraction is a reflection phenomenon which gives a hyperbolic echo profile. It is not a regular reflection, and occurs in the vicinity of any irregularity or discontinuity in an interface, such as a fault, when the radius of curvature of an interface is of comparable or smaller size than the seismic wavelength. Fig. 3.4 shows an example of a reflection profile with many hyperbolic diffraction echoes.

Diffraction cannot be predicted by ray theory, as the wave nature of seismic waves is involved in an essential way. Diffractions are difficult to synthsize for this reason; Trorey (1970) and Hilterman (1970) have produced methods for synthesis of diffractions using surface integrals, but for a constant velocity and a single interface. The modelling system in the next chapter ignores the generation of diffractions, as it is based on ray tracing, not wave theory.

Huygens' Principle can be used to visualize the

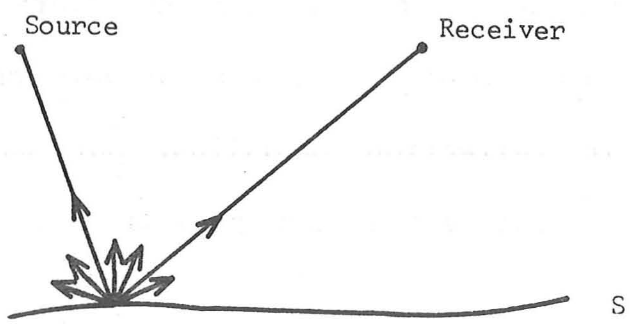

Fig. 3.5
The process of diffraction and Huygens' Principle.

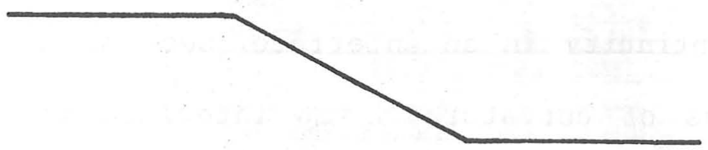

Fig. 3.6
(a) True section

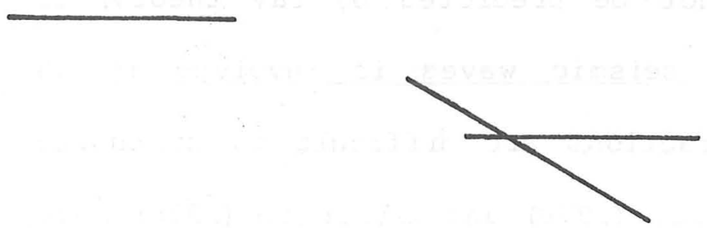

(b) Reflection profile in absence of diffractions.

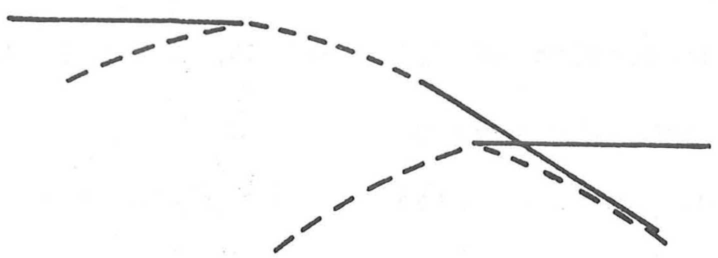

(c) Reflection profile with diffractions

process of diffraction. Consider a source, receiver, and a surface S (Fig. 3.5). Every point of S that receives energy from the source acts as a source of secondary wavelets, and sends out energy in all directions. The envelope of all the secondary waves for all points on the surface is the new wavefront. If S is plane and of infinite extent the secondary wavelets from all points on the surface will add up in phase to a give a reflected wave with equal angles of indicence and reflection. An irregularity in S will cause an irregularity in the envelope of secondary waves and produce diffraction phenomena. The diffraction appears to emanate from this irregularity, but is produced by contributions from the whole of S. This means that a point cannot produce a diffraction; any surface must have dimensions comparable to or greater than the wavelength to have a significant response. A point reflector that gives diffractions is in reality a surface with a very small radius of curvature.

Diffraction Phenomena

Diffractions smooth the continuity of a reflection profile, distributing any sharp changes in amplitude over a larger region. The step in the section in Fig. 3.6 would produce a discontinuous profile in the absence of diffractions; these tend to join up the sections, the two changes in slope acting as point diffractors. Fault planes can often be recognised by their associated diffractions.

There are two branches of a diffraction from each diffracting point or edge, although one branch may be masked by a reflection; the left hand branch of the diffraction from the upper diffracting point in Fig. 3.6 may be masked by the stronger reflection, especially if the source signature is long. The two branches of a diffraction from a diffracting point are identical, whereas a diffraction from the edge of a reflector of otherwise infinite lateral extent in and out of the plane of the section will have a phase shift of 180° between the two diffraction branches (Trorey 1970), so the diffractions generated by points and edges could be distinguished. If the reflector is not of infinite lateral extent out of the plane of the section, but has an out-of-plane convexity, this could also act as a point diffractor, as the seismic system senses out-of-plane contributions, and this would tend to enhance the on-going branch of the diffraction and diminish the reverse branch. This may explain why a reverse branch is rarely seen except with point diffractors, and could also account for the often high amplitude of diffractions.

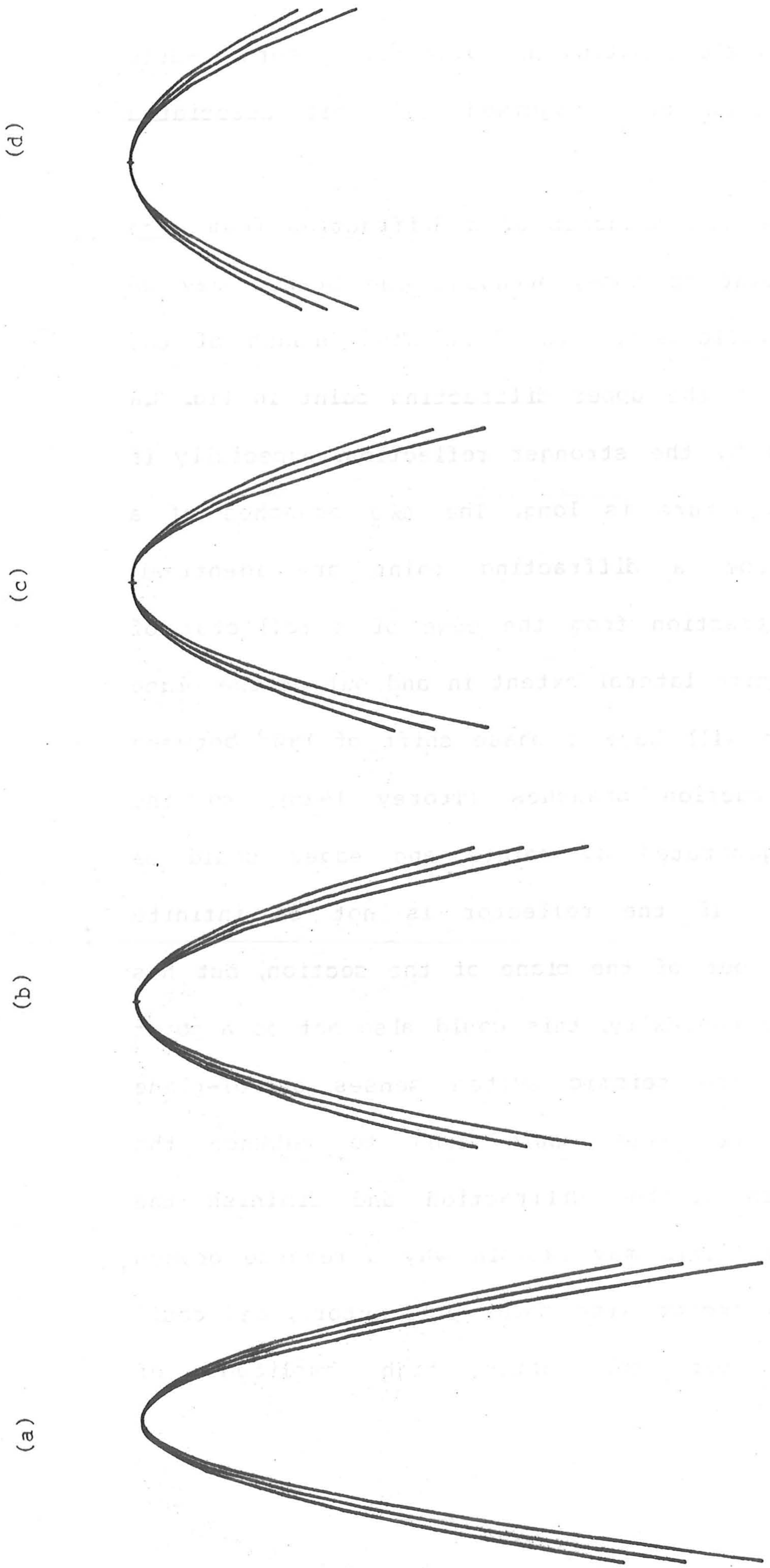

Fig. 3.7
Diffraction curves for 1 km of water and velocities to the diffracting point of 2.5, 3.0, and 3.5 km s^{-1}.
The vertical exaggeration of (d) is half that of (a), (b) and (c).
The two way travel times to the diffracting points are 2,3,4 and 3 s respectively for (a) - (d).

Trorey (1970) showed that at the edge of a reflector, the diffracted wave is identical to the reflection and initially has half the amplitude. This can be used to determine the position of a diffracting edge. The diffraction amplitude decreases with distance from the diffracting point at a rate much faster than that predicted by geometric spreading.

A diffraction curve has a steeper variation of range with distance (slope) than any other geological model. The shape of the curve may be used as a rough estimate of velocities above the diffracting point, but this is not very accurate as the shapes of the curves vary little with velocity and a lot with vertical exaggeration of the profile. Fig. 3.7 shows diffraction curves which I computed by ray tracing for 1 km of sea water, then a velocity of either 2.5, 3.0 or 3.5 km s^{-1}, for different depths and vertical exaggerations. The curves may be compared with real profiles by matching apex curvature and asymptotic slope, but Fig. 3.7 shows that there is little difference between the curves for each velocity and a lot of difference with change in vertical exaggeration, which can be caused by changes in ship speed, or sweep and paper speed of the recorder, and is difficult to determine accurately.

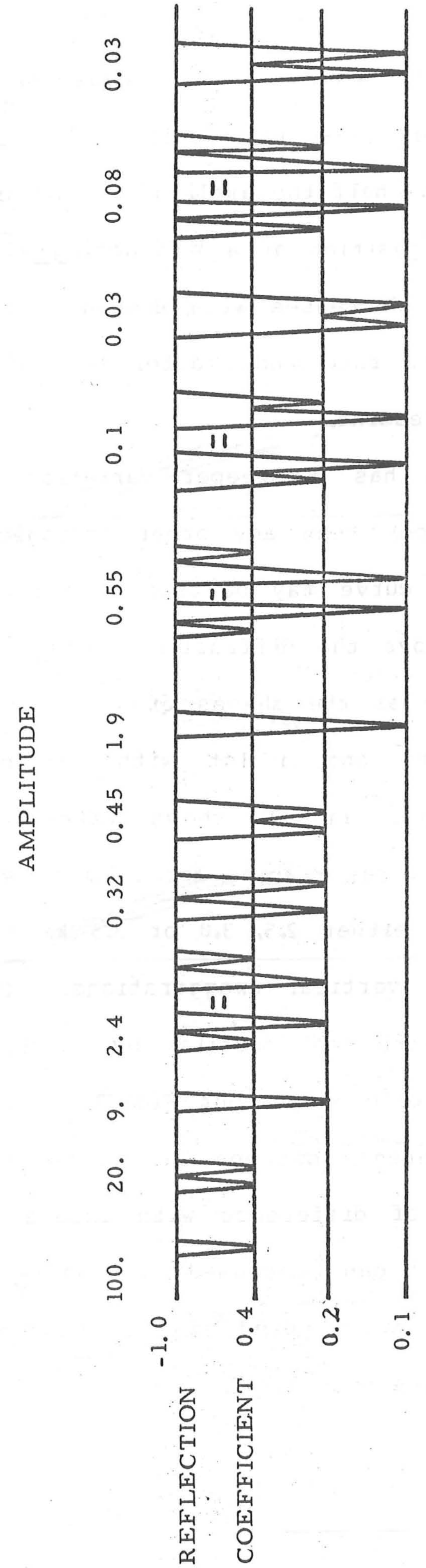

Fig. 3.8
Multiple paths and approximate relative amplitudes for a marine three layer system

3.5 Multiples

Plane horizontal interfaces

The generation of multiples from plane, horizontal reflectors is simple to visualize in terms of ray paths. Multiple reflections in this case will travel along the same paths as primary rays and occur at multiples of the primary travel time. It is possible to generate a continuous succession of multiples from any model, the amplitudes decreasing and travel time inceasing for successive multiples.

An example showing the relative amplitudes of primary and multiple reflections for a simple marine three layer system is shown in Fig. 3.8. The amplitudes are approximate, and include only the effects of geometrical spreading and reflection coefficients, and the layers are equally spaced, Only the first multiple has been considered.

The first water wave multiple in Fig. 3.8 is stronger than the primary reflection from the lower layers, but other multiples are very low amplitude. The water layer multiple is usualy the strongest multiple in reflection profiles as the reflection coefficient at the water-air interface is -1. Water multiples can generally be distinguished from primary reflections and intersedimentary multiples by their travel times and

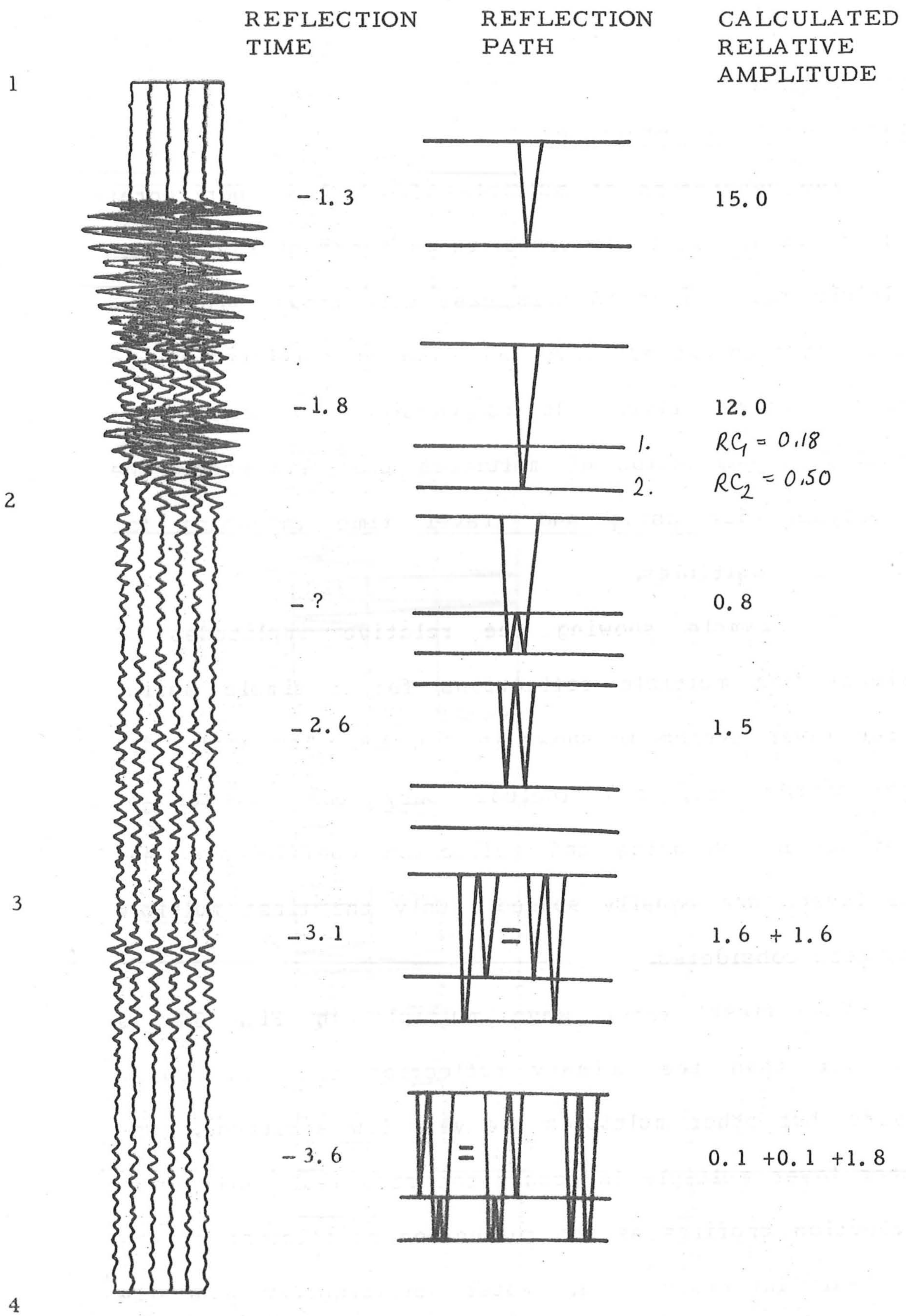

Fig.3.9 A recorded profile with a strong sub-bottom reflector, reflection paths and calculated relative amplitude of reflections, from ray path spreading and reflection coefficients. Reflection coefficients were estimated from primary reflection amplitudes, and used to calculate multiple amplitudes for the ray paths shown.

also frequency content, as attenuation is less in water than the earth, so water layer multiples retain high frequency components. Velocity analyses can distinguish multiples by their moveout velocities. Water layer multiples are a nuisance on reflection records as they can mask deeper reflectors, but stacking of records can be used to attenuate multiples.

Multiple amplitudes may become unexpectedly high in the situation where there are many possible multiple paths having the same travel times.

Intersedimentary multiples have significant amplitudes only when the sub-bottom reflection coefficients are high, which occurs only rarely. An example of a reflection profile with a strong sub-bottom reflector, and its effect on intersedimentary multiples is shown in Fig. 3.9. The section is a true amplitude profile from the eastern Mediterranean, with horizontal reflectors. The strongest primary reflections are the sea bed (1) at 1.3 s, and a sub-bottom reflector (2) at 1.8 s with a weaker reflection between them. There are water layer multiples at 2.6 s and 3.1 s and there is another reflection at 3.6 s. Even with this strong sub-bottom reflector, there is no visible intersedimentary multiple between reflectors 1 and 2 at 2.3 s. This is explained by the amplitudes of the

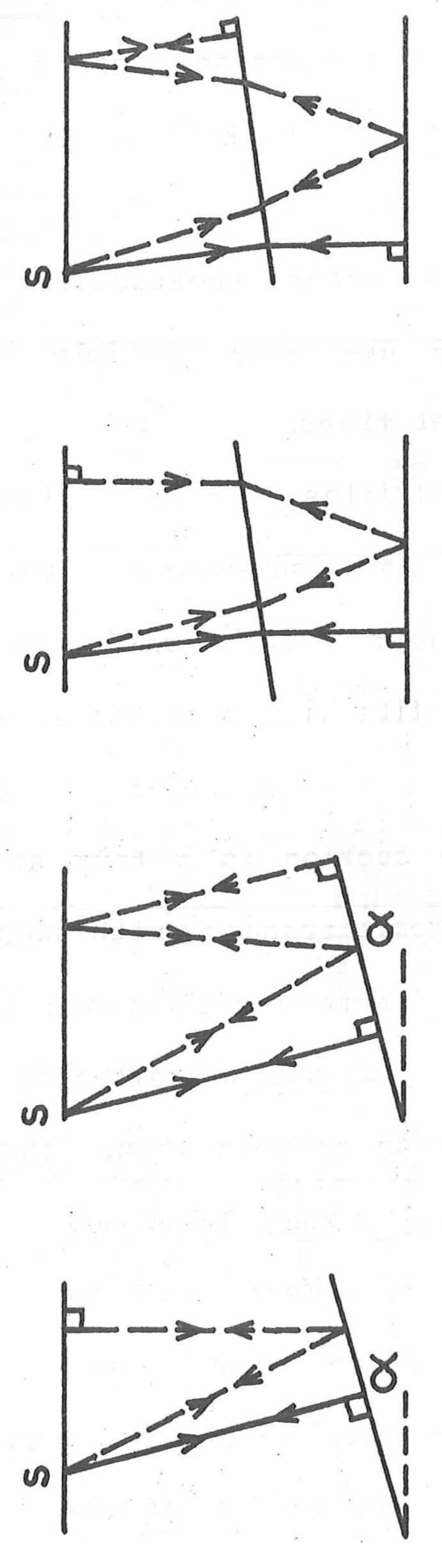

Fig. 3.10
Paths of primary (———) and multiple (- - - - -) reflections for dipping interfaces.
S is the source/receiver position. The rays travel to the reflector and back along the same path.
(a) and (c) are the first multiple paths, (b) and (d) are the second multiple paths.

primaries and multiples calculated from the ray paths and reflection coefficients. The amplitude of the intersedimentary multiple at 2.3 s would be 0.05 times the amplitude of the sea bed reflection, and is lost in the noise. The calculated sea bed multiple amplitude is twice this, and is visible at 2.6 s. The calculated amplitude of the multiple at 3.1 s is about twice the calculated amplitude of the 2.6 s multiple as it has a contribution from two travel paths. The multiple at 3.6 s is visible as it has a contribution from three paths.

Dipping and curved interfaces

When reflectors are not horizontal the situation is more complicated. The multiples generated by a dipping plane reflector are drawn in Fig. 3.10a and b. The multiples have different ray paths from the primary reflection, and the travel times of the multiples from dipping reflectors are not exact multiples of the primary travel times; the first multiple in Fig. 3.10a would have a travel time $2\cos\alpha$ times the primary travel time, and the second multiple in Fig. 3.10b would have a travel time $(4\cos^2\alpha - 1)$ times the primary travel time. For a dip of 10°, this would reduce the first multiple travel time by 1.5%. There are similar expressions for higher order multiples, and the time difference between successive multiples gets progressively shorter.

Multiples with paths other than in the water layer have no simple relationship between angles of dip and travel time, and multiple paths and times have to be determined by ray tracing. Examples of multiples in a two layer dipping system of plane reflectors are shown in Fig. 3.10c and d.

Each water layer multiple will have an opposite sign to the preceeding multiple, as the water-air surface has a reflection coefficient of approximately -1. This can be seen on the autocorrelation of a profile (Anstey 1960). This also applies to any intersedimentary multiples, if the acoustic impedance of each layer is greater than the one above it, as the reflection coefficient for an upgoing ray is negative.

The ray tracing system described in Chapter 4 calculates only water layer multiple reflections, as intersedimentary multiples are generally weak. There are models of the profile in Fig. 3.9 in Chapter 5 (Fig. 5.1), one with only water layer multiple reflections, and the other with intersedimentary multiples also. The inclusion of intersedimentary multiples has little effect on the profile, even with a strong sub-bottom reflector, so the error in limiting the modelling system to the calculation of water layer multiples is small.

CHAPTER 4

A REFLECTION PROFILE MODELLING SYSTEM

4.1 Introduction

This chapter describes a modelling system for seismic reflection profiles. It is two-dimensional, and uses the zero order solution of the asymptotic ray series as a basis for ray tracing, and can be used with arbitrary shaped interfaces. The layers have constant properties of velocity, density and attenuation, but the method could be extended to include continuously varying properties. As many effects as possible are added to the basic ray tracing system for amplitude calculations: the source function, receiver response, geometrical spreading and curved interface amplitude effects, reflection and refraction, attenuation and dispersion. The main limitation is the inability of any ray theoretical methods to model diffractions. A secondary limitation is that this system has not been extended to synthesize processed records.

Modelling systems for reflection profiling have been developed by various authors, but all the systems have limitations: Taner et al (1970) produced a ray tracing system and travel time calculations but no amplitude calculations; Hilterman (1970) and Dunkin &

Levin (1971) produced three-dimensional reflection profile modelling systems, but for one layer only - a constant velocity section down to a single reflector, and Dunkin & Levin do not calculate amplitudes; Dobecki (1973) produced three-dimensional models for arbitrary velocity distributions but limited to plane reflectors and no amplitude calculations.

4.2 The ray-tracing system

Basis

The basis of the ray-tracing system is the zero order solution of the asymptotic ray series, the geometrical optics solution (Chapter 3.1). For a velocity distribution which is dependent on depth only, as with plane horizontal layers or a continuous velocity function which varies with depth, the basis of ray tracing is the parametric equation:

$$p = \sin\theta / v \qquad 4.1$$

where v is velocity and θ is the angle of a ray to the vertical. If velocity is also a function of lateral position the parametric equation is not valid and Snell's law is used as a basis for ray tracing:

$$\text{constant} = \sin\psi / v \qquad 4.2$$

where ψ is the angle to the normal at an interface. This reduces to the parametric equation for horizontal layers.

Shah (1973) has presented an algorithm for ray tracing for arbitrary interfaces in three-dimensions. The interfaces are stored as polynomials, and determination of the point of intersection of a ray and an interface involves the solution of a polynomial. The ray tracing system described here stores interfaces as coordinates of horizontal distance (x) and depth (y) and finds points of intersection of rays and interfaces by a single iterative algorithm, not by the solution of polynomials. This makes ray tracing simpler and faster.

Interface Representation

An interface is a step change in properties of a medium, such as velocity, density or attenuation, of which velocity is the only one that affects the ray tracing system.

The interface may be input either as discrete (x,y) coordinates or as continuous sections of straight lines or circles, from which discrete coordinates can be calculated. A straight line section needs two coordinate pairs to define it, and a circle section needs two coordinate pairs and a centre or three coordinate pairs. The y coordinate is then calculated at fixed intervals of x. The x interval is variable, depending on the resolution required. An estimation of the x interval can be obtained by looking at the area of the ray bundle

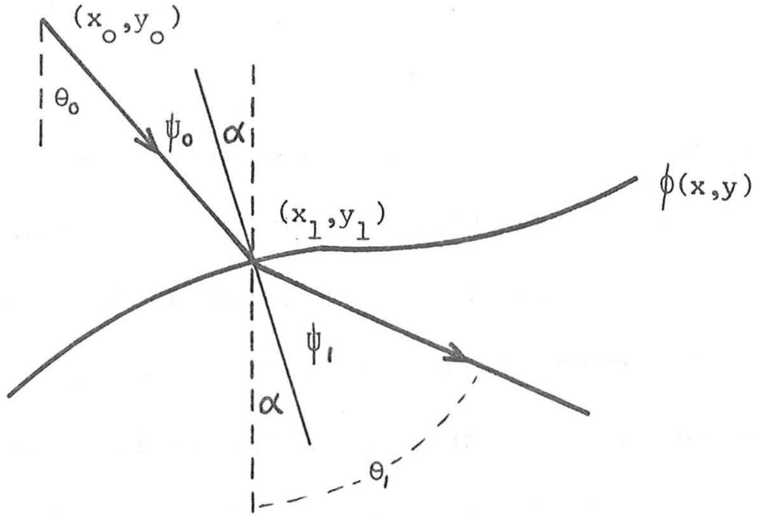

Fig. 4.1a
The effect of an interface on a ray

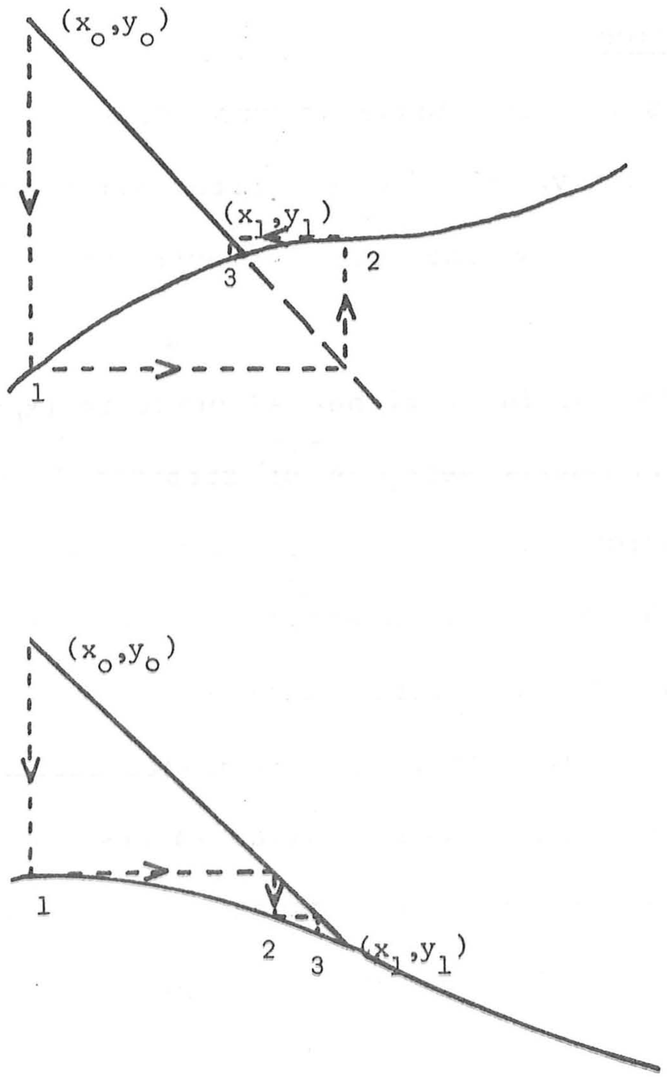

Fig. 4.1b
Successive approximations of the point (x,y) (1, 2, 3...)
to the point of intersection of a ray with an interface (x_1, y_1)

(Chapter 3.1), which is hundreds of metres for frequences of 10-100 Hz and distances of a few kilometres. An x interval of 0.1 km has been found adequate for airgun records. The y values are then smoothed to produce a continuous reflector and the gradient of the reflector calculated at each point.

Although this is contrary to normal practice in ray tracing, where interfaces are input as a series of points and polynomials are fitted to the points, it has the advantage that interfaces with complicated shapes can be handled without the necessity of solving high order polynomial equations which is time consuming. The disadvantages are the greater strorage space needed for the interface points, although this can be written over in later calculations, and also that the interfaces are stored as discrete points, as distinct from the continuous representation by a polynomial equation.

Intersection of a ray with an interface

Consider a ray initially at (x_o, y_o) and at an angle θ_o to the vertical (Fig. 4.1a). If the velocity in the layer is constant then the ray will travel in a straight line to the interface $\phi(x,y)$. The coordinates of the intersection of the ray with the interface (x_1, y_1) are usually found in ray tracing systems by solving the equation of the ray (a straight line passing through $(x_o,$

y_o) with a gradient given by θ_o) with the polynomial equation to the interface. This ray tracing system uses the following iterative algorithm to find (x_1,y_1), which initially calculates the intersection assuming a vertically travelling ray, and then iteratively adjusts the calculated coordinates for the gradient of the ray and the shape of the interface.

Initially set

$$y = y_o$$

and compute

$$x = x_o + (y-y_o)/\tan(90-\theta_o) \qquad 4.3$$

Equation 4.3 is repeated with a new value of y each time, where y is the y coordinate of the point on the interface corresponding to x, the calculated x coordinate. Th point (x,y) converges to the point (x_1,y_1) (Fig. 4.1b) and ten iterations are generally sufficient. This is much faster than the solution of polynomials, but may not work if the dip of the interface exceeds 45°, but as a dip higher than this is rare on a real profile this is not a great limitation.

The angle of the normal to the surface at (x_1,y_1) to the vertical, α, is calculated from the gradient of the interface at (x_1,y_1):

$$\alpha = \pm \tan^{-1} \frac{\partial \phi}{\partial x} \qquad 4.4$$

The sign is opposite to that of the slope of the interface.

The incident angle, the angle of the ray to the normal at the interface, ψ_0, is calculated from θ_0 and α:

$$\psi_0 = \theta_0 \pm \alpha \tag{4.5}$$

the sign is negative if the ray and normal have gradients with the same sign, otherwise positive (Fig. 4.1a).

A ray transmitted at the interface into the layer with velocity V_1 will have a refracted angle, ψ_1, given by Snell's Law:

$$\sin\psi_1/V_1 = \sin\psi_0/V_0 \tag{4.6}$$

The transmitted ray has an angle to the vertical, θ_1, given by:

$$\theta_1 = \psi_1 \pm \alpha \tag{4.7}$$

The sign is negative if the ray and normal have gradients with the same sign, otherwise positive.

The equations of the incident and transmitted rays are calculated from their angles to the vertical and that they pass through the point (x_1,y_1). The travel time of the ray in the layer is calculated from the distance between the points (x_0,y_0) and (x_1,y_1) and the velocity in the layer:

$$t_0 = ((x_1-x_0)^2 + (y_1-y_0)^2)^{1/2}/V_0 \tag{4.8}$$

Extension to layers with continuously varying velocity

The straight line ray paths and the above equations assume a constant velocity. A continuously varying velocity function will give a ray path that is a continuous curve. The curvature of a ray at any point depends on the gradient of the velocity function at that point, V(x,y). For a continuous velocity function which is dependent on depth only, V(y), the parametric equation 4.1 can be differentiated to obtain a relationship between the angle of the ray to the vertical and the velocity at any point, from with the ray path can be calculated:

$$\cos\theta . d\theta/dy = p . dV/dy \qquad 4.9$$

where $d\theta/dy$ is the curvature of the ray.

4.3 Use of the ray-tracing system for a coincident source and receiver

The modelling system developed in this chapter is for continuous seismic profiles, and the source and receiver will be assumed to be at the same point, which is a valid approximation for deep water profiles, when the water depth is great compared with the source and receiver offset. This assumption greatly simplifies the ray tracing system, as the rays can be assumed to travel to the reflector and back along the same path, with the

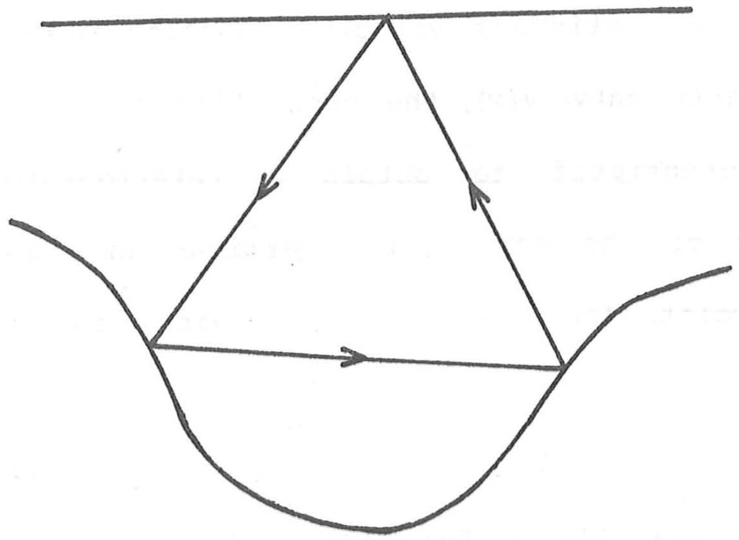

Fig. 4.2
A ray path when the dip of a reflector is greater than 45°

ray normal to the reflecting interface. It may not be valid in the presence of dips greater than 45° (Fig. 4.2) but examples of this are rare.

Ray theory assumes that the wave field can be decomposed into an infinite set of rays. In practice, this is usualy replaced by a partial ray expansion (eg Hron et al 1974) so that only a limited number of rays are used in the expansion. The conventional method of ray tracing for this modelling system would be to trace a partial set of rays from the source and determine which of them returned to the source area. The problem with a partial ray expansion is the selection of rays to trace; some of the rays which could return to the source area may be omitted, and to prevent this happening it is necessary to trace a large number of rays.

Continuous profiling has the advantage that rays returned to the source area have the same travel path to and from the reflector and are reflected normal to the reflector, and this is used to make a faster ray tracing system. Rays are traced from points on a reflector upwards, instead of from the source to the reflector, with the initial direction of the ray normal to the reflector. The ray is traced through the upper layers to the surface using equations 4.3 to 4.8. This is repeated at intervals along the reflector, on all reflectors. Only a few of these rays reach the surface at a shot point, or within a tolerated distance of a shot point, and these rays are collected for that shot point.

The spacing of rays traced along a reflector determines the accuracy of this method. Fewer rays need to be traced if it is possible to tolerate small errors introduced by interpolating rays in between the traced rays if adjacent rays span a shot point, and an interpolation can produce the ray that reaches the shot point. A sufficient number of rays must be traced originally so that this error is small; a spacing of 0.1 km along the reflectors produces a sufficiently dense ray diagram for marine airgun records.

Fig. 4.3 is an example of ray tracing for a three-layer model. This shows only half the rays traced for clarity. The rays from equally-spaced interface points do not produce rays at equally-spaced surface points. Fig. 4.4 is a ray tracing showing the collection of rays at equally-spaced surface points.

The structure of the modelling program is shown in Fig. 4.5. The ray-tracing part of the program is in the main program and subroutines SURFCE, RAYS1 and RAYS2. The subroutine SURFCE calculates y coordinates for each x coordinate at equal intervals of x along interfaces,

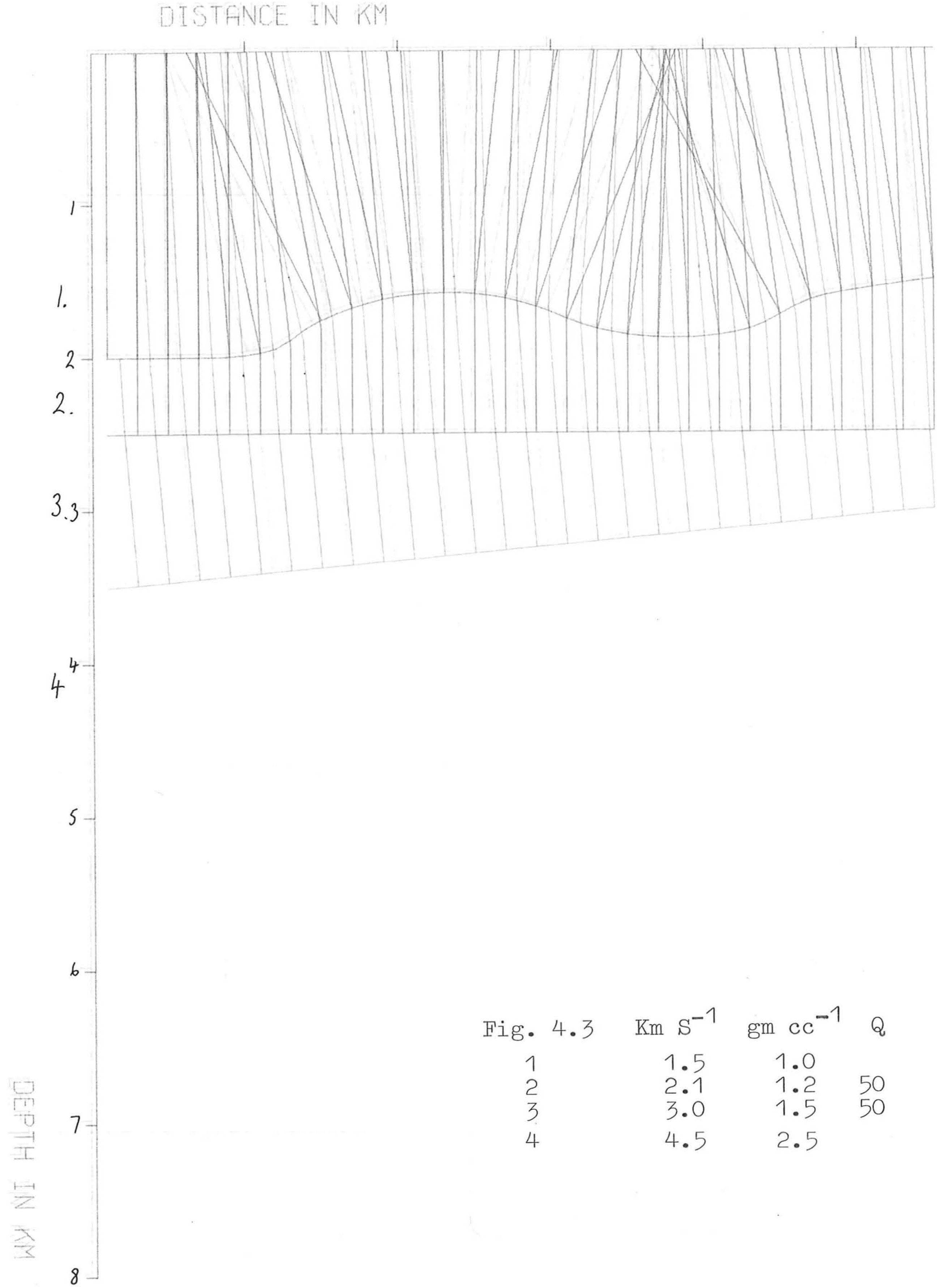

Fig. 4.3	Km S^{-1}	gm cc^{-1}	Q
1	1.5	1.0	
2	2.1	1.2	50
3	3.0	1.5	50
4	4.5	2.5	

Fig. 4.3

A ray tracing for a three-layer model with rays from equally-spaced interface points 0.2 km apart.

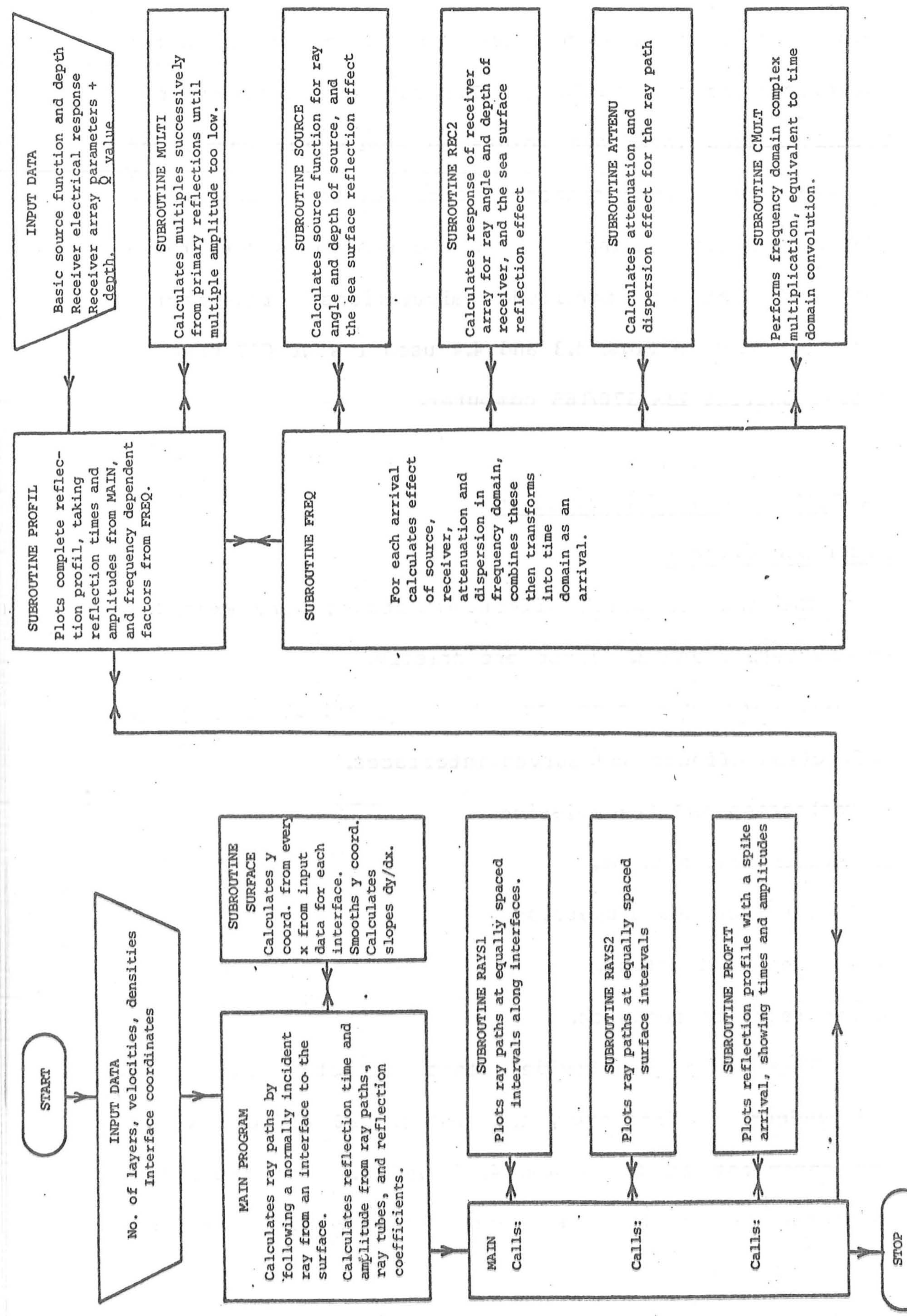

Fig. 4.5 The logical structure of the modelling program.

frequency dependent effects slow as computations have to be done for each frequency.

Values of properties used

The ray tracing system and reflection coefficient calculations need values for velocities in the layers. Velocities can be measured continuously or discontinuously during profiling, from moveout velocities across a multi-section array in shallow water profiling, or from variable angle reflections and refractions using disposable sonobuoys.

The reflection coefficient calculation needs a value of density. It may be possible to get an indication of density values in the layer below the sea bed from the amplitudes of reflections and multiple reflections from the sea bed, if velocities are known and assuming amplitude loss due to geometric spreading and a lossless water layer. Density can also be estimated from standard velocity-density curves, such as Nafe & Drake (1963) or Woollard (1962).

Determination of attenuation values is difficult, as the effects of density and attenuation are difficult to separate; the amplitude of sub-bottom reflections depends on attenuation as well as reflection coefficient. Anstey (pers. comm. 1974) has found it possible in some cases to determine the effects of density and attenuation separately using reflection amplitudes from the top and the underside of an interface, but this demands flat layers and very careful processing. Otherwise, attenuation values must be inspired guesses, and adjusted to fit the data.

The source function and receiver response is calculated or measured as in Chapter 2. The far field source function in the absence of interfaces is the basic input for the source function, and the electrical receiver response and the spatial parameters of the array — number and spacing of hydrophones is the receiver response input. The depths of the source and receiver are also needed to calculate the sea surface reflection effect; these are usually measured continuously.

Travel time and amplitude modelling

Modelling is divided into two parts, travel time modelling and amplitude modelling. Travel time modelling is relatively simple and fast, involving little more than ray tracing, and can be used for structural purposes — determining the effects of dip and structures on a profile. Amplitude calculation is complex and slower, involving the calculation of many frequency dependent effects and is used to elucidate properties of the subsurface by comparison of the amplitude and waveform shape of models with real profiles.

4.5 Travel time modelling

The one-way travel time of a ray in each layer is calculated using equation 4.8, and the travel times for each layer are summed to give the travel time of the ray. The travel times form the basis of the trace received by a shot point. Two basic amplitude effects are calculated for each arrival, and these are used with travel times to synthesize a spike profile for structural modelling. The amplitude effects are ray path spreading and reflection coefficients, which are independent of frequency and rapid to compute.

The ray path spreading effect on amplitude is calculated by tracing a ray tube for each arrival; a ray on either side of the arrival ray and at a fixed small angle to the arrival ray is traced from the surface to the reflector. The distance between the two rays at the reflector is the diameter of the ray tube, and is a measure of the wavefront area of the tube (Fig. 3.1). This is inversely proportional to the amplitude of the arrival due to ray path spreading (Chapter 3.1) so by comparison of the diameter of the ray tubes, relative amplitudes can be calculated. Amplitudes cannot be calculated at a focus by ray tracing, as the wavefront

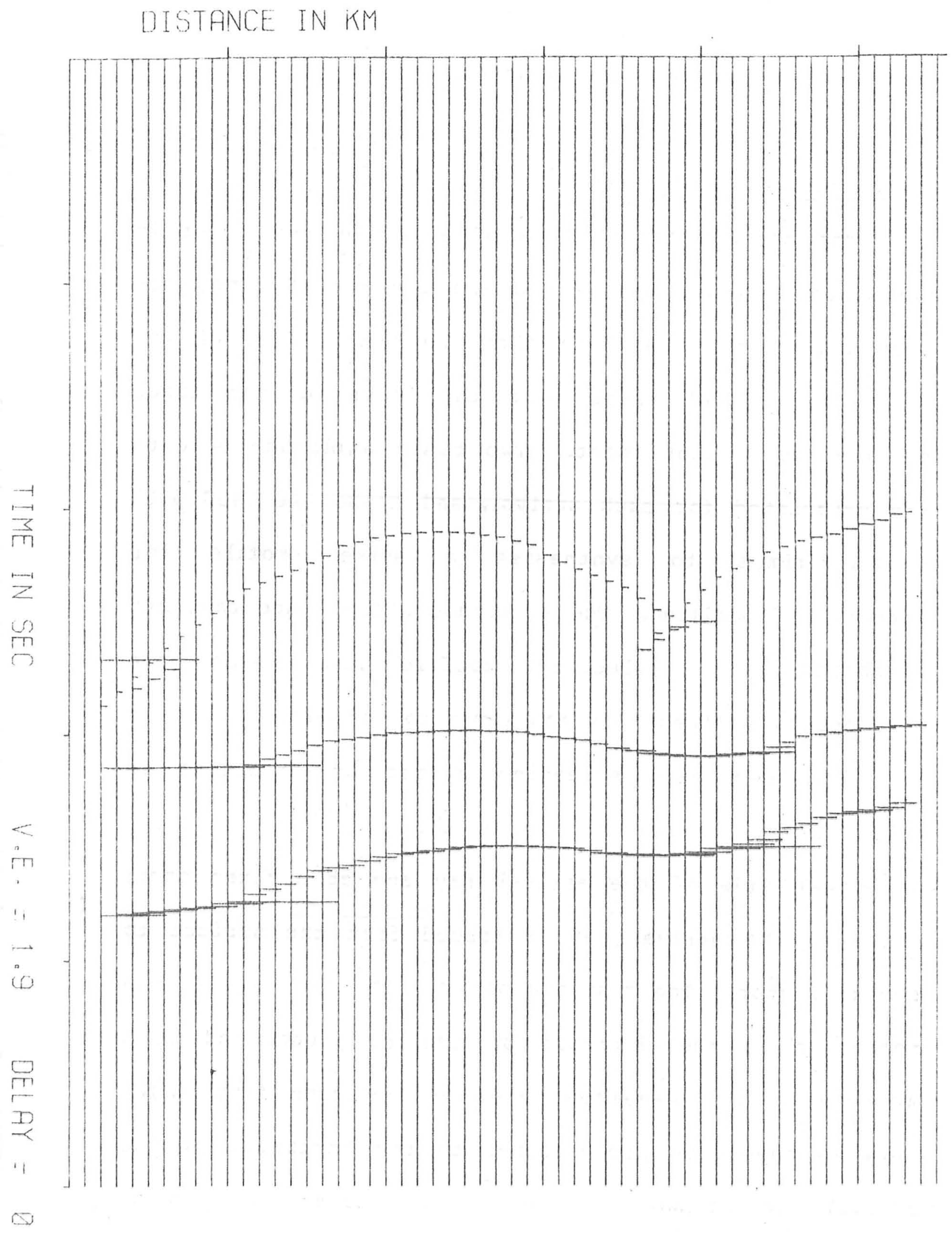

Fig. 4.6
Travel time modelling for the model in Figs. 4.3 and 4.4

area of the ray tube would be zero, which predicts an infinite amplitude. The phase change associated with the passage of a ray through a focal plane or caustic surface (Chapter 3.1) must be included when the frequency dependent effects on amplitude are calculated (Section 4.6).

The reflection coefficient at each interface is calculated using values of velocity and density on either side of the interface, and the incident angle. Wave conversion is ignored and equation 3.11 used. The combined reflection coefficient for the ray path is calculated by equation 3.12.

Ray tube tracing and reflection coefficient calculation is done by the main program (Fig. 4.5). The subroutine PROFIT collects the travel times and approximate amplitudes for all the rays arriving at the shot points and plots the reflection profile obtained from this with arrivals shown as spikes of various amplitudes. Fig. 4.6 is an example of this, corresponding to the ray tracing models of Figs. 4.3 and 4.4. The structure seen on the profile appears very different to the geological model, showing the use of travel time modelling. The sea bed anticline appears wider than on the model and the syncline narrower and the buried focus of the syncline causes more than one reflection from the sea bed to be received at the shot points above the buried focus. The lower two interfaces appear curved because of the effect of the upper curved interface. Travel time modelling is fast; the model in Fig. 4.6 took about 1 s of CPU time on an IBM 370/165.

4.6 Amplitude modelling

Complete synthesis of reflection profiles requires the calculation of the amplitude and waveform shape for each arrival. It includes the effects of multiple reflections, attenuation, dispersion, the source and the receiver into the modelling system. The frequency dependent factors are slow to compute, as each effect needs to be computed for each frequency considered. Including these effects in the calculations increases the computing time by twenty to thirty times, so full reflection profile modelling is usually only executed when the structure has been finalised using travel-time modelling.

The subroutine PROFIL is the controlling subroutine for amplitude modelling. It takes the ray paths, travel times and frequency independent basic amplitude effects of ray path spreading and reflection coefficients from the main program, and initiates the generation of multiple reflections and frequency dependent amplitude effects.

Multiple Reflections

The subroutine MULTI generates multiple reflections from primary arrivals. The calculations are approximate as the exact generation of multiples would require a separate multiple ray-tracing system, which would be more complicated and time consuming. The following assumptions are made, which are of limited validity:

1. The water layer multiple is the only multiple with a significant amplitude. This is usually valid except in areas with high sub-bottom reflection coefficients. (Chapter 3.5).

2. The multiple path is composed of the primary reflection path and one or more primary water layer paths. This is strictly only valid for flat reflectors, but is a good approximation for low angles of dip.(Chapter 3.5).

MULTI adds successsive water layer travel paths to primary reflection paths and calculates the reduction in amplitude due to ray path spreading and reflection for each multiple. The generation of successive multiples is stopped when the amplitude falls below a fixed value or the travel time of the next multiple would exceed that of the section to be plotted.

Frequency domain calculations

Frequency dependent effects are calculated in the frequency domain. Each effect is calculated separately, then they are combined and transformed into the time domain. The process of frequency domain multiplication and then fast Fourier transformation (FFT) is equivalent to time domain convolution, and is done because it is much faster and because the attenuation-dispersion effect is calculated in the frequency domain. The relative times of the processes for an n point series are:

frequency domain multiplication: time proportional to n;

FFT: time proportional to nlogn;

time domain convolution: time proportional to n^2.

The relative times for the time and frequency domain processes for a 512 point series is about 60:1.

The number of points used in the series depends on the frequency band of interest, and the time duration of the arrival needed. If we are interested in frequencies up to a frequency F_N and assume that frequencies above F_N are not present, then

$$\Delta t = 1/2F_N \tag{4.10}$$

where Δt is the time interval between points in the time domain. The number of points, n, needed is given by

$$n.\Delta t = T \qquad 4.11$$

where T is the time duration of the arrival. The spacing of points in the frequency domain is given by

$$\Delta f = 1/n.\Delta t \qquad 4.12$$

and

$$F_N = n.\Delta f/2 \qquad 4.13$$

F_N is called the Nyquist frequency. The points above the Nyquist frequency are the complex conjugates of the points below the Nyquist frequency, with the $(\frac{n}{2}+1+K)^{th}$ point corresponding to the $(\frac{n}{2}+1-K)^{th}$ point for an even n.

The value of the F_N used depends on the highest useful frequency in the reflection profile. High resolution sparker profiling may have useful frequencies up to 200 Hz (Lucas 1974). Deeper profiling needs sources with energy concentrated in a lower frequency band, as the attenuation increases with distance travelled in the earth and is greater for high frequencies. The airgun records modelled here have F_N chosen as 167 Hz, which corresponds to a sampling interval, Δt, of 3 ms (equation 4.10). The source waveform was calculated at a sampling interval of 1 ms, low pass filtered at below 167 Hz to reduce aliasing and resampled at 3 ms.

The number of points used depends on Δt and the total time duration of the waveform (equation 4.11). The airgun waveforms are assumed to have a maximum length of 0.5 s, which gives n as 167.

There are three additional problems in choosing the value of n.

1. The first is that FFT routines are much faster when n is a power of 2; a 256 point (2^8) transform is about ten times as fast as a 167 point transform, so it is advantageous to expand the 167 point series to 256 points by adding points with a value of zero to the end of the 167 point series. This has no effect on the shape of the frequency spectrum of the time series, but increases the number of points in the frequency spectrum, giving a smaller frequency interval between points (equation 4.12). The increase in frequency domain multiplication time with the longer series is not as great as the decrease in transformation time.

2. The second problem is inherent in doing convolution by frequency domain operations. The source waveform is lengthened by the effects of attenuation-dispersion, the line receiver effect, the sea surface reflections and the electrical response of the receiver. If all these effects were combined by convolution in the time domain, the received waveform would be lengthened, as convolution of the two series of length a and b, for example, gives a new series of increased length a+b-1.

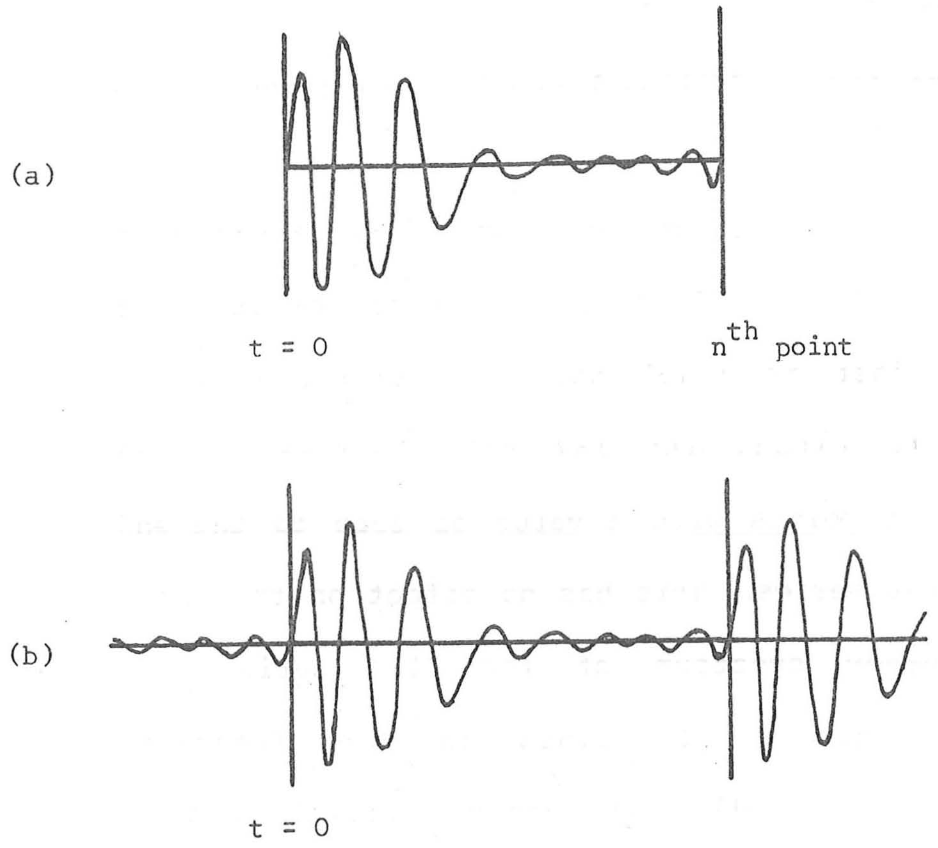

Fig. 4.7 A received waveform of the type in (a) calculated by FFT, multiplication and FFT, is a periodic waveform (b), and has a non-causal precursor before the arrival time of the waveform t = 0, due to the non-zero tail of the waveform.

Experimental time domain convolutions of the 167 point waveform with the above effects gave a received waveform about 200 points long, at which point the amplitude had decreased to less than 10^{-3} of the maximum amplitude.

Convolution by frequency domain operations does not allow for any extension in the waveform length. To get a longer received waveform by frequency domain operation the 167 point source waveform must by extended by adding zeros to a length at least as great as the expected received waveform, before it is transformed into the frequency domain. An extension from 167 to 256 points is sufficient for the airgun system.

3. The third problem is caused by trying to describe continuous data by discrete samples, as time and frequency domain operations are only exactly equivalent for continuous data. The result of discrete sampling was to produce causality problems, and this almost caused me to have to work in the time domain, using a greater amount of computing time.

A causal time series is zero before a certain time. The Fourier transforms used are discrete, and periodic; for example a received waveform of the type in Fig. 4.7a, with a non-zero tail, transformed from the frequency domain is a periodically repetitive waveform as in Fig.

4.7b, and would be non-causal — there is no finite arrival time before which the waveform is zero.

The source waveform used is of finite length and as it has been low pass filtered it can be represented reasonably accurately (not perfectly as the filter cannot have a perfectly sharp cutoff so a small amount of aliasing is introduced) by a finite number of points, say n, and no more than n samples are required to describe it in any domain.

However the waveform is really continuous and of finite length, so would extend infinitely in frequency, so there is a fundamental problem in going from continuous to discrete data and a related problem in doing time domain operations by their equivalents in the frequency domain, as the time and frequency domain operations are not exactly equivalent for discrete sampled data. Although the frequency domain operations cannot be made exactly equivalent to time domain operations, an adequate description of the data is possible by careful choice of the sampling rate and number of points. The sampling rate is determined by the highest frequency (equation 4.10) and has already been chosen as 3 ms. The number of points to use for an adequate description is less obvious.

Transformation of a 256 point source waveform (167 points increased to 256 by zeros) instead of a 167 point source waveform decreases the spacing of points in the frequency domain (equation 4.12). The points to be combined with the source waveform are calculated in the frequency domain at this frequency spacing. The lowest frequency calculated corresponds to a period of 256 points, and although the source waveform has little energy at this frequency (it is zero after 167 time points) if any of the effects have a significant response at this frequency the low frequency information introduced will make the time series non-causal. This is what happened when I worked with 256 points; the response at the lowest frequency was large enough to give a transformed time series with significant amplitude up to 256 points.

This can be improved by increasing the length of the time series by adding more zeros before transformation. This decreases the lowest frequency calculated, but if the extra low frequency information introduced decreases with decreasing frequency the effect of adding low frequency information is less. The disadvantage of this is that more points are needed, which increases the computing time, and a compromise must be found between an adequate description of the data and computing time needed. Increasing the 256 point source waveform to 512 before transformation reduced the amplitude at the end of the received waveform to less than 10^{-3} of the maximum amplitude, which I considered acceptable, so n was finally chosen as 512.

Source waveform

The subroutine SOURCE combines the basic source function and its sea surface reflection in the time domain to give the downward travelling source waveform (Chapter 2.2). It uses as input the basic source waveform in the absence of interfaces, the depth of the source and the initial angle of the ray to the vertical. This is calculated for each arrival. The 167 point waveform is extended to 512 points by adding zeros and then transformed into the frequency domain.

Receiver response

The line receiver response and the sea surface reflection effect of the receiver is calculated in subroutine REC2 for each arrival (Chapter 2.4) given the number and spacing of receivers in the receiver array, and the angle of the ray to the vertical at the receiver, and the depth of the receiver. The calculations are in the frequency domain (Chapter 2.4).

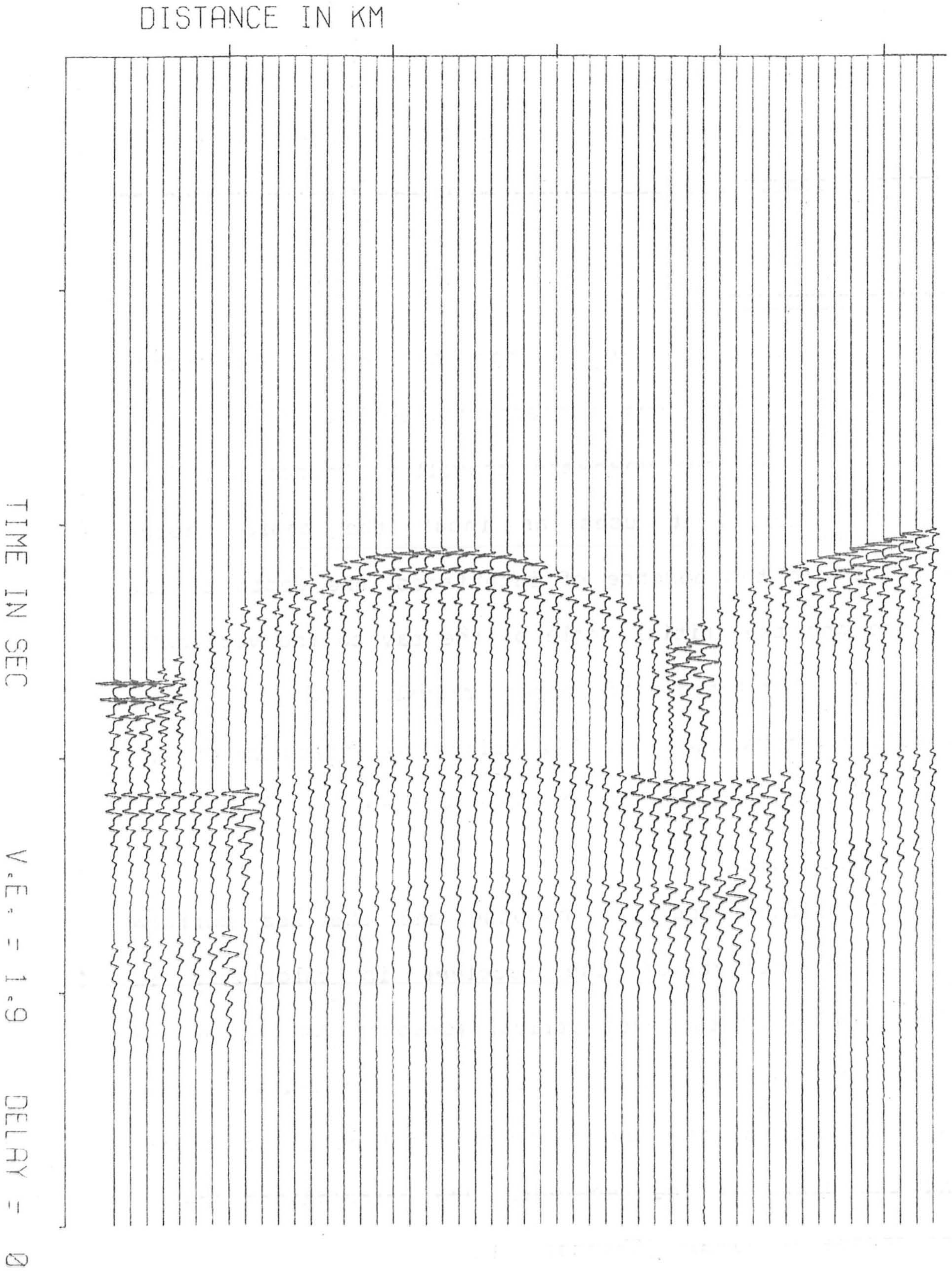

Fi.g. 4.8
Reflection profile modelling for the model in Figs. 4.3 and 4.4

Attenuation and dispersion

Subroutine ATTENU calculates the attenuation and dispersion effects, given the ray path, attenuation values, and velocities, using equations 3.13 - 3.16. The water layer is assumed non-attenuating and non-dispersive (Chapter 3.3) which for the short travel times of interest in reflection profiling is a good assumption. Because of this, water layer multiples having similar travel times as deeper primary reflections have a high frequency content. A separate value of Q may be used for each layer, or one total value used.

Combination of frequency dependent effects

FREQ is the subroutine controlling the frequency domain calculations. It initiates the subroutines SOURCE, REC2 and ATTENU for each arrival, and calls subroutine CMULT which combines the frequency spectra from SOURCE, REC2 and ATTENU, and also the electrical response of the receiver. FREQ transforms the result into the time domain, truncates it to 256 points from 512 and returns the arrival waveform to the subroutine PROFIL for each arrival. PROFIL combines the waveform for each arrival at the calculated travel times with other arrivals, and plots the reflection profile obtained.

Fig. 4.8 is the reflection profile calculated from the model of Figs. 4.3 and 4.4. This took about 30s of CPU time on an IBM 370/165. It shows the reduction in amplitude over anticlines and increase above synclines. The flat interfaces below the seabed appear curved on the profile due to refraction at the sea bed. Reflections from the sub-bottom interfaces show the effect of attenuation, in the reduction of amplitude and the change in waveform shape; the reflection from the lowest interface is very weak and low frequency. The multiples are weak.

They are visible mainly when the primary reflection is strong, as from the syncline or from planar interfaces.

The next chapter gives examples of this modelling system, for comparison with standard models and real profiles, and discusses the use and limitations of the system.

CHAPTER 5

USE OF THE MODELLING SYSTEM

5.1 Introduction

This chapter gives examples of the modelling system, for standard models such as synclines, anticlines and faults, and more complicated models for comparison with observed profiles. It looks at the usefulness of the modelling system for interpretation, and at its limitations, and discusses ways in which the system could be developed further.

All the observed profiles in this chapter are from the eastern Mediterranean, which has very complicated structures that provide a good test of the modelling system and where good quality records are normally obtained because of the prevailing good weather. The profiles are made with an airgun profiling system, with either a 30 in^3 free-firing gun or a 160 in^3 electrically-fired gun, and a single active section hydrophone array, an input amplifier and analogue frequency-modulated tape recording system, and played out with true amplitudes as a trace on an x-t recorder. The input parameters used for modelling are:

1. The source wavefrom predicted by the theory of Ziolkowski (1970) using airgun volume, pressure and depth

(Chapter 2.3).

2. The source and receiver depths, which were continuously recorded, and an average value of depth for each is used for the model.

3. The impulse response of the recording electronics (Smith & Owen 1975).

4. Hydrophone arrray parameters: equally spaced and weighted with 50 hydrophones 1.17 m apart.

5. Velocities from disposable sonobuoy results or from published velocities if available.

6. Densities estimated roughly from velocity-density curves (Woollard 1962; Nafe & Drake 1963) and adjusted to match the observed amplitudes.

7. Attenuation is known to lie within the broad range of Q = 20 - 100 for depths of a few kilometres (Chapter 3.3) and is adjusted within this range for the waveform shape of the reflections.

8. Structure is estimated from the observed profile and adjusted until the model fits the profile.

5.2 Standard models and observed profiles

Horizontal layers

A simple horizontally layered profile shows how the modelling system can model an observed profile reasonably closely, and how it assists in distinguishing closely spaced layers, and demonstrates the effects of ignoring sub-bottom multiples and varying the value of attenuation.

Fig. 5.1a is an observed profile interpreted as a sequence of three flat reflectors, one with a stong sub-bottom reflection coefficient. This was the profile used in the discussion of intersedimentary multiples in Chapter 3.5. The observed profile has well controlled source and receiver parameters, but the values of velocity, density and attenuation are unknown. Reflection coefficients were roughly estimated from the primary reflection amplitudes and travel times, and velocity and density calculated from the reflection coefficients and velocity-density curves and then checked by modelling and comparing the amplitudes of observed and multiple reflections with the observed profile. Attenuation is estimated from the shape of the sub-bottom primary and multiple reflections and knowledge of the probable range of attenuation, and again checked by modelling.

These estimates are likely to be unsatisfactory because observed amplitudes are affected by both reflection coefficient and attenuation and it is difficult to distinguish the effects. When the velocity can be measured by other means, such as variable angle reflection, and the density estimated from

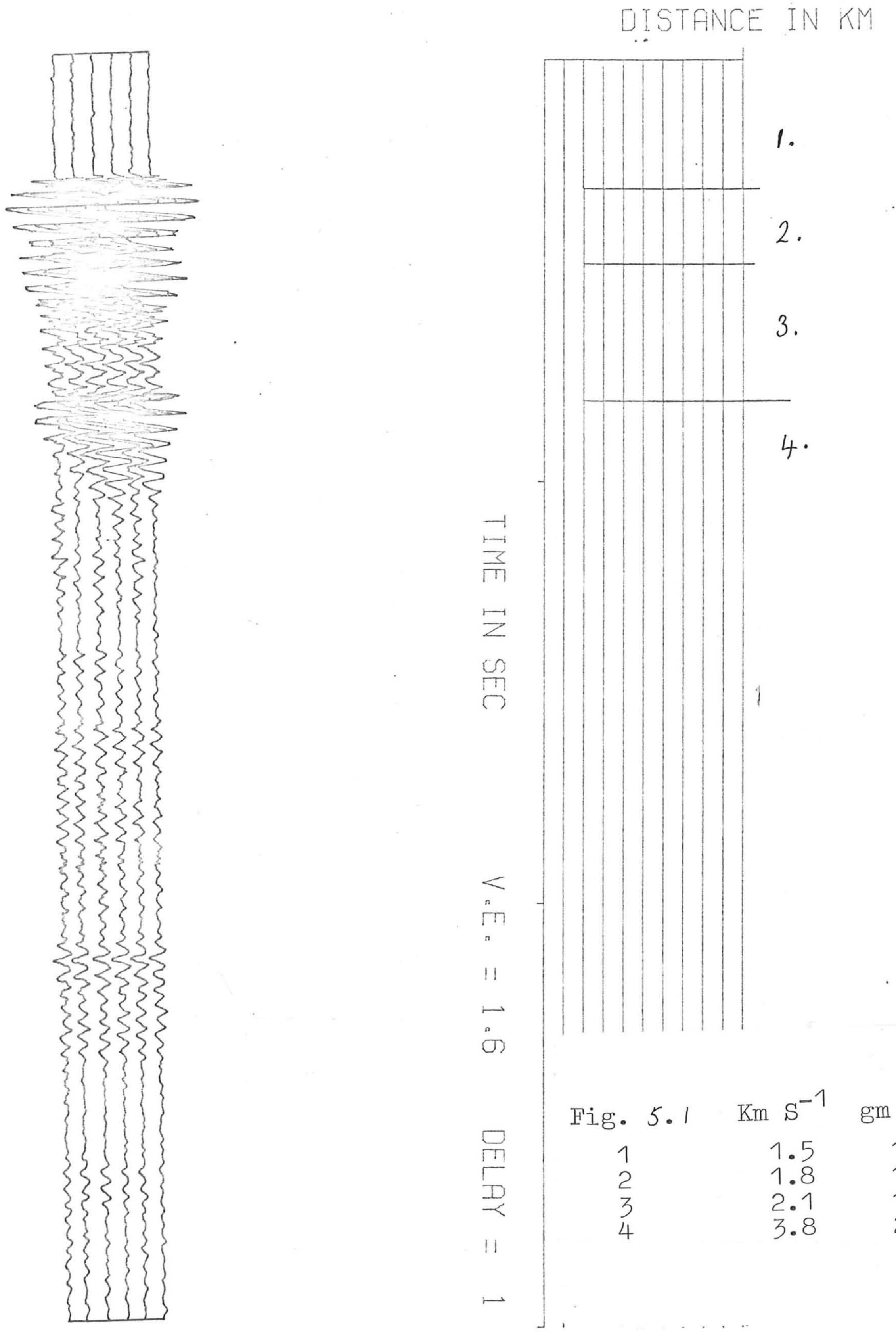

Fig. 5.1	Km S^{-1}	gm cc^{-1}	Q
1	1.5	1.0	
2	1.8	1.2	50
3	2.1	1.5	50
4	3.8	2.2	

(a) (b)

Fig. 5.1

(a) A true amplitude observed profile from the eastern Mediterranean.

(b) Spike profile for modelling.

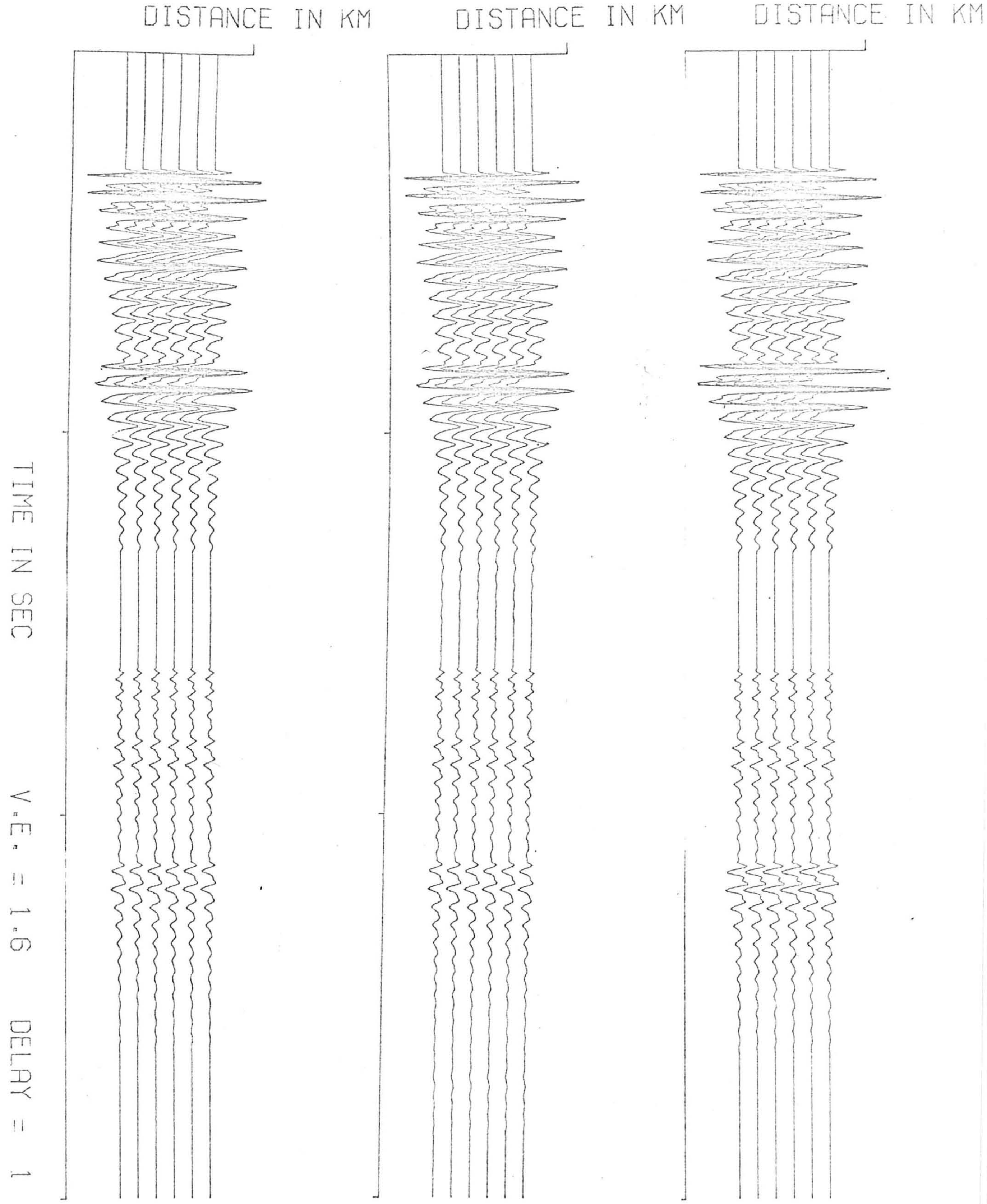

(c) (d) (e)

Fig. 5.1

(c) Synthetic reflection profile, Q = 50

(d) Synthetic reflection profile, including sub-bottom multiples, Q = 50

(e) Synthetic reflection profile, Q = 100 velocity-density curves, only attenuation has to be estimated from the profile, so a more accurate estimate is possible.

Fig. 5.1b is a spike profile calculated from travel times and approximate amplitudes and Fig. 5.1c is the synthetic reflection profile. This matches the observed profile quite closely, wiggle for wiggle in most parts. It was difficult to place the reflector below the sea bottom accurately without modelling, as it overlaps with the sea bottom reflection, but by adjusting its position on the model and comparing the synthetic with the observed profile it was possible to get its position reasonably precisely.

The greatest discrepancy between the observed and synthetic profiles is the 3.6 s reflection on the observed profile, which is not predicted by the modelling system. This is produced by a combination of three multiple paths and is relatively strong due to the strong sub-bottom reflector at 1.8 s. The ray paths of this multiple are drawn in Chapter 3.5. As an estimate of the error in the modelling system ignoring sub-bottom multiple refections, I wrote a subroutine to generate all multiples, including intersedimentary multiples, within a fixed travel time for horizontal reflectors, and this was applied to the model in Fig. 5.1b, to give the synthetic profile Fig. 5.1d. The difference between this and Fig. 5.1c, generated without intersedimentary multiples is small, but weak multiples are visible at 2.3 and 3.6 s. Most reflection profiles have much weaker sub-bottom reflections than this profile, so the error in the modelling system generating only water-layer multiples is generally very small.

The synthetic profile Fig. 5.1c was calculated with a Q of 50 for the two sediment layers. A profile calculated with a Q of 100 is shown in Fig. 5.1e, and it has higher amplitudes and frequency content for sub-bottom primary and multiple reflections. The primary ampltudes and the multiple shapes and amplitudes are a worse match to the observed profile than Fig. 5.1c, with Q = 50, indicating the degree of control provided by profile matching.

Synclines and Basins

Two synthetic profiles of a single layer syncline are used to show the effects of structural and amplitude changes due to reflector curvature. The two profiles have the same shaped syncline, one at a depth of 0.8 km (Fig. 5.2a) and the other at a depth of 2.8 km (Fig. 5.3a).

Fig. 5.2b is the synthetic profile calculated from the model of Fig. 5.2a. The profile has no vertical exaggeration. Structurally the modelled syncline is

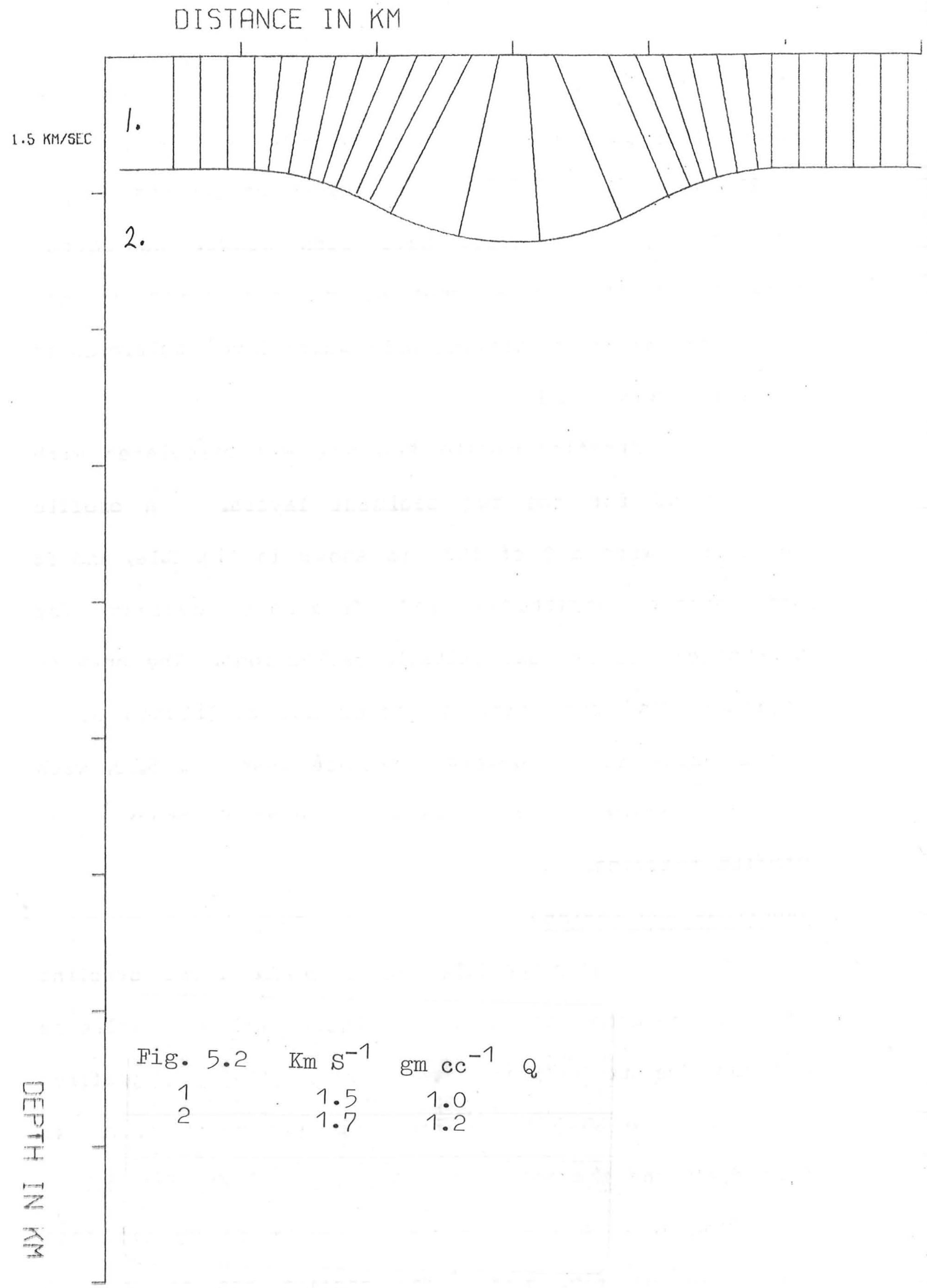

Fig. 5.2	Km S^{-1}	gm cc^{-1}	Q
1	1.5	1.0	
2	1.7	1.2	

Fig. 5.2a
Ray tracing for shallow syncline model

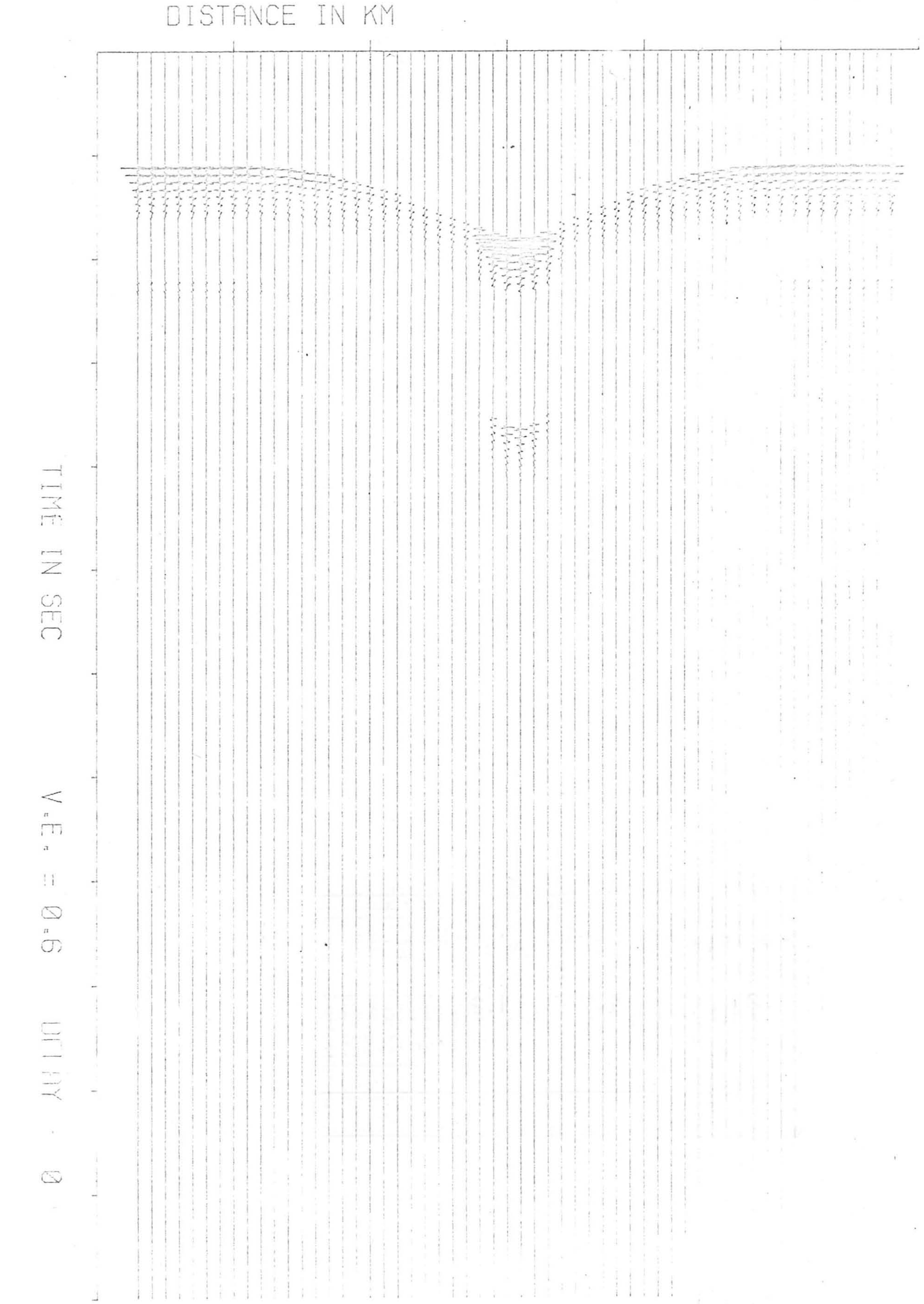

Fig. 5.2b
Synthetic profile from shallow syncline model

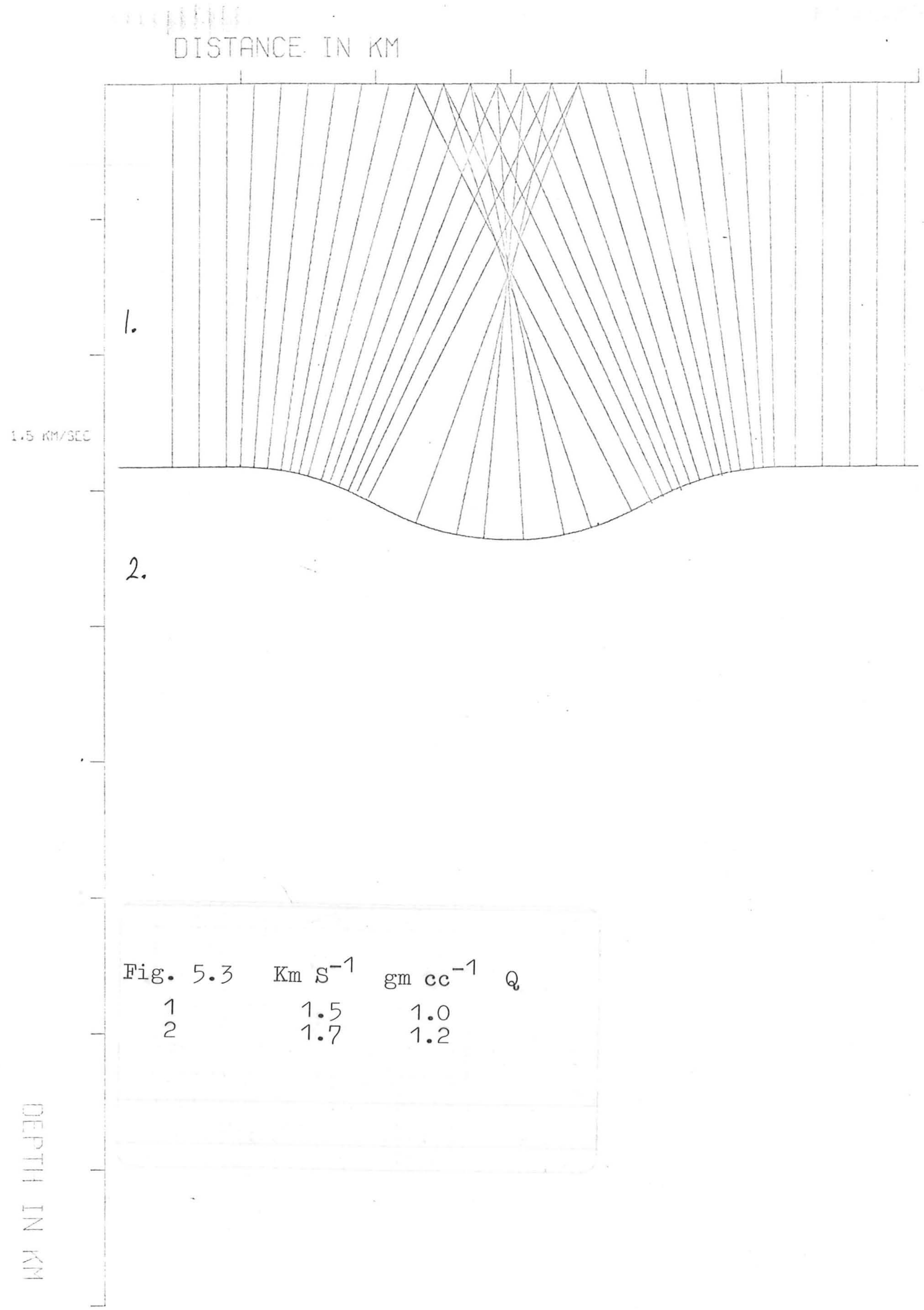

Fig. 5.3	Km S^{-1}	gm cc^{-1}	Q
1	1.5	1.0	
2	1.7	1.2	

Fig. 5.3a

Ray tracing from deep syncline model

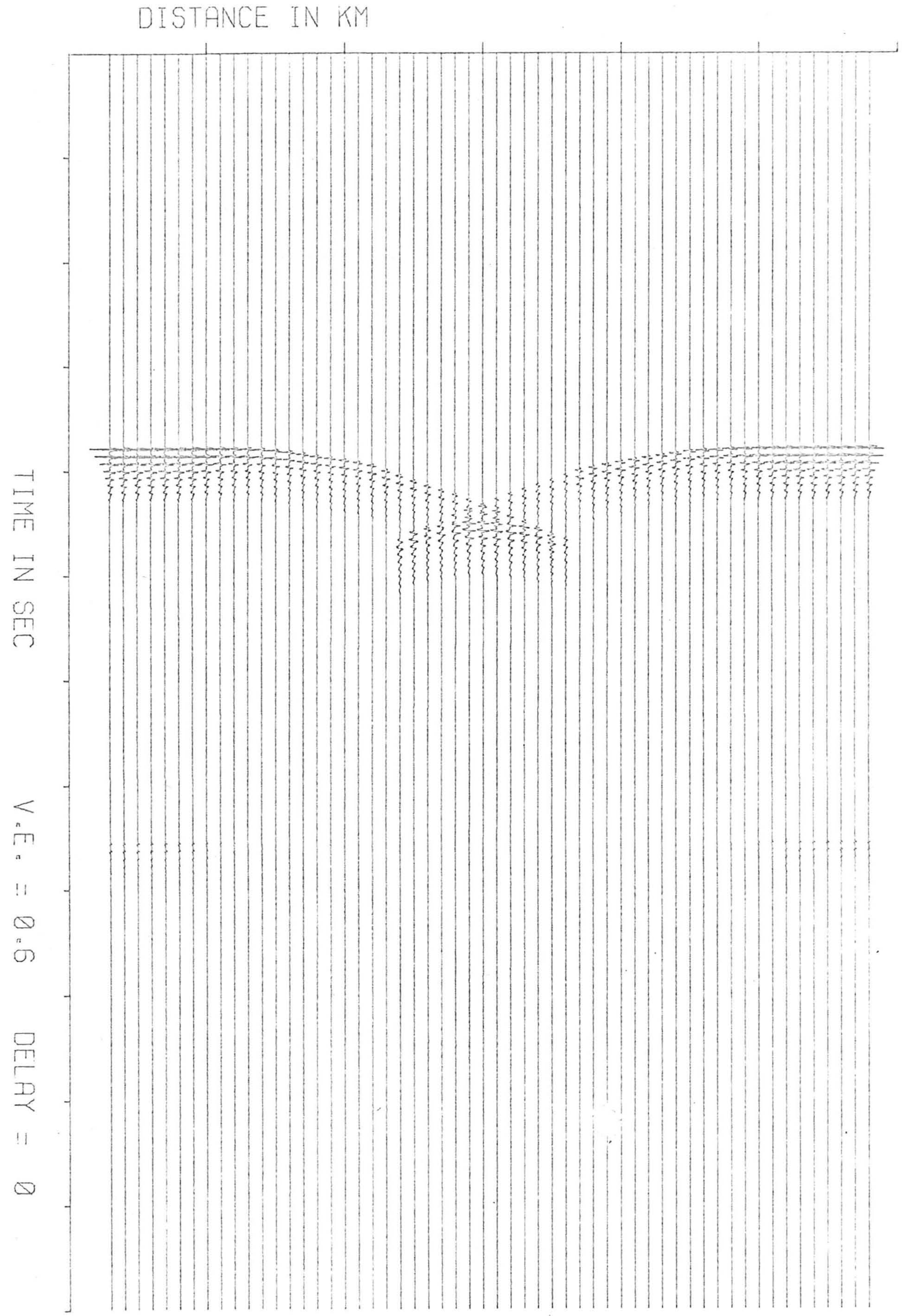

Fig. 5.3b

Synthetic profile from deep syncline model narrower at the bottom than the model, which gives it a more V-shaped appearance. This is a geometrical distortion effect, due to non-vertical ray paths. There is a constant amplitude from the horizontal sides of the syncline, which decreases as the surface begins to slope downwards, due to the convex-upwards curvature which causes divergence of rays reflected at the surface. Reflections from the bottom of the syncline have higher amplitudes due to the focussing effect of the concave-upwards surface, than those from the horizontal planar parts of the surface. The only multiple visible comes from the strong reflections at the bottom of the syncline.

Fig. 5.3b is the synthetic profile calculated from the deeper syncline model Fig. 5.3a. The radius of curvature of the syncline is less than the depth of the syncline in this case, so there is a buried centre of curvature and the effect is seen in the triplication of travel times from the shot points over the centre. The reflections from the sides of the syncline cross above the bottom of it, forming a V-shape which is very characteristic of a buried centre of curvature.

The amplitude variations are similar to those of the shallow syncline, but the reflections from the bottom of the syncline are weaker, as they are diverging

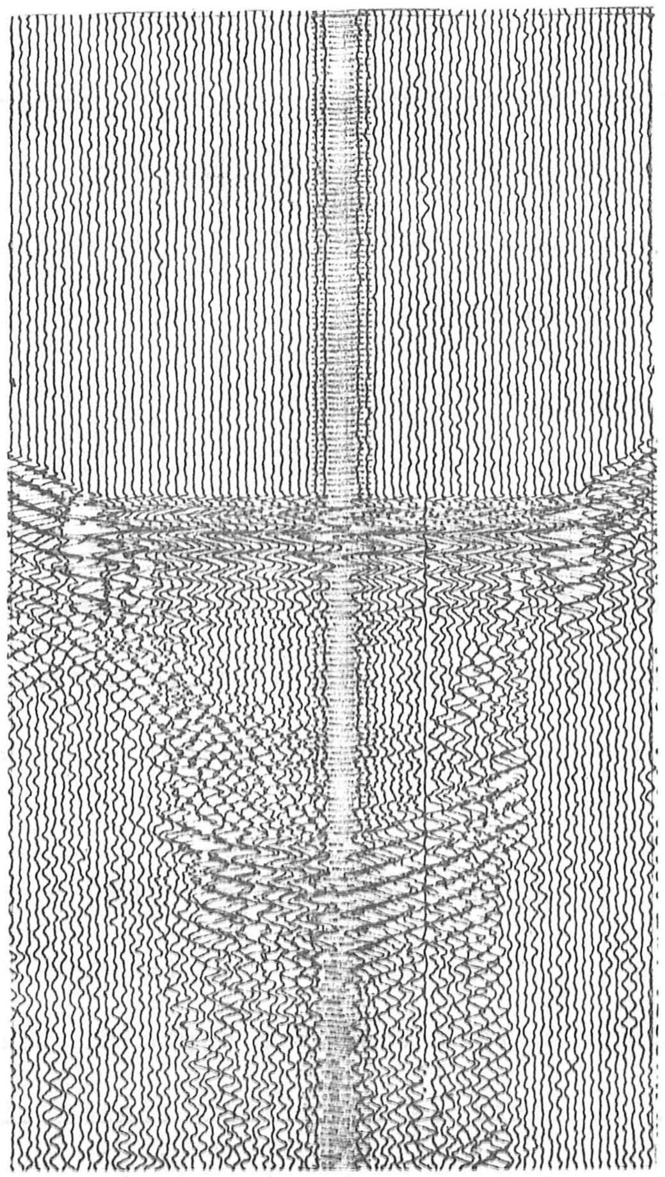

Fig. 5.4a

Observed profile of a basin.

The vertical line is a time mark.

FORTRAN UNIT NUMBER 8

WCAV J550SGS1 WIGGLE GUN 160

START JOB 550 9.56.03 PM 3 JUL 75 * * *

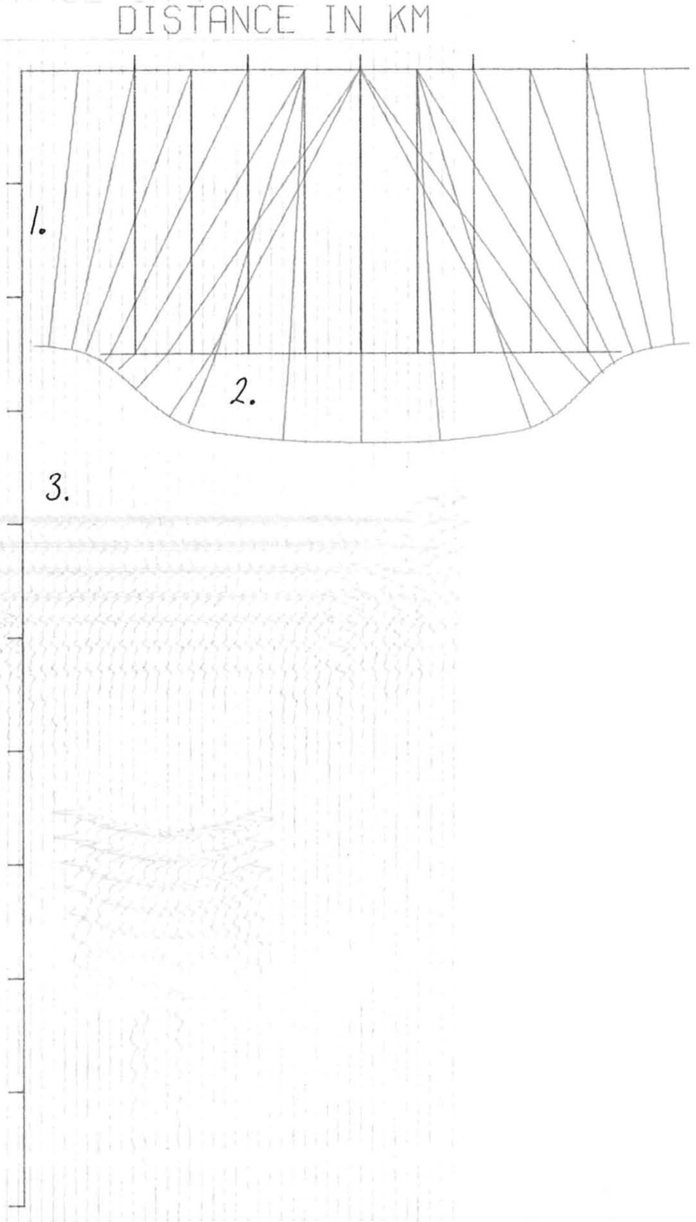

Fig. 5.4	Km S^{-1}	gm cc^{-1}	Q
1	1.5	1.0	
2	1.8	1.5	50
3	3.5	2.1	

Fig. 5.4b

Model and ray tracing for the basin of Fig. 5.4a

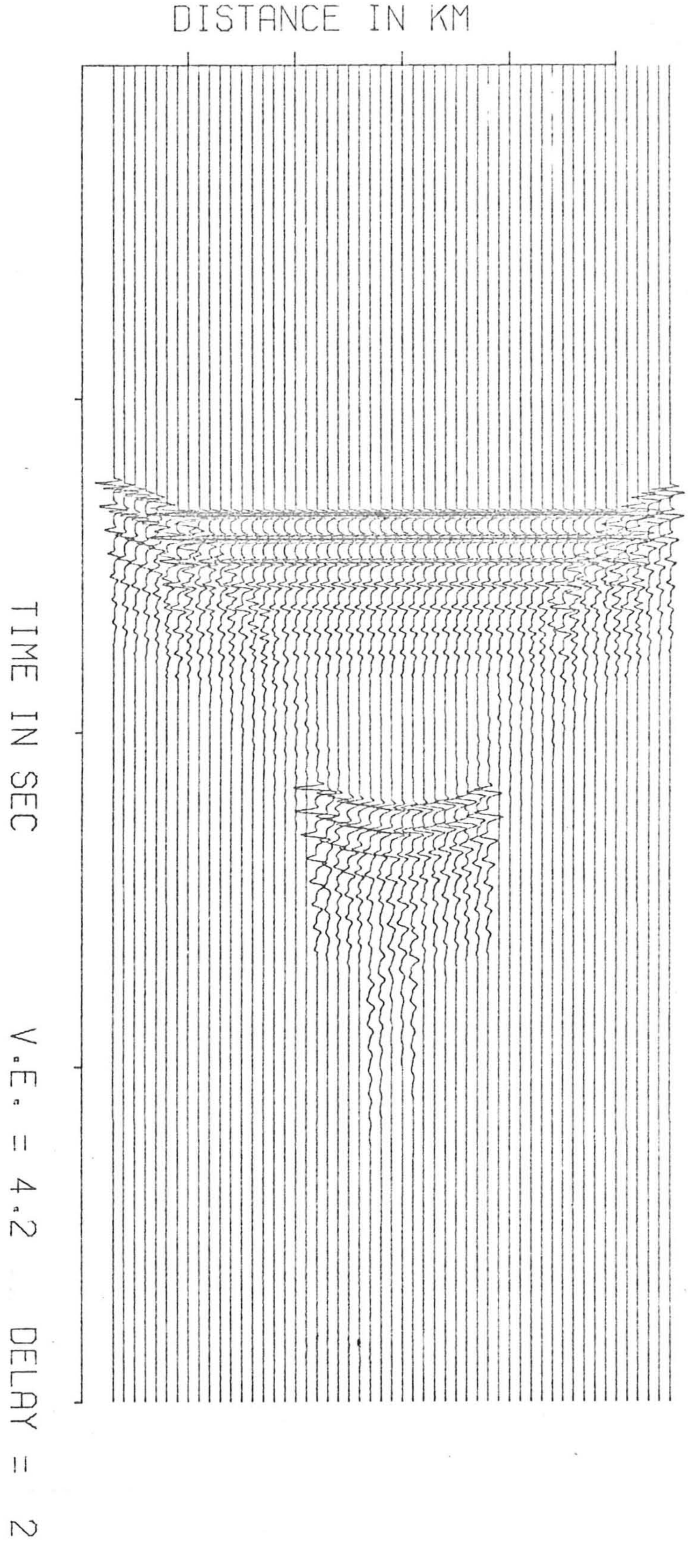

Fig. 5.4c
Synthetic profile for comparison with the observed profile fig. 5.4a

from the centre of curvature and have travelled a greater distance relative to the reflections from the horizontal parts of the syncline than in the shallow syncline model. The amplitude would be very high if the depth of the syncline was the same as its radius of curvature, so that the centre of curvature was near a shot point. The inverted part of the syncline should be extended to each side by diffractions, which rapidly decrease in amplitude with distance (Hilterman 1970), and the inability of the system to predict this is a significant limitation.

The deeper syncline synthetic has a gain four times that of the shallow syncline.

Fig. 5.4a is an observed profile of a basin with a gently curving bottom, strongly curving sides and filled with sediment with a horizontal surface. It has many characteristics shown by the syncline model profiles, such as triplication of travel times. Fig. 5.4b is an interpreted model and ray tracing, which has been adjusted to produce a synthetic profile (Fig. 5.4c) to match the observed profile. The basin appears narrower on the profile than the model, and the flanks extend further into the basin than the sides of the sediment surface and the sides of the basin bottom; the real width of the basin is the width of the sediment surface and basin bottom, not the position of the flanks. The synthetic profile matches the observed profile quite well, in structural features and amplitude variations. The reflection amplitude is strong from the flat sediment surface and concave-upwards basin bottom, and weak on the basin sides due to divergence of the rays.

The reflections that have passed through focal planes (Figs. 5.3a and 5.4b) should have a phase change of $\pi/2$ (Chapter 3.1). This is not incorporated in the system at the moment, due to the difficulty of getting the system to recognise when it has passed through a focal plane.

Anticlines and Domes

These are structures with a convex-upward curvature and as in the case of synclines they produce large variations in amplitude due to their curvature. Figs. 5.5a and 5.6a show models of two domes with a flat reflector beneath them, and Figs. 5.5b and 5.6b show the profiles synthesized from them. Dome 1 curves sharply into the flat reflector on either side, whereas dome 2 curves gently into the reflector. The reflection amplitude over the domes is low compared with the reflection amplitude from the horizontal part of the surface to either side, due to divergence of reflected rays. There is a buried centre of curvature on either

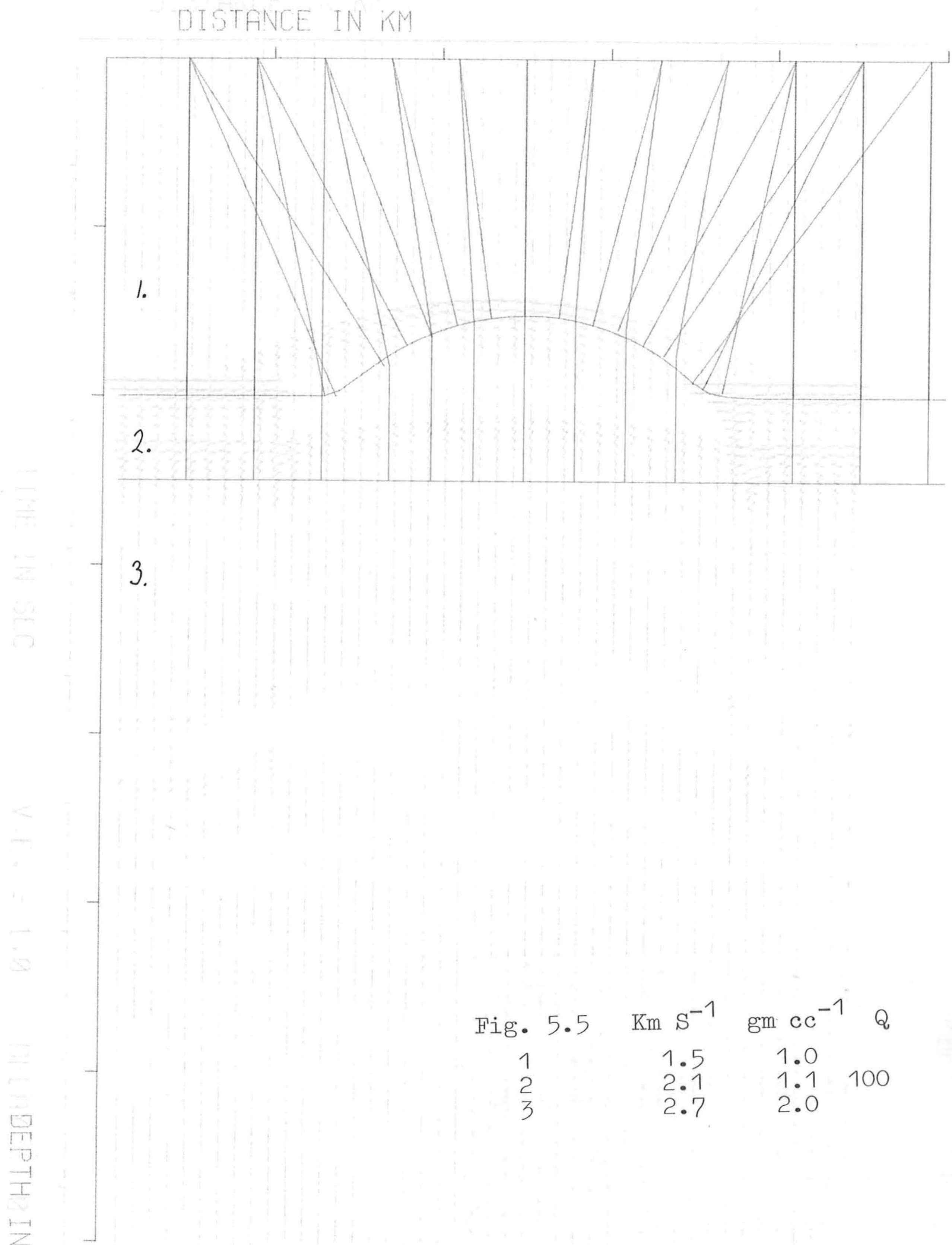

Fig. 5.5	Km S^{-1}	gm cc^{-1}	Q
1	1.5	1.0	
2	2.1	1.1	100
3	2.7	2.0	

Fig. 5.5a

Ray tracing from Dome 1 model.

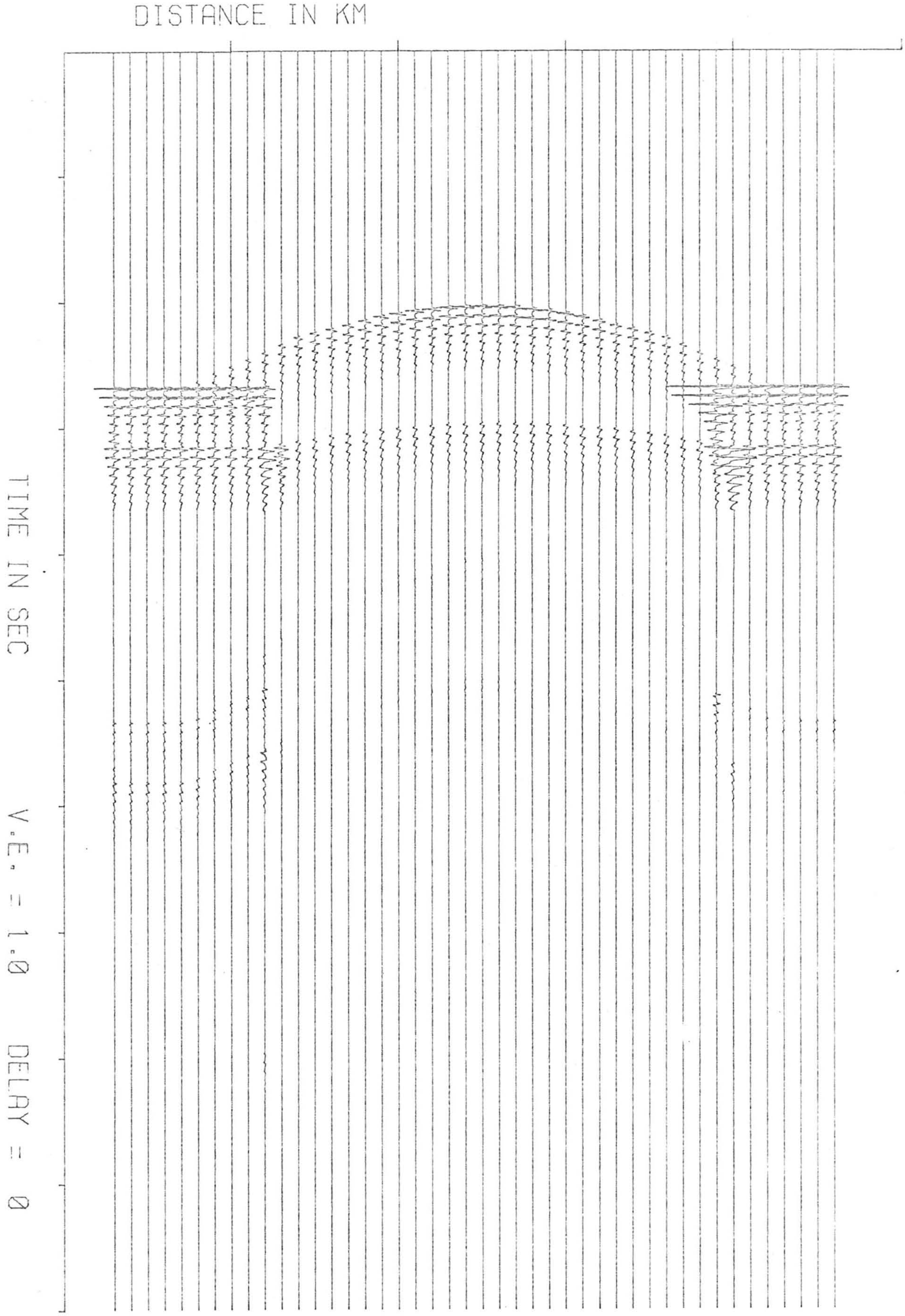

Fig. 5.5b

Synthetic profile from Dome 1 model

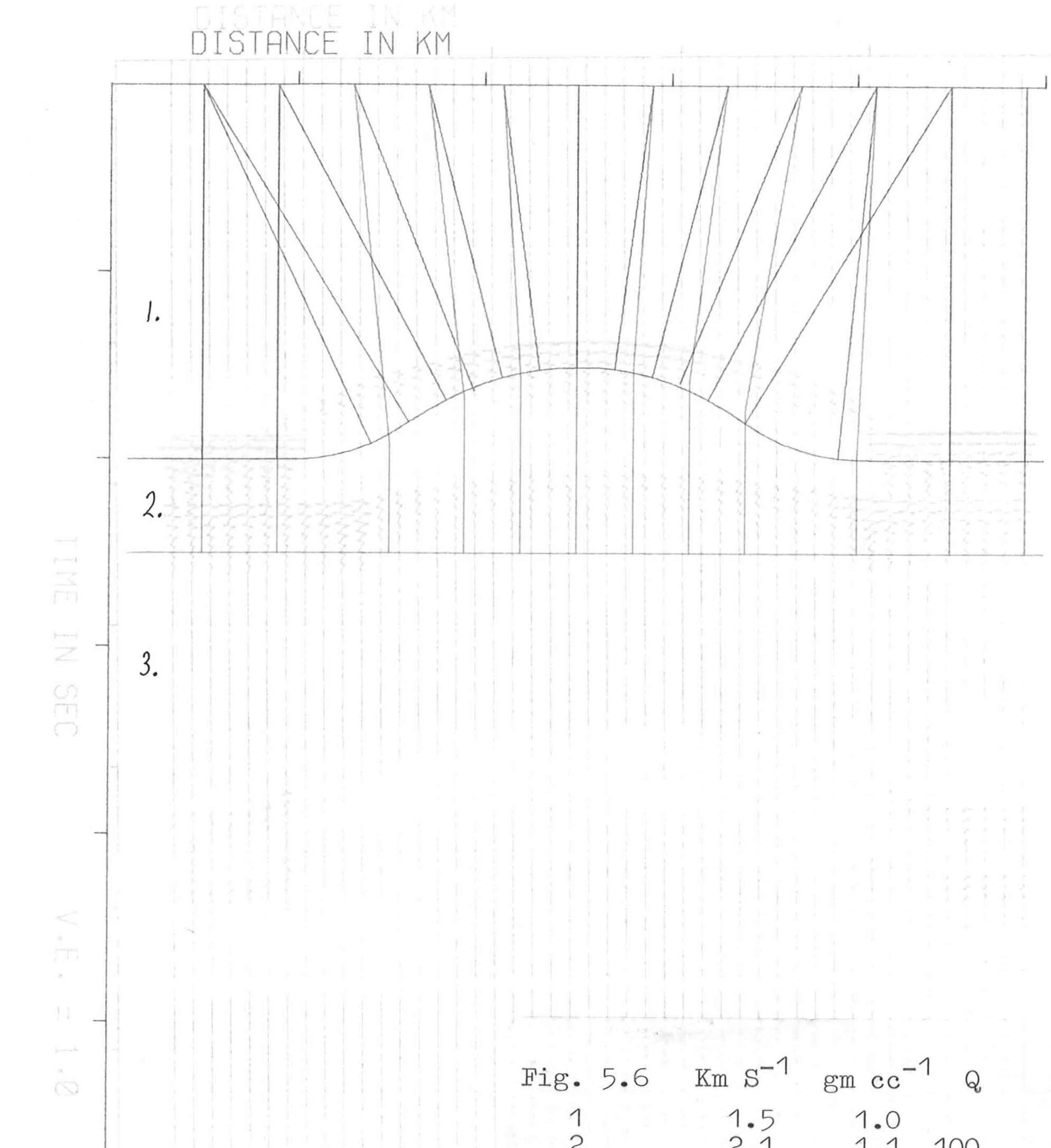

Fig. 5.6	Km S^{-1}	gm cc^{-1}	Q
1	1.5	1.0	
2	2.1	1.1	100
3	2.7	2.0	

Fig. 5.6a

Ray tracing from Dome 2 model

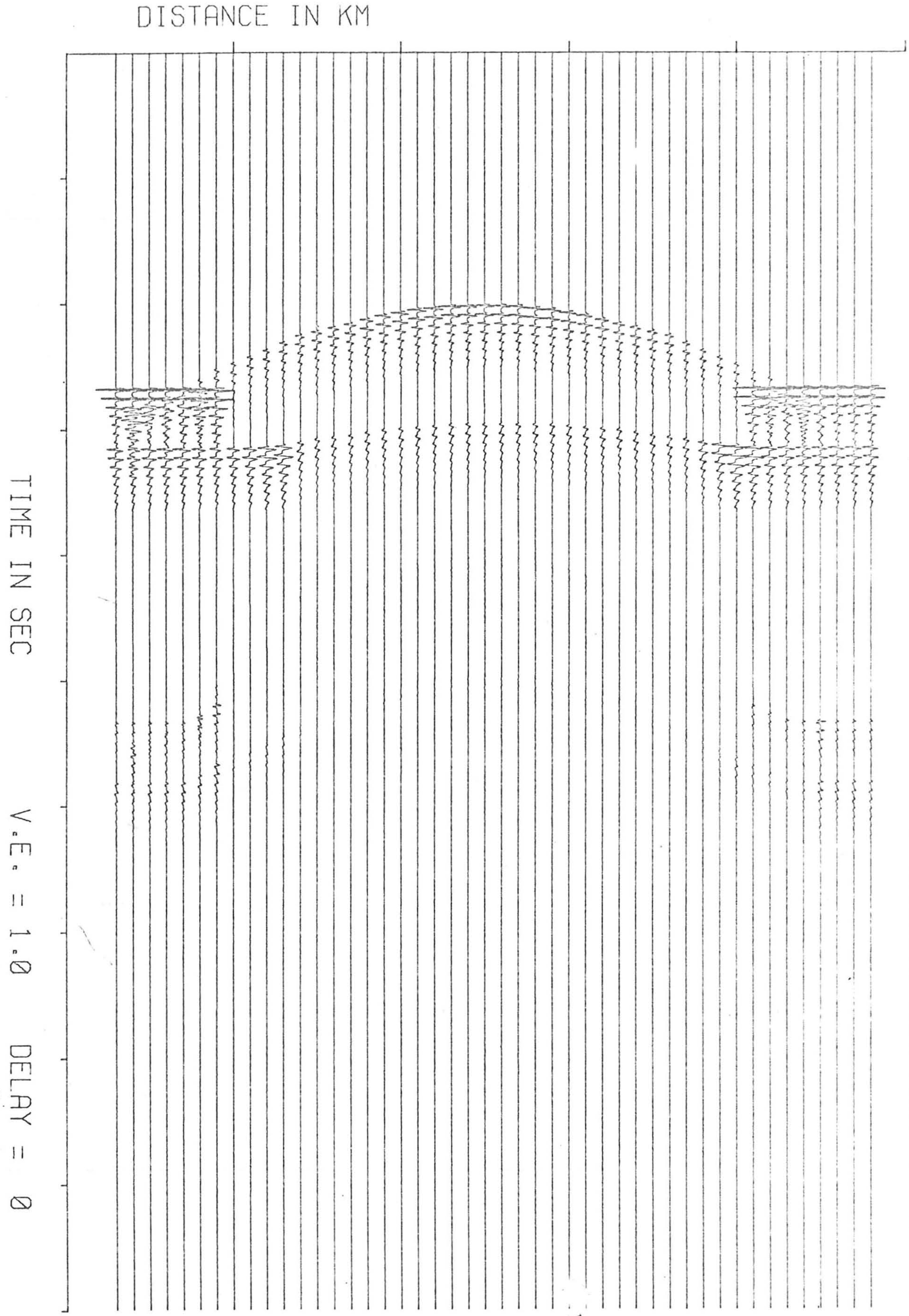

Fig. 5.6b

Synthetic profile from Dome 2 model

side of the dome, giving triplication of travel times from the shot points above it, and the sides of the domes overlap the flat reflector making the dome appear wider than it is. Dome 1, with higher slopes at its sides, extends further to either side on the profile than dome 2.

The flat reflector underneath the dome has a reduction in travel time below the dome due to the higher velocity of the sediments than the water (pull-up) and a reduction in amplitude due to divergence of the rays. The reflection amplitude may become low enough to be lost in the noise on the record, so that it is impossible to tell whether there is any reflection continuing beneath the dome, or whether the reflectors are truncated at the sides. An example of this on an observed profile is shown in Fig. 5.7a. This has a sea bed reflection and a strong lower reflection on either side of a small dome, which does not appear to continue beneath the dome, but to be truncated sharply on either side. There are diffractions from the truncated edges of the lower reflector. A model was made of this and adjusted to fit the observed profile, assuming a continuous reflector beneath the dome, to see whether this would be distinguishable if it did exist. (Figs. 5.7b and c). The amplitude of the reflection beneath the

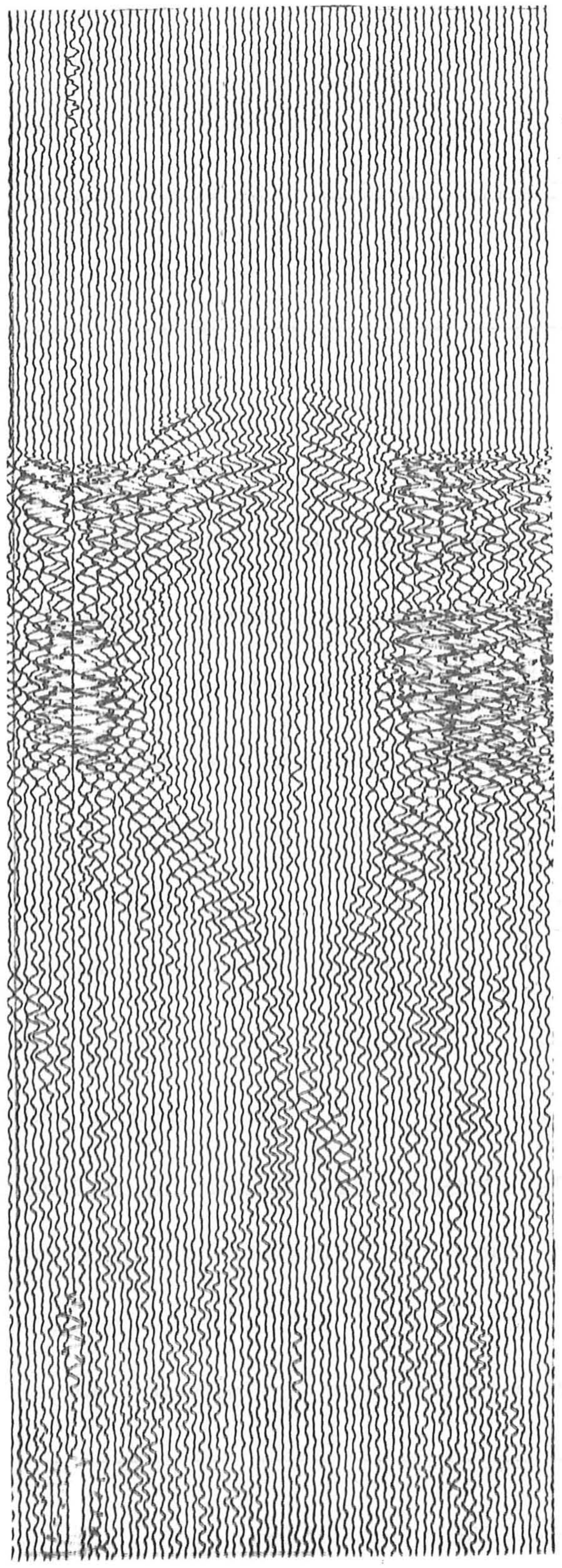

Fig. 5.7a
Observed profile of a dome with no reflectors visible beneath it.

FORTRAN UNIT NUMBER 8
WCAV J723SGS1 CSP HEROD BASIN
START JOB 723 3.21.47 PM 1 JUL 75 * * *

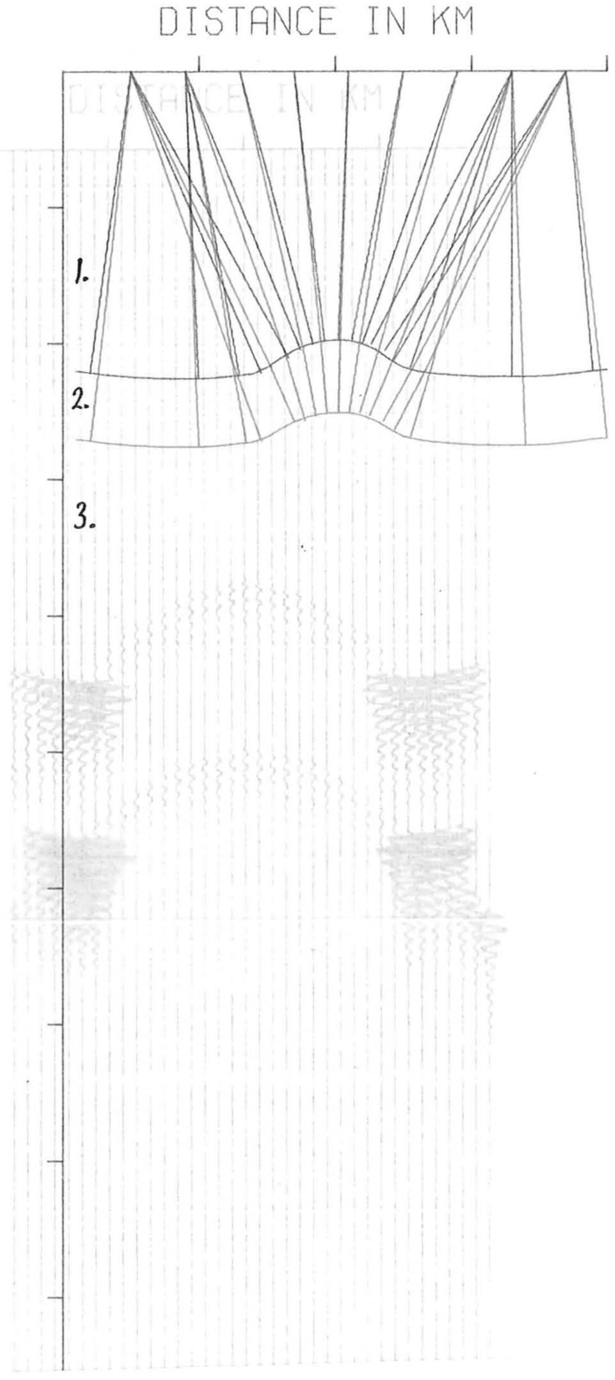

Fig. 5.7	Km S^{-1}	gm cc^{-1}	Q
1	1.5	1.0	
2	1.7	1.2	100
3	2.7	2.0	

Fig. 5.7b
Model and ray tracing for the dome of Fig. 5.7a

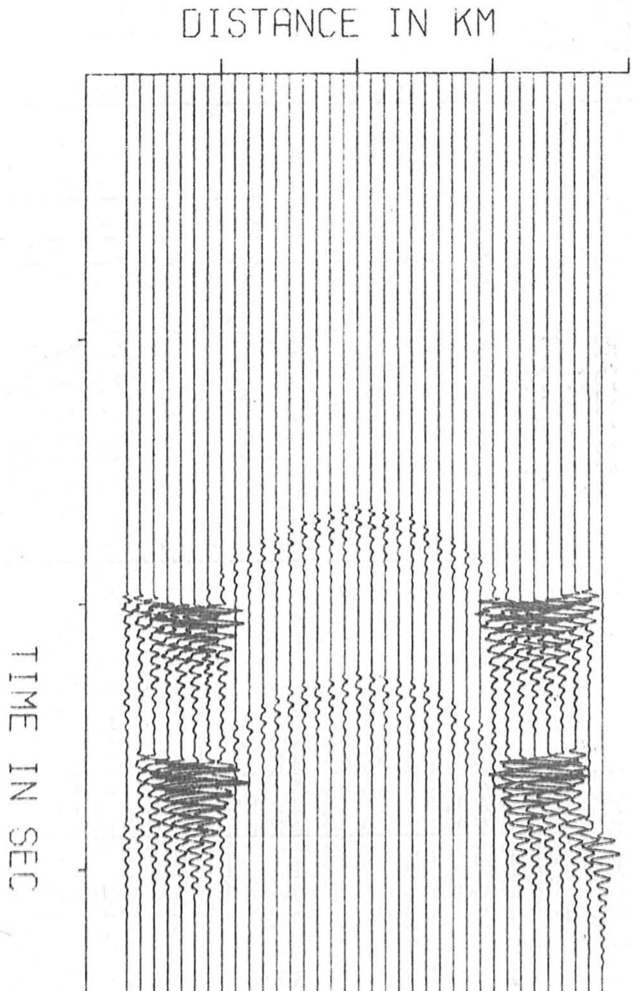

Fig. 5.7c
Synthetic profile for comparison
with the observed profile Fig. 5.7a

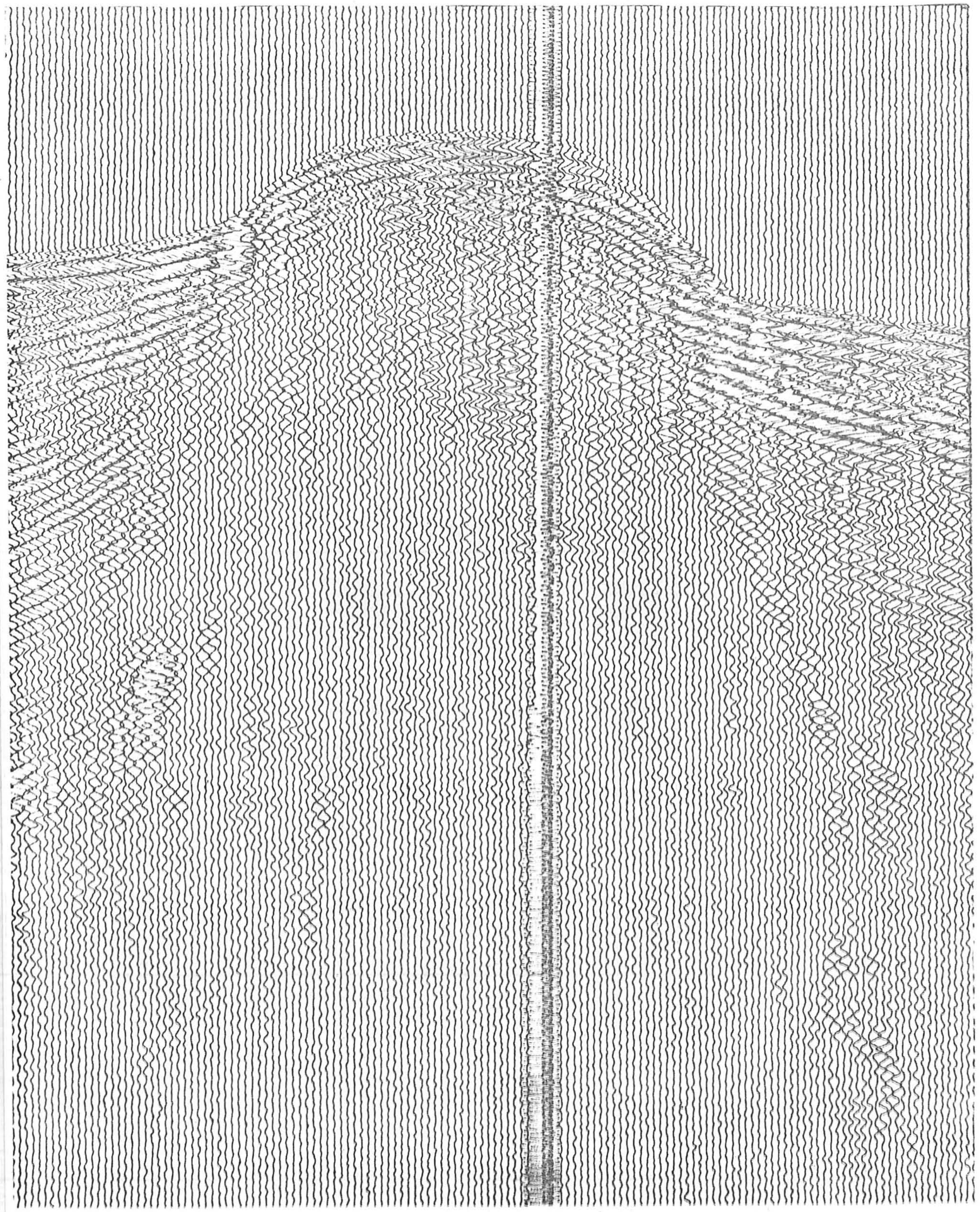

Fig. 5.8a

Obsreved profile of a dome with reflectors visible beneath it.

The vertical line is a time mark.

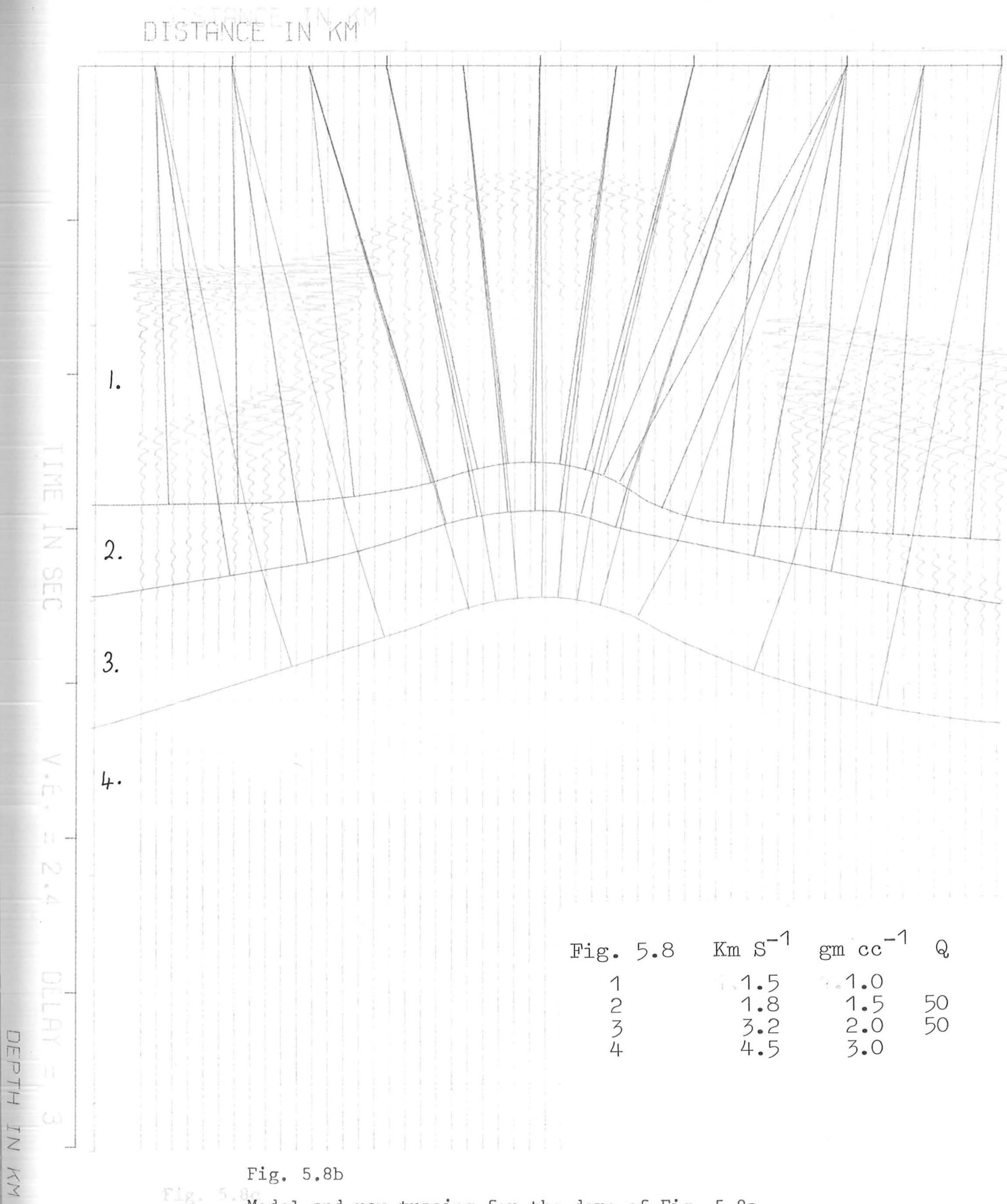

Fig. 5.8	Km S^{-1}	gm cc^{-1}	Q
1	1.5	1.0	
2	1.8	1.5	50
3	3.2	2.0	50
4	4.5	3.0	

Fig. 5.8b

Model and ray tracing for the dome of Fig. 5.8a

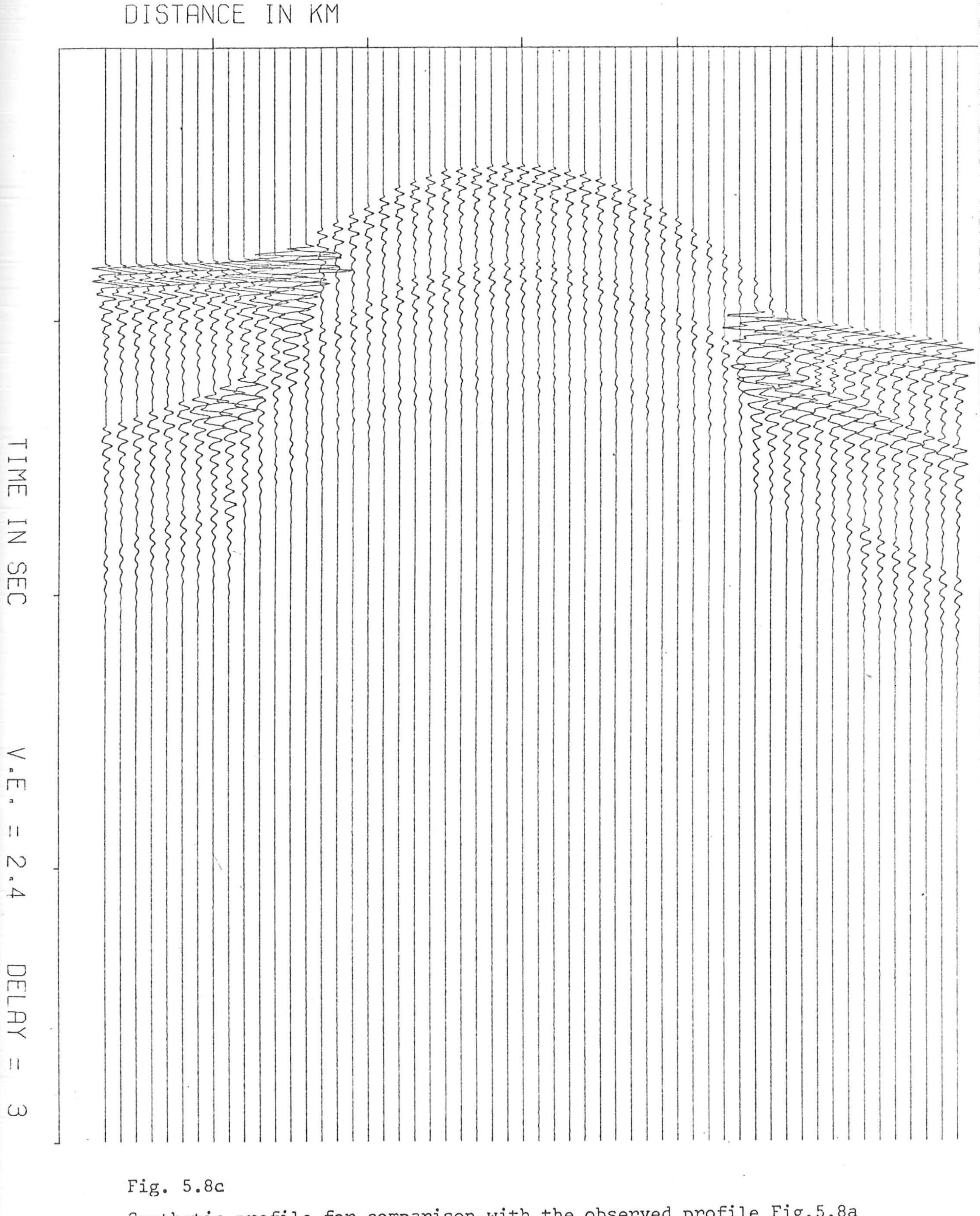

Fig. 5.8c

Synthetic profile for comparison with the observed profile Fig.5.8a dome is very low, about 0.1 of the reflection amplitude to either side of the dome, which could be lost in the noise, giving the impression that there are no reflectors inside the dome. This result is of importance to the interpretation of domes in oil-bearing areas, as what may appear to be a structureless dome on a profile may have reflectors continuing through it.

Fig. 5.8a is an observed profile of a dome in which reflectors can just be seen continuing beneath it, and Figs. 5.8b and c are the model and synthetic profile for this dome. The layers thin slightly over the dome. The dome has a larger radius of curvature than the dome in the previous profile, and because of this the reduction in reflection amplitude under the dome is less, and the lower reflectors are visible.

A similar effect is seen in the Cilicia grid survey profiles (Chapter 6) which has domes of varying sizes. Reflections from domed sediments are seen below the larger domes, with the lowest curvatures, whereas the smaller domes appear transparent. This may be caused by the above geometrical effect, and cannot be interpreted definitely as a change in dome structure.

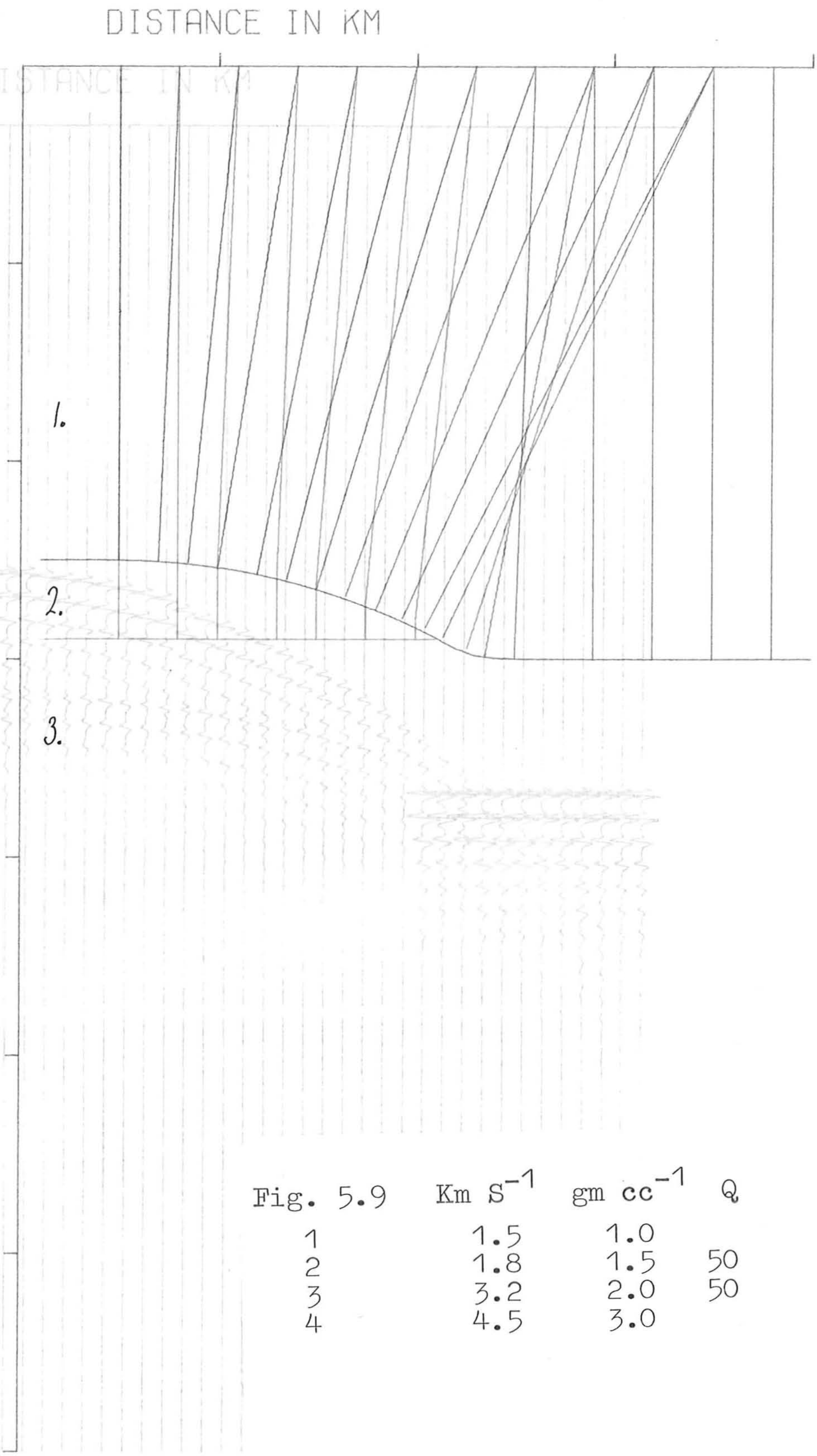

Fig. 5.9	Km S^{-1}	gm cc^{-1}	Q
1	1.5	1.0	
2	1.8	1.5	50
3	3.2	2.0	50
4	4.5	3.0	

Fig. 5.9a

Ray tracing of a cliff model.

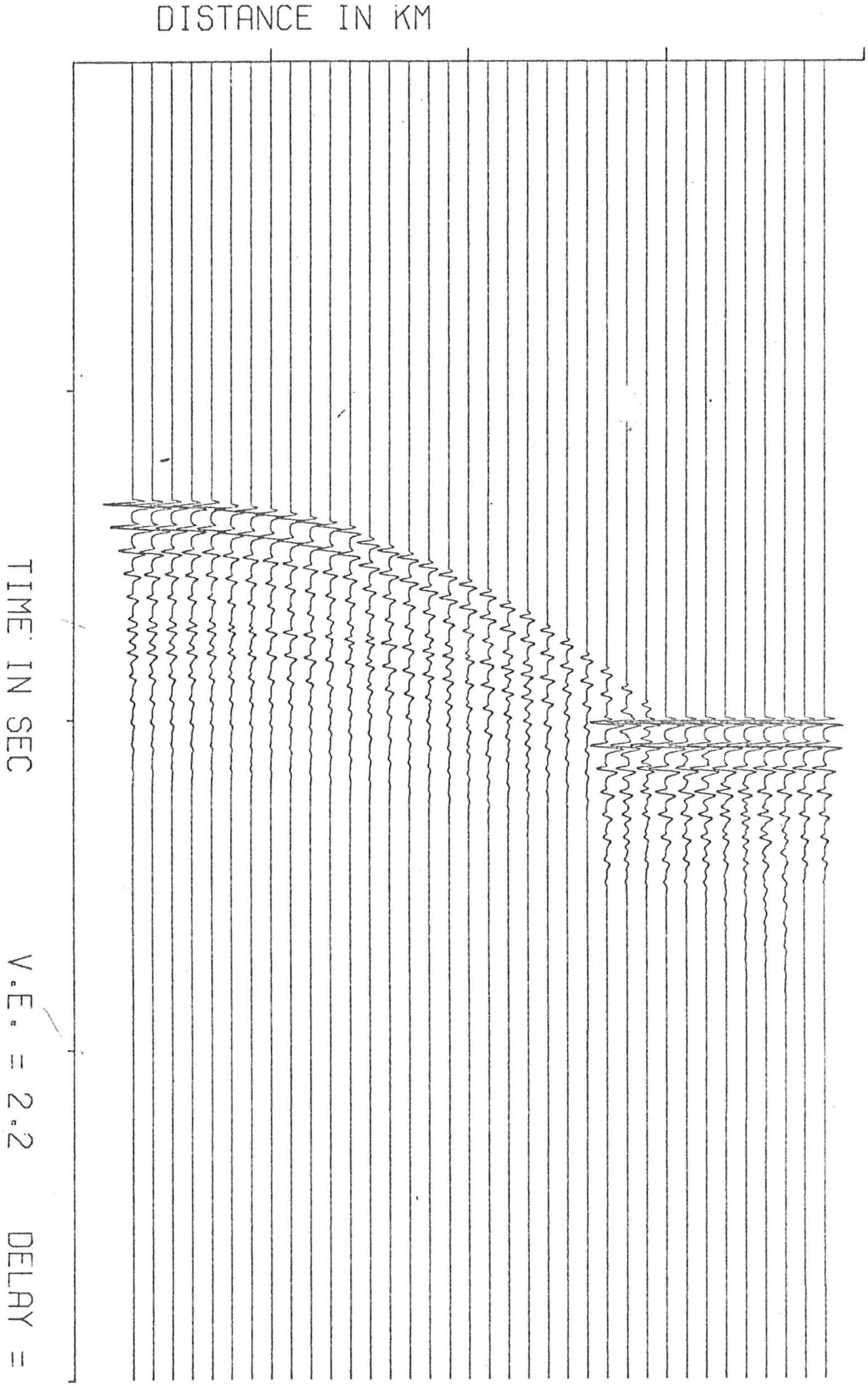

Fig. 5.9b

Synthetic profile for the cliff model

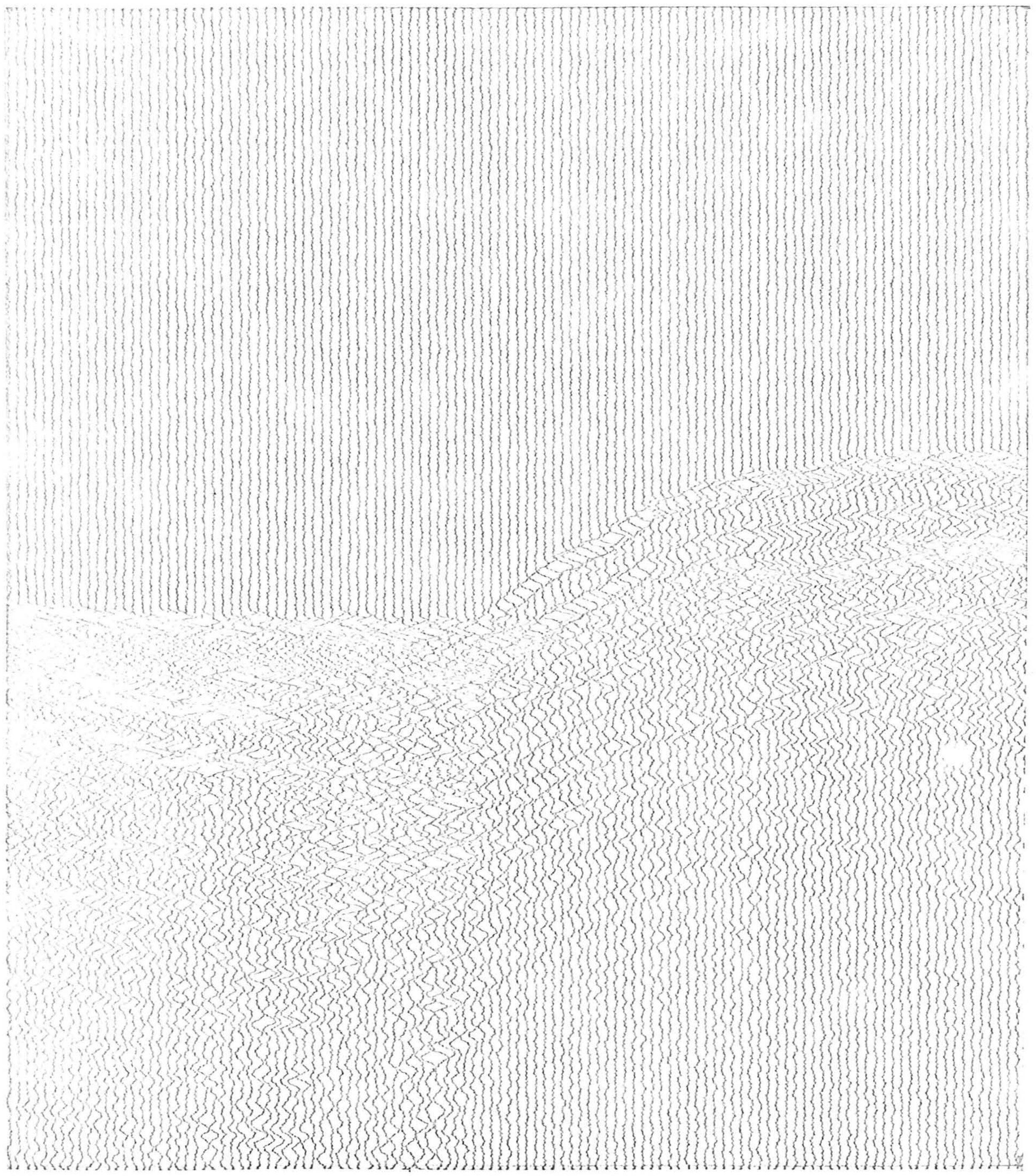

Fig. 5.10a
Observed profile of a cliff

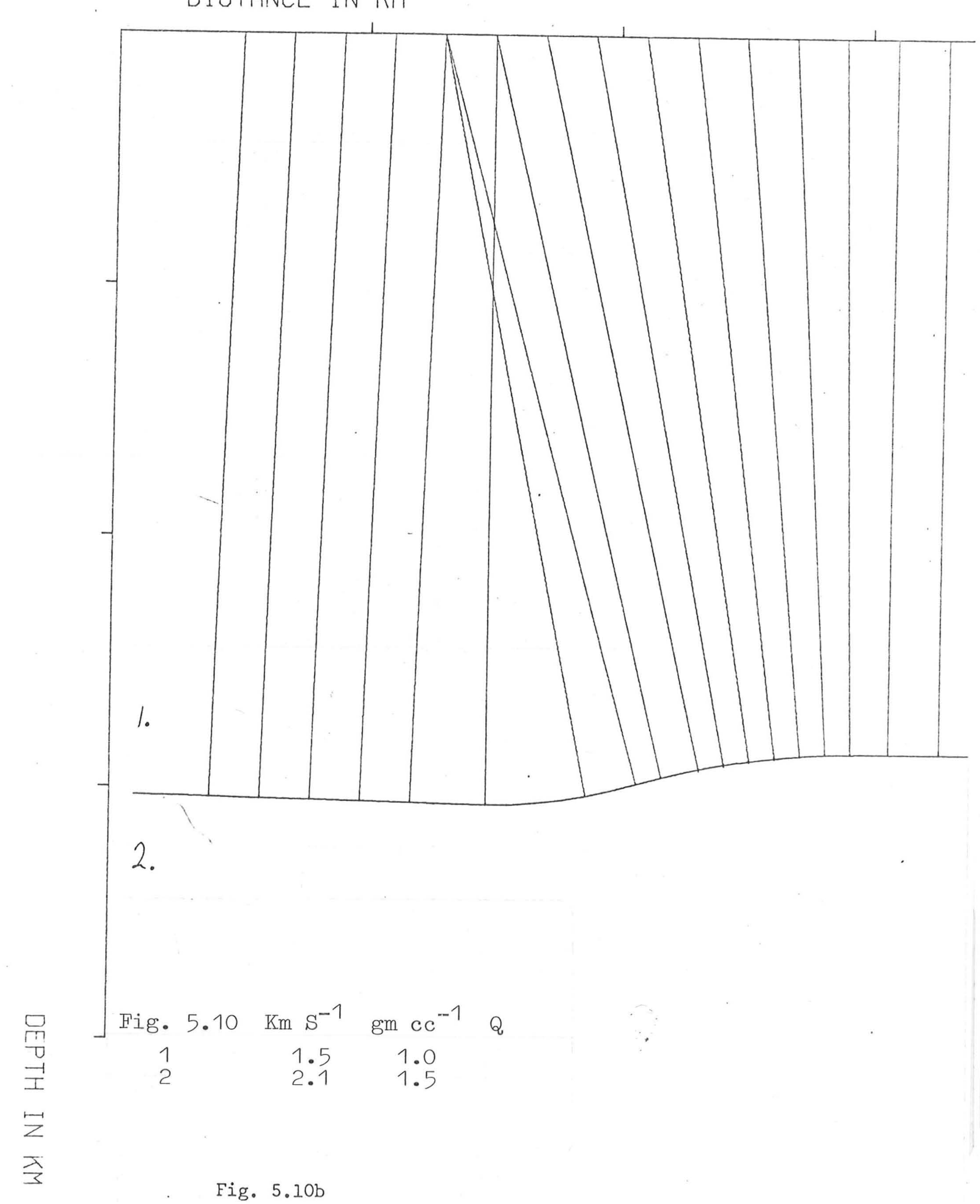

Fig. 5.10	Km S^{-1}	gm cc^{-1}	Q
1	1.5	1.0	
2	2.1	1.5	

Fig. 5.10b
Model and ray tracing for the cliff of Fig. 5.10a

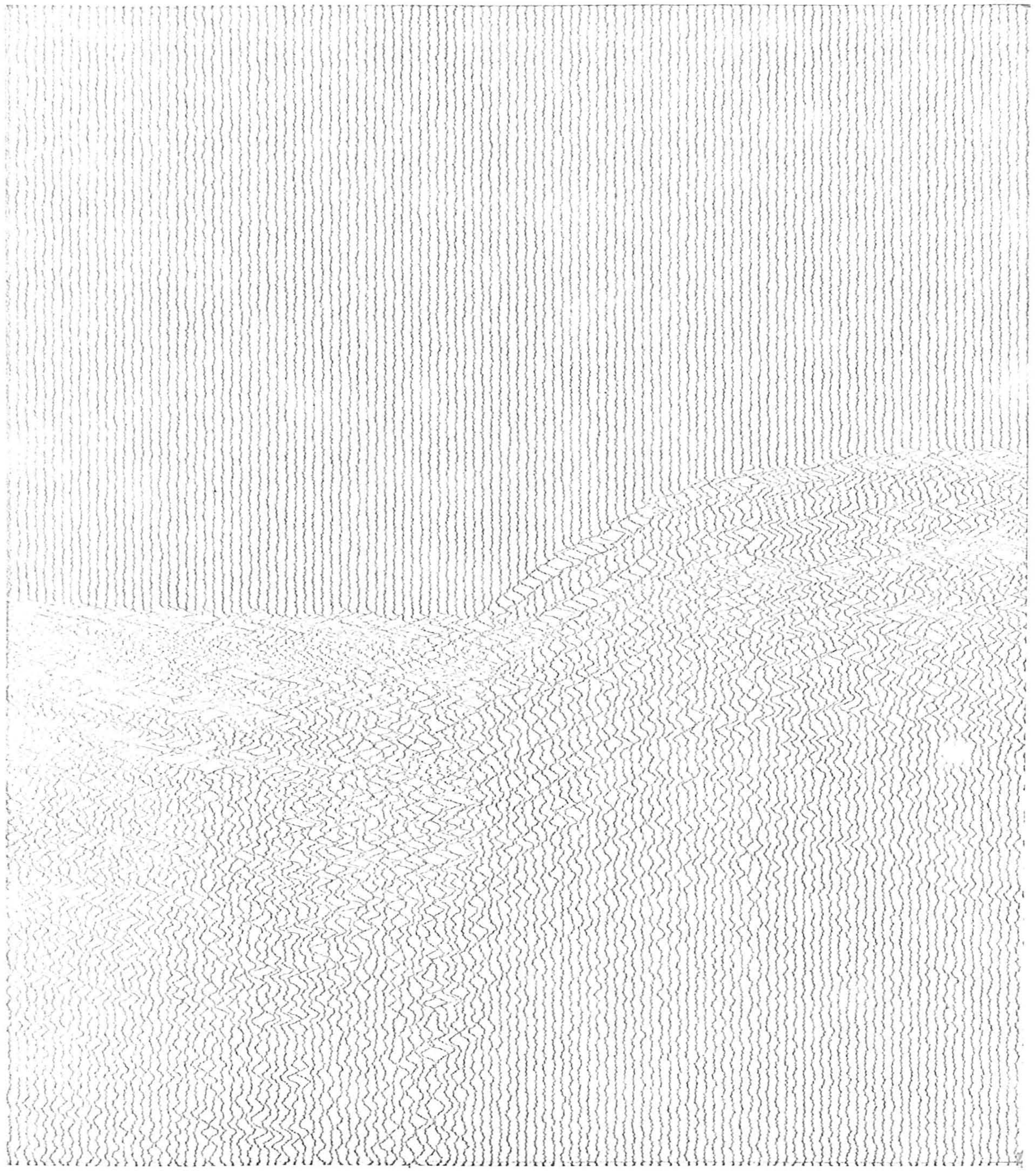

Fig. 5.10a
Observed profile of a cliff

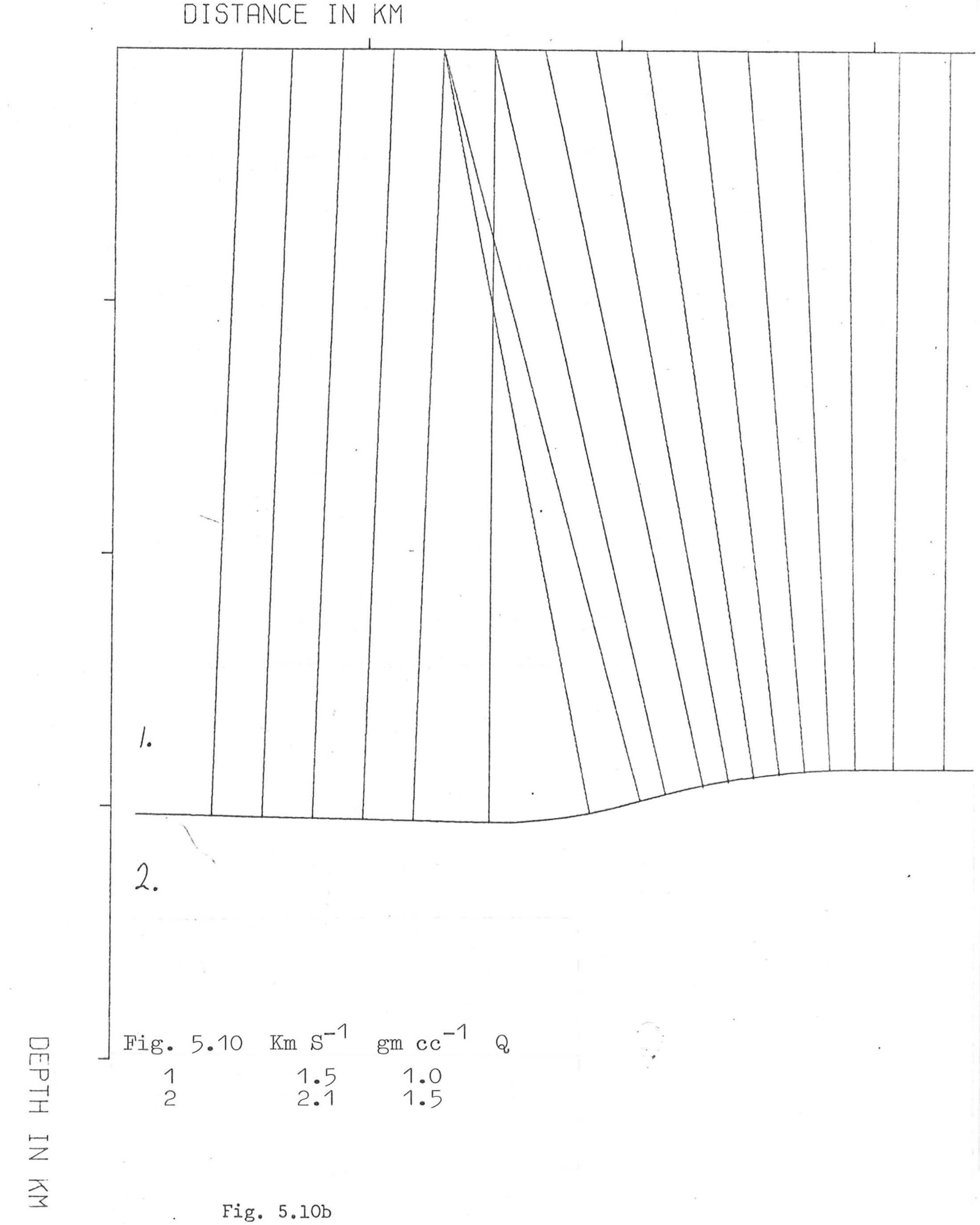

Fig. 5.10	Km S^{-1}	gm cc^{-1}	Q
1	1.5	1.0	
2	2.1	1.5	

Fig. 5.10b
Model and ray tracing for the cliff of Fig. 5.10a

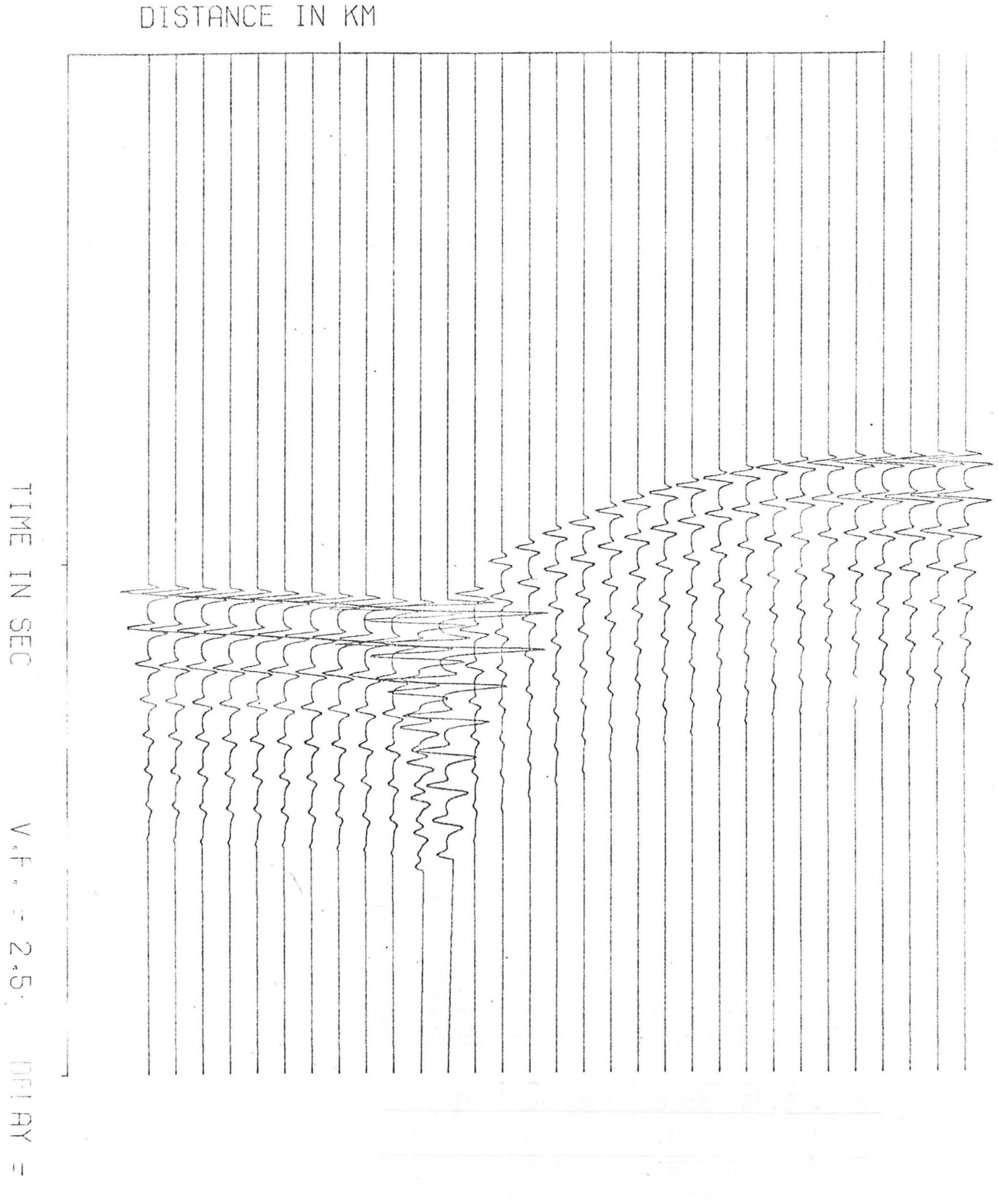

Fig. 5.10c
Synthetic profile for comparison with the observed profile Fig. 5.10a

Cliffs and faults

Cliffs and faults have steep changes in slopes. Figs. 5.9a and b are a model and synthetic profile of a cliff with a gradual change in slope at its upper edge and a sharp change at its lower edge. It is similar to one side of a dome. The model has a flat reflector beneath the cliff, and on the profile this appears curved in a downwards direction towards the cliff edge, due to the two effects of refraction of rays from the sloping cliff edge which increases the ray path, and the greater travel time due to passage through more water and less of the higher velocity sediment. Down sloping layers which end against a cliff edge must therefore be treated with suspicion and checked by modelling as they may be flat.

A real profile would have diffractions from the bottom on the cliff, where there is a rapid change in curvature.

Figs. 5.10a, b and c are an observed profile of a cliff in the Herodotus grid survey (Chapter 6), a model, and the computed synthetic profile. These show low amplitudes over the curve of the cliff edge, and strong amplitudes at the base due to focussing. The cliff slope is relatively low, about 10^{o}, but the amplitude variations are quite large.

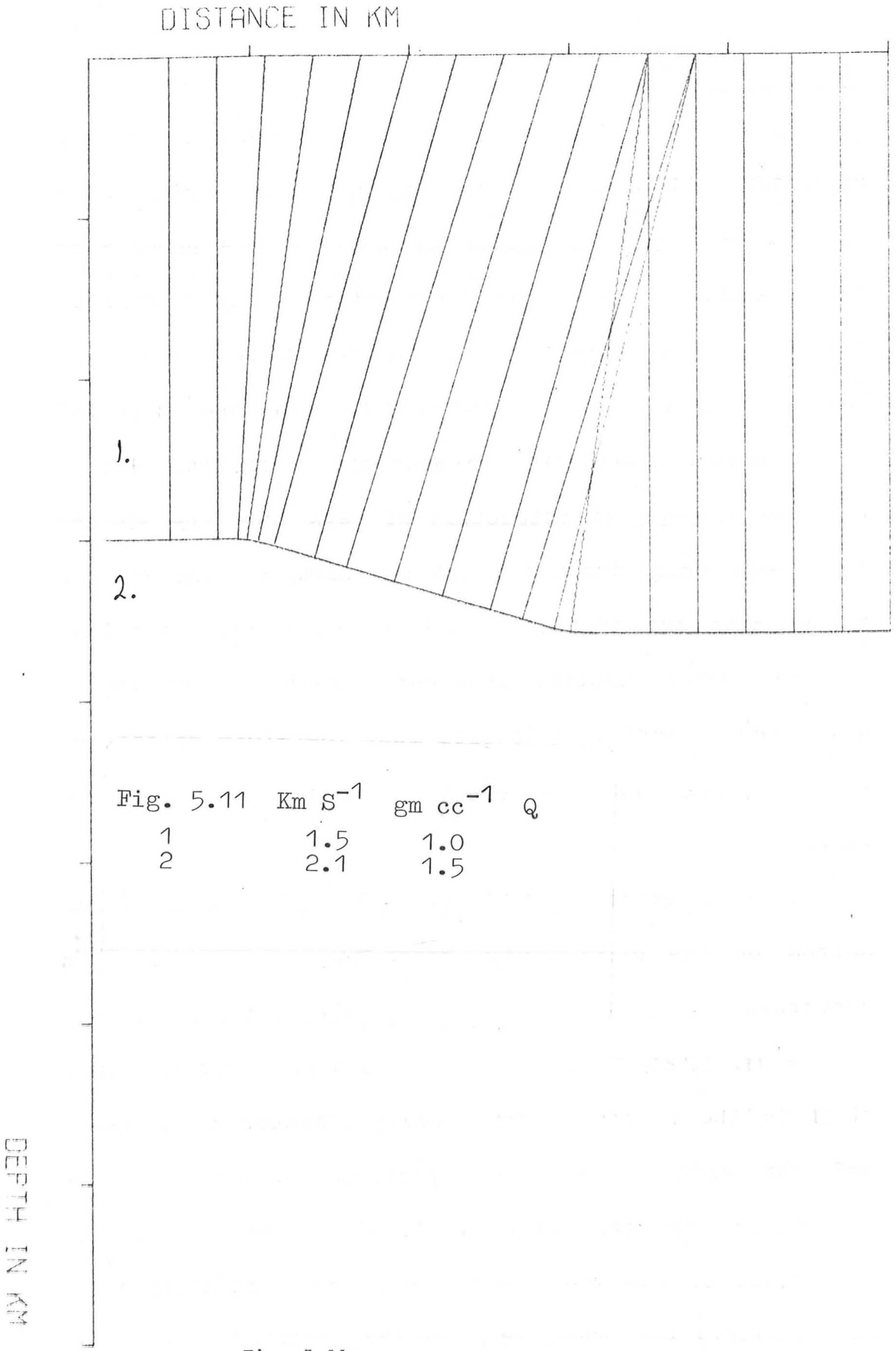

Fig. 5.11a
Ray tracing for a fault model

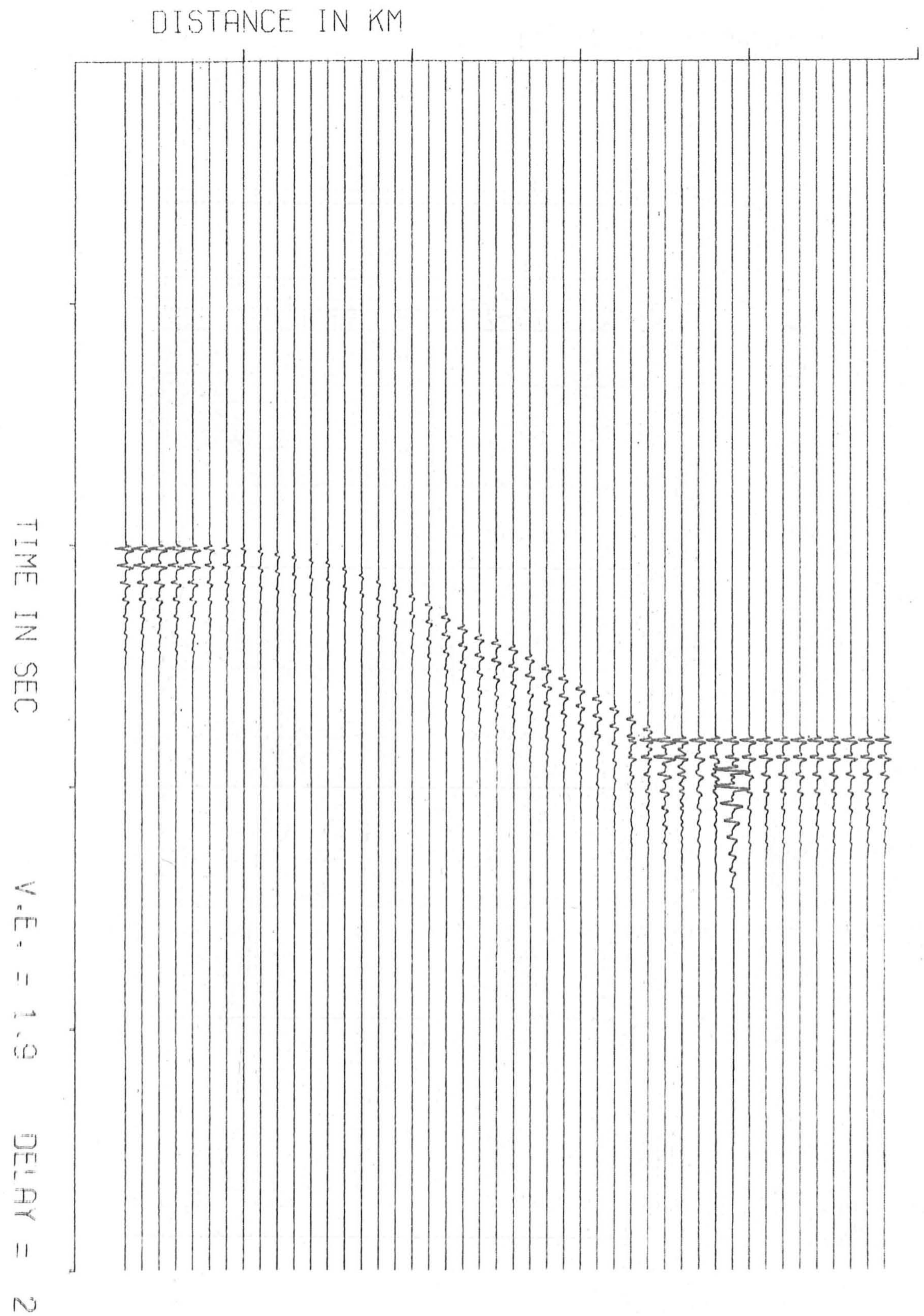

Fig. 5.11b
Synthetic profile for the fault model

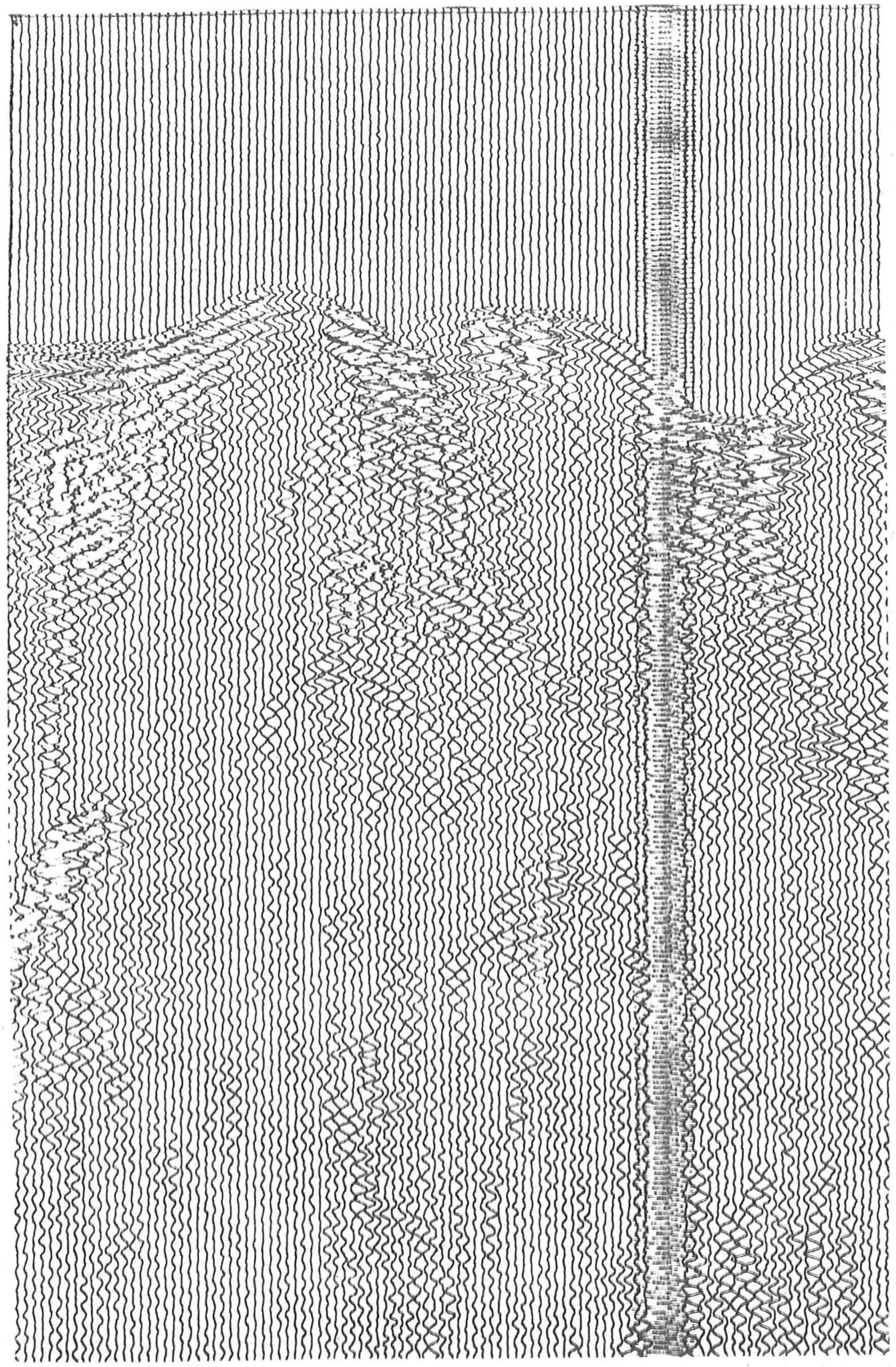

Fig. 5.12a
Obsreved profile of domes and basins.
The vertical line is a time mark.

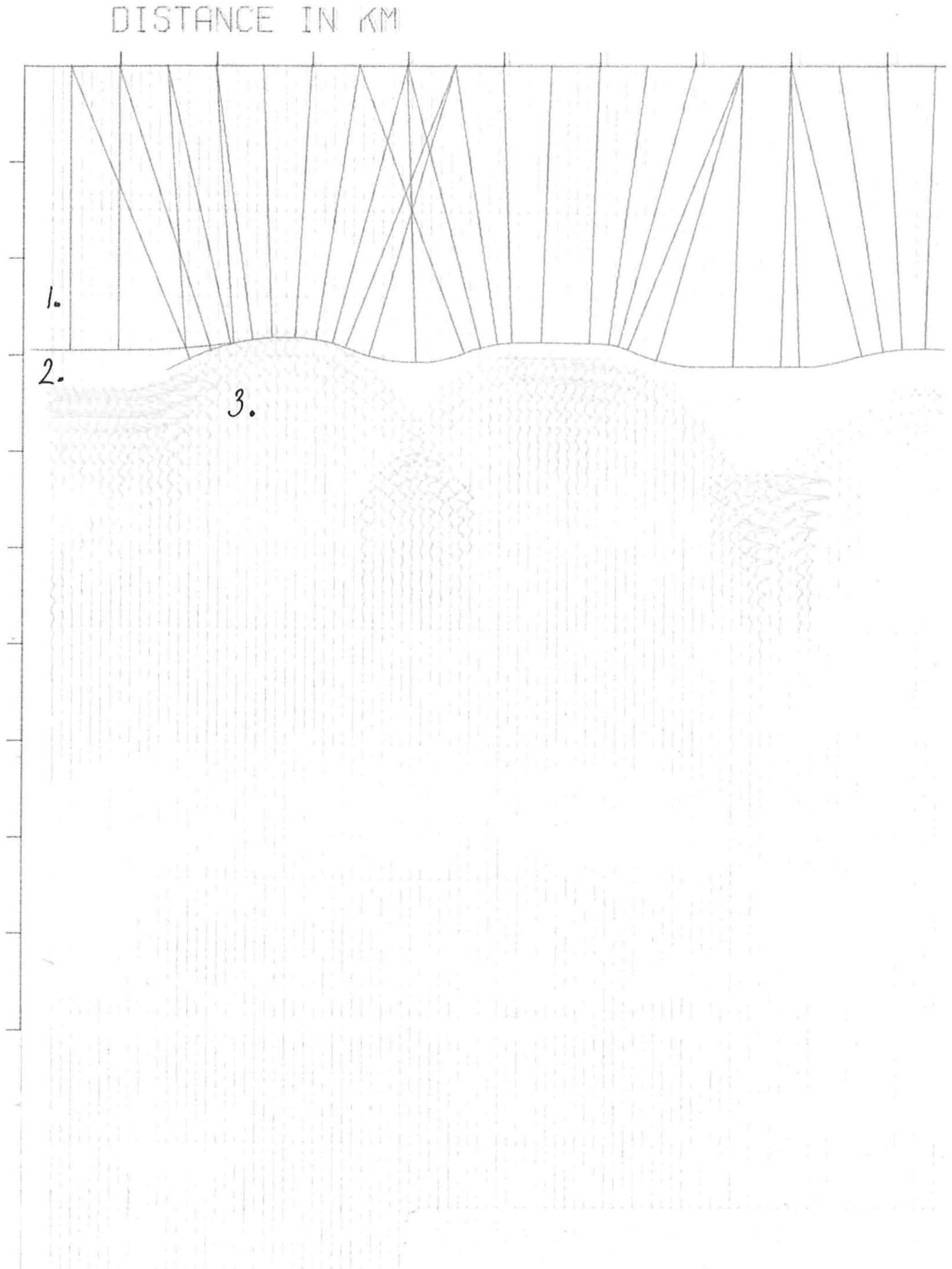

Fig. 5.12	Km S^{-1}	gm cc^{-1}	Q
1	1.5	1.0	
2	1.7	1.5	50
3	2.7	2.0	

Fig. 5.12b
Model and ray tracing for the
dome and basin profile of Fig. 5.12a

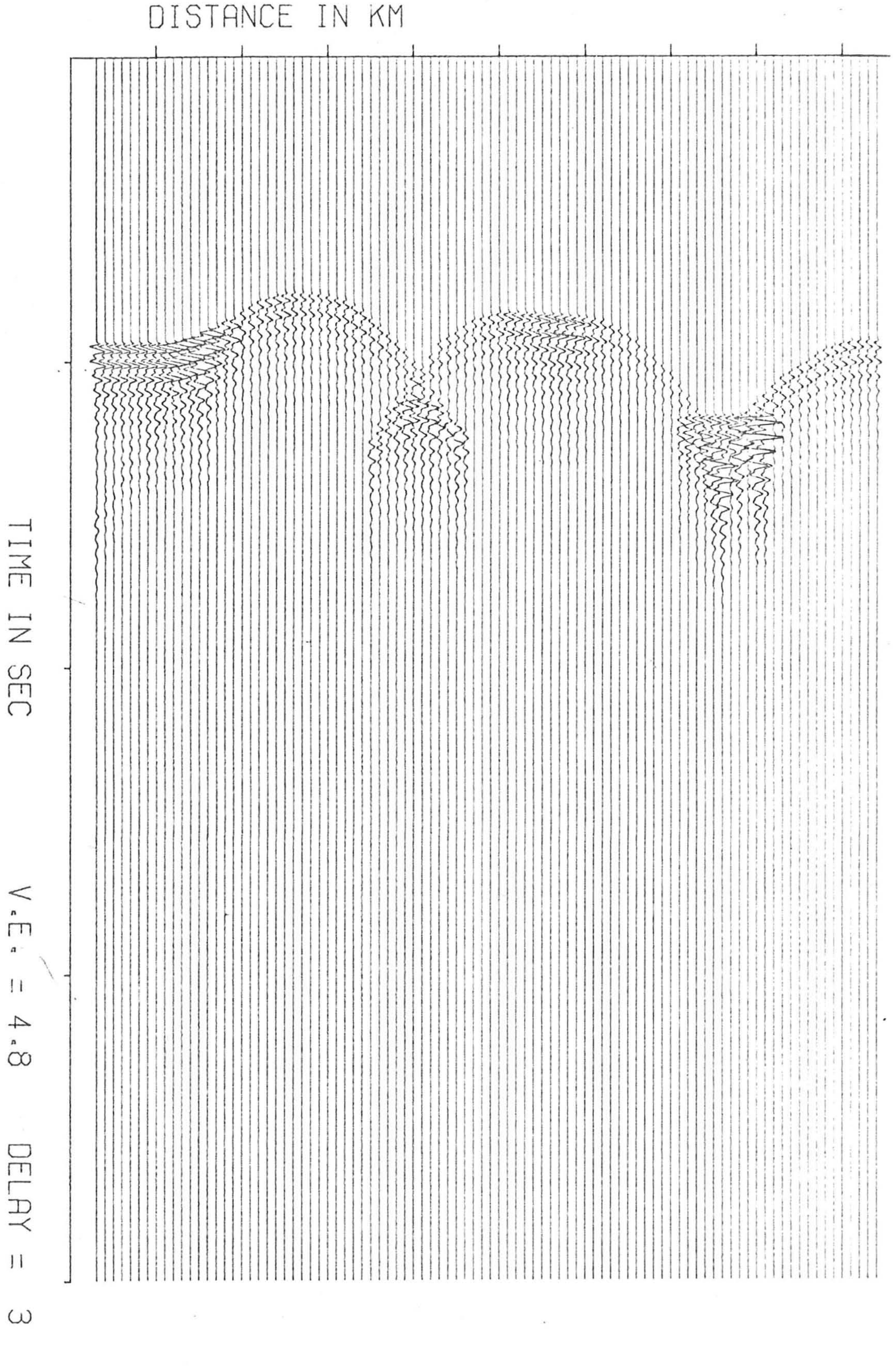

Fig. 5.12c
Synthetic profile for comparison with the observed profile of Fig. 5.12a

A sharp step or fault in a layer produces three areas of strong reflection, (Figs. 5.11a and b) from the flat upper surface, the flat lower surface, and the flat sloping surface, which appears displaced downdip due to non-vertical ray paths. The position of these strong reflections may be used to distinguish the position of the fault plane, although this may be slightly difficult as the reflection from the sloping surface may interfere with the reflection from the lower surface (Fig. 5.11b). A fault has very sharp changes in curvature and should produce many associated diffractions (Chapter 3.4).

5.3 Models of more complicated profiles

Domes and basins

Fig. 5.12a is part of an observed profile in a complicated area with domes, valleys and basins. It has very large variations in amplitude, low over domes, higher from flat parts and very high in valleys and basins. The effects of buried centres of curvature show in the triplication of travel times between the two main domes and associated with the narrow valley or basin to the right. Fig. 5.12b and c are the model and synthetic profile for the sea bed reflector only, as although there are deeper reflections on the profile no continuous reflector can be identified. The hollow to the left of the domes has been modelled as a basin, as an upper and a lower surface can be seen, but the hollow to the right has been modelled as a valley; this is very narrow and reflections from it are confused, and it could also be interpreted as a basin.

The synthetic profile models the amplitude variations quite well, although there are some differences in structural detail. The valley or basin has about the same width as each dome on the model, which is not apparent from the observed profile.

Some of the shot points are near the centres of curvature of parts of the surface, and there is a problem of how to estimate amplitudes at these points, as ray theory breaks down in this case and predicts infinite amplitudes, due to zero area ray tubes and reflections from many points. I have limited the maximum amplitude possible, chosen by examination of the largest amplitude variations seen on records. This is eight times the amplitude that would be obtained by reflection from a flat surface.

Undulating structure

Figs. 5.13a, b and c show an observed profile, a model, and a synthetic profile for a gently undulating three-layer structure. The dips are quite low, especially the sea bed, but they cause quite large variations in

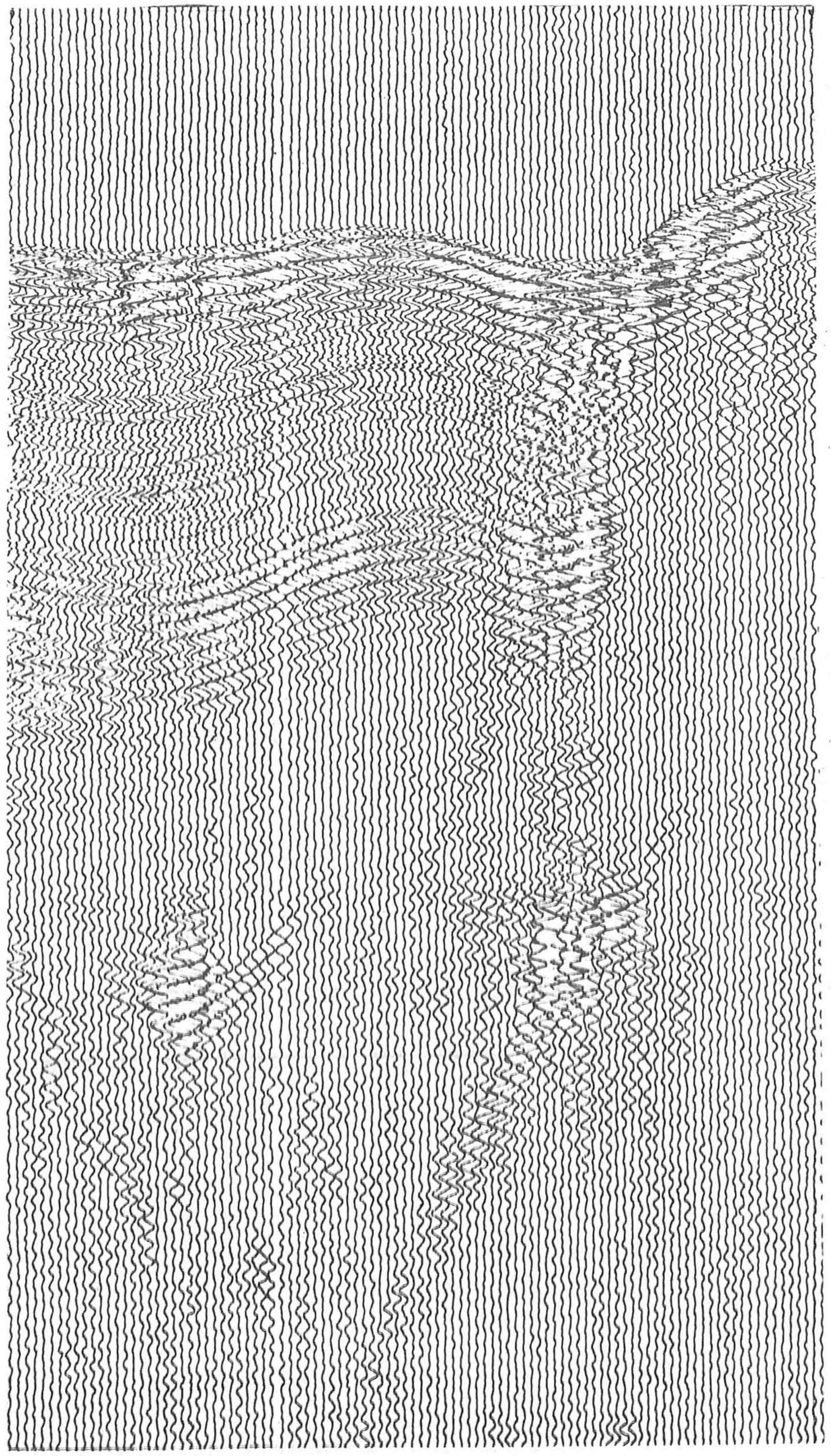

Fig. 5.13a
Observed profile of an undulating structure

FORTRAN UNIT NUMBER 8
WCAV J038SGS1 CSP PLOT TEST
START JOB 38 6.04.54 PM 2 JUL 75 * * *

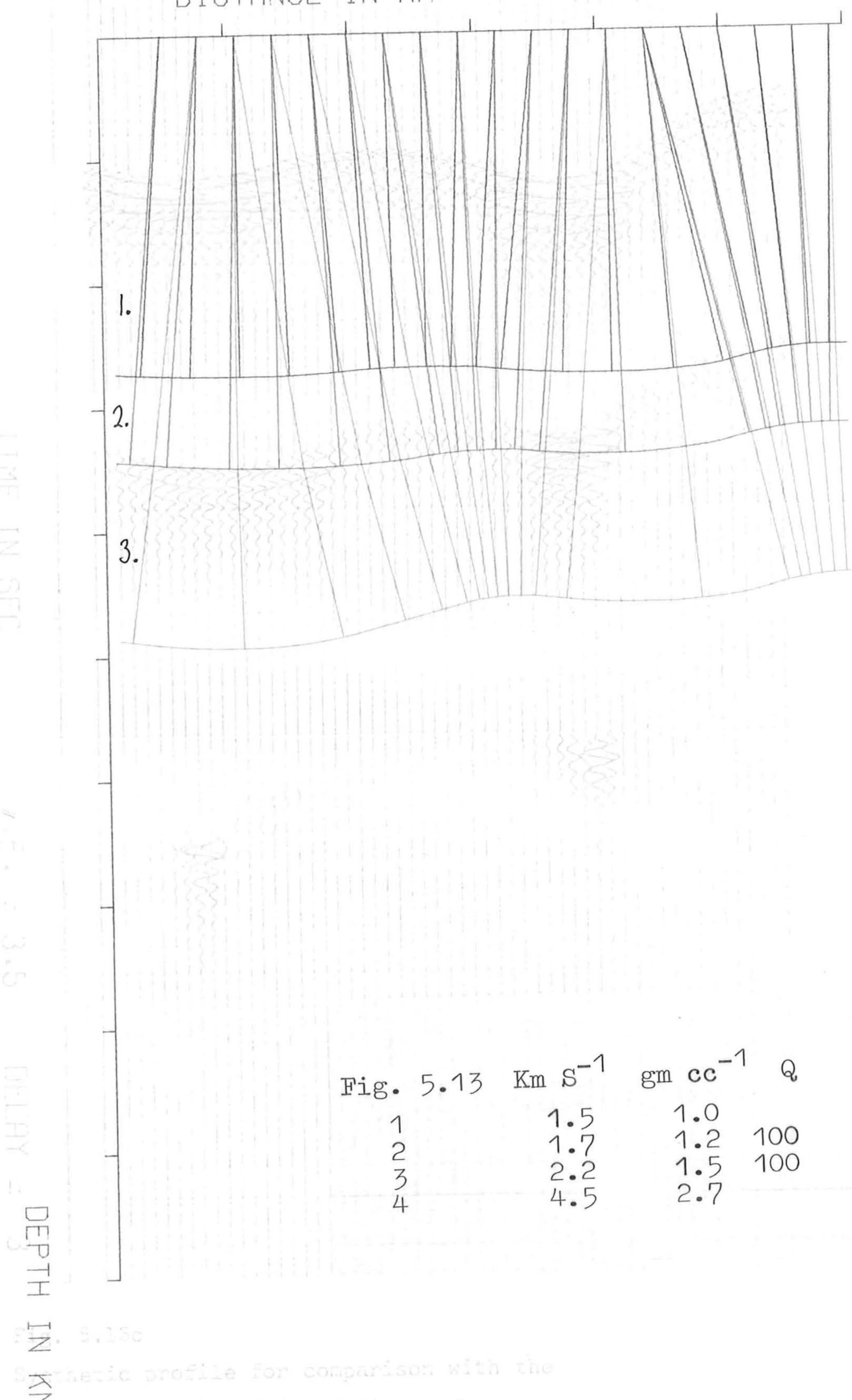

Fig. 5.13	$Km\ s^{-1}$	$gm\ cc^{-1}$	Q
	1.5	1.0	
1	1.7	1.2	100
2	2.2	1.5	100
3	4.5	2.7	
4			

Fig. 5.13b
Model and ray tracing for the
undulating structure of Fig. 5.13a

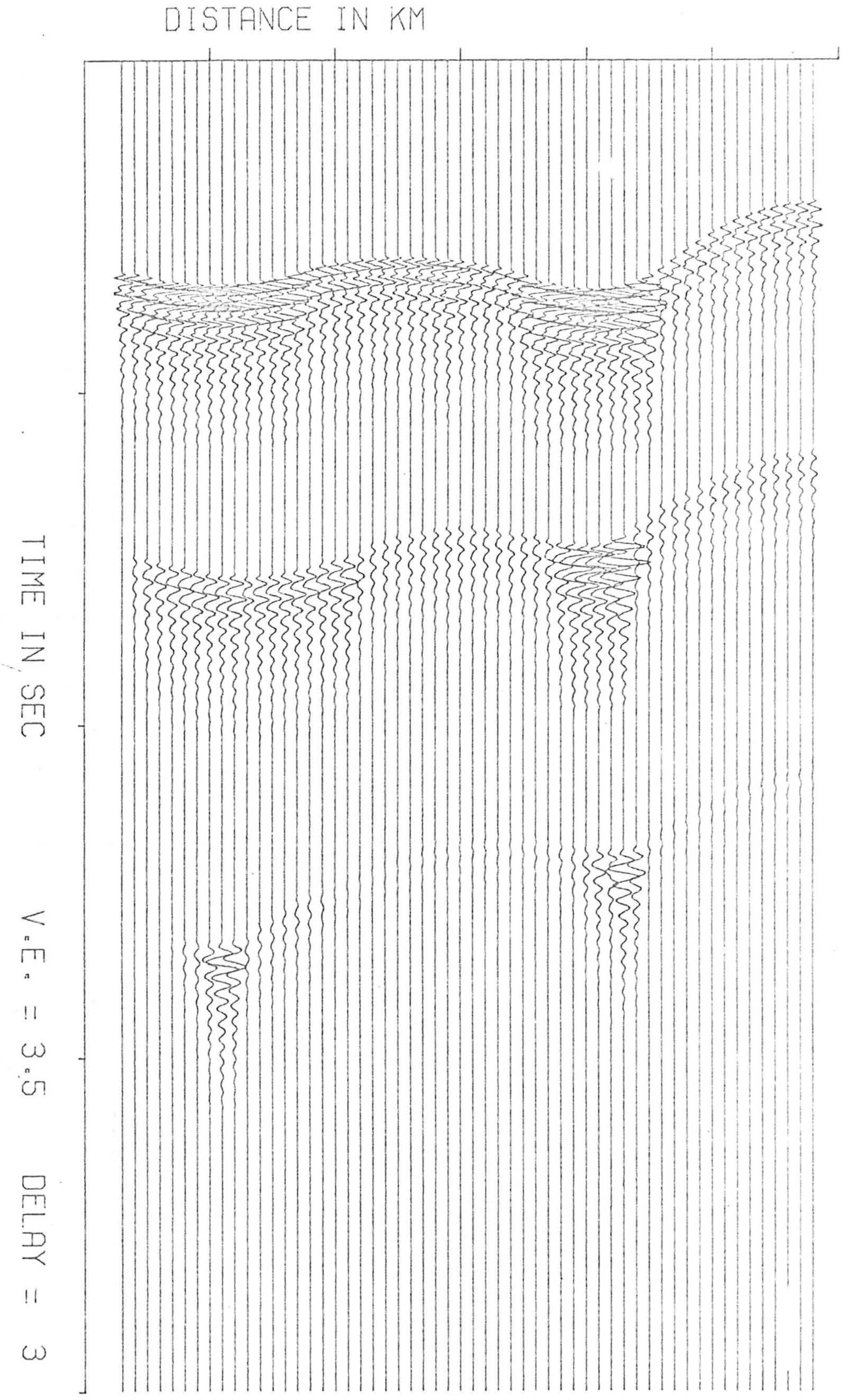

Fig. 5.13c

Synthetic profile for comparison with the observed profile of Fig.5.13a amplitude. The synthetic profile matches the observed profile very well, although the model needed many successive adjustments to get this match. The model had to be adjusted to give a match in both structure and amplitude, which provided quite a tight control on the model, and slight alterations have quite drastic effects on the synthetic. The amplitude is very low over the anticline parts, and can be very high in the syncline parts, as the rays are focussed, and produce warnings from the program that some amplitudes are constrained to the maximum, as the shot point is too near a centre of curvature, as is the reflection from the third interface for the shot point at 4.1 km. The anticline parts of the third interface are hardly visible on the observed profile, and the synthetic shows this also.

The reflection coefficient of the third interface needed to be very high for the reflection to be visible from this depth below the sea bed. The change in waveform with depth of the reflection below the sea bed is also apparent on the observed profile; the sea bed reflection has a spiky waveform, whereas refections from the third interface have lost all their spiky character and approximate to a damped sinusoid of the bubble oscillation frequency. It is this change in waveform shape which determines the value of Q to use in the

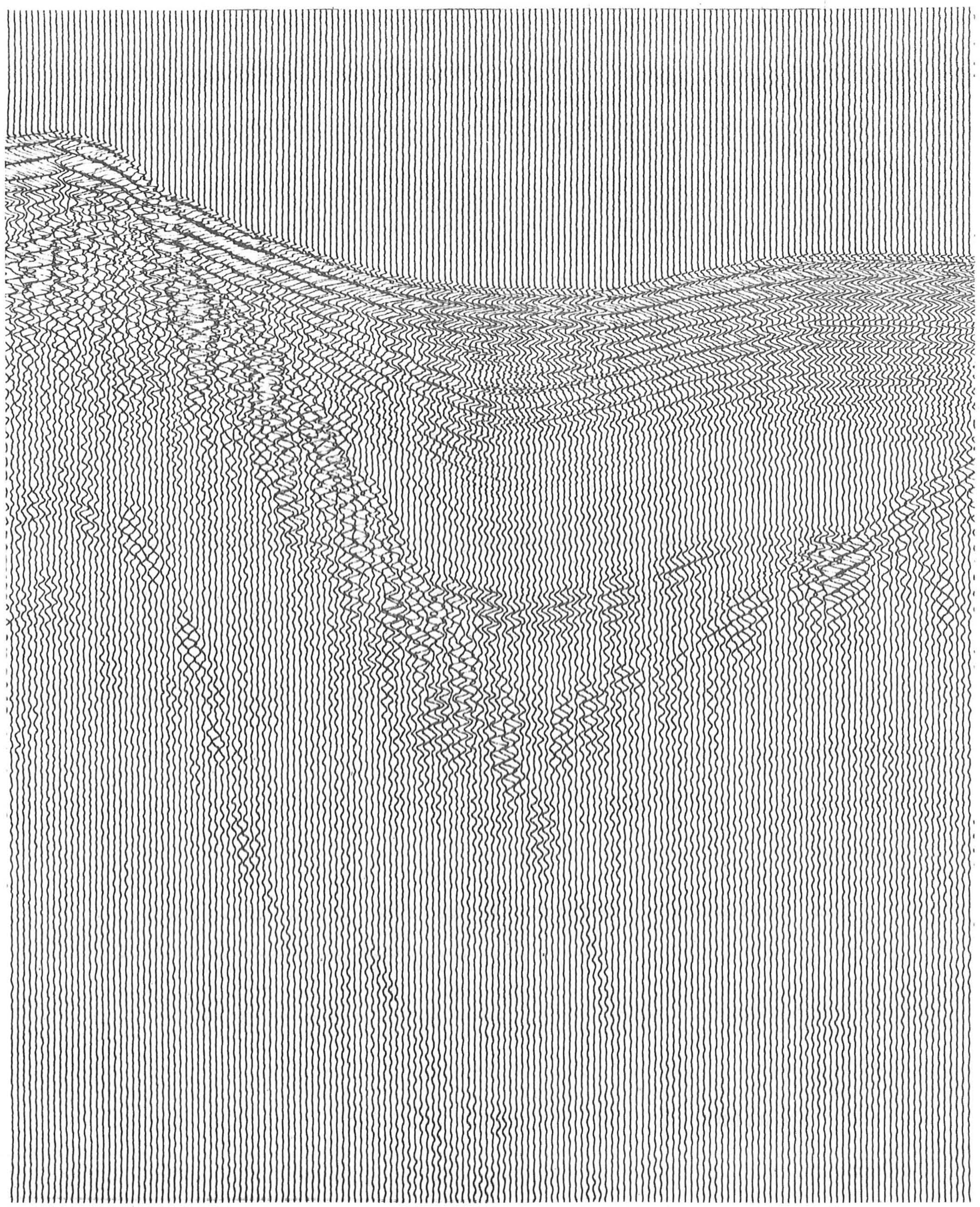

Fig. 5.14a

Observed profile of a basin.

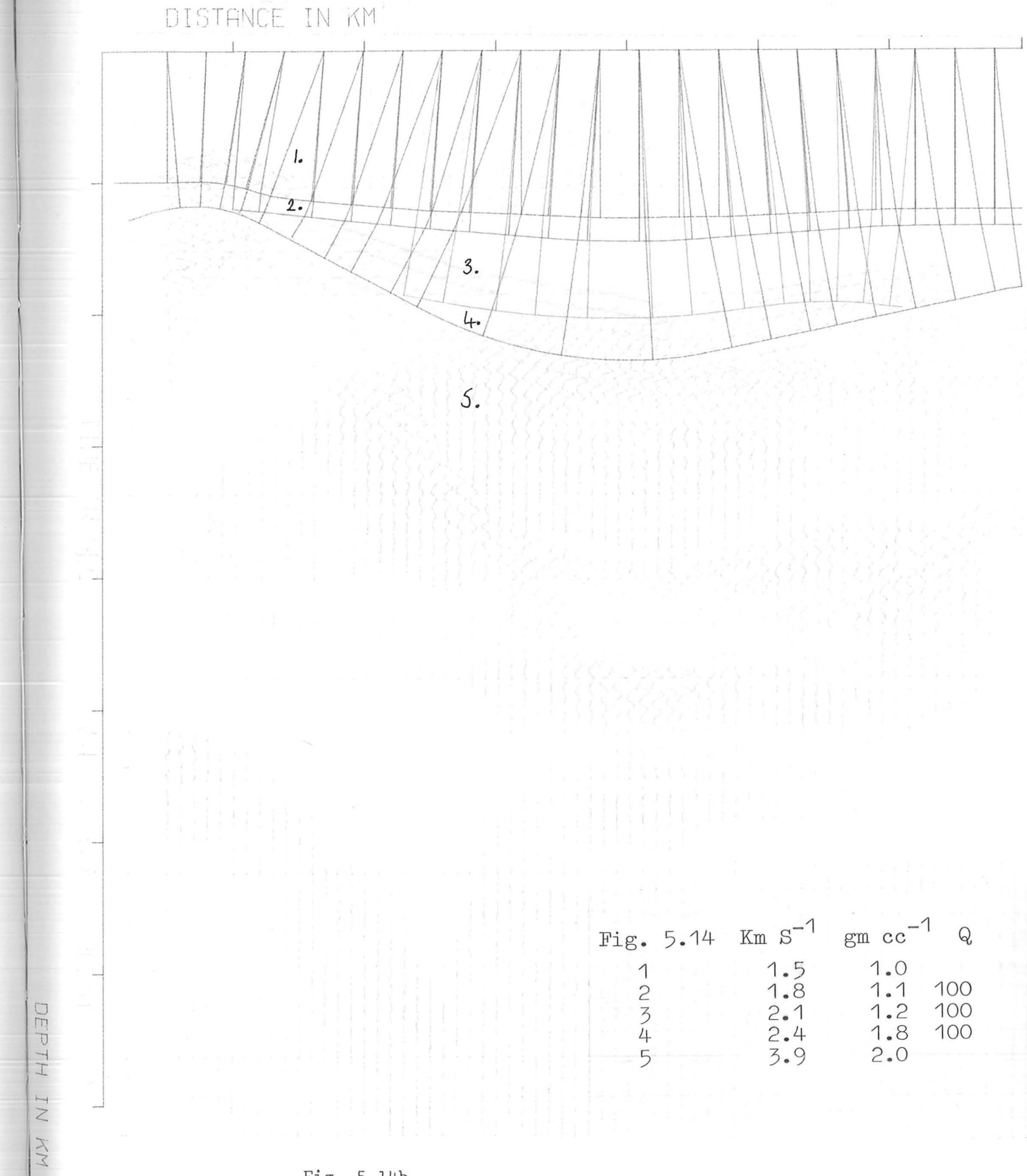

Fig. 5.14	Km S^{-1}	gm cc^{-1}	Q
1	1.5	1.0	
2	1.8	1.1	100
3	2.1	1.2	100
4	2.4	1.8	100
5	3.9	2.0	

Fig. 5.14b

Model and ray tracing for the basin of Fig. 5.14a

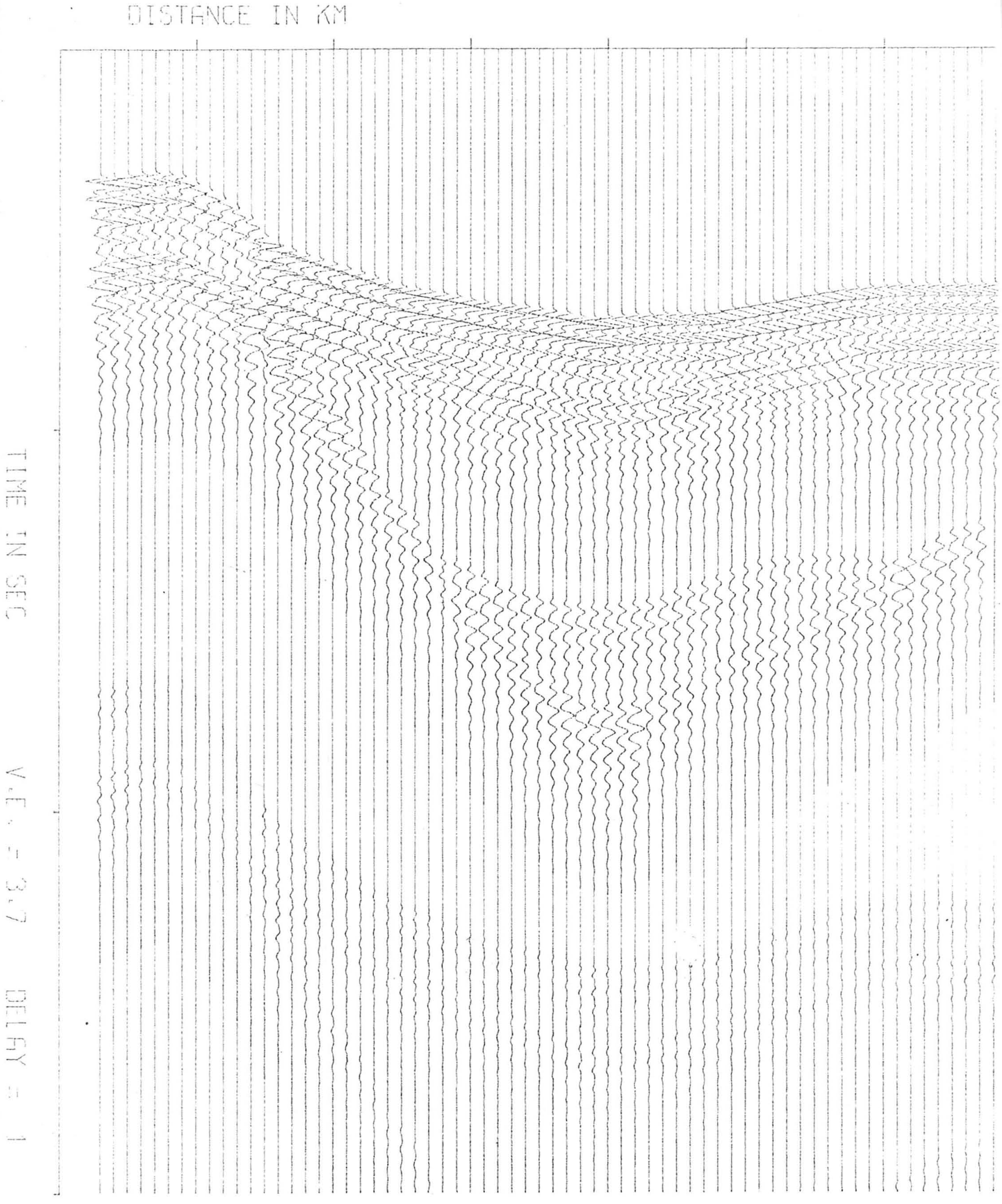

Fig. 5.14c

Synthetic profile for comparison with the observed profile of Fig. 5.14a model; a Q of 50 for both sediment layers is used in this case.

Basin

Fig. 5.14a is an observed profile of part of a basin, with a sequence of curved interfaces, whose curvature increases with depth suggesting that the basin was sinking during deposition of sediment in the basin. The sea bed reflection continues over the edges of the basin, but the two lower reflections end against the sides of the basin. The basin bottom has a relatively strong reflection, even through the upper layers of sediment, so it must have a relatively high reflection coefficient.

Figs. 5.14b and c are a model and synthetic profile of the basin, and as for the previous model it had to be adjusted many times to produce a well fitting model. Some of the reflectors are relatively closely spaced; the distance between reflectors 1 and 2 is about 200 m, but they can be distinguished reasonably easily on the observed profile as they are not exactly parallel, and the interference effects between the two vary with their separation. The correct position of reflector 2 was determined by modelling, and then adjusting the model until the synthetic profile matched the observed profile.

The general match between the observed and synthetic profile is quite good, amplitudes matching quite well, with the main differences being due to slight variations in structure.

5.4 Limitations and further development of the modelling system

The modelling system produces synthetic profiles which are a surprisingly good match with observed profiles, considering its crude basis of geometrical optics ray tracing. It provides a very rapid check for interpreted structure using the spike synthetic profiles, and provides a reasonably fast method for synthesis of complete profiles.

The reason that the system provides such a good match with observed profiles is probably the accurate inclusion of all the source and receiver effects into the system. Using a more accurate ray or wave theory basis would cause little change in the synthetic profile obtained in general, whereas leaving out any of the effects of source and receiver would have a drastic effect on the synthetic profile (see for example the effect of the receiver on waveforms, Fig. 2.12). Many of the synthetic seismogram methods that have been developed for earthquakes and refraction or variable angle reflections use only a very simple source function and completely ignore the impulse response of the receiver, whilst producing very accurate and time consuming ray or wave theory models. The inclusion of source and receiver effects into the system increases the computation time much less than using more sophisticated ray and wave theory propagation models. It is difficult to calculate or measure source functions and instrumental responses, but very necessary (Smith 1975).

The modelling system, although useful, has limitations, some of which could be removed by further development, and some of which cannot be removed or are not worth the extra computing time needed to remove them. The limitations are of three main types:

1. <u>Insufficient knowledge of input parameters</u>

It is impossible to measure the correct source function during profiling but possible to do so in carefully controlled experiments (Smith 1975 and Chapter 2.3). The source function also varies with change in parameters, so many measured source functions would be needed for different conditions. If the source function can be predicted accurately for any conditions this is much simpler, but it is only possible at the moment for chemical explosives or airguns (Chapter 2.2). Other sources, such as sparkers or airguns with wave shapers must use a measured source function. The impulse response of the receiver can generally be calculated if the system is not too complicated, or measured reasonably accurately. Continuous measurement during profiling of the parameters which affect the source and receiver response, such as depth, is usually straightforward.

Seismic velocity can be estimated from variable-angle data, but there is no general indpendent method of measuring density and attenuation (Chapter 4.4), and estimates have to be made from velocity-density curves and the observed profiles. This produces very crude estimates, and any subtleties in the profile due to variation of these parameters are not synthesized.

2. Programming limitations

The program assumes constant properties within layers at the moment. It could be extended to include continuously varying properties both laterally and vertically, but this has not been done so far as the method of measurement of the properties calculates an average for a layer (velocities from variable-angle reflection), or the properties are known too inaccurately (density and attenuation). If accurate data on variation of these properties within a layer were available, such as from bore holes, it would be useful to extend the system for continuously varying properties.

The calculation of multiples includes only water layer multiples, and assumes that the multiple reflection path is a combination of the primary reflection path and one or more primary water layer paths. The first assumption is reasonably good, as even in areas of strong sub-bottom reflectors the error involved in ignoring intersedimentary multiples is small (section 5.2), but the second assumption is only strictly valid for flat reflectors and the error increases with angle of dip (Chapter 3.5). A dip of 10^{o}, for example, would give an error of 1.5% in the calculated multiple time, which for a 3 s travel time is 45 ms, and is of the order of a bubble oscillation period so can cause inaccuracies in the interference relationships between multiples and primary reflections. The multiples could be calculated exactly if necessary by developing a multiple generation system which traces rays to get multiple paths, but this would involve tracing many rays and use more computing time than the primary ray tracing so has not been included in the system so far.

The modelling system will not model profiles that have been processed. A processed record has the appearance of a normal incidence profile, but is compiled from traces with varying source and receiver offsets, which travel along different ray paths from the normal incidence path, and so are subjected to different effects. The offset traces are corrected for moveout and stacked to produce a pseudo-normal incidence profile, and then further processed to reduce bubble oscillations and multiples and are subjected to amplitude controls. The moveout correction reduces travel times to those of normal incidence ray paths, but the amplitude and shape of arrivals cannot be accurately reduced to a normal incidence travel path, because the offset ray path arrivals have different characteristics, such as the change in reflection coefficient with angle of incidence and change in frequency response of an array with angle to the vertical.

A ray-tracing and modelling system which traces rays for variable offsets of source and receiver would be needed to model processed profiles, and the offset models then processed by the same techniques applied to the processed profiles. The theory of this is simple, but it involves programming a completely new ray tracing system as some of the techniques for normally incident reflections are not applicable, such as tracing rays initially normal to a reflector through upper layers to the surface. This has not been developed as the observed profiles I have used have not been processed, but could be done.

Perhaps the greatest difference between the synthetic and observed profiles is the absence of noise on the synthetic profiles. Noise is the unwanted parts of the signal, and is of two types, background noise, which is always present, and source generated noise which is only noise in the sense that it cannot be interpreted. It is difficult to include noise on a synthetic profile as it varies with time and area, and source generated noise varies in additiion with the amount of energy present — time after the shot. If noise is to be included measurement of its average amplitude and frequency spectrum must be made on the observed profile, and used as controls for a random number generating process. The inclusion of noise would make a synthetic profile look more realistic, but it is not very useful, and could be misleading due to its random nature. It would be some use in determining which reflections would be lost in noise, but this can usually be estimated quite simply and accurately by comparison with the observed profile.

3. Theoretical limitations

The modelling system is limited by the validity of geometrical optics ray theory, which was discussed in Chapter 3.1. It is most inaccurate where amplitude varies rapidly, at foci, caustics and critical points, or where the radius of curvature of an interface is less than the wavelength. Focussing of rays occurs at the centre of curvature of structures for normally incident reflections, and when this coincides with a shot point ray theory would predict infinite amplitude, which necessitates the use of a relatively arbitrary maximum amplitude possible in the system. A more valid method of computing amplitudes at foci would be useful. Critical points occur very rarely in a profiling system as rays are usually near vertical and dips of interfaces are low.

Diffractions should be produced when the radius of curvature of an interface is less then the wavelength, but these are not predicted by ray theory, and this is one of the most severe limitations of the system, as diffractions can be very common on profiles. Diffractions can only be generated by wave theoretical methods, as has been done for single interfaces and a constant velocity layer by Hilterman (1970) and Trorey (1970), but it is difficult to see how these methods could be applied generally to synthesize profiles, and the computing time needed would be enormously longer.

varies rapidly, at foci, caustics and critical points, or where the radius of curvature of an interface is less than the wavelength. Focussing of rays occurs at the centre of curvature of structures for normally incident reflections, and when this coincides with a shot point ray theory would predict infinite amplitude, which necessitates the use of a relatively arbitrary maximum amplitude possible in the system. A more valid method of computing amplitudes at foci would be useful. Critical points occur very rarely in a profiling system as rays are usually near vertical and dips of interfaces are low.

Diffractions should be produced when the radius of curvature of an interface is less then the wavelength, but these are not predicted by ray theory, and this is one of the most severe limitations of the system, as diffractions can be very common on profiles. Diffractions can only be generated by wave theoretical methods, as has been done for single interfaces and a constant velocity layer by Hilterman (1970) and Trorey (1970), but it is difficult to see how these methods could be applied generally to synthesize profiles, and the computing time needed would be enormously longer.

CHAPTER 6

REFLECTION PROFILING GRID SURVEYS IN THE EASTERN MEDITERRANEAN

6.1 Side reflections

The problem

Normal reflection interpretation and modelling of necessity makes the assumption that all reflections originate in the vertical plane of the profile because insufficient information exists to justify any other assumption. This chapter examines the geometries which give rise to reflections outside this plane (side reflections) and the conditions under which their origin can be deduced from the profile.

Because the incident and reflected ray must be normal to an interface in reflection profiling, a reflector that is dipping gives a reflection from a point which is not vertically below the shot point. Reflections from points which lie in the plane of the profile can be dealt with by normal two-dimensional migration techniques, whereas those interfaces that have a component of dip perdendicular to the plane of the profile will give rise to side reflections which give an erroneous impression of the interface.

Side reflections may be strong as there is little

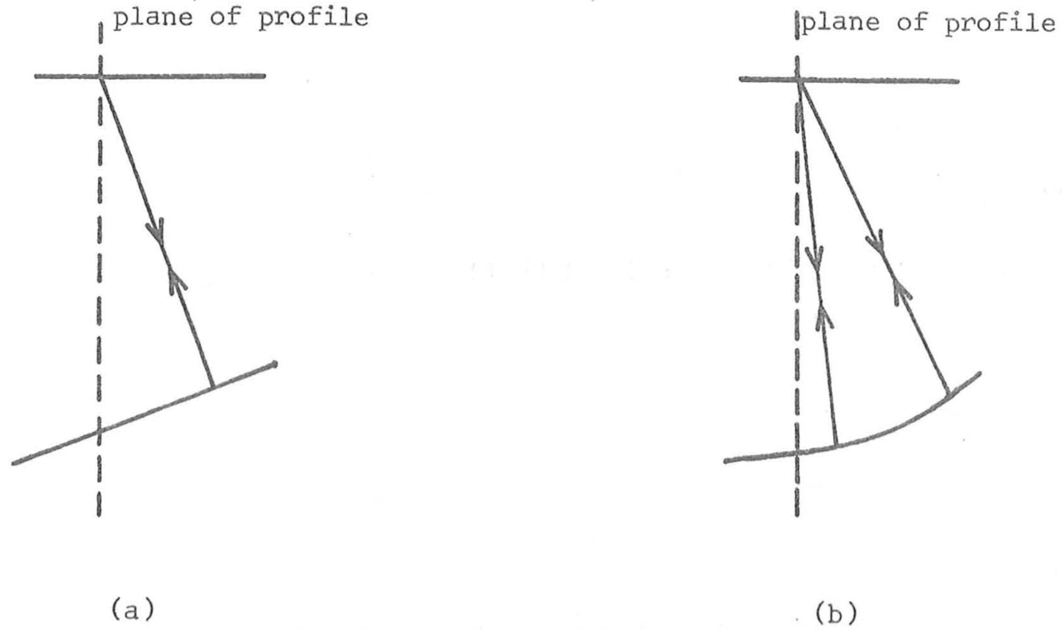

Fig. 6.1
The generation of side reflections from dipping interfaces.
The line of the profile is perpendicular to the page.
(a) single side reflections
(b) compound side reflections

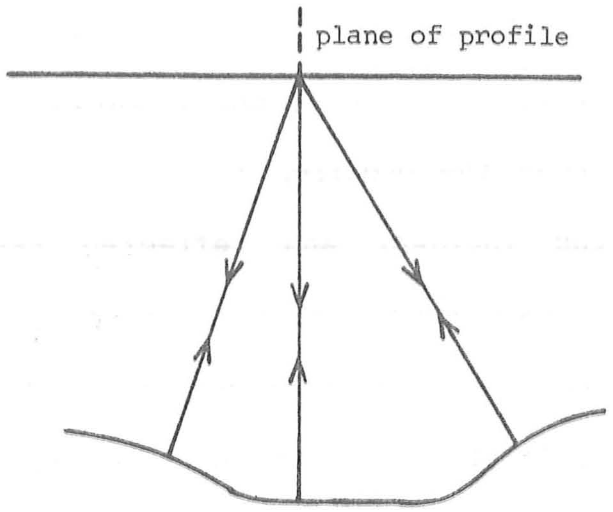

Fig. 6.3
Side reflections generated by a profile along a valley

angular discrimination in the plane perpendicular to the profile plane, the only discrimination being due to the effect of the sea surface reflection, whereas angular discrimination within the profile plane is high due to the linear nature of the receiver array.

Recognition

Where an interface gives rise to a single reflection (Fig. 6.1a) it is not possible to distinguish the plane in which that reflection occurs, and a three-dimensional survey is necessary to determine the dip perpendicular to the profile plane, and this three-dimensional information could then be used as a basis for migration of reflections for three-dimensional dip. Reflectors have not been migrated for the surveys in this chapter except for specific cases where true dips and positions were needed in looking for possible side reflections. An automatic three-dimensional migration system would be very complicated, and use a vast amount of computer time, and as far as I know, has not been developed. Depth contour maps have been used as a basis for the structure in these surveys, and migrations calculated roughly where necessary.

Where the geometry of an interface is such that several side reflections (compound side reflections) are produced (Fig. 6.1b) it may be possible to recognise these

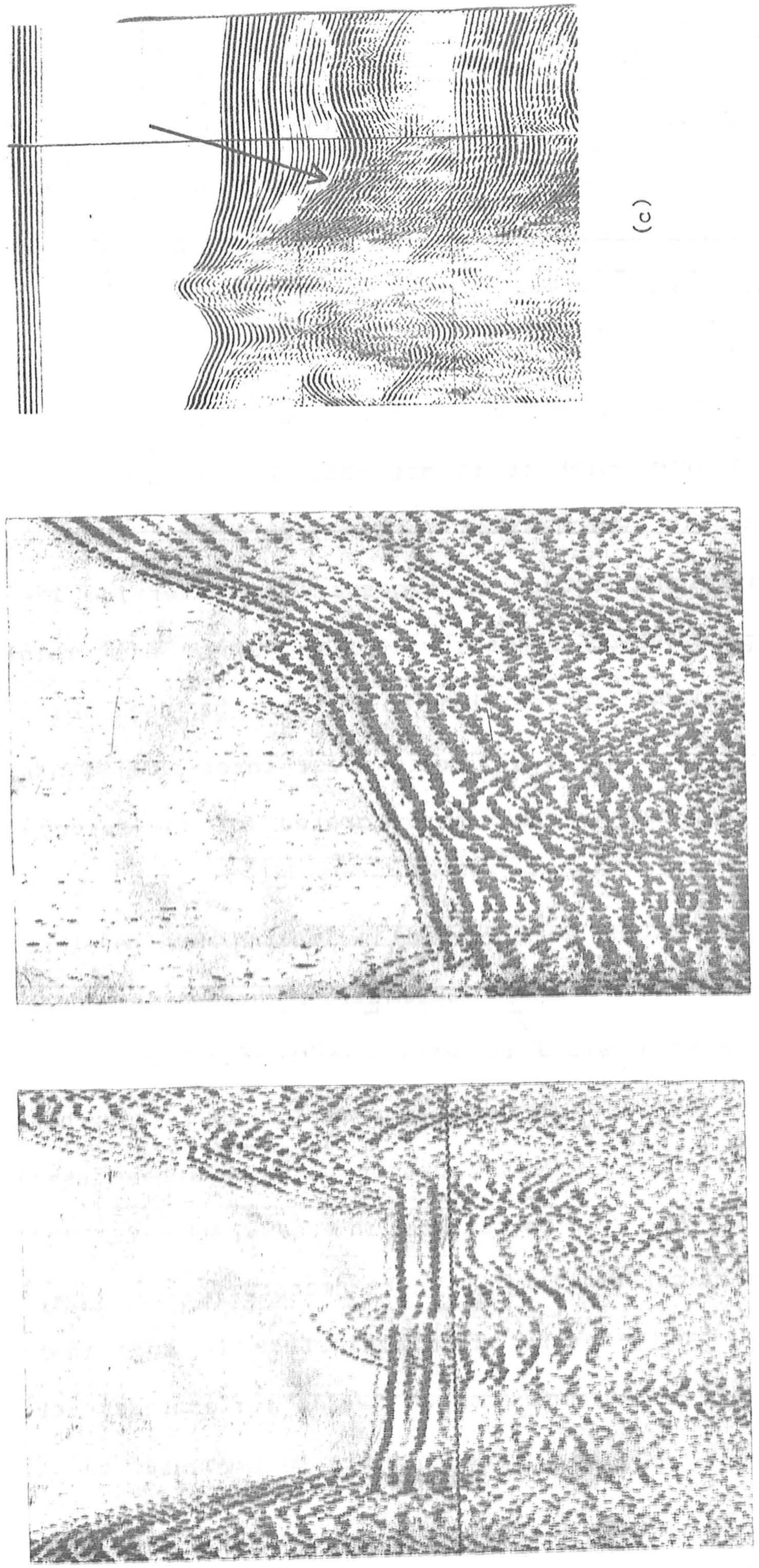

(a) (b) (c)

Fig. 6.2
Cross-cutting side reflections

on a single profile.

Compound side reflections may produce cross-cutting reflections which can be easily recognised as due to side reflections. Figs. 6.2a and 6.2b show isolated small bumps cutting the surface of a sedimentary basin; these are probably side reflections or side diffractions.

Compound side reflections may not give cross-cutting reflectors, which makes identification as a side reflection more complicated. A profile along a valley parallel to the contours (Fig. 6.3) could produce a sequence of three horizontally-layered reflectors, all of which are sea bed reflections, two of them being side reflections. Identification of the reflectors as side reflections and not as a layered sequence of reflectors would be difficult in this case. In practice change in angles of dip and direction of the side slopes of the valley would give variations in the amplitude and travel time of reflections 2 and 3 which could indicate that these may be side reflections. A reduction in dip of the valley sides, for example, would give no valley side reflections 2 and 3.

Side reflections can also be generated from sub-botttom reflectors. Fig. 6.2c is an example of cross-cutting sub-bottom reflectors, probably due to a side reflection. A side reflection arriving at a travel

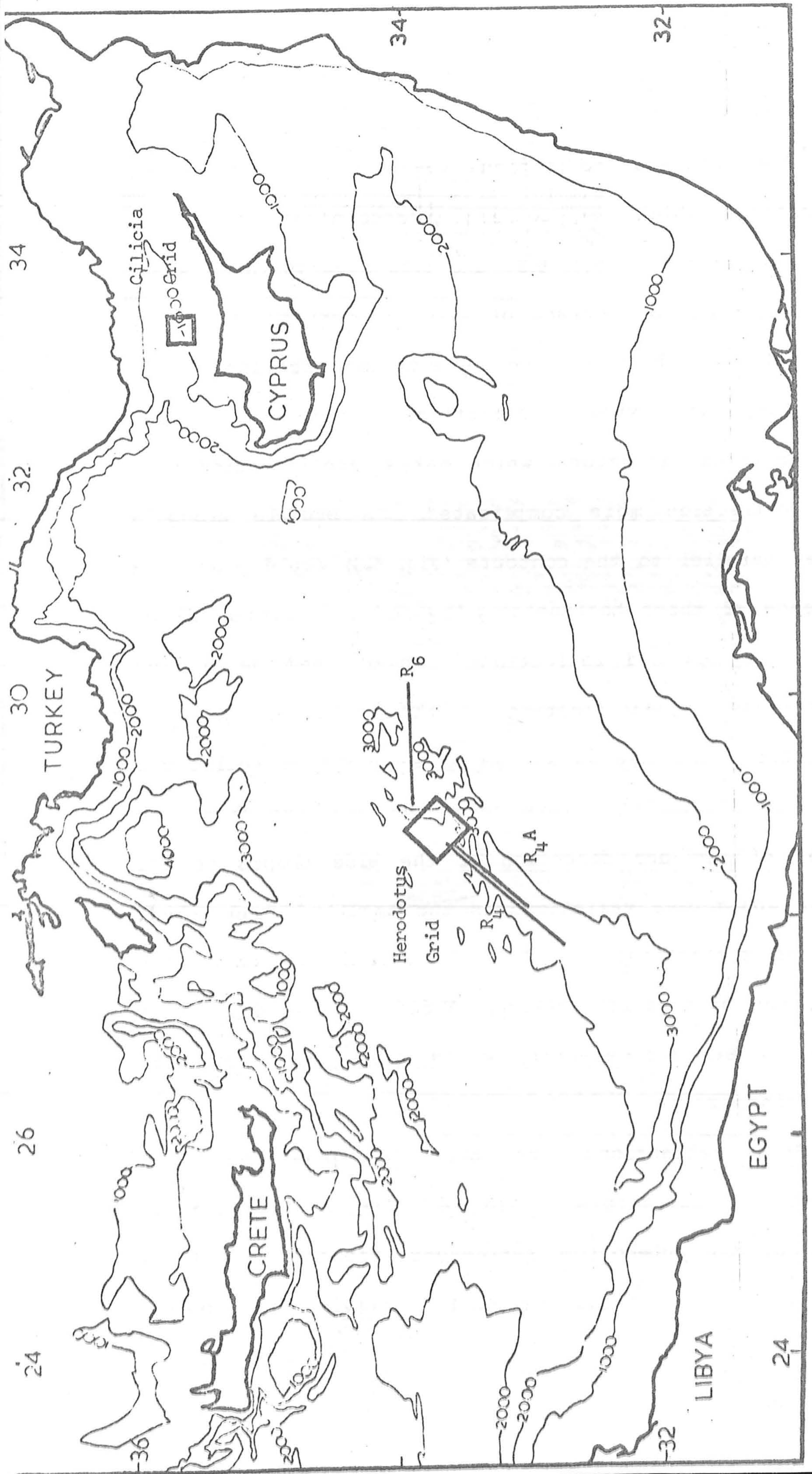

Fig 6.4 The location of the grid survey areas in the eastern Mediterranean. R_6, R_4 and R_4A are refraction lines after Lort et al (1974)

time greater than most reflections is also reasonably distinctive. The side reflection at 1640/145 in Fig. 6.12 is an example of this.

The character of a reflection can also indicate a side reflection. Side reflections generated by the situation in Fig. 6.3 would have the high frequency characteristics of sea bed reflections, although they appeared to be sub-bottom reflections.

Two reflection profiling grid surveys were made in the eastern Mediterranean in May and June 1974 in areas where side reflections should occur, to study their generation and recognition.

6.2 The Grid Surveys

The two areas chosen are in the Herodotus basin, and the Cilicia basin (Fig. 6.4). Existing reflection profiles showed that they were areas with complicated structures, small enough to be covered by a grid survey in the time available, and with slopes of the structures proabably high enough to produce side reflections. There were too few existing profiles to determine the extent, three-dimensional shape, and probable origin of the structures, so the profiling surveys also provided a detailed picture of the geological structure.

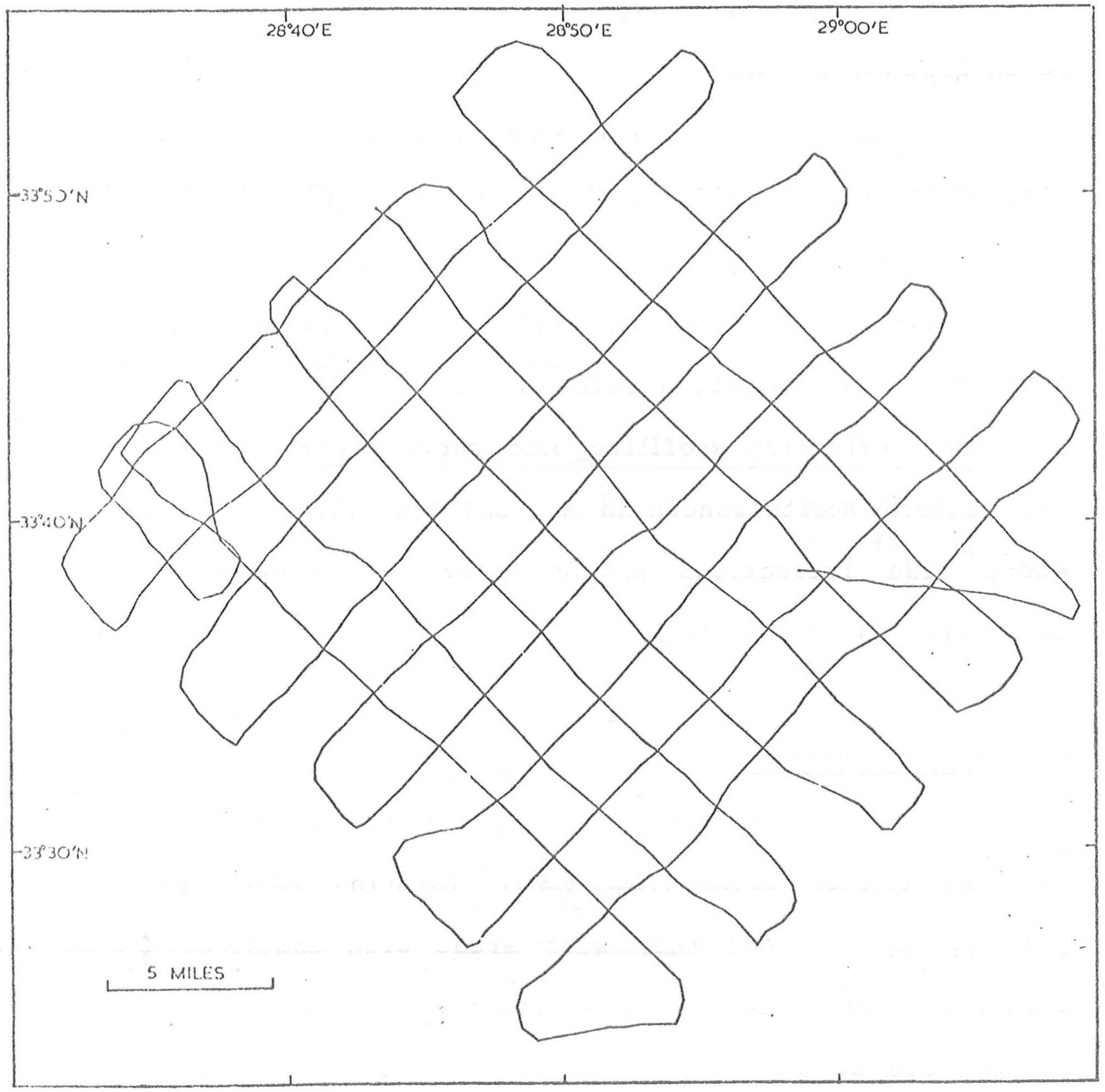

Fig. 6.5
Tracks of the Herodotus Basin survey

6.3 The Herodotus basin survey

Location

The structures in the Herodotus basin were estimated from existing profiles to have a wavelength of 10 - 20 km and to extend between 30 and 50 km in a north-south direction and an unknown distance east-west. The survey was planned as a rectangular grid of 8 lines in a northeast-southwest direction and 8 lines perpendicular to these. The lines were 45 km long and the spacing was 5 km. The northeast-southwest direction was the axial direction of the basin. Fig. 6.5 is the track chart of the survey.

Navigation

the survey was navigated using a radar transponder buoy and satellite navigation. The buoy was moored at the centre of the survey area, and a transponded echo was received at all positions in the survey, a maximum range from the buoy of 27 km. A radar fix on the transponder buoy was taken every 5 minutes. It was difficult to keep the ship on the planned survey lines because of wind and currents, so some of the lines are not very straight. An error in heading of 2^{o} at the beginning of a line would give a distance off the line of 1.5 km at the end of the line, so the heading had to be adjusted carefully; when the distance off the line

Map	Mean Crossover Error	Contour Interval
Herodotus bathymetry	11 m	50 m
Herodotus depth to reflector M	73 m	250 m
Herodotus magnetics uncorrected	12 γ	-
Herodotus magnetics corrected for daily variation	7 γ	20 γ
Cilicia bathymetry	10 m	50 m
Cilicia depth to reflector S	36 m	100 m

Table 6.1. Mean crossover errors and contour intervals for the survey contour maps.

reached 0.3 km a course alteration was made to bring the ship back onto the line. This demanded very accurate steering, as the course alterations were only a few degrees, and the auto-pilot was set to allow the minimum possible deviation from the desired course. The maximum sea state during the survey was 3.

Turning at the end of a line demanded particularly careful navigation, and a 180° turn was accomplished by turning 90° at 10° per minute, continuing on that course and using radar fixes to estimate the time to commence the final 90° turn at 10° per minute. The total 180° turn took about 30 minutes. The show rate of turning was used as rapid turning put too much strain on the receiver array, and the array would take a long time to straighten after the turn. The deviation of the ship from the planned lines was usually greatest at the beginning of the lines, because of the turn and difficulty of adjusting to wind and current on a new course.

The absolute position of the transponder buoy was determined by satellite navigation. The buoy was checked for drift during the survey by taking a radar fix on the buoy at the time a satellite fix was received. The buoy did not drift significantly during the survey, but the satellite and radar fixes showed that the mean position

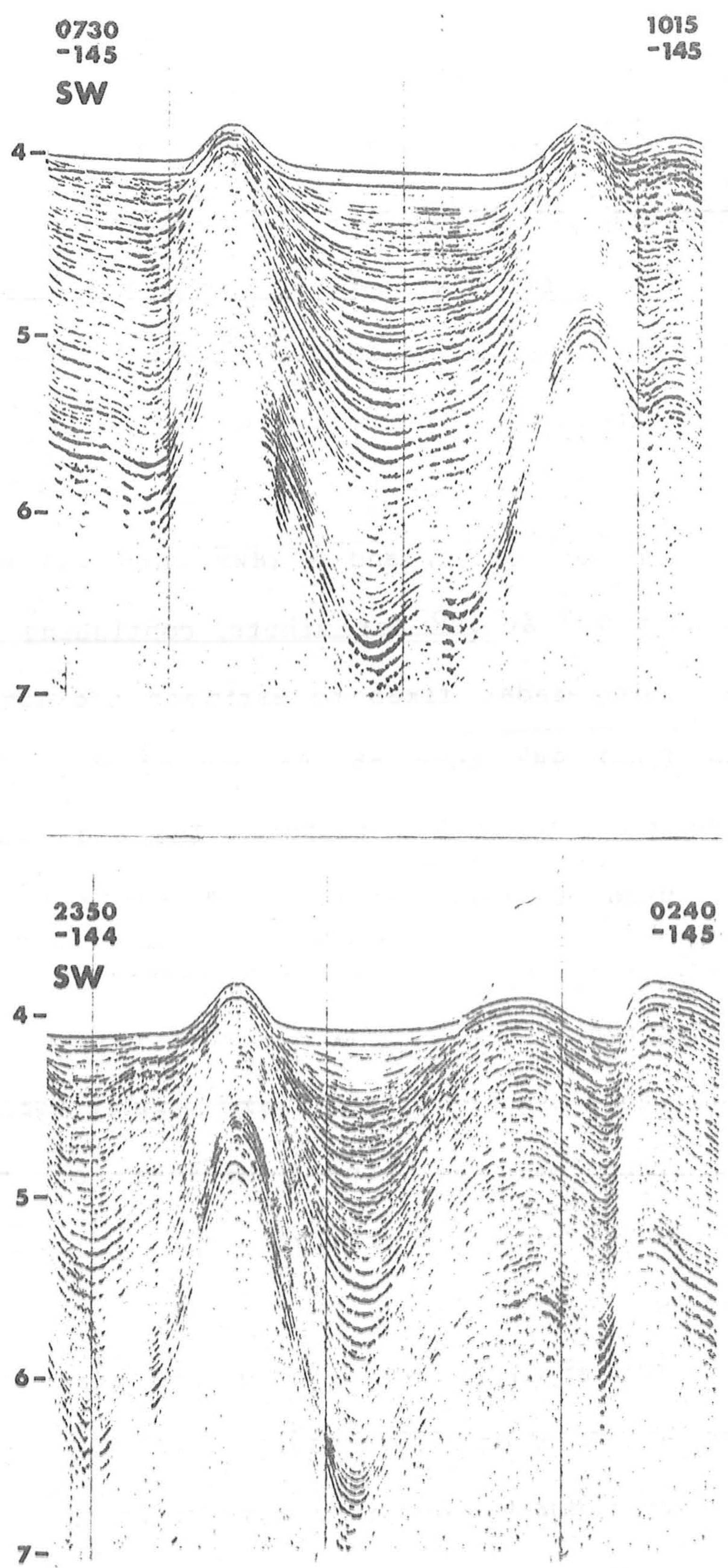

Fig. 6.6
Herodotus survey profiles in a direction SW-NE. The numbers at the side of the profile are two-way times in seconds. The vertical lines are hour marks, approximately 12 km apart. The vertical exaggeration is x 12. There is a time-variant gain on the records of approximately x 4, initiated by the sea bed. The records are filtered 5-150 Hz.

of the buoy altered slightly with time, and the final navigation was computed using a mean buoy position for each day; the daily buoy positions were within 0.5 km.

The accuracy of the navigation positions varied with distance from the transponder buoy; radar fixes from the buoy were probably accurate to 0.1 km at distances of less than 5 km, and 0.3 km at distances greater than 20 km. The crossover errors in bathymetry and sub-bottom bathymetry of the surveys indicate a mean navigational error of 0.3 km, using mean gradients for the values (Table 6.1).

General Features

The survey area is in the deep basin betweeen the Nile cone and the Mediterranean ridge and has a considerable thickness of sediment. The water depth is about 3 km. The area is 200 km to the south of the seismically active plate margins (McKenzie 1972) and is not associated with the Mediterranean ridge structures.

The profiling system was a 160 in^3 Bolt Par airgun, electrically fired with a firing repitition rate of 10 s, and a Géomechanique array with a single active section, having 50 hydrophones in a 60 m length.

Typical profiles are shown in Figs. 6.6 and 6.7. The area is not an abyssal plain; it has sediment ponded between highs of an underlying sedimentary layer. The

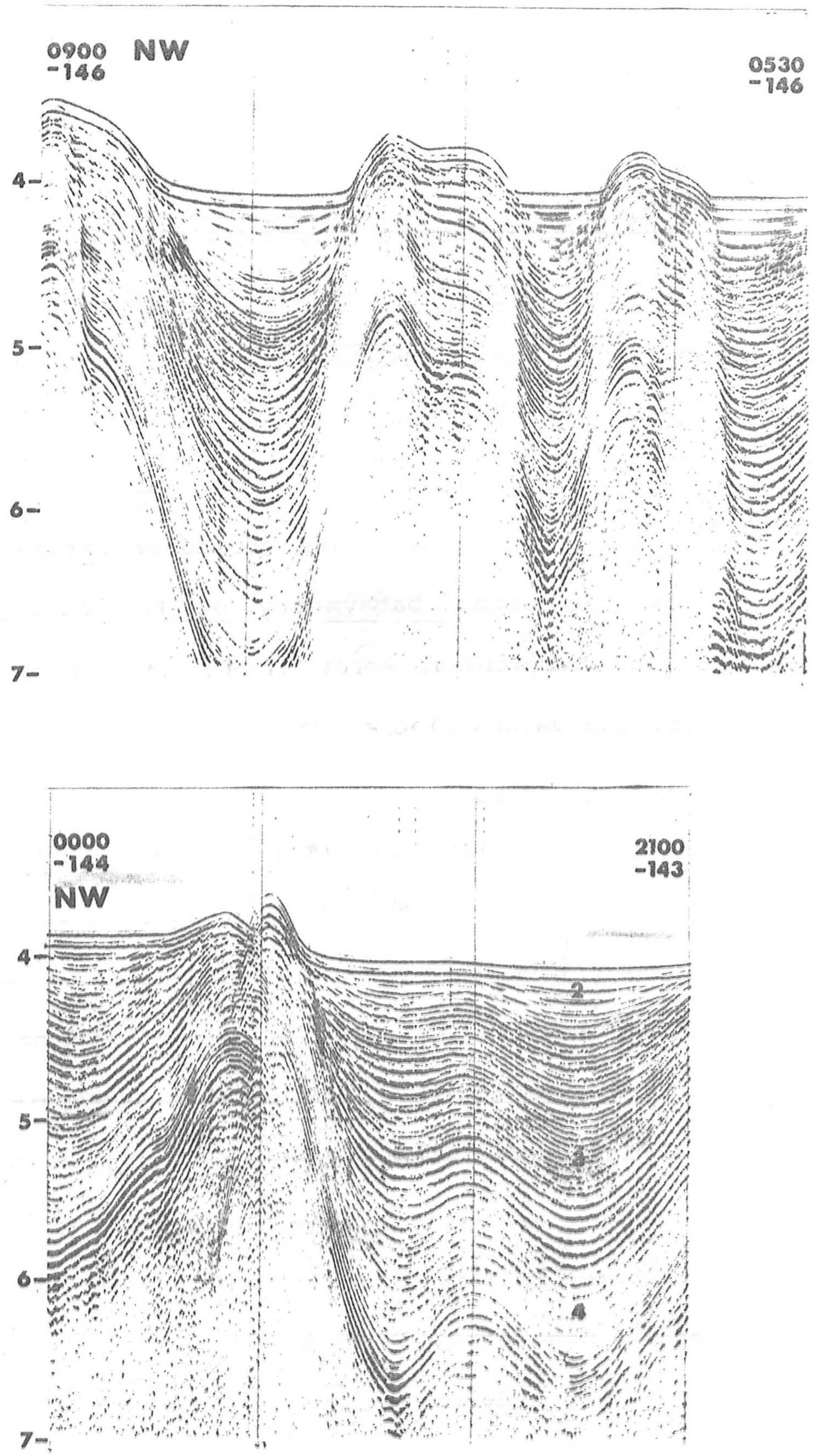

Fig. 6.7
Herodotus survey profiles in a direction NW-SE.
The figures 2,3 and 4 on the lower profile are the layers corresponding to the velocity structure in Table 6.2

highs reach 0.5 km above the level of the sediment ponds. The ponded sediment bends upward at the edges of the ponds, and as this would have been deposited initially flat this indicates that there is still differential movement between the highs and basins. Below the ponded sediment there is a sequence of reflectors, the lowest ones having the greatest dips. The sediment layers thin across the highs, but they are continuous over them, and their thickness increases with depth in the basins. There is faulting over some highs.

The deepest continuous reflector that can be traced over the area reaches a depth of 3.5 s below the sea bed. It has been traced by Woodside (1974) over most of the eastern Mediterranean and was thought to be the same as the reflector M traced by Ryan et al (1970) in the western Mediterranean. A Messinian evaporite sequence has been identified below reflector M in the western Mediterranean (Ryan et al 1972). The deepest reflector in the Herodotus survey will subsequently be referred to as reflector M.

Sediment Velocities

A 300 in^3 airgun and disposable sonobuoys were used to obtain sediment velocities in two of the basins in the Herodotus plain. One velocity determination was centred at $33^{o}35'N$, $28^{o}53'E$ in the survey area, and one at

Sonobuoy	Layer	Velocity kms^{-1}	Depth in km to bottom of layer
1	water	1.53	3.13
	2	1.72	3.35
	3a	2.40	3.79
	3b	2.48	4.85
	4	3.26	6.73
2	water	1.53	3.12
	2	1.70	3.62
	3	2.54	5.20
	4	3.32	5.55

Table 6.2. Velocity structure in the Herodotus survey area from disposable sonobuoy data.

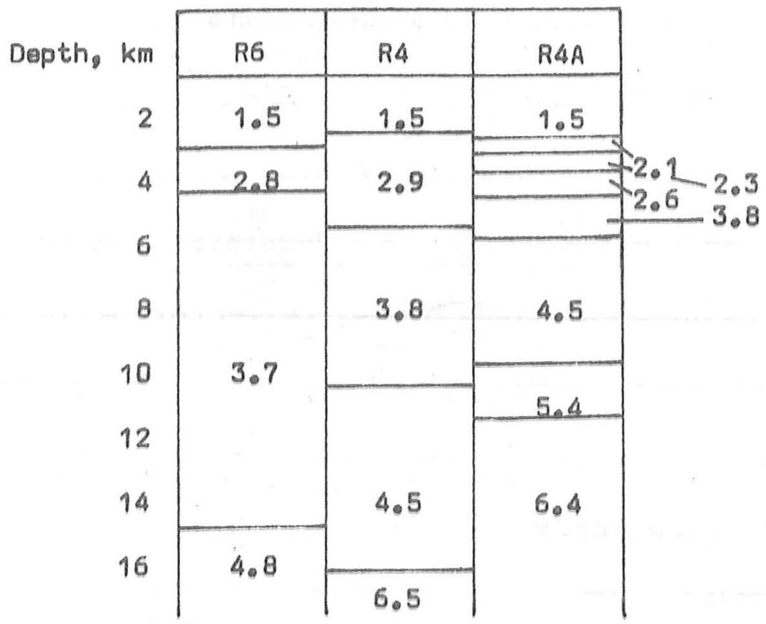

Fig. 6.8. Velocity structure in the Herodotus basin from refraction lines (R6 and R4) and a variable angle reflection/refraction line (R4A) after Lort et al (1974).

33°28′N, 28°35′E in a large basin to the southwest of the area. The velocity structure was obtained from variable angle reflections and refractions and the results are in Table 6.2. The results are similar in both basins, suggesting that they are probably similar over the grid area.

There are a few hundred metres of ponded sea bed sediment with a velocity of 1.7 km s^{-1}; about 1.5 km of deeper sediment with a velocity of 2.4 - 2.5 km s^{-1}; then a variable thickness of sediment with a velocity of 3.3 km s^{-1} overlying reflector M down to a depth of about 6 km. The layers corresponding to this velocity structure are marked in Fig. 6.7. No deeper reflections could be identified, and no refraction was found for the layer below 4, so the velocity below this could not be determined.

Refraction results in the Herodotus plain have been published by Lort et al (1974). Their location is shown in Fig. 6.4, and velocity structures from the three lines are summarised in Fig. 6.8. R_6 is a refraction line, with a velocity structure calculated for the point 33°54′N, 29°00′E which is to the northeast of the survey area and just outside it. R_4 is a refraction line with the velocity structure calculated for the point 33°33′N, 28°42′E, just inside the southwest edge of the survey.

Sonobuoy	Layer	Velocity kms^{-1}	Depth in km to bottom of layer
1	water	1.53	3.13
	2	1.72	3.35
	3a	2.40	3.79
	3b	2.48	4.85
	4	3.26	6.73
2	water	1.53	3.12
	2	1.70	3.62
	3	2.54	5.20
	4	3.32	5.55

Table 6.2. Velocity structure in the Herodotus survey area from disposable sonobuoy data.

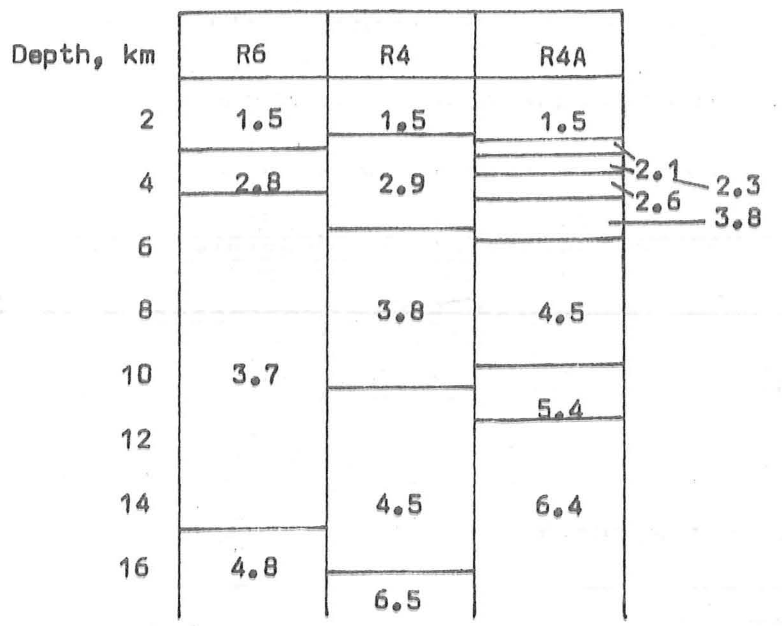

Fig. 6.8. Velocity structure in the Herodotus basin from refraction lines (R6 and R4) and a variable angle reflection/refraction line (R4A) after Lort et al (1974).

$33^{\circ}28'$N, $28^{\circ}35'$E in a large basin to the southwest of the area. The velocity structure was obtained from variable angle reflections and refractions and the results are in Table 6.2. The results are similar in both basins, suggesting that they are probably similar over the grid area.

There are a few hundred metres of ponded sea bed sediment with a velocity of 1.7 km s^{-1}; about 1.5 km of deeper sediment with a velocity of 2.4 - 2.5 km s^{-1}; then a variable thickness of sediment with a velocity of 3.3 km s^{-1} overlying reflector M down to a depth of about 6 km. The layers corresponding to this velocity structure are marked in Fig. 6.7. No deeper reflections could be identified, and no refraction was found for the layer below 4, so the velocity below this could not be determined.

Refraction results in the Herodotus plain have been published by Lort et al (1974). Their location is shown in Fig. 6.4, and velocity structures from the three lines are summarised in Fig. 6.8. R_6 is a refraction line, with a velocity structure calculated for the point $33^{\circ}54'$N, $29^{\circ}00'$E which is to the northeast of the survey area and just outside it. R_4 is a refraction line with the velocity structure calculated for the point $33^{\circ}33'$N, $28^{\circ}42'$E, just inside the southwest edge of the survey.

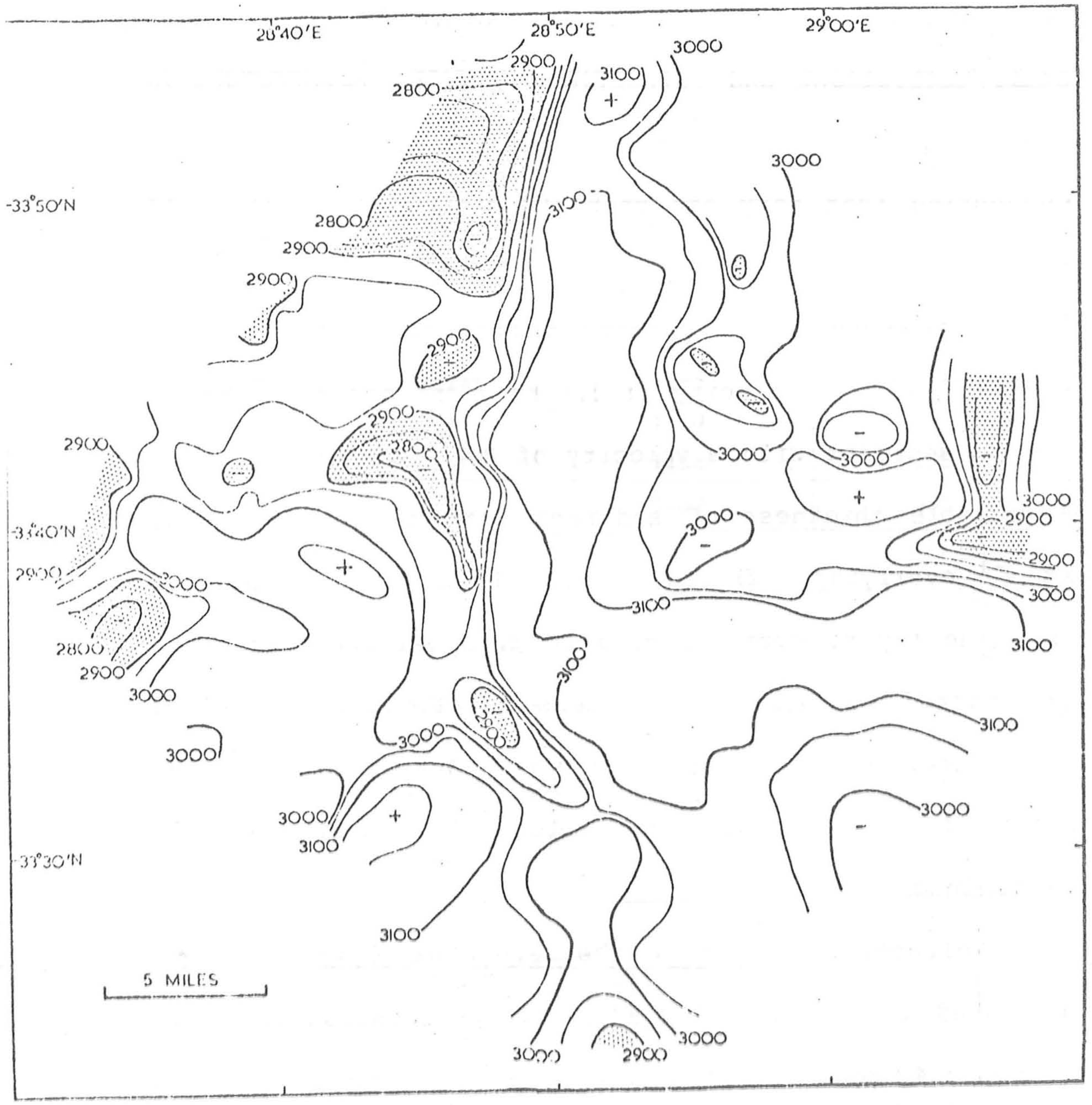

Fig. 6.9

Bathymetry of the Herodotus survey. The contour interval is 50 m and highs are shaded

R_4A is a variable angle reflection and refraction line with a velocity structure calculated for the whole line, 33°33'N, 28°42'E to 32°34'N, 28°09'E, the northeast end of which is inside the southwest edge of the survey area. R_6 and R_4 have velocities 3.7 - 3.8 km s^{-1} below 6 km, but R_4A has a velocityof 4.5 km s^{-1}, so it is difficult to use these results to infer the velocity below reflector M in the survey area.

<u>Bathymetry</u>

A bathymetric map of the area was compiled from survey data, and is Fig. 6.9. The water depth is about 3 km. The map shows highs, some of which are approximately circular, and flat sediment ponds, which may be at diffferent levels if isolated by highs, as in Fig. 6.7.

<u>Depth to reflector M</u>

The depth to reflector M was calculated from travel times and sediment velocities and is shown in Fig. 6.10. The depth varies from 4 to 7 km over the area, with gradients up to 30°. The striking feature of the map is the strong linear north-south trending high and basin. Superimposed on the high, and in other parts of the area are smaller, approximately circular highs.

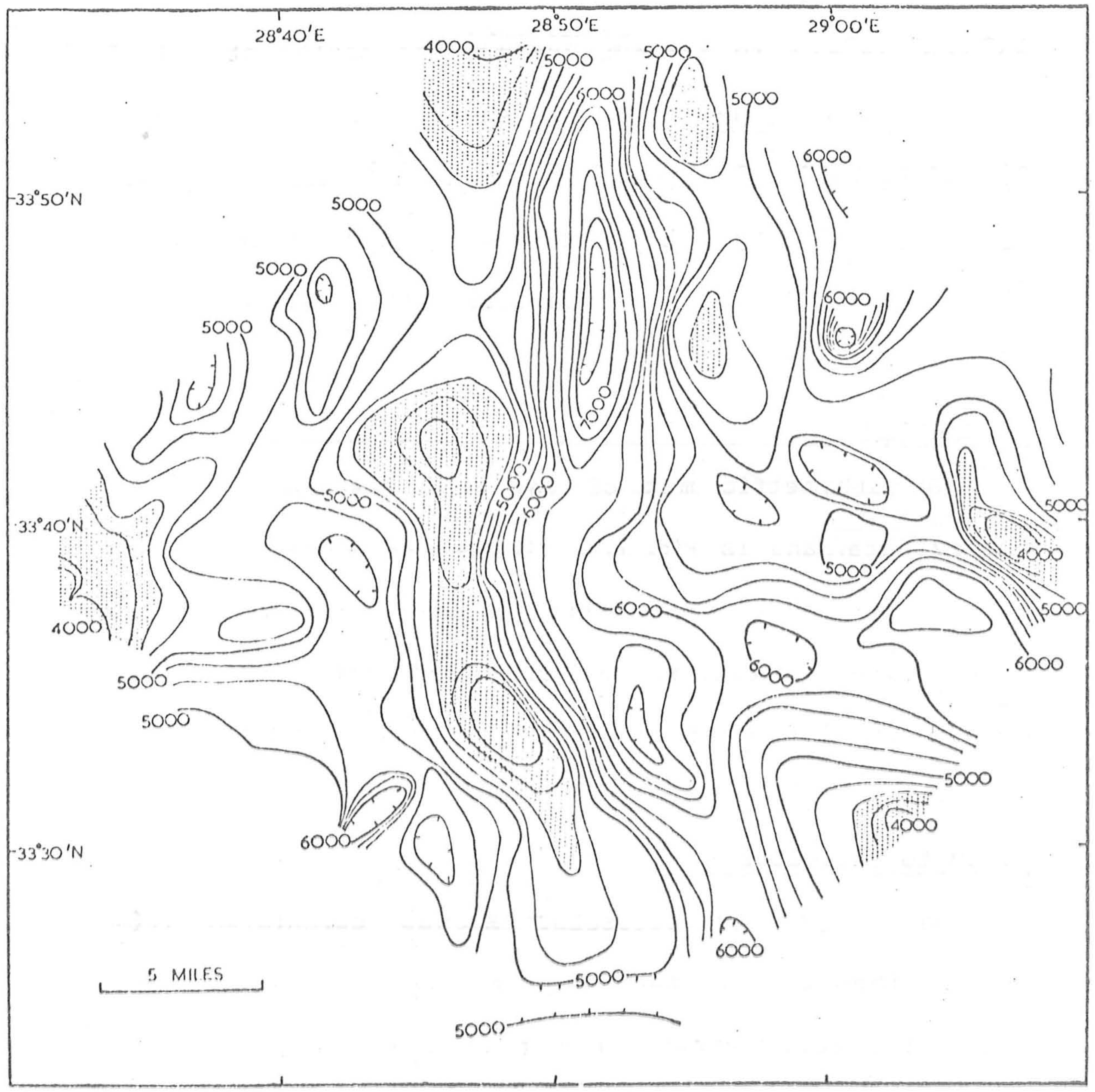

Fig. 6.10
Depth to reflector M in the Heródotus survey.
The contour interval is 250 m and highs are shaded.

Magnetic anomalies

Fig. 6.11 shows the magnetic anomalies in the area, computed by removing the International Geomagnetic Reference Field (IAGA 1967) from total field values. Initial computations gave crossover errors that were very high (Table 6.1); a mean error of 12γ in a total range of 120γ, which was hgher than could be caused by navigational error, and only a very coarse contour interval could be used. The error was caused mainly by daily variation of the magnetic field, and the amplitude of this, about $\pm 20\gamma$ at this latitude is significant in a survey area of this size and without high amplitude anomalies, so an attempt was made to correct the magnetic values for daily variation. A moored station magnetometer would be the only accurate method of measuring daily variation but unfortunately this was not available for the survey. The nearest land obsevatories are in Greece, Israel and Egypt, all a considerable distance away, and it has so far proved impossible to get any data from them for the time of the survey. This leaves correction by theoretical daily variation curves as the only possibility. The anomalies were corrected using a total field daily variation computed from mean three-component daily variation curves for the magnetic inclination and declination of the survey area (Chapman

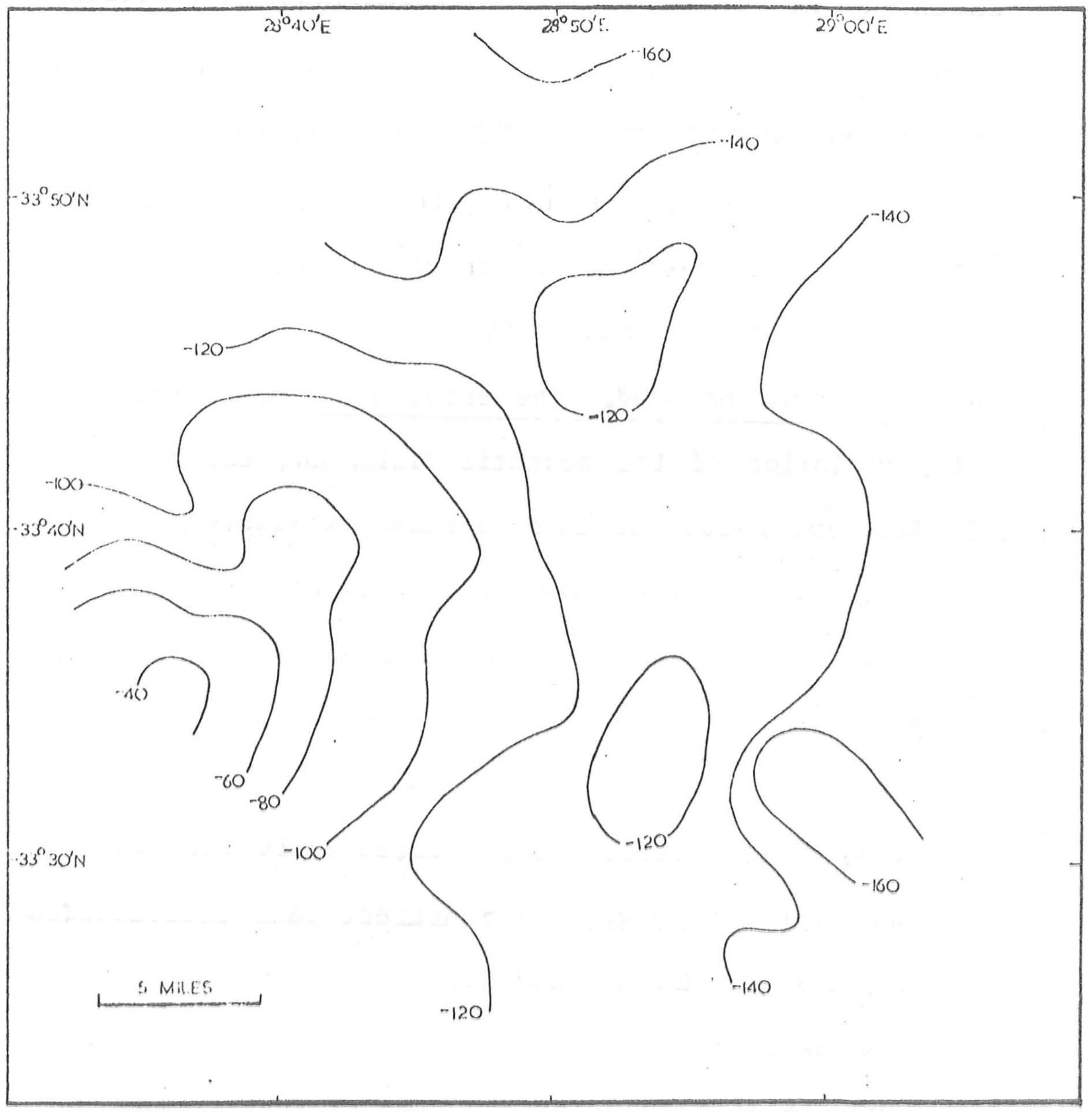

Fig. 6.11

Magnetic anomalies in the Herodotus survey. The contour interval is 20 γ

and Bartels 1940). These theoretical daily variation values will be in error if the days are magnetically disturbed; the K_p index, the world index of magnetic disturbance, shows that for the four days of the survey three of the days are normal and one is disturbed (World Data Centre A 1974). The daily variation estimate will be in error at least for the one disturbed day, but in the absence of a station magnetometer this is the best estimate that can be made. Correction of the magnetic anomalies for daily variation reduced the mean crossover error to 7γ, and made it possible to contour the values with a 20γ contour interval.

The grid is in an area of regional negative anomalies, and the values range from -40 to -160γ. This is consistent with the zero value of -100γ used for the eastern Mediterranean by Matthews (1974).

There is an anomaly at the southwest side of the grid of $+80\gamma$ relative to the rest of the grid. Only one side of the anomaly is inside the survey area but a very rough estimate of the maximum depth of the magnetic body can be made by measuring the width of the maximum gradient and comparison with models for vertical sided blocks (Vacquier et al 1951). This gives a maximum depth of about 8 km. There are no shorter wavelength anomalies associated with the highs in reflector M, including the linear north-south high.

Origin

The structure of the area could be caused by syn-depositional folding or diapirism.

The evidence in favour of syn-depositional folding is the general structure of the area, the linear north-south feature, and the thickening of the sediment layers in basins. Against this hypothesis is the detailed structure of the area, such as the formation of domes, the restriction of structures to a relatively small area, and the recent sediment rising at the edges of the basins, which shows that there is still movement at the present time. This would require a compressive force in the area, which is not expected as the area is not near a plate margin, and is not associated with Mediterranean ridge structures.

Diapirism provides a better explanation of the structure of the area. The shapes of domes, rim synclines, the gradient at the sides of the domes and faulting above the domes could all be caused by diapirism. The diapiric material must be below reflector M, as this is continuous over the area.

Diapirism can be caused by movement of sedimentary or igneous material. The magnetic anomalies in the area show that the diapirism is not of igneous origin as there are no anomalies associated with the domes. Sediment diapirism is indicated by the concentration of the domes in this relatively small area of about 60 km square, in the deepest parts of the Herodotus basin with the greatest thickness of sediment, and by the similarity to the sediment diapirs in the western Mediterranean, although reflctor M is continuous over the survey area unlike in the western Mediterranean where it is pierced by diapirism.

The sedimentary diapirism may be evaporite (salt) or mud diapirism, but there is no definite evidence to suggest which. Unfortunately no velocities below reflector M could be measured or could be used from published velocity data. The area may be similar to the western Mediterranean in having a salt layer below reflector M. Gravity measurements over similar domes near this area have sharp negative Bonguer anomalies associated with the domes, (Woodside 1974) showing that there is a low density material at depth beneath the domes, which suggests salt rather than mud.

The reason for the north-south trends in the area is difficult to determine. Linear salt features in an area generally have the same trend, so this may be a regional trend. In northern Europe there is a trend which is thought to be basement controlled (Murray 1966), but there are no magnetic anomalies associated with the north-south trends in the survey area so basement structures are not the cause. The Gulf of Mexico has salt structures which are controlled by a sediment loading effect and are parallel to a coastline or delta; the Nile cone which supplies the sediment to the Herodotus basin has a northeast-southwest edge adjacent to the basin in this area so sediment loading does not provide a good explanation.

Side reflections

The depth contour maps Figs. 6.9 and 6.10 give the unmigrated magnitude and direction of dip for reflection positions, from which the sideways distance and direction of reflection points can be calculated. Migration would alter the structures on the contour maps by reducing the width of the rises, increasing the width of the basins, and increasing the depth of dipping layers (chapter 5 models).

The sideways distance of a reflection point for a side reflection from the line of the profile depends on the slope of the interface. The maximum slope on the bathymetry map is 1 in 5, and for a vertical depth of 2.9 km for the reflecting point the sideways distance of the point is 0.6 km. The travel time to this point is not very different from a vertical travel time so compound side reflections from the sea bed should arrive at about the same time as the first sea bed reflection. A side reflection could probably only be identified by a cross-cutting relationship in this case and there would need to be a suitable high angle slope less than 0.6 km distant.

This applies to regular reflections, but diffractions could be produced from any angle, at any distance, although diffractions are generally lower amplitude.

Side reflections can also be generated from the sub-bottom reflectors. These have higher slopes, and the side reflection points can be further away. The maximum slope on reflector M is 1 in 2 and the maximum sideways distance of a reflecting point for a vertical depth of 5 km would be 2.5 km, ignoring ray path refraction in the upper sediments, which gives a two-way travel time of about 7 s.

The bathymetry map was overlaid with the track chart and the track examined for positions where compound side reflection could occur. The criterion used was a steep slope with contours roughly parallel to the track and less than 0.6 km distant, or less steep slopes nearer the track, and a flat or gently dipping area below the shot point. Diagrams were drawn of possibilities and

Predicted		Observed		
Position	Travel time	Position	Travel Time	Characteristics
1750–1810/144	6.5	not observed		
1840–1850/144	6.7	1850/144	6.8	high frequency
0840–0900/145	6.3	not observed		
1640–1650/145	6.8	1640/145	6.2	high frequency
0520–0600/146	6.5	not observed		
1200–1220/146	6.5	1210/146	6.2–6.5	low frequency
1330–1350/146	6.7	1340/146	6.6	low frequency

Table 6.3. Herodotus survey side reflection predictions from the reflector M contour map, and observed side reflections.

dippping reflectors migrated back to their true positions.

An example in which compound sea bed side reflections could occur could not be found. This was because the steep slopes are mainly north-south or occasionally east-west in direction, whereas the grid lines are at 45° to these so they not not run parallel to the steep slopes. A survey with north-south and east-west tracks might have produced sea bed side reflections. There are also very few examples on the profiles of compound sea bed reflections in the plane of the profile — there are only a few cliffs with overlapping reflections (Chapter 5 models) eg. Fig. 6.6 at Ø215/145; Fig. 6.7 at 23ØØ/143, which suggests that similarly there should be few, if any, compound sea bed side reflections.

The deeper layers with higher slopes should have more possibilites for side reflections as reflections could come from a greater distance sideways. More overlapping compound reflections from the deeper reflectors in or near the profile plane are seen on the profiles. The steeper slopes of reflector M are mainly but not totally in a north-south directions. Seven possibilities were found for compound side reflections from the reflector M contour map, of which four could be

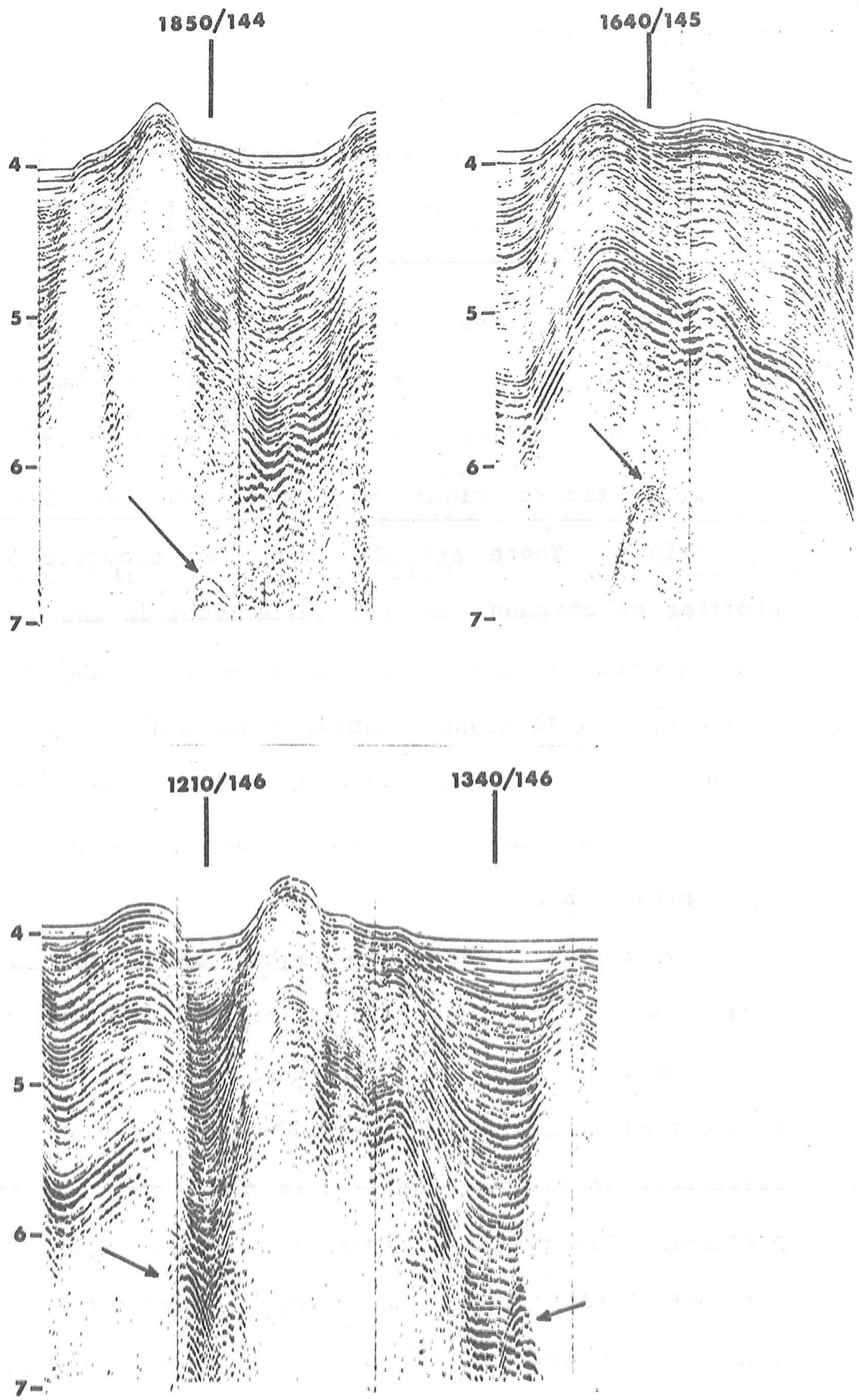

Fig 6.12
Possible side reflections in the Herodotus survey profiles

seen on the profiles, at 1850/144, 1640/145, 1210 and 1340/146 and these are shown in Fig. 6.12. Table 6.3 details these predicted and observed side reflections. Two of the observed side reflections, at 1850/144 and 1640/145 are hyperbolic-shaped reflections or diffractions with a greater reflection time than the other reflections. The other two show cross-cutting sub-bottom reflections at normal travel times.

The shape and frequency content of side reflections provides an indication of their origin. The hyperbolic side reflection at 1640/145 has the high frequency waveform characteristics of a sea bed reflection. The reflection at 1850/144 is too weak for the frequency characteristics to be identified, but both this and the 1640/145 reflection have hyperbolic shapes corresponding to calculated diffraction hyperbolae for the travel time and water velocity. Estimation of velocities using diffraction hyperbolae is not a very accurate method of determining velocities (Chapter 3.4) but this does at least indicate that the side reflections at 1850/144 and 1640/145 are probably sea bed diffractions, not from reflector M. Their travel times indicate that they must come from a horizontal distance of about 4 km from the profile. The bathymetry map shows that there are rises at approximately these distances that could give diffractions. The side reflections at 1210 and 1340/146 have the frequency content of deep reflections and probably come from reflector M.

The five side reflections from reflector M which were predicted but not seen on the profiles either cannot be distinguished, or not exist, probably bacause of inaccuracies in detail in the reflector M contour map, as small differences in slope or direction of contours could prevent side reflections occurring. No other side reflections could be seen on the profiles except the four described in Table 6.3, two of which were probably sea bed diffractions and two side reflections or diffractions from reflector M. This is surprising, as more cross-cutting compound reflections which appear to come from in or near the profile plane are seen on the profiles, suggesting that there should be significant number of side reflections. These may not exist, perhaps due to the orientation of the profile tracks at 45° to the main structures, or may not be visible on profiles if they not not produce distinctive cross-cutting reflections.

6.4 The Cilicia basin survey

Location

The area of complex structures in the Cilicia basin was estimated to be smaller than in the Herodotus basin,

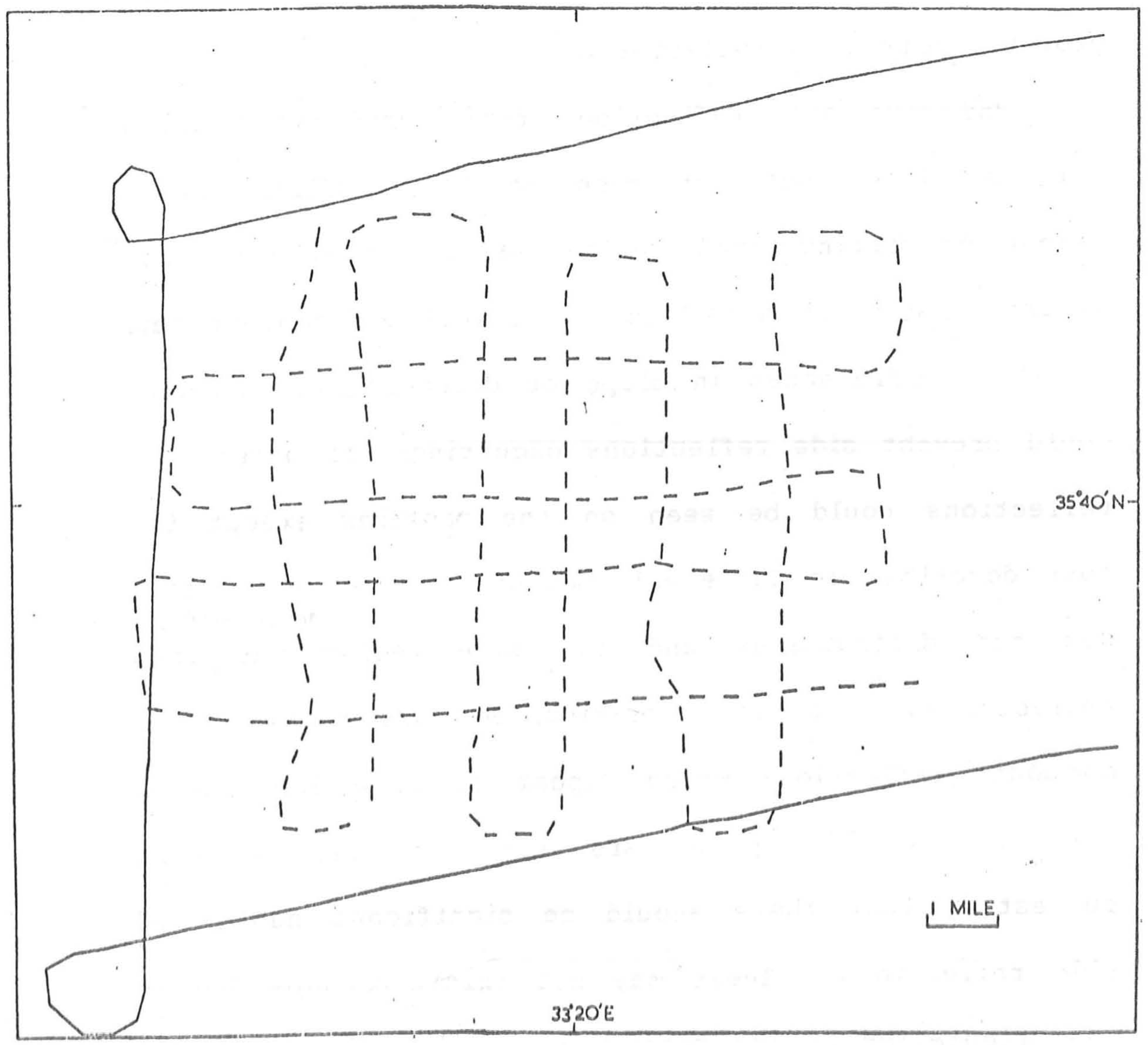

Fig. 6.13
Tracks for the Cilicia Basin survey.
The dashed lines are sparker tracks and the solid lines are airgun tracks

and a smaller survey was planned. The wavelength of structures was also smaller, and a closer line spacing was used. The survey grid was rectangular, with 6 north-south lines 15 km long and 4 east-west lines 20 km long, with a line spacing of 3 km. Fig. 6.13 is a track chart of the survey.

Navigation

The survey was navigated with a radar transponder buoy and satellite navigation, as in the Herodotus survey. The planned survey had a small area and closely spaced lines, and the structures of interest were in the top 1 s of the sediment, so to enable faster turns to be made than is possible with an airgun system, a 5 KJ sparker and sparker array were used. The sparker lines are the dashed lines in Fig. 6.13. The transponder buoy did not move significantly during the survey, and a single transponder buoy was used for the whole survey. The accuracy of computed positions is similar to that in the Herodotus survey. Crossover errors in bathymetry and sub-bottom bathymetry give a mean total navigational error of about 0.3 km.

General features

The survey area is in a water deth of about 1 km between Cyprus and Turkey. The general tectonics of this area are not well understood; McKenzie (1972)

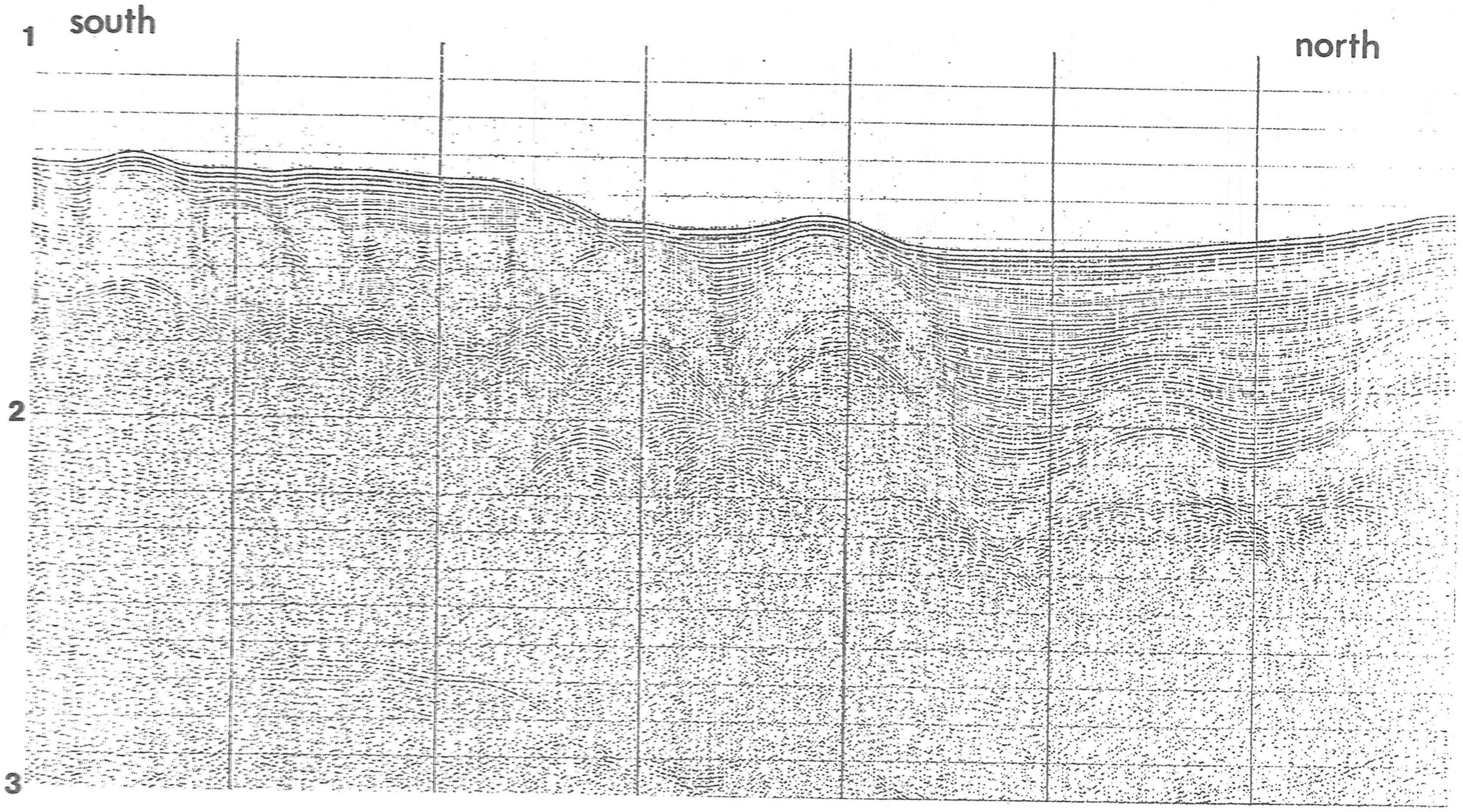

Fig. 6.14 Cilicia survey profile in a S-N direction. The numbers at the side of the profile are two-way travel times in seconds. The vertical lines are 10 minute marks, approximately 2 km apart. The vertical exaggeration is x 4. The profile is filtered 80-200 Hz and there is no time-variant gain.

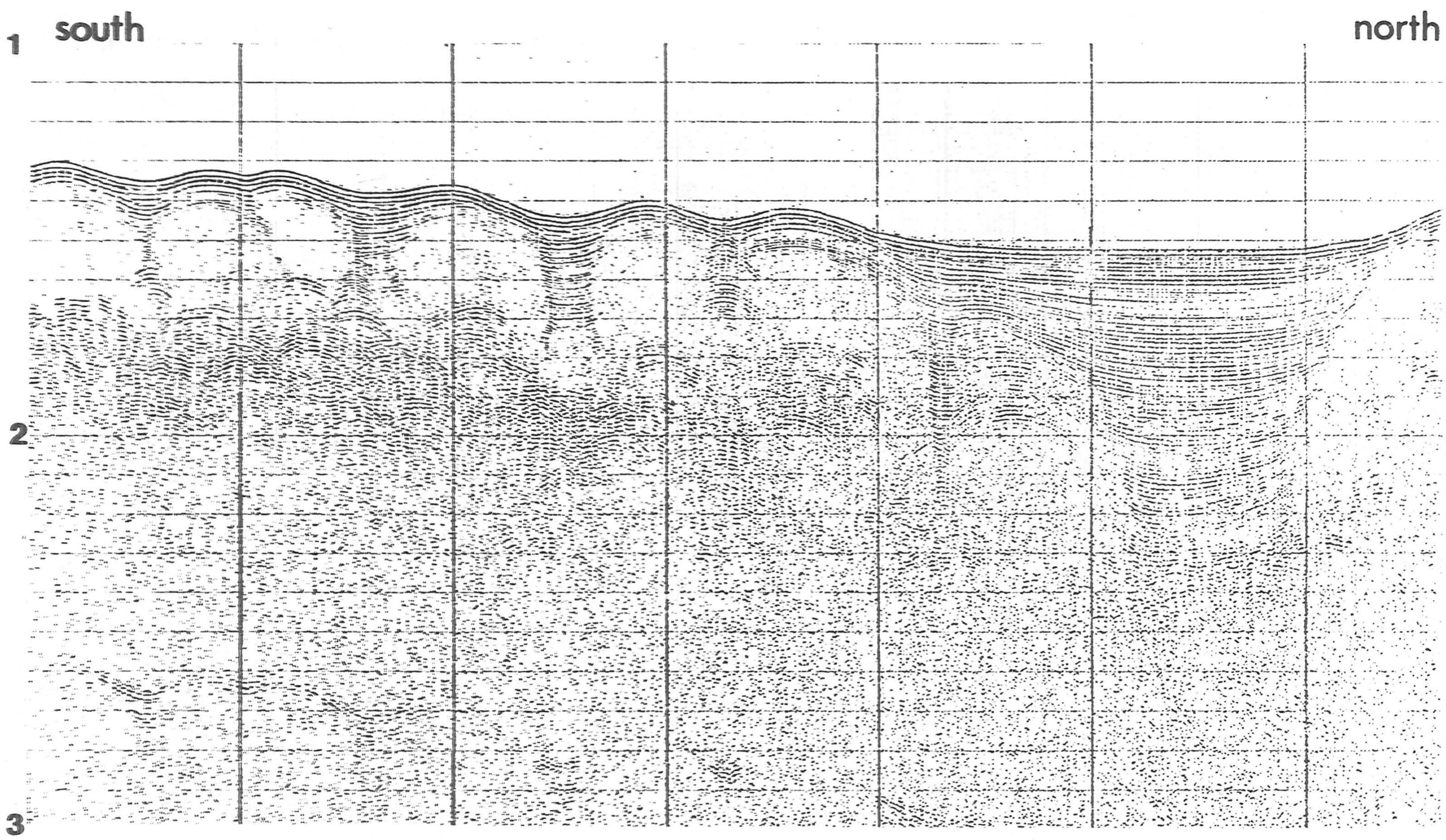

Fig. 6. 15 Cilicia survey profile in a S-N direction

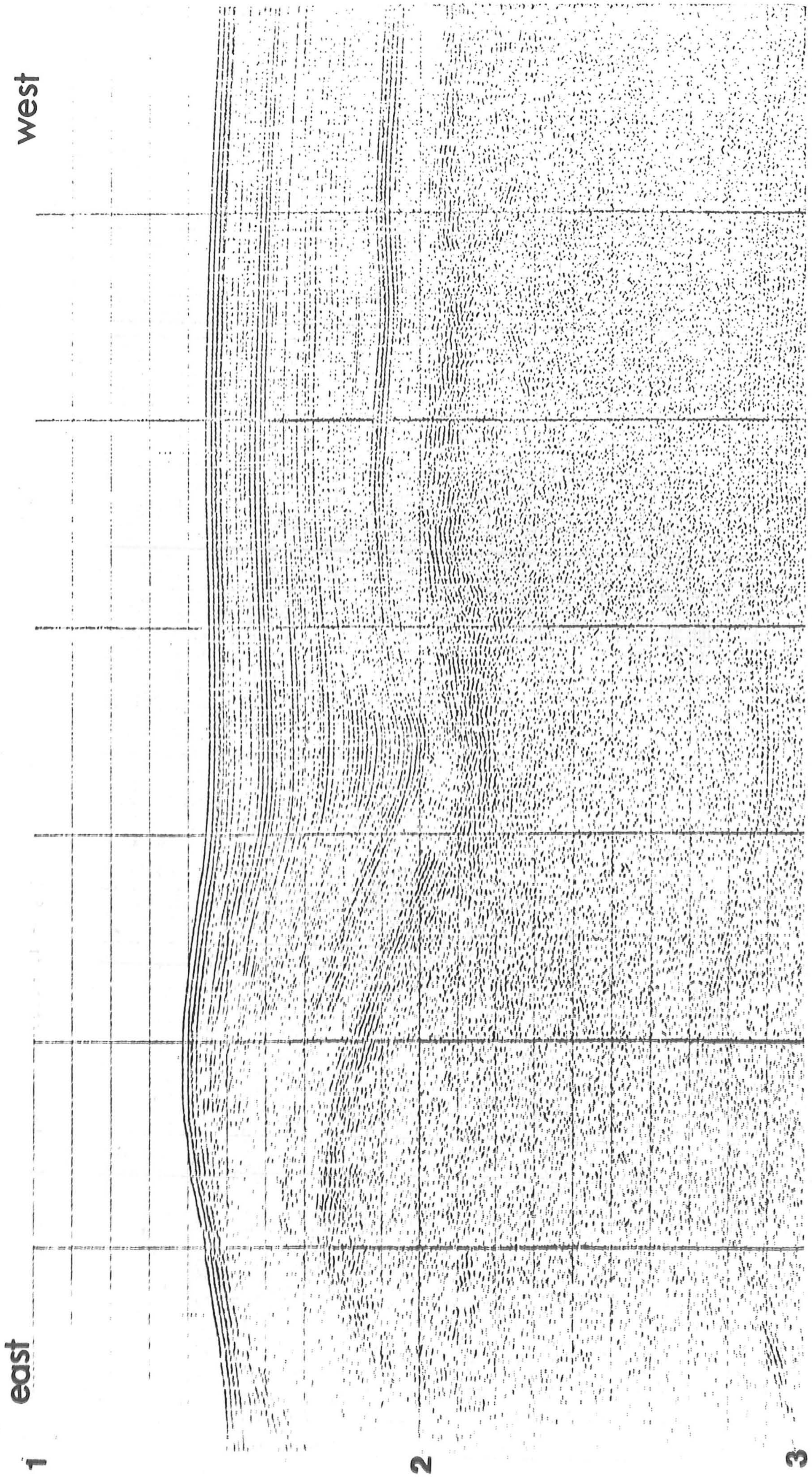

Fig. 6.16 Cilicia survey profile in a E-W direction

suggests a plate margin extending from the Gulf of Iskenderun through Cyprus to join the Cretan arc near Rhodes. This would be a northward dipping trench consuming the African plate at the western end of the arc, changing to strike-slip motion at the eastern end, and the Cilicia basin would be in a back-arc area. The scarcity of earthquakes in this area makes this a very tentative suggestion. It is also unknown whether structures in the Kyrenia range in Cyprus continue beneath the Cilicia basin into Turkey.

Figs. 6.14 to 6.17 are typical profiles of the survey. Their quality is inferior to the Herodotus survey profiles as the source is less powerful and the array noisier. The penetration is much less, up to 0.8 s, compared with 4 s for the Herodotus survey, because of the lower sparker power and higher frequency signal which is attenuated more rapidly.

The profiles show a layered sequence of reflectors and a deeper reflector which is broken and discontinuous, and in some parts is an overlapping sequence of hyperbolic diffractions. This may be reflector M, but as this survey is not connected to Woodside's (1974) profiles positive identification of this is not possible, so this reflector will be called subsequently reflector S. The depth of reflector S varies from 0.3-0.8 s below

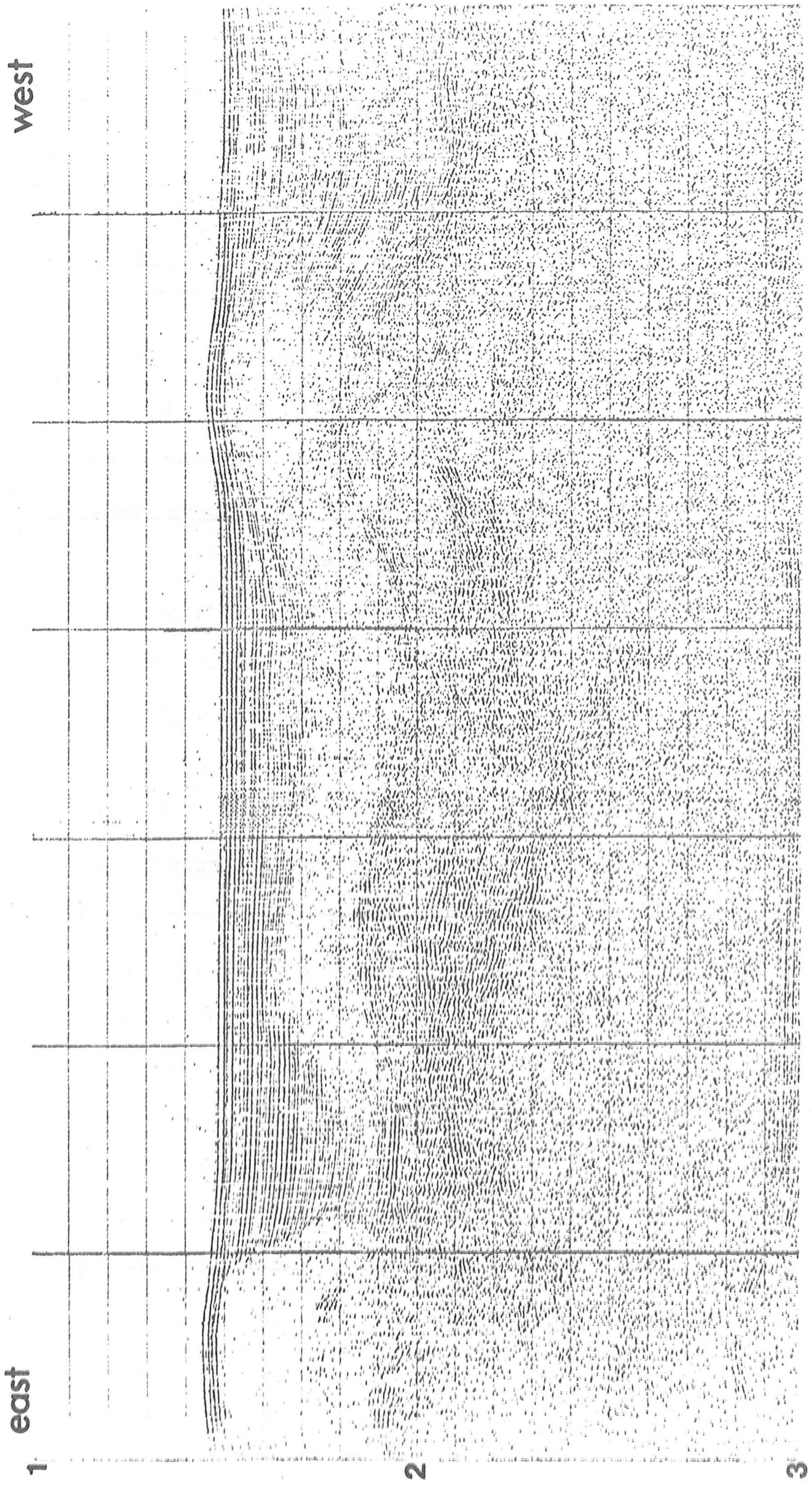

Fig.6.17 Cilicia survey profile in a E-W direction

the sea bed, and no coherent reflections can be seen from below this.

The north-south tracks (Figs. 6.14 and 6.15) show that there are small rises of less than 0.05 s amplitude and 1-4 km across in the southern part of the area. These have a transparent layer beneath them in which no reflectors can usually be seen except the lower reflector S, which is continuous below the rises in most cases, generally rising also, or is occasionaly very broken with many associated diffraction hyperbolae, suggesting faulting. The upper sediment layers end abruptly against the rises or the reflectors die out into the rises. There is a marked focussing effect in the synclines between rises, with the reflections having high amplitudes.

The rises decrease in frequency and increase in wavelength and amplitude in the northern part of the area, and reflectors can be seen continuing across most of the rises, being domed. The two east-west profiles (Figs. 6.16 and 6.17) are relatively flat or have long wavelength rises, suggesting that structures in the area are probably east-west in direction.

Sonobuoy	Layer	Velocity kms^{-1}	Depth in Km to bottom of layer
2	water	1.53	0.92
	2	1.96	1.25
3	water	1.53	1.00
	2	2.10	1.54
4	water	1.53	1.13
	2	2.12	2.08
	3	4.30	-
5	water	1.53	1.10
	2a	2.02	1.52
	2b	2.22	1.83
	2c	2.88	2.15
	3	3.30	3.52
	4	6.66	4.00

Table 6.4. Velocity structure in the Cilicia survey area from disposable sonobuoy data.

Sediment velocities

A 300 in^3 airgun and disposable sonobuoys were used to obtain sediment velocities in the less disturbed areas on three sides of the grid. The airgun tracks are shown as solid lines in Fig. 6.13. Five sonobuoys were used and good results were obtained from four; sonobuoy 1 had a noisy hydrophone suspension which made picking arrivals very difficult and no useful results were obtained from it. The interpreted velocity structure is given in Table 6.4.

Sonobuoys 2 and 3 obtained reflections from only one sub-bottom reflector, which by comparison with travel times at vertical incidence was identified as reflector S. The depth to this is 0.3-1 km below the sea bed, and the velocity in the sediments above it is about 2.0 km s^{-1}. Sonobuoy 4 obtained a refraction velocity of 4.3 km s^{-1} for the layer below reflector S. This is high, and may be a salt layer. The thickness by this layer is unknown as no arrivals were obtained from below this.

Sonobuoy 5, on the track to the north of the survey area, had the deepest arrivals. It recorded arrrivals from three layers above reflector S, with velocities 2.0-2.9 km s^{-1}, and from two layers below it; 3.3 km s^{-1} to a depth of 2.5 km below the sea bed, and 6.7 km s^{-1} to

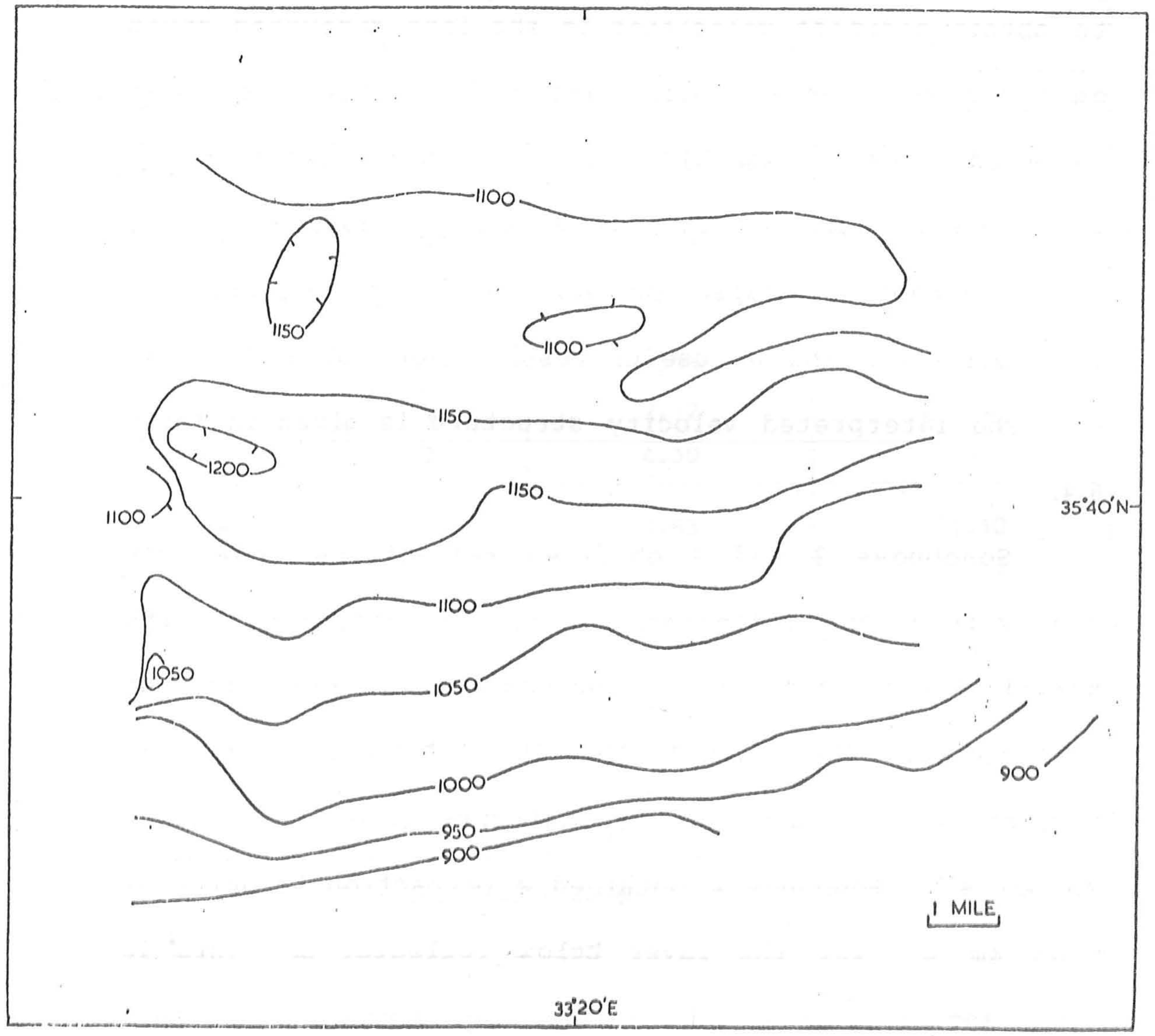

Fig. 6.18
The bathymetry of the Cilicia survey.
The contour interval is 50 m.

a depth of 3 km. These can be identified with reflections on the normal incidence airgun profile. The absence of the 4.3 layer in this position is puzzling, as sonobuoy 5 was dropped only about 12 km from sonobuoy 4; if there is a layer intermediate in velocity between the 3.3 and 6.7 layers for sonobuoy 5 this may not be visible because the reflection coefficient is too low, or its upper surface is too broken in this position for the propagation of head waves along the interface. A broken upper surface of a salt layer may also be the reason that no refractions were obtained from the reflector M interface in the Herodotus area.

Bathymetry

Fig. 6.18 is the bathymetry map of the area compiled from survey data. Crossover errors for this and the following map are given in Table 6.1. The sea bed increases in depth from 900 m in the south to 1100 m in the north of the area, towards the deeper parts of the Cilicia basin, and has an east-west valley of 1150 m in the nothern part of the area. The contours run roughly east-west. The larger bumps on the profiles show on the bathymetry map in the northern part of the area, and have an east-west elongation. The smaller bumps seen on the profiles to the south are too low amplitude to appear on the bathymetry map at the

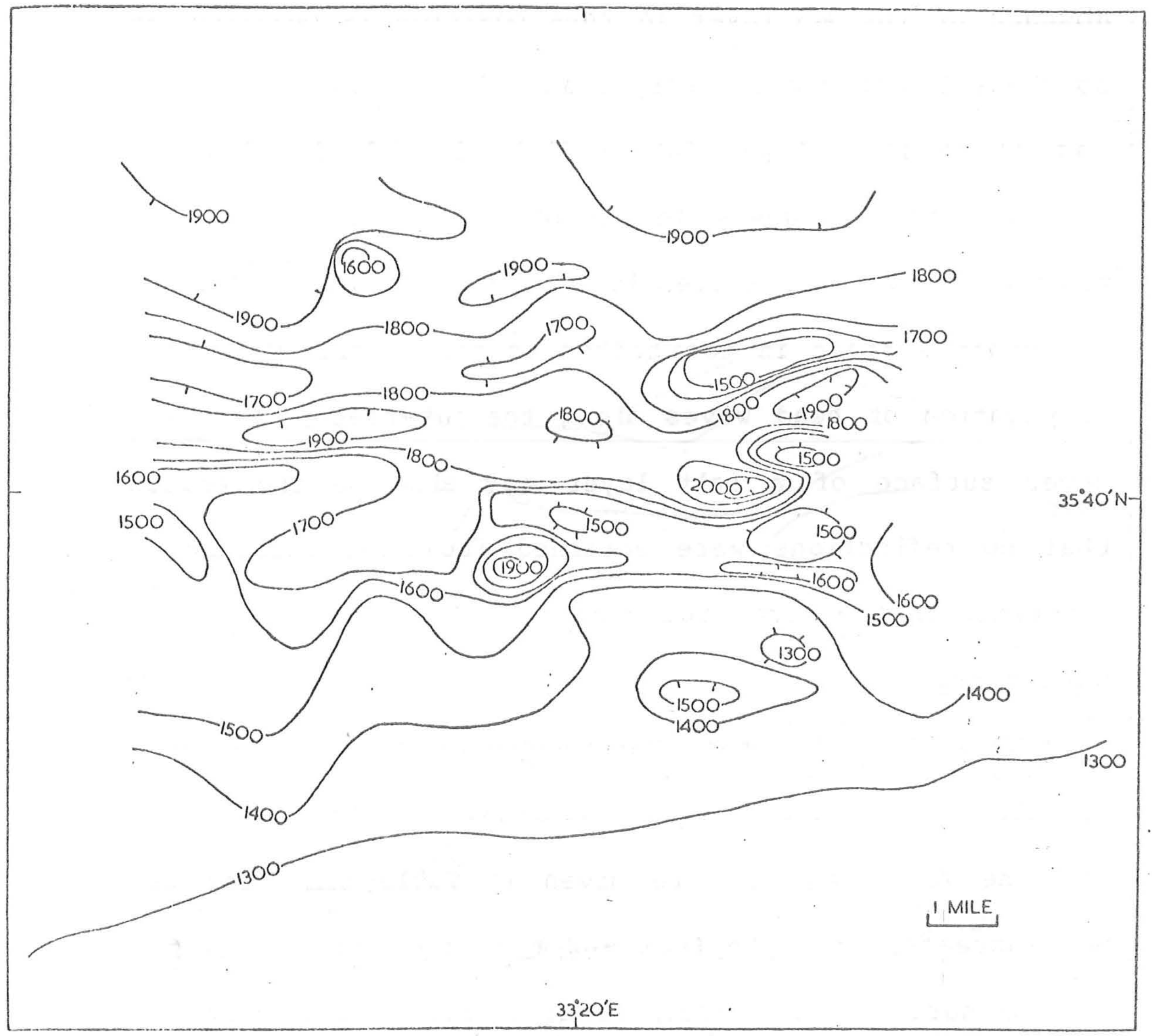

Fig 6.19
Depth to reflector S in the Cilicia survey.
The contour interval is 100 m.

contour interval of 50 m.

Depth to reflector S

The depth to reflector S was calculated using a velocity in the upper sediments of 2.1 km s^{-1} and is shown in Fig. 6.19. The reflector increases in depth from 1300 m in the south to 1900 m in the north. There is an east-west structural trend and there are also high amplitude bumps, up to 400 m, which are circular or elongated in an east-west direction. The larger bumps to the north appear on the contour map but the bumps seen on the profiles to the south are too small. The structure appears to be a series of circular domes superimposed on reflectors dipping to the north, causing elongation of the domes in an east-west direction.

Origin

The bumps in the area are probably sedimentary domes — reflectors can be seen continuous and domed under the larger bumps, and reflector S is continuous under all the bumps, although very broken in places. The transparent effect under the smaller bumps could be a geometrical effect of a small dome which reduces the reflection amplitude (Chapter 5 models).

Theories of the origin of the structures in this area must explain the east-west trend, the domes, and their restriction to a small area, as other profiles show that doming does not exist further south or north, and not immediately to the east or west.

A compessional plate margin through Cyprus would produce north-south compression in the area giving east-west folds, but this does not explain the elongated domes and the restriction of structures to this area.

The domes could be due to diaprisim, and the east-west structures could be caused by a sediment loading effect causing structures parallel to the coast of Cyprus and Turkey and the source of sediment, or folding on which diapirism is superimposed. The diapiric movement occurs below reflector S, as this is continuous although broken, and the transparent domes are probably not diapirs themselves but sediment doming in response to underlying diapirism. Unfortunately magnetic data for the survey is not available; this could have shown whether the diapirism was sedmimentary or igneous. The velocity of 4.3 km s^{-1} below reflector S could be either salt or igneous. Evidence against salt diapriism is that it would be expected to occur in the deepest and thickest parts of the Cilicia basin, assuming that there was salt deposition throughout the basin, and the survey area is not the deepest nor thickest part of the basin. The diapirs may be of igneous origin, perhaps associated with the possible back-arc location of the area; Jongsma

(1975) has found a ridge, which is probably igneous in the back-arc area of the nearby Cretan Arc. However structures in this area are discrete domes, not a ridge, and also similar domes exist in other parts of the eastern Mediterranean near Cyprus; to the northwest of Cyprus (Lort et al 1974) and to the northeast of Cyprus (unpublished Cambridge data). These also occur in localised areas, not necessarily associated with the greatest sediment thickness nor the deepest parts of basins.

The velocity of 6.7 km s^{-1} is high to find at 3 km depth below the sea bed, and is probably the basement, which can be seen on other reflection profiles dipping in to the Cilicia basin from the coasts of Cyprus and Turkey but goes too deep to be followed beneath the basin and has not been connected between Cyprus and Turkey. It may be possible to trace this with a more powerful profiling system.

Side reflections

The depth contour maps Figs. 6.18 and 6.19 give the unmigrated magnitude and direction of dip for reflection positions and could be used as a basis for migration, which would alter slightly the structures on the contour map.

The maximum sea bed slope observed in the area is

1 in 10, which is proabaly too low to give distinct compound side reflections, as for a water depth of about 1 km the maximum sideways distance of a reflecting point would be 100 m. A very rapid change in slope would be needed for a compound side reflection to be produced, from zero to 1 in 10 in 100 m, which is a very tight radius of curvature of the surface, and exists in only a few positions in the survey. An example is in Fig. 6.14, 28 minutes from the south end of the profile where there is a sea bed cliff with a small radius of curvature at its lower edge, giving a distincive overlapping reflection of an in-plane compound reflection (Chapter 5 models). Reflections come from a finite area, not just a point (Chapter 3.1) so reflections from 'points' 100 m apart will be difficult to distinguish. Single side reflections will be probably the only side reflections from the sea bed that can be distinguished.

The deeper layers have steeper slopes, and have more possibilities of generating compound side reflections. The maximum slope of reflector S is high, 1 in 1.5, and could give a reflection point up to 1 km distant with a travel time of about 2 s. Reflector S is associated with many diffraction hyperbolae, and sideways diffractions could also occur. The east-west survey lines are parallel to the structures, and is the

Predicted	
Position	Travel time
0805	1.8
1250	1.9
2050	1.8
2320	2.0

Table 6.5. Cilicia survey side reflection predictions from the reflector S contour map.

direction for detecting compound side reflections if they exist.

There are only four positions in the survey with high slopes having contours approximately parallel to the track where compound side reflections could be generated, and these are detailed in Table 6.5. Reflector S on the profiles in these positions is very broken with associated diffraction hyperbolae so that any compound side reflections could not be recognised. This is unfortunate, as although the area had structures and slopes which should be sufficient to produce compound side reflections, because of the broken nature of reflector S they cannot be recognised on the profiles by cross-cutting relationships or greater travel times.

6.5 Conclusions

The two surveys have yielded only eleven positions from which compound side reflections could be expected, and of these only two were seen on the records, with a further two side diffractions. The areas had complex structures with high slopes from which many compound side reflections could have been expected, which suggests that compound side reflections that can be distinguished on profiles are probably rare, even when there is an indication from a grid survey that they should be present.

The Herodotus survey area may have produced more side reflections if the tracks had not been oriented at 45^{o} to the main structures, and side reflections may have been recognised in the Cilicia survey if reflector S had not been so broken, so other areas may produce profiles with many side reflections, but the results of this chapter indicate that this is probably rare, and the error in modelling a three-dimensional reflection profile with a two-dimensional structure may not be very significant unless the structure is required very accurately, as for example for drilling.

The only side reflections that can be recognised on a single profile are compound side reflections, which can be recognised by cross-cutting reflections, greater travel times, and frequency and shape characteristics. A three-dimensional survey is the only way the plane of a single side reflection can be determined, and three-dimensional information is necessary for migrating dipping reflectors back to their true positions, as conventional migration techniques have to assume that all reflections come from the plane of the profile.

In many cases a three-dimensional survey is useful on its own for determining structures without the involvement of migration, as has been done for the two surveys in this chapter, provided the effects of dip are recognised; The true structure should have the width of rises reduced, the width of the basins increased and the depth of the dipping layers increased. Two-dimensional modelling is useful in determining the effects of dip on structures.

REFERENCES

ANSTEY, N.A. 1960. Geophys. Prospect. 8 242-259. Attacking the problems of the synthetic seismogram.

ARONS, A.B. 1948. J. Acoust. Soc. Amer. 20 277-282. Secondary pressure pulses due to gas globe oscillation in underwater explosion.

BARNHARD, P. 1967. Geophysics 32 827-832. Signal strength of marine seismic explosives.

BEDENBENDER, J.W. 1970. Geophysics 35 1054-1072. Electroacoustic characteristics of marine seismic streamers.

BLUNDELL, D.J. & PARKS, R.L. 1971. Geophys. Prospect. 19 339-344. Comparison of "Aquaflex" with conventional explosive for seismic refraction measurements.

BORN, M. & WOLF, E. 1959. Pergamon. Principles of Optics.

BULLEN, K.E. 1963. Cambridge University Press. Introduction to the Theory of Seismology.

ČERVENY, V. & RAVINDRA, R. 1971. University of Toronto Press. Theory of seismic head waves.

CHAPMAN, S. & BARTELS, J. 1940 Oxford University Press. Geomagnetism, vol.1.

CISTERNAS, A., BETANCOURT, O., & LEIVA, A. 1973. Bull. Seism. Soc. Amer. 63 143. Body waves in a real earth, Part 1.

CLOWES, R.M. & KANASEWICH, E.R. 1970. J. Geophys. Res. 75 6693-6705. Seismic attenuation and the nature of reflecting horizons within the crust.

DIX, C.H. 1953. Harper & Bros. Seismic prospecting for oil.

DOBECKI, T.L. 1973. Geophys. Prospect. 21 330-339. Three dimensional seismic modelling for arbitrary velocity distributions.

DUNKIN, J.W. & LEVIN, F.K. 1971. Geophysics 36 1099-1137. Isochrons for a 3-D seismic system.

EWING, M., JARDETSKY, W.S. & PRESS, F. 1957. McGraw Hill. Elastic waves in layered media.

FUTTERMAN, W.I. 1962. J. Geophys. Res. 67 5279-5291. Dispersive body waves.

GILES, B.F. 1968. Geophys. Prospect. 16 21-53. Pneumatic Acoustic Energy Source.

GILES, B.F. & JOHNSTON, R.C. 1973. Geophys. Prospect. 21 77-101. System approach to airgun array design.

GIRLING, F.E.J. & GOOD, E.F. 1969. Wireless World 75 403-408. Active Filters.

HILTERMAN, F.J. 1970. Geophysics 35 1020-1037. Three dimensional seismic modelling.

HRON, F., KANASEWICH, E.R. & ALPASLAN, T. 1974. Geophys. J. Roy. Astr. Soc. 36 607-626. Partial ray expansion required to suitably approximate to the exact wave solution.

IAGA. 1967. J. Geophys. Res. 74 4407-4408. International Geomagnetic Reference Field 1965.0.

JENKINS, F.A. & WHITE, H.E. 1957. McGraw Hill. Fundamentals of Optics.

JONGSMA, D. 1975. Ph.D Thesis, University of Cambridge. A marine geophysical study of the Hellenic Arc.

KRAMER, F.S., PETERSON, R.A. & WALTER, W.C. 1968. Presented at 38th Annual meeting of the Society of Exploration Geophysicists. Seismic Energy Sources 1968 Handbook.

LAVERGNE, M. 1970. Geophysics 35 419-435. Emission by underwater explosions.

LIMOND, W.Q. 1972. Ph.D. Thesis, University of Cambridge. Deep seismic reflection profiling at sea.

LORT, J.M. & GRAY, F. 1974. Nature 248 745-747. Cyprus: seismic studies at sea.

LORT, J.M., LIMOND, W.Q. & GRAY, F. 1974. Earth. Planet. Sci. Lett. 21 355-366. Preliminary Seismic Studies in the Mediterranean.

LUCAS, A.L. 1974. Geophys. Prospect. 22 667-682. A high resolution seismic survey.

MATTHEWS, D.H. 1974. 14th Congres-Assemblee pleniere de la CIESM. Magnetic anomalies and bathymetry of the Eastern Mediterranean Sea.

MAYNE, W.H. & QUAY, R.G. 1971. Geophysics 36 1162-1173.

MAYNE, W.H. & QUAY, R.G. 1971. Geophysics 36 1162-1173.
Seismic signatures of large air guns.

McDONAL, F.J., ANGONA, F.A., MILLS, R.A., SENGBUSH, R.L., VAN NOSTRAND, R.G., & WHITE, J.E. 1958. Geophysics 23 421-439. Attenuation of shear and compressional waves in Pierre Shale.

McKENZIE, D.P. 1972. Geophys. J. Roy. Astr. Soc. 30 109-185.
Active Tectonics of the Mediterranean Region.

MURRAY, G.E. 1966. Amer. Ass. Pet. Geol. 50 439-478.
Salt structures of Gulf of Mexico Basin - a Review.

NAFE, J.E. & DRAKE, C.L. 1963. The Sea, 3, Ed. M.N. Hill. 794-815. Physical Propeties of Marine Sediments.

NEWMAN, P. 1973. Geophysics 38 481-488. Divergence effects in a layered earth.

O'BRIEN, P.N.S. 1960. Geophys. J. Roy. Astr. Soc. 3 29-44.
Seismic Energy from Explosions.

O'BRIEN, P.N.S. & LUCAS, A.L. 1971. Geophys. Prospect. 19 1-26. Velocity dispersion of seismic waves.

OFFICER, C.B. 1958. McGraw Hill. Introduction to the theory of sound transmission.

PRESS, F. 1964. J. Geophys. Res. 69 4417-4418. Seismic wave attenuation in the crust.

RYAN, W.B.F., STANLEY, D.J., HERSEY, J.B., FAHLQUIST, D.A., & ALLEN, T.D. 1970. The Sea, 4 Ed. A.E. Maxwell.
The tectonics and geology of the Mediterranean.

RYAN, W.B.F., HSU, K.J. et al. 1972. DSDP Initial Reports 13. Introduction.

SAVIT, C.H., BRUNSTAD, J.T. & SIDER, J. 1958. Geophysics 23 1-25. The moveout filter.

SCHOENBERGER, M. 1970 Geophysics 35 1038-1053. Organisation and implementation of marine seismic arrays.

SCHULZE-GATTERMANN, R. 1972. Geophys. Prospect. 20 155-192. Physical Aspects of the "Airpulser".

SHAH, P.H. 1973. Geophysics 38 600-604. Ray tracing in three-dimensions.

SHUMWAY, G. 1960. Geophysics 25 451-467. Sound speed and absorption studies of marine sediments by a resonance method.

SMITH, S.G. 1972. Dept. Geodesy & Geophysics internal report. The basics of seismic reflection profiling.

SMITH, S.G. & OWEN, T.R.E. 1973. Dept. Geodesy & Geophysics internal report. G^2 sonobuoys: impulse responses and gains.

SMITH, S.G. 1974. 14th Congres-Assemblee pleniere de la CIESM. A three-dimensional reflection profiling survey in the Eastern Mediterranean.

SMITH, S.G. 1975. Geophys. J. Roy. Astr. Soc. 42 273--283. Measurement of Airgun Waveforms.

SMITH, S.G. & OWEN, T.R.E. 1975. Dept. Geodesy & Geophysics internal report. G^2 reflection system: frequency response.

STRICK, E. 1970. Geophysics 35 387-403. A Predicted Pedestal Effect for Pulse Propagation in Constant-Q Solids.

TANER, M.T., COOK, E.E., & NEIDELL, N.S. 1970. Geophysics 35 551-573. Limitations of the reflection seismic system; lessons from computer simulations.

THORP, W.H. 1965. J. Acoust. Soc. Amer. 38 648. Deep-Ocean Sound Attenuation in the Sub-and Low-Kilocycle-per -second region.

TREITEL, S. & ROBINSON, E.A. 1969 Geophys. Prospect. 17 248-293. Optimum Digital Filters for signal to noise ratio enhancement.

TROREY, A.W. 1970. Geophysics 35 762-784. A simple theory for seismic diffractions.

TULLOS, F.N. & REID, A.C. 1969. Geophysics 34 516-528. Seismic Attenuation for Gulf Coast Sediments.

VACQUIER, V., STEENLAND, N.C., HENDERSON, R.G. & ZIETZ, I. 1951. Geol. Soc. Amer. Memoir. 47. Interprertation of Aeromagnetic Maps.

WOODSIDE, J.M. 1974. 14th Congres-Assemblee pleniere de la CIESM. Seismic reflection survey in the Easten Mediterranean Sea.

WOODSIDE, J.M. 1974 14th Congres-Assemblee pleniere de la CIESM. Gravity anomalies in the Eastern Mediterranean and their implications.

WOOLLARD, G.P. 1962. Wisconsin Univ. Geophysics & Polar Research Centre, Research Dept. Ser. no. 62-9. The relation of gravity anomalies to surface elevation, crustal structure and geology.

WORLD DATA CENTRE A. 1974. Boulder Colorado 80302. Geomagnetic and Solar Data.

WUENSCHEL, P.C. 1965. Geophysics 30 539-551. Dispersive Body Waves - an experimental study

ZIOLKOWSKI, A. 1970. Geophys. J. Roy. Astr. Soc. 21 137-161. A method for calculating the output pressure waveform from an airgun.

ZIOLKOWSKI, A. 1971 Geophys. J. Roy. Astr. Soc. 23 499-530. Design of a marine seismic reflection profiling system using air guns as a sound source.